SMIP20

SMIP20 SEMINAR ON
UTILIZATION OF STRONG-MOTION DATA

October 22, 2020

PROCEEDINGS

Sponsored by

California Strong Motion Instrumentation Program
California Geological Survey
California Department of Conservation

Co-Sponsors

California Seismic Safety Commission
California Governor's Office of Emergency Services
Office of Statewide Health Planning and Development
California Department of Transportation

California
Department of
Conservation
California Geological Survey

The California Strong Motion Instrumentation Program (CSMIP), a program within the California Geological Survey (CGS) of the California Department of Conservation, records the strong shaking of the ground and structures during earthquakes for analysis and utilization by the engineering and seismology communities, through a statewide network of strong motion instruments (www.conservation.ca.gov/CGS/smip). CSMIP is advised by the Strong Motion Instrumentation Advisory Committee (SMIAC), a committee of the California Seismic Safety Commission. Major program funding is provided by an assessment on construction costs for building permits issued by cities and counties in California, with additional funding from the California Governor's Office of Emergency Services (Cal OES), the Office of Statewide Health Planning and Development (OSHPD) and the California Department of Transportation (Caltrans)

In July 2001, the California Governor's Office of Emergency Services (Cal OES) began funding for the California Integrated Seismic Network (CISN), a newly formed consortium of institutions engaged in statewide earthquake monitoring that grew out of TriNet, funded by FEMA, and including CGS, USGS, Caltech and UC Berkeley. The goals are to record and rapidly communicate ground shaking information in California, and to analyze the data for the improvement of seismic codes and standards (www.cisn.org). CISN produces ShakeMaps of ground shaking, based on shaking recorded by stations in the network, within minutes following an earthquake. The ShakeMap identifies areas of greatest ground shaking for use by OES and other emergency response agencies in the event of a damaging earthquake.

The Center for Engineering Strong Motion Data (CESMD) is operated by the CSMIP in cooperation with the National Strong-Motion Project (NSMP), a part of the Advanced National Seismic System (ANSS) of the U.S. Geological Survey (USGS). The CESMD builds on and incorporates the CISN Engineering Data Center and will continue to serve the California region while expanding to serve other ANSS regions. The Data Center provides strong-motion data rapidly after a significant earthquake in the United States. Users also have direct access to data from previous earthquakes and detailed information about the instrumented structures and sites. The CESMD also provides access to the U.S. and international strong ground motion records through its Virtual Data Center (VDC). The Data Center is co-hosted by CGS and USGS at www.strongmotioncenter.org

DISCLAIMER

SMIP20

SMIP20 SEMINAR ON
UTILIZATION OF STRONG-MOTION DATA

October 22, 2020

PROCEEDINGS

Edited by

Daniel Swensen

Sponsored by

California Strong Motion Instrumentation Program
California Geological Survey
California Department of Conservation

Co-Sponsors

California Seismic Safety Commission
California Governor's Emergency Services
Office of Statewide Health Planning and Development
California Department of Transportation

PREFACE

The California Strong Motion Instrumentation Program (CSMIP) in the California Geological Survey of the California Department of Conservation established a Data Interpretation Project in 1989. Each year CSMIP funds several data interpretation contracts for the analysis and utilization of strong-motion data. The primary objectives of the Data Interpretation Project are to further the understanding of strong ground shaking and the response of structures, and to increase the utilization of strong-motion data in improving post-earthquake response, seismic code provisions and design practices.

As part of the Data Interpretation Project, CSMIP holds annual seminars to transfer recent research findings on strong-motion data to practicing seismic design professionals, earth scientists and post-earthquake response personnel. The purpose of the annual seminar is to provide information that will be useful immediately in seismic design practice and post-earthquake response, and in the longer term, useful in the improvement of seismic design codes and practices. Proceedings and individual papers for each of the previous annual seminars are available at http://www.conservation.ca.gov/cgs/smip/seminar in PDF format. Due to State budget constraints, CSMIP did not hold an annual seminar in 2010 or 2011. The SMIP20 Seminar is the twenty-ninth in this series of annual seminars.

The SMIP20 Seminar is divided into two sessions in the morning and two sessions in the afternoon. There are seven presentations on the results from CSMIP-funded projects and two invited presentations. The sessions in the morning include four presentations. The first session will focus on ground motion issues. Professor Stewart of UCLA will present on the application of HVSR parameters in ergodic site response modeling. He will be followed by a presentation from Professor Bozorgnia of UCLA on ground motions recorded during the 2019 Ridgecrest earthquake sequence. The second session will also focus on ground motion issues. Professor Taciroglu of UCLA will present on nonlinear dynamic soil properties characterized from geotechnical array data. Doctor Roten of San Diego State University will then present on site amplification estimates from geotechnical array data.

The two sessions in the afternoon include five presentations which focus on structural response topics. In the third session, Professor Kunnath of UC Davis will present on ASCE-41 acceptance criteria for linear and nonlinear procedures. He will be followed by a presentation from Professor Zareian of UC Irvine on code torsional provisions for semi-rigid diaphragms. The last session will include a presentation on bridge health monitoring by Professor Mosalam of UC Berkeley, and two invited presentations on structural health monitoring topics by Doctor Farrar of Los Alamos National Laboratory and Professor McCallen of the University of Nevada Reno. Individual papers and the proceedings are available for download by the SMIP20 participants at the provided link, and will be available at the CSMIP website in the future.

Daniel Swensen
CSMIP Data Interpretation Project Manager

Appreciation to Members of the Strong Motion Instrumentation Advisory Committee

Main Committee

Farzad Naeim, Chair, Farzad Naeim, Inc.
Norman Abrahamson, Pacific Gas & Electric Company
Bruce Clark, Leighton & Associates
Martin Eskijian, California State Lands Commission (retired)
David Gutierrez, GEI Consultants
Wilfred Iwan, California Institute of Technology
Mark Mahan, Caltrans
Marshall Lew, Wood
Bret Lizundia, Rutherford + Chekene
Chris Tokas, Office of Statewide Health Planning and Development
Robert Anderson (ex-officio), Seismic Safety Commission

Ground Response Subcommittee

Marshall Lew, Chair, Wood
Zia Zafir, Kleinfelder
Geoffrey Martin, Univ. of Southern California

Buildings Subcommittee

Bret Lizundia, Chair, Rutherford + Chekene
Lucie Fougner, Degenkolb Engineers
Ifa Kashefi, City of Los Angeles (retired)
Michelle Yu, City of San Francisco
Eduardo Miranda, Stanford University
Roy Lobo, Office of Statewide Health Planning and Development
Chia-Ming Uang, UC San Diego

Lifelines Subcommittee

Martin Eskijian, Chair, California State Lands Commission (retired)
David Gutierrez, GEI Consultants
Mark Mahan, Caltrans
Faiz Makdisi, SAGE Engineers

Data Utilization Subcommittee

Wilfred Iwan, Chair, California Institute of Technology
Representatives from each Subcommittee

TABLE OF CONTENTS

SMIP20 SEMINAR ON UTILIZATION OF STRONG-MOTION DATA

October 22, 2020

FINAL PROGRAM

9:00 am **WELCOMING REMARKS**
Farzad Naeim, Chair, Strong Motion Instrumentation Advisory Committee (SMIAC)
Steve Bohlen, Acting State Geologist, California Geological Survey (CGS)

9:20 am **INTRODUCTION**
Hamid Haddadi, Program Manager, California Strong Motion Instrumentation Program
Dan Swensen, Senior Civil Engineer, California Strong Motion Instrumentation Program

Session I

Moderator: *Marshall Lew*, Wood and SMIAC

9:30 am **Towards Application of HVSR Parameters in Ergodic Site Response Modeling: Database and Implementation Issues**
Tatiana Gospe, Paolo Zimmaro, Pengfei Wang, Tristan Buckreis, Scott J. Brandenburg and *Jonathan P. Stewart*, UC Los Angeles

Sean Ahdi and Alan Yong, US Geological Survey

10:00 am **Analysis of Ground Motions Recorded During the 2019 Ridgecrest Earthquake Sequence**
Silvia Mazzoni, Pengfei Wang, Chukwuebuka Nweke, Nicolas Kuehn, Jonathan Stewart and *Yousef Bozorgnia*, UC Los Angeles

Tadahiro Kishida, Khalifa University of Science and Technology

Sean Ahdi, US Geological Survey

10:30 am **Break**

Session II

Moderator: *Zia Zafir*, Kleinfelder and SMIAC

11:00 am **Characterization of Nonlinear Dynamic Soil Properties from Geotechnical Downhole Array Data**
S. Farid Ghahari and *E. Taciroglu*, UC Los Angeles

11:30 am **Estimation of Site Amplification from Geotechnical Array Data using Neural Networks**
Daniel Roten and Kim B. Olsen, San Diego State University

12:00 pm **Lunch Break**

Session III

Moderator: *Bret Lizundia*, Rutherford + Chekene and SMIAC

1:00 pm **Assessing ASCE-41 Acceptance Criteria for Linear and Nonlinear Procedures using Instrumented Building Data**
Laura Hernandez-Bassal and *Sashi Kunnath*, UC Davis

1:30 pm **Critical Assessment of Code Torsional Provisions for Low-Rise Buildings with Semi-Rigid Diaphragms**
Farzin Zareian, UC Irvine

2:00 pm **Break**

Session IV

Moderator: *Martin Eskijian*, California State Lands Commission and SMIAC

2:30 pm **Human-Machine Collaboration Framework for Bridge Health Monitoring**
Sifat Muin, Chrystal Chern and *Khalid M. Mosalam*, UC Berkeley

3:00 pm **Recent Developments in Structural Health Monitoring**
Charles R. Farrar, Los Alamos National Laboratory

3:20 pm **An Optical Sensor and Wireless Mesh Network for Direct Measurement of Building Interstory Drift**
David McCallen, Floriana Petrone and Patrick Laplace, University of Nevada Reno

3:40 pm **Adjourn**

HVSR DATABASE AND MULTI-MEASUREMENT CONSISTENCY FOR CALIFORNIA SITES

T. Gospe[(1)], P. Wang [(1)], P. Zimmaro[(1,2)] , J.P. Stewart[(1)]

[(1)] Department of Civil & Environmental Engineering, UCLA
[(2)] University of Calabria, Italy

Abstract

Frequency-dependent horizontal-to-vertical spectral ratios (HVSR) can provide information on site resonant frequencies, which are potentially useful for predicting site amplification. We adapt a relational database developed to archive and disseminate V_S data to include HVSR and investigate the consistency of HVSR derived from different measurements of ambient noise (temporary instruments, permanent instruments) and earthquake recordings. The database as a whole consists of 2,797 sites in California. HVSR consistency is analyzed using subsets of sites with multiple data sources; noise and seismic data are consistent for 60% of sites, whereas different noise measurements have about 75% consistency.

Keywords: horizontal-to-vertical spectral ratios, resonant frequencies, site response, relational database

Introduction

Seismic site response is influenced by several factors, including: resonance, nonlinearity, amplification due to impedance contrasts, and amplification related to wave propagation in sedimentary basins. Ground-motion models predict site response conditioned on relatively simple site parameters such as the time-averaged shear wave velocity (V_S) to 30 m depth (V_{S30}) and the depth to 1 km/s or 2.5 km/s V_S ($z_{1.0}$ or $z_{2.5}$) (Bozorgnia et al., 2014). These models are referred to as ergodic (Anderson and Brune, 1999) even if the site parameters are measured on site. The underlying models are ergodic because they are derived from large global or regional databases, and as such are not site-specific.

Any particular site would be expected to produce site amplification that departs from the ergodic estimate for a variety of reasons related to location-specific geologic conditions. A site amplification model that accounts for the effects of these features on site amplification is non-ergodic (e.g., Stewart et al., 2017). One common feature of non-ergodic site response is resonance at one (fundamental site frequency, f_0) or more site frequencies (Di Alessandro et al., 2012; Bonilla et al., 2002; Bonilla et al., 1997), which produce peaks that are smoothed out in ergodic models. While not currently used in NGA models nor in general practice, horizontal-to-vertical Fourier amplitude spectral ratio (HVSR) vs. frequency plots have the potential to add this site-specific attribute to predictions of ergodic site response at low cost, relative to non-ergodic procedures. While V_{S30} provides a reasonable, first-order estimate of site response over a wide frequency range (Seyhan and Stewart 2014), f_0 can be effective at describing site amplification for frequencies proximate to f_0, but it has limited utility elsewhere. Hence, the two parameters serve different purposes and we postulate that they can be most effectively utilized together (Cadet et al., 2012; Gofrani et al., 2013).

Current HVSR-based site amplification models, whether using HVSR parameters solely (e.g., Zhao and Xu 2013; Ghofrani et al. 2013; Hassani and Atkinson 2016), or in combination with V_{S30} (Cadet et al. 2012; Kwak et al. 2017; Hassani and Atkinson 2017, 2018; Hashash et al. 2020), are derived using HVSR computed from the same earthquake ground motion data that is being predicted by the model. This model development practice is inconsistent with how the models would be used in forward applications, which will typically be for sites without earthquake recordings. We posit that for HVSR to gain traction in California practice, several technical issues need to be addressed. Among these are the following:

1. Practical best practices for collecting and analyzing HVSR data need to be developed and agreed upon by the informed technical community.

2. A database of HVSR data, assembled to the extent possible in a manner consistent with best practices, should be provided and made publically available.

3. Procedures for identifying when HVSR peaks are present and should be used in model development are needed, as well as procedures for characterizing those peaks (i.e., frequency, amplitude, width).

4. The reliability of HVSR peaks as established from a particular noise-based measurement is needed, under the assumption that the measurement is made by a credible analyst. The issue in this case is the repeatability of HVSR when measured from noise at different times or with different equipment.

5. The consistency of HVSR peaks as established from earthquake data and noise is needed. Noise-based measurements will dominate practical forward applications, but they are intended to predict earthquake shaking attributes. As a result, consistency between HVSR from these two data sources is desirable.

6. Development of HVSR-based site amplification models conditioned on interpretations of HVSR data (i.e., identification of peaks, peak parameters) in combination with V_{S30} and perhaps sediment depth.

The aforementioned models derived from ground motion-based HVSR in effect assume that earthquake- and noise-based HVSR are perfectly consistent (Issue 5) and that noise-based HVSR measurement are fully repeatable (Issue 4).

This paper presents work on the first five issues described above. We extend a V_S profile database (PDB), an early version of which is described by Ahdi et al. (2018), to incorporate HVSR data. Gospe et al. (2020) present a schema for the HVSR components of the database, which shows information that is stored and the results that can be readily extracted for ground motion studies. That paper also explains the data processing procedures and the procedures used to compute HVSR from the data. We describe here the data acquisition process and external (to the database) routines that can be used to evaluate the presence of peaks and identify HVSR-related parameters used for site response studies. The 4th and 5th issues above are also taken up in a preliminary manner using a subset of the full dataset for which noise signals are available from two sources and earthquake recordings are available.

Data Sources

Instrument Types

The database is structured to allow entry of HVSR data from three sources: (1) microtremor array measurements (MAM) obtained from temporary deployments of three-component seismometers specifically targeting noise measurement (Yong et al., 2013); (2) three-component instruments installed temporarily or in permanent housings to record ground motions, but which can also be used to record non-seismic natural ground vibrations noise) -- often these instruments continuously stream data that can be captured; and (3) seismic strong motions (Hassani et al., 2019). Most of the data in NGA databases is from strong motion accelerographs, some of which currently operate with continuous streaming and others of which are triggered. Moreover, modern deployments often feature strong motion accelerographs and co-located relatively sensitive seismometers. Among sites with accelerometers, we have collected HVSR data from sites with co-located continuously-streamed seismometers and we are currently in the process of evaluating the potential for doing this for sites having only accelerometers. For the development of HVSR-based site amplification models, sources 1 and 2 are preferred because these match the data type that would generally be used in forward applications.

Source 1 obtains data from velocity transducers such as Trillium sensors, which are broadband seismometers, whereas Sources 2 and 3 may utilize seismometers or accelerometers. Figure 1 demonstrates the bandwidth and gain for different sensors. Different colors correspond to different sensors, and the dotted vertical line indicates the threshold for the sensors' frequency range. The 40T1, L28, L22, L4C, S13, HS10 and the STS2, 3T, ESP, 40T30, TR240, TR120, TR40 are short period and broadband sensors, respectively (Figure 1). The sensors with the largest bandwidth and highest gain are ideal for our analysis because these sensors provide the best signal resolution. Source 2 may come from velocity transducers or 24-bit accelerometers, and the sensor response with respect to period and signal amplitude is illustrated in Figure 2. In Figure 2, broadband seismometers such as the STS1 capture low earth noise, and accelerometers capture earthquakes. In our study 24-bit accelerometers are likely required so that microtremor signals can be captured.

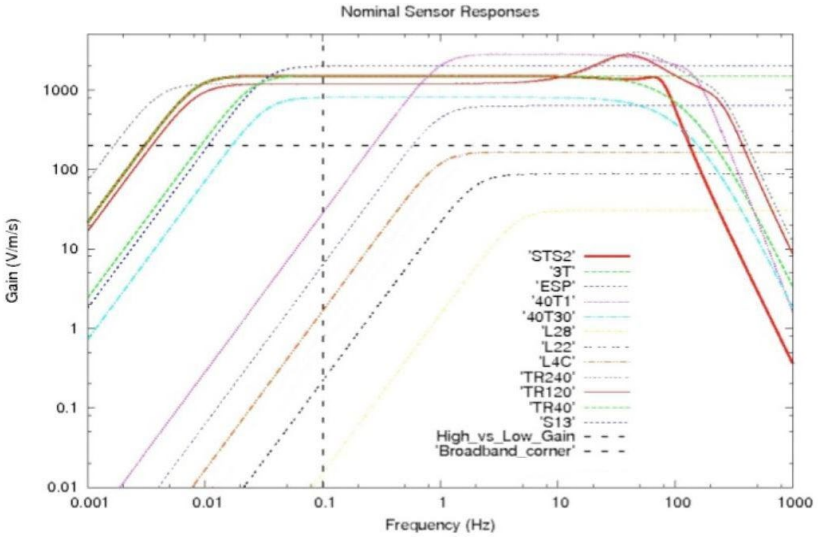

Figure 1. Different sensor responses and the cutoff between broadband and short period sensors as well as low versus high gain sensors. (after IRIS PASSCAL, 2020)

A potential challenge with the use of accelerometers, as might be used with Sources 2-3, is their ability to capture meaningful signals over the frequency range of interest. As shown in Figure 2, the motions from "low earth noise" fall below the range from accelerometers; if true, this suggests that accelerometers cannot record meaningful noise signals for HVSR analysis. Anecdotal evidence, shown in Figure 3, in which HVSR from co-located seismometers and accelerometers are compared, demonstrates how HVSR from accelerometers may not capture low-frequency peaks (in this case below 3 Hz).

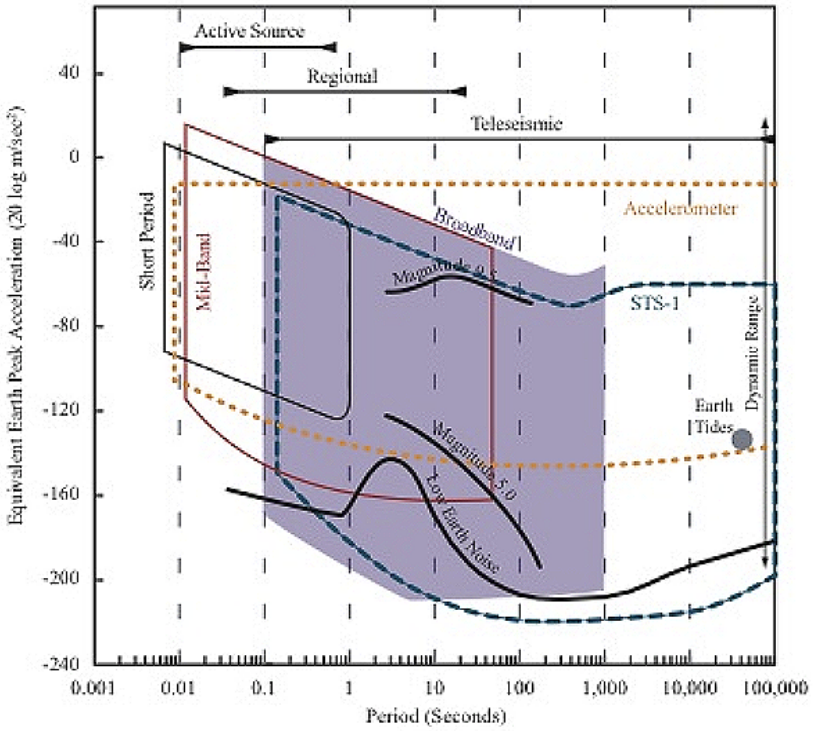

Figure 2. Period and signal amplitudes with respect to sensor response.

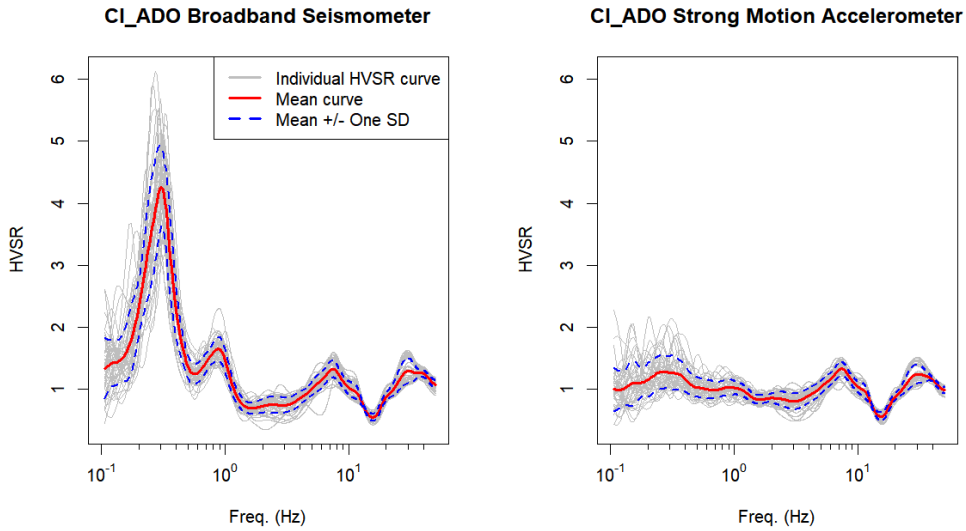

Figure 3. Comparison of HVSR between broadband seismometer and strong motion accelerometer

HVSR Site Inventory

While in California around 1,700 *Vs* profiles are publicly available via the PDB (Ahdi et al., 2018), no HVSR site data was available from a public repository in California prior to the present effort. We have assembled a database for HVSR data, which is an extension of the PDB. Because of its preferred utility for site response model development, we have emphasized Source 1 and 2 data in populating the database.

The largest inventory of Source 1 HVSR data at strong motion stations is Yong et al. (2013). The study (aka: American Recovery and Reinvestment Act funded project; hereafter as ARRA project) presents data from 191 strong-motion stations, the majority of which are located in California (187 stations), with an additional four stations in the central and eastern United States. The ARRA data was provided as time-domain signals, which was processed in the manner described in Section 3 of this paper. Yong et al. (2013) provide 589 HVSR results for the 191 sites, due to multiple measurements at most sites. Another major data source is Geometrics, which shared HVSR from 638 sites. This data was provided as mean HVSR-frequency curves, which has been digitized and added to the database. Additional Source 1 contributions included in the database include:

1. 33 sites in the Sacramento-San Joaquin Delta (T. Buckreis, personal communication, 2020).

2. 40 ground motion accelerograph sites maintained by the California Strong Motion Instrumentation Program (CSMIP), part of the California Geological Survey (CGS). Reports are from GEOVision (GEOVision, 2016), Petralogix (Petralogix, 2017), and GEOVision (GEOVision, 2018).

3. 24 sites, some of which are ground motion stations, investigated as part of non-ergodic ground motion investigations by ENGEO (D. Teague, personal communication, 2020).

Time series data from the Delta sites was processed as in Section 3 below. For the CSMIP and ENGEO sites, we obtained mean HVSR-frequency plots, which were added to the database following digitization.

For Source 2, we queried three data centers: Incorporated Research Institutions for Seismology (IRIS), Southern California Earthquake Data center (SCEDC), and the Northern California Earthquake Data Center (NCEDC) (IRIS, 2020; SCEDC, 2013; NCEDC, 2014). We sampled continuously streamed data for 404 sites instrumented with high-gain seismometers with sampling rates between 80-250 Hz. The time series from these data were processed using procedures in Section 3.

Altogether, the database currently contains HVSR data for 1330 sites, locations of which are shown in Figure 4. Many of these sites, including all of the ARRA sites, have HVSR from both Source 1 and Source 2, which causes the number of HVSR entries (1728) to exceed the number of sites (1330). Of the 1330 sites with HVSR, 668 are located in the immediate vicinity of strong motion stations.

Using the data currently incorporated into the PDB, Figure 5 shows the relative number of *Vs* profiles and HVSR sites in California. Whereas various techniques have been

used to collect profile data since the 1960s, the collection of HVSR data is much more recent. The sudden jump in microtremor data is from the present project, using the above sources.

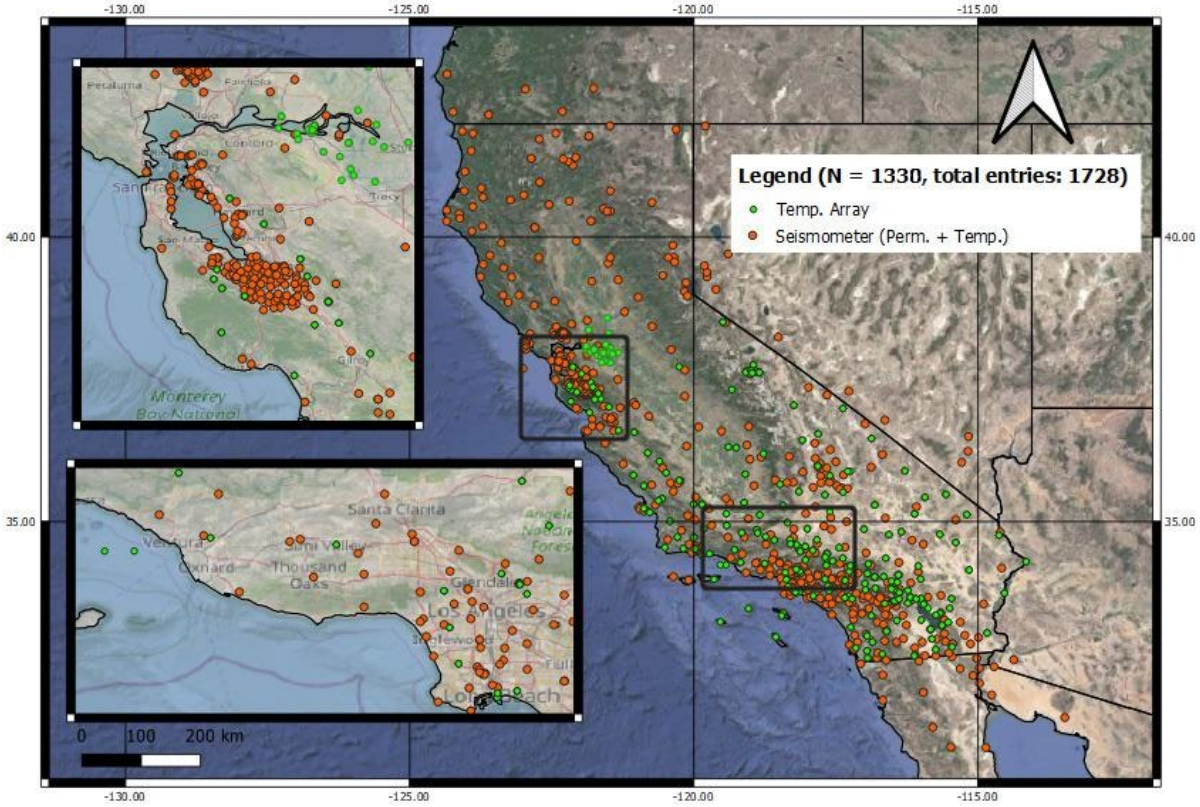

Figure 4. Locations of sites in PDB with HVSR from either temporary deployments (MAM) or continuously streaming ground motion sensors (seismometers).

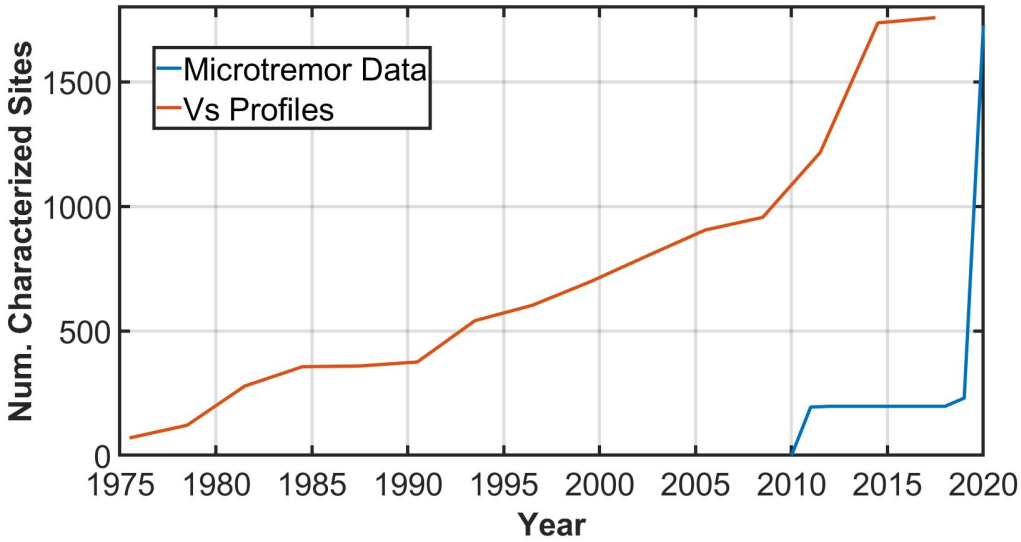

Figure 5. Cumulative distribution of V_S profiles and HVSR data in California versus time.

Data Interpretation Tools

The HVSR database provides plots of median-component (RotD50, per Boore 2010) or geometric mean HVSR between time windows and tables showing azimuthal variations

but does not provide specific parameters derived from these results, such as might be used as site parameters to supplement V_{S30}. To facilitate such applications, the HVSR data archived in the relational database can be accessed via online Jupyter Notebook tools (example output in Figure 6) or R-scripts. These tools interact with the data to interpret the data. The interpreted parameters include (1) identification of features as peaks; (2) plots of azimuthal variations of HVSR; and (3) for each peak in the median-component HVSR, fitting of a pulse function to evaluate peak frequency, peak amplitude, and width of peak. Jupyter notebooks are currently available for (2) and R-scripts are available for (1) and (3) (Jupyter notebooks for these tasks are in preparation as of this writing). We envision that such post-processing tools will be used to analyze the data in the cloud without the need to download data locally.

Figure 6 shows an example RotD50 HVSR for the CI.GR2 site (Griffiths Park Observatory) in Los Angeles, California. Site CI.GR2 is located near the nose of a ridge in the Santa Monica Mountains; azimuths from approximately 0-45 deg align approximately with the ridgeline axis, whereas azimuths of 90-180 deg are oriented down-slope for different portions of the ridge nose. The strongest 1 Hz resonance is between azimuths ≈ 110-170 deg, which roughly aligns with the down-slope directions. In these down-slope directions, we expect topographic amplification effects to be strongest (Di Giulio et al., 2009).

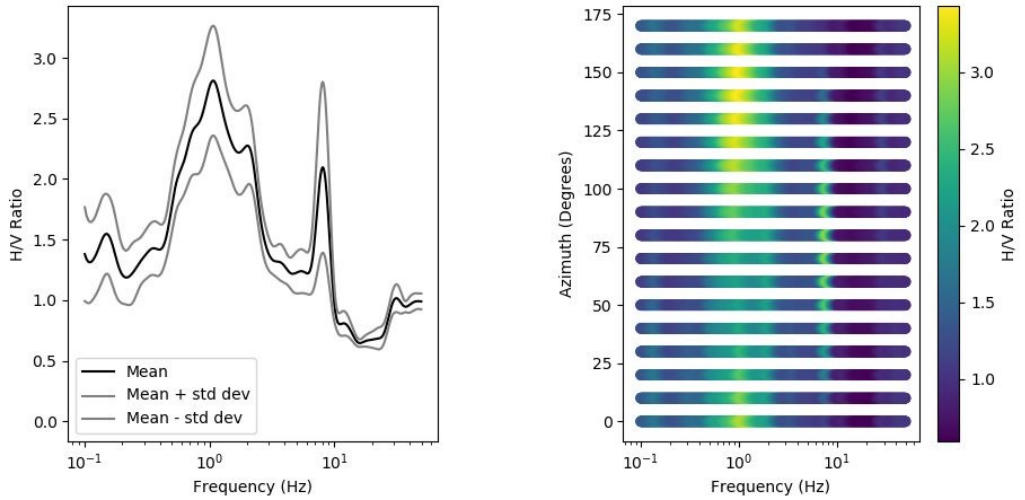

Figure 6. A site near the Griffith Park Observatory in Los Angeles (CI.GR2). Left: frequency versus HVSR from a microtremor recording; right: azimuthal variation of the same recording.

Peak Identification

HVSR plots can generally be classified as containing no peaks, one peak, or multiple peaks. If there are multiple peaks, we identify the first two peaks (i.e., the two peaks at the lowest frequencies). A peak generally indicates the site has strong impedance contrast(s) near one or more modal frequencies (e.g., Tuan et al., 2011) whereas multiple peaks may indicate multiple impedance contrasts at different depths. When there is no peak present in an HVSR, this suggests the site is either underlain with a sediment-filled depth profile that lacks a significant impedance contrast or it is a rock site with nearly depth-invariant near-surface velocities.

The mean HVSR curve is used for peak identification. SESAME guidelines (SESAME, 2004) provide a procedure for the identification of peaks that first considers three criteria that assess the reliability of the HVSR curve and then considers six conditions intended to establish the presence of a clear HVSR peak. The first two criteria for the

reliability of HVSR curves constrain the minimum required number of sub-windows and duration; these requirements are accounted for in the query and processing procedures described by Gospe et al. (2020). Hence, the additional procedures used to identify peaks are the third reliability criterion and the six conditions, which are listed in Table 1.

Table 1. Reliability criterion and conditions for peak identification from SESAME (2004)

Parameters	CESAME
Reliability 3: $f_{\text{peak}} > 0.5\,\text{Hz}, f \in [0.5f_{\text{peak}}, 2f_{\text{peak}}]$	$\sigma_A(f) < 2$
Reliability 3: $f_{\text{peak}} < 0.5\,\text{Hz}, f \in [0.5f_{\text{peak}}, 2f_{\text{peak}}]$	$\sigma_A(f) < 3$
Clear 1: $f \in [0.25f_{\text{peak}}, f_{\text{peak}}]$	$A_{H/V}(f) < 0.5A_{\text{peak}}$
Clear 2: $f \in [f_{\text{peak}}, 4f_{\text{peak}}]$	$A_{H/V}(f) < 0.5A_{\text{peak}}$
Clear 3:	$A_{\text{peak}} >= 2$
Clear 4: peak of SD curve $f_{\text{peak}}[A_{H/V}(f) - \sigma_A(f)]$	within $[f_{\text{peak}}/1.05, 1.05f_{\text{peak}}]$
Clear 4: peak of SD curve $f_{\text{peak}}[A_{H/V}(f) + \sigma_A(f)]$	within $[f_{\text{peak}}/1.05, 1.05f_{\text{peak}}]$
Clear 5: $f_{\text{peak}} < 0.2\,\text{Hz}$	$\sigma_f < 0.25f_{\text{peak}}$
Clear 5: $f_{\text{peak}} \in [0.2, 0.5)\,\text{Hz}$	$\sigma_f < 0.2f_{\text{peak}}$
Clear 5: $f_{\text{peak}} \in [0.5, 1.0)\,\text{Hz}$	$\sigma_f < 0.15f_{\text{peak}}$
Clear 5: $f_{\text{peak}} \in [1.0, 2.0]\,\text{Hz}$	$\sigma_f < 0.1f_{\text{peak}}$
Clear 5: $f_{\text{peak}} > 2.0\,\text{Hz}$	$\sigma_f < 0.05f_{\text{peak}}$
Clear 6: $f_{\text{peak}} < 0.2\,\text{Hz}$	$\sigma_A(f_{\text{peak}}) < 3$
Clear 6: $f_{\text{peak}} \in [0.2, 0.5)\,\text{Hz}$	$\sigma_A(f_{\text{peak}}) < 2.5$
Clear 6: $f_{\text{peak}} \in [0.5, 1.0)\,\text{Hz}$	$\sigma_A(f_{\text{peak}}) < 2$
Clear 6: $f_{\text{peak}} \in [1.0, 2.0]\,\text{Hz}$	$\sigma_A(f_{\text{peak}}) < 1.78$
Clear 6: $f_{\text{peak}} > 2.0\,\text{Hz}$	$\sigma_A(f_{\text{peak}}) < 1.58$

In Table 1, f_{peak} is the peak frequency of interest (there could be multiple f_{peak} values in a single curve); f is the independent frequency; $A_{H/V}(f)$ is the amplitude of the HVSR mean curve at frequency f; A_{peak} is the amplitude at f_{peak}; $\sigma_A(f)$ is the standard deviation of $A_{H/V}(f)$ at f; $\sigma_A(f_{\text{peak}})$ is the standard deviation of $A_{H/V}(f)$ at f_{peak}; and σ_f is the standard deviation of f_{peak}. In Table 1, the rows labelled Reliability 3, Clear 5, and Clear 6 are f_{peak}-dependent. The greater f_{peak} is, the more stringent are the standards for establishing a peak as reliable and clear.

The six conditions consider factors such as the amplitude of the peak relative to ordinates at neighboring frequencies and the width of the peak. In the case of the CI.GR2 site, the conditions are all satisfied except for #5, which is not satisfied (the peak is too wide).

Examination of similar results from many sites suggest that the criteria in SESAME (2004) are too conservative. Alternative criteria are developed that are more effective at identifying the presence of peaks at California sites (Wang 2020). These criteria were established based on visual inspections of HVSR to identify sites with peaks, and for the subset of those sites that fail SESAME criteria, identification of the SESAME criteria that are not satisfied. The new recommended criteria are summarized in Table 2 which excludes the Clear 5 condition and weakens other conditions.

Table 2. Suggested new reliability criterion and peak identification conditions, modified from SESAME (2004) by Wang (2020).

Parameters	New Criteria
Reliability 3: $f_{\text{peak}} > 0.5\,\text{Hz}, f \in [0.5f_{\text{peak}}, 2f_{\text{peak}}]$	$\sigma_A(f) < 2$
Reliability 3: $f_{\text{peak}} < 0.5\,\text{Hz}, f \in [0.5f_{\text{peak}}, 2f_{\text{peak}}]$	$\sigma_A(f) < 3$
Clear 1: $f \in [0.25f_{\text{peak}}, f_{\text{peak}}]$	$A_{H/V}(f) < 0.6A_{\text{peak}}$
Clear 2: $f \in [f_{\text{peak}}, 4f_{\text{peak}}]$	$A_{H/V}(f) < 0.6A_{\text{peak}}$
Clear 3:	$A_{\text{peak}} >= 1.6$
Clear 4: peak of SD curve $f_{\text{peak}}[A_{H/V}(f) - \sigma_A(f)]$	within $[f_{\text{peak}}/1.15, 1.15f_{\text{peak}}]$
Clear 4: peak of SD curve $f_{\text{peak}}[A_{H/V}(f) + \sigma_A(f)]$	within $[f_{\text{peak}}/1.12, 1.12f_{\text{peak}}]$
Clear 5: $f_{\text{peak}} < 0.2\,\text{Hz}$	-
Clear 5: $f_{\text{peak}} \in [0.2, 0.5)\,\text{Hz}$	-
Clear 5: $f_{\text{peak}} \in [0.5, 1.0)\,\text{Hz}$	-
Clear 5: $f_{\text{peak}} \in [1.0, 2.0]\,\text{Hz}$	-
Clear 5: $f_{\text{peak}} > 2.0\,\text{Hz}$	-
Clear 6: $f_{\text{peak}} < 0.2\,\text{Hz}$	$\sigma_A(f_{\text{peak}}) < 3$
Clear 6: $f_{\text{peak}} \in [0.2, 0.5)\,\text{Hz}$	$\sigma_A(f_{\text{peak}}) < 2.5$
Clear 6: $f_{\text{peak}} \in [0.5, 1.0)\,\text{Hz}$	$\sigma_A(f_{\text{peak}}) < 2$
Clear 6: $f_{\text{peak}} \in [1.0, 2.0]\,\text{Hz}$	$\sigma_A(f_{\text{peak}}) < 1.78$
Clear 6: $f_{\text{peak}} > 2.0\,\text{Hz}$	$\sigma_A(f_{\text{peak}}) < 1.58$

An R script implements these criteria and determines if an HVSR curve contains a peak. The R script allows the user to select the conditions to be satisfied for assessing the presence of a peak, and notifies the user of which conditions the a particular peak satisfies.

Peak Fitting

For mean HVSR plots with a peak, we fit a Gaussian pulse function adapted from Hassani and Atkinson (2016) as follows (Wang 2020):

$$F_{H/V,i} = c_{0,i} + c_{1,i} exp\left[(-\frac{1}{2}\left(\frac{ln(f/f_{pi})}{2w_i}\right)^2\right] \quad (1)$$

where f_{pi} is the fitted peak frequency, $c_{1,i}$ is the peak amplitude relative to $c_{0,i}$, w_i is peak width, $c_{0,i}$ is a frequency-independent constant, i is the order of peak, and f is frequency in Hz. The fit is performed using nonlinear regression in R with the *Optim* function, which minimizes the sum of squared errors. Figure 7 shows results for the CI.GR2 site, which contains a peak of amplitude 2.8 at frequency 1.2 Hz.

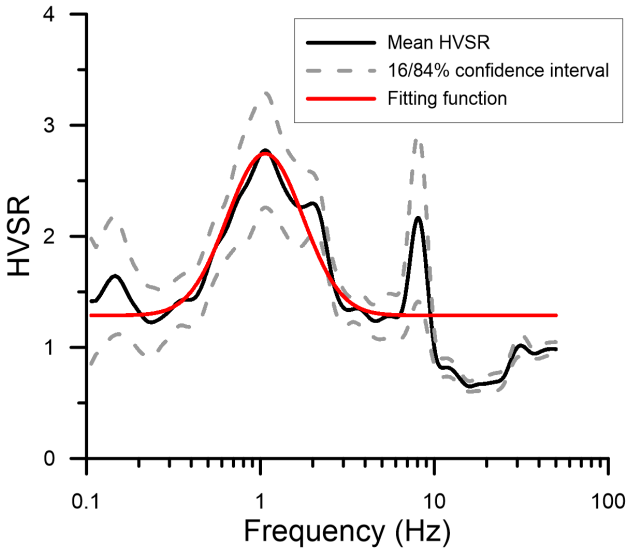

Figure 7. RotD50 HVSR for CI.GR2 site with Gaussian fit to the peak using Eq. (1).

HVSR Comparisons Between Data Sources

In the HVSR database, we have processed and stored three types of data, microtremor array measurements (MAM), microtremor noise queried from permanently installed seismometers continuously streamed data (CSD), and recorded seismic ground motions. As described in the Introduction, the reliability and consistency of HVSR are important questions related to the eventual development of practice-oriented HVSR models. Here we perform a preliminary investigation of these questions using a dataset consisting of 102 sites with both MAM and CSD HVSR, and a related dataset of 138 sites with both noise and seismic HVSR. In the following subsections, we investigate differences in noise-vs-seismic HVSR and noise-based HVSR. The comparisons are made in terms of presence of peaks, fitted peak frequencies, and fitted peak amplitudes.

Comparison Between Earthquake- and Noise-Based HVSR

As described in Section 3.1, HVSR mean curves can be classified into two broad categories, clear peaks and no peaks. Using the criteria in Section 3.1, we have identified the presence of peaks for a group of 138 sites with HVSR from common instruments that have recorded earthquake motions and CSD. The 138 sites can be divided into four groups: (1) both data sources produce peaks, (2) both data sources produce no peak, (3) earthquake ground motion HVSR has a peak but CSD HVSR does not, and (4) CSD HVSR has a peak but earthquake ground motion HVSR does not. The breakdown of sites into these four groups is presented in Table 3. Figure 8 shows examples of "P-P", "N-N", "N-P", and "P-N" sites.

Table 3. The comparison of peaks presence from HVSR computed using strong motion and CSD

Eqk: CSD	**Pk.: Pk.**	**No Pk. : No Pk.**	**No Pk. : Pk.**	**Pk.: No Pk.**
Count	39	45	35	19
Percent	~28%	~33%	~25%	~14%

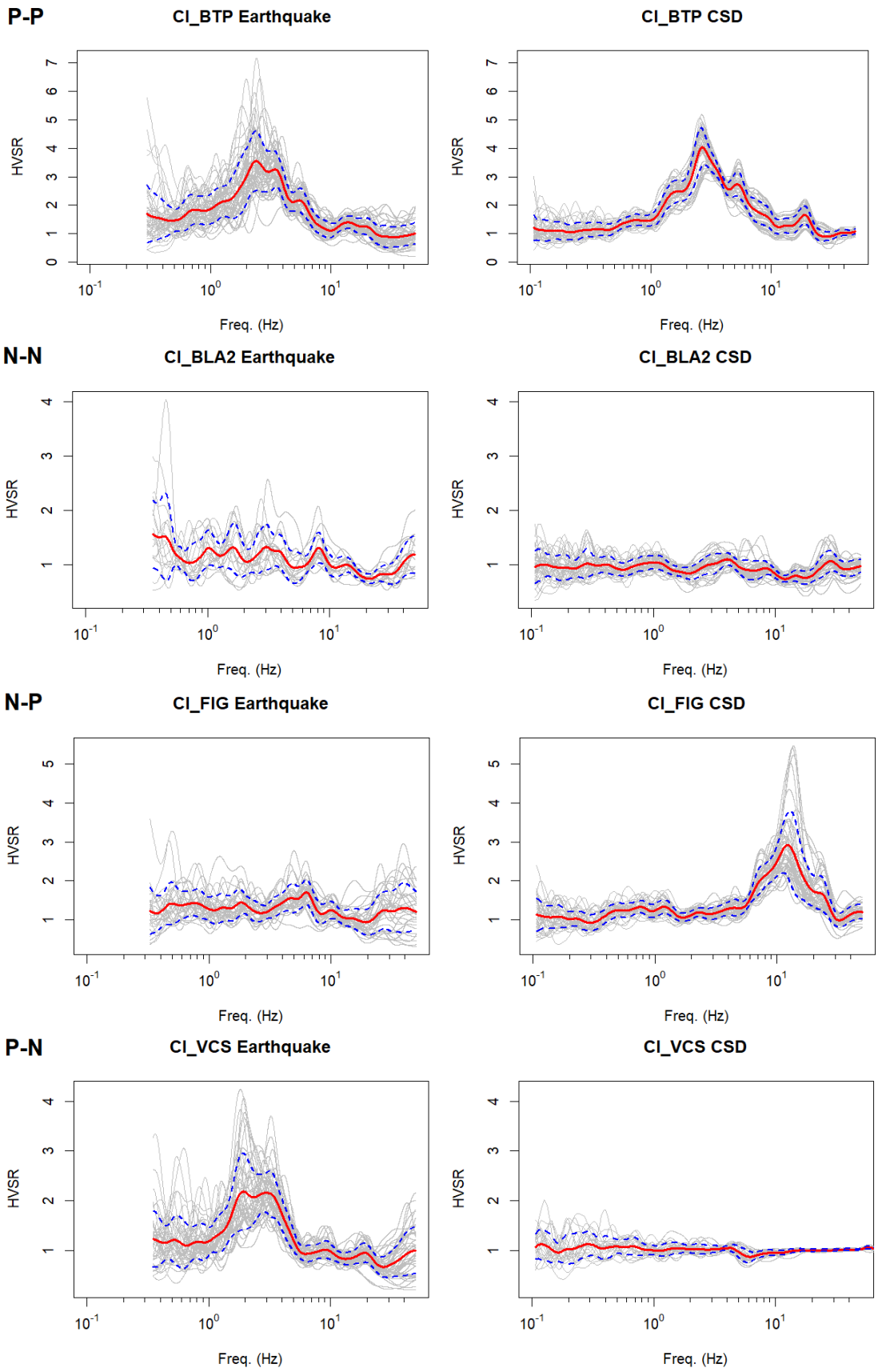

Figure 8. The examples of HVSR for "P-P", "N-N", "N-P", and "P-N" sites.

Table 3 shows that 61% of sites produce consistent results from the noise and earthquake HVSR ("P-P" and "N-N" groups) . Among the 74 sites with peaks from noise-based HVSR, approximately half have peaks in seismic HVSR. This suggests the potential for a significant rate of "false positives" (peaks identified from noise that are not present in ground motions). Among the 64 sites without peaks from noise-based HVSR, approximately ⅔ also lack peaks in seismic HVSR. This suggests a relatively low rate of false negatives. If these rates of false positives and false negatives persist in the larger database that will be used for model development, it will add uncertainty to HVSR-based models.

An additional important question is: if HVSR from both data sources have peaks, then how do the fitted coefficients from the two sources compare? To investigate this question, we compare fitted parameters for the 39 "P-P" sites in Figure 9. The figure shows that most points are along the 45-degree line (15 sites have f_p misfits < 20%), however, 9 sites have misfits that exceed a factor of four. Overall, the peak frequencies are moderately correlated (correlation coefficient, $\rho = 0.65$). The plot of a_p indicates a weaker correlation. There are more points below the 45-degree line, which indicates that peak amplitudes from earthquake HVSR are generally slightly larger than those from noise HVSR. This finding is consistent with strong motion versus noise comparisons found in soft sites in Mexico (Lermo and Chávez-García, 1994), sites in Iceland (Field et al., 1995), Greece (Atakan et al., 1997), the Garner Valley array in California (Lachet et al., 1996), southern Italy (Theodulidis et al., 1996), and various sites across Europe (Mucciarelli et al., 2003), the Caribbean, and Tehran (Haghshenas et al., 2008).

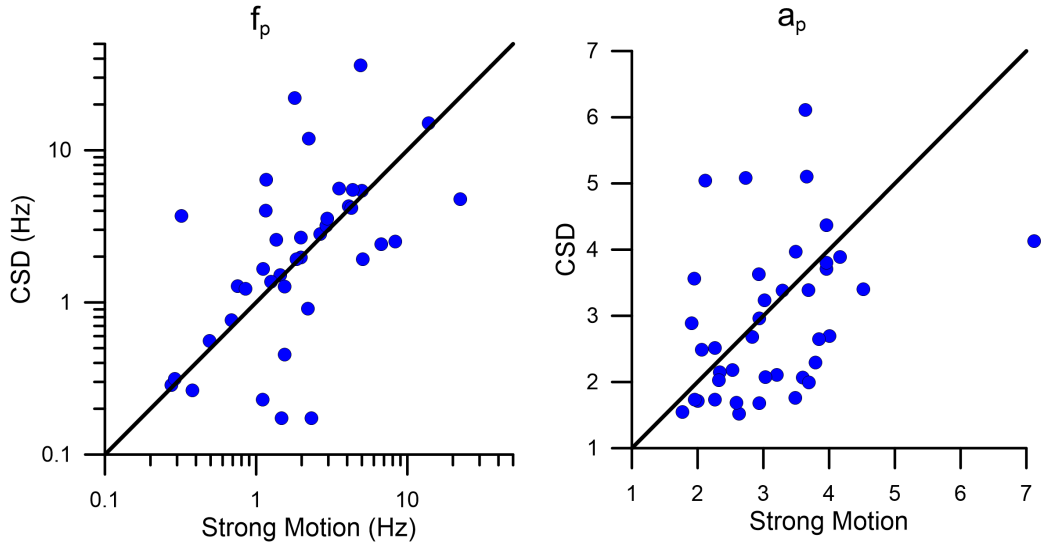

Figure 9. Comparison of peak fitted parameters f_p and a_p from earthquake and noise (CSD) data

Comparison Between Microtremor- and Continuously Steamed Noise HVSR

Similar to Section 4.1, we have identified the presence of peaks for a group of 102 sites with HVSR derived from ambient noise as recorded by MAMs and CSD. The instruments that made these recordings are not co-located, because the MAM sensors could not always be positioned directly adjacent to the strong motion station (Yong et al. 2013). The statistics of peaks and no peaks are presented in Table 4. Figure 10 illustrates examples of "P-P", "N-N", "N-P", and "P-N" sites.

Table 4. The comparison of peaks presence from HVSR computed using MAM and CSD

Eqk: CSD	Pk.: Pk.	No Pk. : No Pk.	No Pk. : Pk.	Pk.: No Pk.
Count	52	24	8	18
Precent	~51%	~24%	~8%	~17%

Table 4 shows that 75% of sites produce consistent peak identification results from the two noise-based HVSR ("P-P" and "N-N" groups). We have no reason to suspect one noise measurement is preferred to another, so these data reflect the reliability of HVSR when only a single measurement is made (there is a ¾ chance that a second measurement would produce a similar outcome regarding the presence of a peak).

We compare the fitted coefficients from the two sources for the 52 "P-P" sites in Figure 11. Of the 52 sites, 80% have f_p values within 20% of each other, and only 20% have misfits > a factor of four. The correlation coefficient is 0.87. Inspections of sites that are located off of the 1:1 line (Figure 12) show that the peaks in these cases are relatively weak, falling only marginally within the peak category. As this work progresses and the peak identification procedures are refined, some of these sites might be re-classified as no-peak sites. The plot of peak amplitudes (a_p) in Figure 11 indicates a weaker correlation (ρ=0.64) than the f_p results.

Discussion

As explained in the *Introduction*, the purpose for measuring and compiling HVSR data is to use it for the derivation of site parameters that can be used in ground motion models, as an augment to V_{S30}. In a typical forward application (i.e., use of a model to predict ground motions that have not yet occurred), an engineer will measure HVSR at the site of interest, decide if a peak is present, and if so, identify peak parameters. The comparisons in Section 4.2 shows that had the engineer made the noise measurement in a slightly different manner, and perhaps at a different time, the likelihood of obtaining a significantly different outcome is small but not negligible. Studies of this type, comparing results from multiple noise-based measurements, are relatively rare in the literature, so we are unable to compare to previous findings.

The results in Section 4.1 show that if a peak is identified, there is only about a 50% chance that a peak will also be present in seismic HVSR data. This high rate of false-positives will decrease, but not eliminate, the effectiveness of models conditioned on HVSR peak parameters. On the other hand, if no-peak is identified, there is a strong likelihood that the seismic HVSR also lacks peaks. The consistency of seismic and noise-based HVSR peaks has been studied previously, with most investigators finding consistent results (Lermo and Chávez-García, 1994; Field et al., 1995; Atakan et al., 1997; Lachet et al., 1996; Theodulidis et al., 1996; Mucciarelli et al., 2003; Haghshenas et al., 2008; and Hassani et al. 2019) and a few finding some inconsistent results (Satoh et al. 2001). Comparisons of HVSR from the two vibration sources might well vary depending on site geology, so further investigation of this issue for site conditions in California is needed.

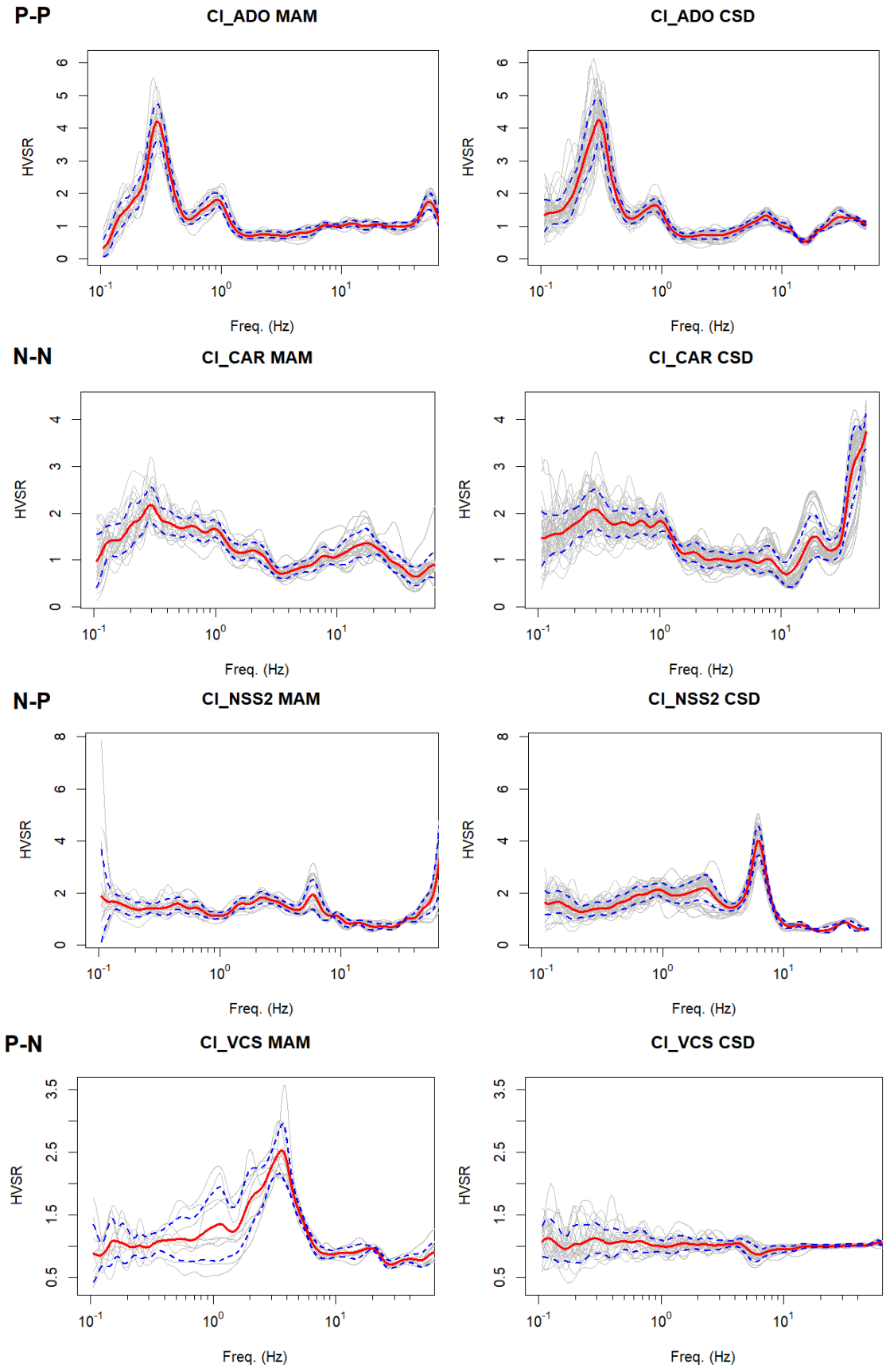

Figure 10. The examples of HVSR for "P-P", "N-N", "N-P", and "P-N" site for MAM versus CSD.

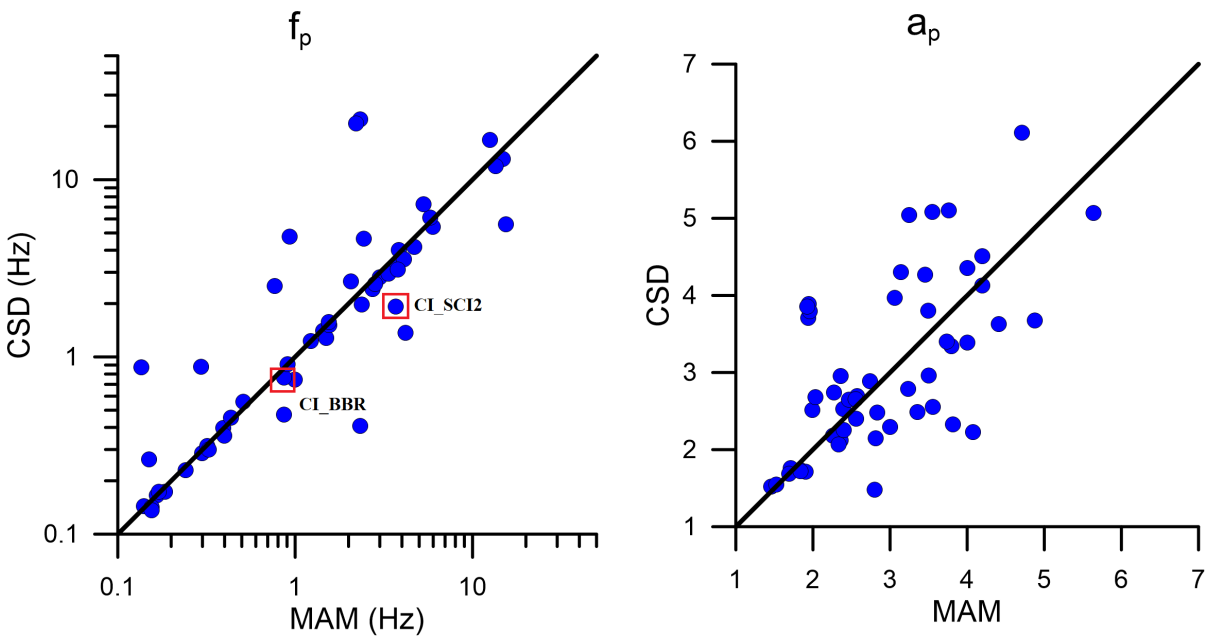

Figure 11. Comparison of f_p (left) and a_p (right) of peak fitted parameters between CSD and MAM.

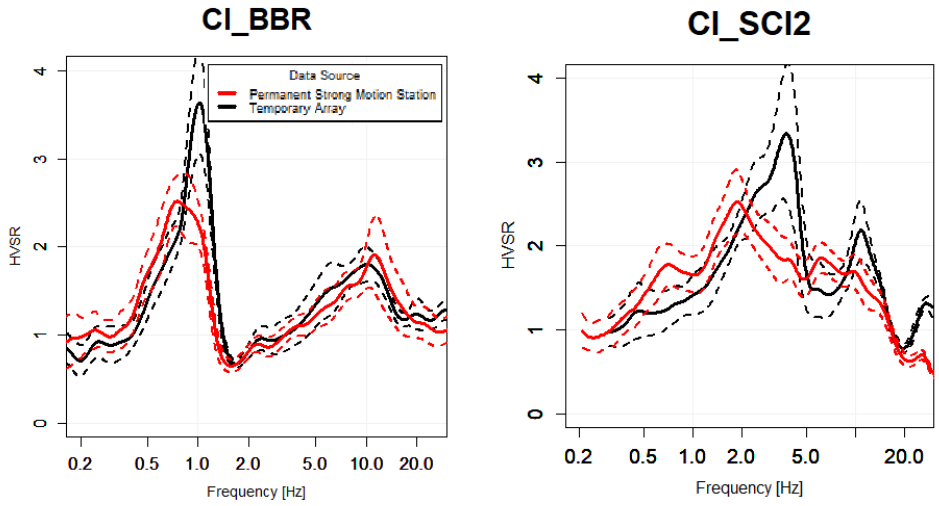

Figure 12. HVSR for permanent strong motion stations and temporary arrays.

Conclusions

Because HVSR-based parameters are not used currently in ground motion prediction applications, a number of steps are required to support eventual model development and utilization in practice. This study represents a step in that direction. We have created an open-source relational database of HVSR and associated processing parameters and incorporated this information into an existing community *Vs* Profile Database (PDB) in the United States. Users can utilize and analyze the processed records through interactive Jupyter Notebook tools that evaluate azimuthal dependence, identify the presence of peaks in an HVSR, and fit peaks using Eq. (1).

To demonstrate the value of the compiled data, we compare HVSR attributes for seismic and noise based data, and for two different noise measurements. The different noise measurements are more consistent with each other than the noise-to-seismic comparison. Of the California sites considered, about 30-40% do not have peaks. Accordingly, it will be important for eventual HVSR-based models to be able to accommodate this common result of HVSR testing.

Acknowledgments

Funding for this study is provided by California Strong Motion Instrumentation Program, California Geological Survey, Agreement 1016-985 and 1018-569. We gratefully acknowledge this support. We also thank Antony Martin from GEOVision for sharing his expertise on processing the HVSR data. Site data was provided for addition to the database by Alan Yong (USGS), Koichi Hayashi (Geometrics), David Teague (Engeo), and Tristan Buckreis (UCLA); this data sharing and cooperation are deeply appreciated. We thank Silvia Castellaro, Seth Carpenter, Brady Cox, Hiroshi Kawase, Shinichi Matsushima, Robert Nigbor, Stefano Parolai, Marco Pilz, Lisa Schleicher, Jamison Steidl, Alan Yong, and Wang Zhenming for their input on this research. Any use of trade, firm, or product names is for descriptive purposes only and does not imply endorsement by the U.S. Government.

References

Ahdi, S.K., O. Ilhan, S. Sadiq, Y. Bozorgnia, Y.M.A. Hashash, D. Park, A. Yong, and J.P. Stewart, 2018. Development of a United States Community Shear Wave Velocity Profile Database, *5th Conference on Geotechnical Earthquake Engineering and Soil Dynamics (GEESD-V)*, June 10–13, 2018, Austin, Texas.

Anderson, J. G. and J. Brune, 1999. Probabilistic seismic hazard analysis without the ergodic assumption." *Seism. Res. Lett.*, **70**, 19-28.

Atakan, K., B. Brandsdottir, P. Halldorsson, and G.O. Fridleifsson, 1997. Site response as a function of near-surface geology in the South Iceland seismic zone. *Natural Hazards*, *15*(2-3), 139-164.

Bonilla, L. F., J. H. Steidl, G. T. Lindley, A. G. Tumarkin, and R. J. Archuleta, 1997. Site amplification in the San Fernando Valley, California: Variability of site-effect estimation using the S-wave, coda, and H/V methods, *Bull. Seismol. Soc. Am.* **87,** 710-730.

Bonilla, L.F., J. H. Steidl, J.-C. Gariel, and R.J. Archuleta, 2002. Borehole response studies at the Garner Valley downhole array, Southern California, *Bull. Seismol. Soc. Am.* **92,** 3165-3179.

Boore, D. M., 2010. Orientation-independent, nongeometric-mean measures of seismic intensity from two horizontal components of motion. *Bull. Seismol. Soc. Am.* **100,** 1830-1835.

Bozorgnia, Y., N. A. Abrahamson, L. .A. Atik, T. D. Ancheta, G. M. Atkinson, J. W. Baker, A. Baltay, D. M. Boore, K. W. Campbell, B. S.-J. Chiou, R. Darragh, S. Day, J. Donahue, R. W. Graves, N. Gregor, T. Hanks, I. M. Idriss, R. Kamai, T. Kishida, A. Kottke, S. A. Mahin, S. Rezaeian, B. Rowshandel, E. Seyhan, S. Shahi, T. Shantz, W. Silva, P. Spudich, J. P.

Stewart, J. Watson-Lamprey, K. Wooddell, and R. Youngs, 2014. NGA-West 2 research project*, Earthq. Spectra*, **30**, 973-987.

Cadet, H., P.-Y. Bard, A.-M. Duval, and E. Bertrand, 2012. Site effect assessment using KiK-net data: Part 2—Site amplification prediction equation based on f0 and Vsz, *Bull. Earthq. Eng.* **10**, 451–489.

Di Alessandro, C., L. F. Bonilla, D. M. Boore, A. Rovelli, and O. Scotti, 2012. Predominant-period site classification for response spectra prediction equations in Italy, *Bull. Seismol. Soc. Am.* **102**, 680–695.

Di Giulio G., F. Cara, A. Rovelli, G. Lombardo, and R. Rigano, 2009. Evidences for strong directional resonances in intensely deformed zones of the Pernicana fault, Mount Etna, Italy. *J. Geophy. Res.*, **114**, B10308.

Field, E. H., A.C. Clement, K.H. Jacob, V. Aharonian, S.E. Hough, P.A. Friberg, H.A. Abramian, 1995. Earthquake site-response study in Giumri (formerly Leninakan), Armenia, using ambient noise observations. *Bull. Seismol. Soc. Am.*, **85**(1), 349-353.

GEOVision, 2016. Surface Wave Measurements Report, Riverside County, California. Report 16192-01 Rev 2. Prepared for State of California Department of Conservation, California Geological Survey, Strong Motion Instrumentation Program.

GEOVision, 2018. Surface Wave Measurements, Santa Clara, Santa Cruz, San Benito, and Monterey Counties. Report 18045-01. Prepared for State of California Department of Conservation, California Geological Survey, Strong Motion Instrumentation Program.

Ghofrani, H., G.M. Atkinson, and K. Goda, 2013. Implications of the 2011 M 9.0 Tohoku Japan earthquake for the treatment of site effects in large earthquakes, *Bull. Earthq. Eng.* **11,** 171-203.

Gospe, T., P. Zimmaro, P. Wang, T. Buckreis, S.K. Ahdi, A.K. Yong, S.J. Brandenberg, J.P. Stewart, 2020. Supplementing shear wave velocity profile database with microtremor-based H/V spectral ratios, *Proc. 17th World Conf. on Earthquake Engineering*, Sendai, Japan, September 14-18 2020. Paper 003010.

Haghshenas, E., P.Y. Bard, N. Theodulidis, and Sesame WP04 Team, 2008. Empirical evaluation of microtremor H/V spectral ratio. *Bull. Earthq. Eng.*, **6**(1), 75-108.

Hashash, Y.M.A., O. Ilhan, B. Hassani, G.M. Atkinson, 2020. Significance of site natural period effects for linear site amplification in central and eastern North America: Empirical and simulation-based models, *Earthq. Spectra*, **36**, 87-110.

Hassani, B. and G.M. Atkinson, 2016. Applicability of the site fundamental frequency as a V_{S30} proxy for Central and Eastern North America, *Bull. Seismol. Soc. Am.* **106**, 653–664.

Hassani, B., and G.M. Atkinson, 2017. Site-effects model for central and eastern North America based on peak frequency and average shear-wave velocity, *Bull. Seismol. Soc. Am.* **107**, 338-350.

Hassani, B., and G.M. Atkinson, 2018. Application of a site-effects model based on peak frequency and average shear-wave Velocity to California, *Bull. Seismol. Soc. Am.* **108**, 351-357.

Hassani, B., Yong, A., Atkinson, G. M., Feng, T., and Meng, L. (2019). Comparison of site dominant frequency from earthquake and microseismic data in California. *Bull. Seismol. Soc. Am.*, **109**(3), 1034-1040.

Incorporated Research Institutions for Seismology (IRIS), IRIS PASSCAL,https://www.passcal.nmt.edu/content/instrumentation/sensors/sensor-comparison-chart, last accessed <10/12/2020>

Kwak, D.Y., J.P. Stewart, S.U.J. Mandokhail, and D. Park, 2017. Supplementing V_{S30} with H/V spectral ratios for predicting site effects. *Bull. Seismol. Soc. Am.* **107**, 2028-2042.

Lachet, C., D. Hatzfeld, P.Y. Bard, N. Theodulidis, C. Papaioannou, and A. Savvaidis, 1996. Site effects and microzonation in the city of Thessaloniki (Greece) comparison of different approaches. *Bull. Seismol. Soc. Am.*, **86**, 1692-1703.

Lermo, J., and F.J. Chávez-García, 1994. Are microtremors useful in site response evaluation?. *Bull. Seismol. Soc. Am.*, **84**, 1350-1364.

Mucciarelli, M., M. R. Gallipoli, and M. Arcieri, 2003. The stability of the horizontal-to-vertical spectral ratio of triggered noise and earthquake recordings. *Bull. Seismol. Soc. Am.* **93**(3), 1407-1412.

NCEDC, 2014, Northern California Earthquake Data Center. UC Berkeley Seismological Laboratory. Dataset. doi:10.7932/NCEDC.

Petralogix, 2017. VS30 Site Characterization Report, Los Angeles, Orange, Ventura, San Bernardino, and Riverside Counties. Report 2017-00006.

Satoh, T., H. Kawase, and S. Matsushima, 2001. Differences between site characteristics obtained from microtremors, S-waves, P-waves, and codas, *Bull. Seismol. Soc. Am*. **91**, 313–334.

SCEDC, 2013. Southern California Earthquake Data Center. Caltech. Dataset. doi:10.7909/C3WD3xH1

SESAME, 2004. Guidelines for the Implementation of the H/V spectral ratio technique on ambient vibrations—Measurements, processing and interpretation: European Commission, Project No. EVG1-CT-2000-00026, accessed September 2012, at http://sesame-fp5.obs.ujf-grenoble.fr/

Seyhan, E., and Stewart, J. P. 2014. Semi-Empirical Nonlinear Site Amplification from NGA-West2 Data and Simulations, *Earthq, Spectra*, **30**, 1241-1256.

Stewart, J. P., K. Afshari, and C. A. Goulet, 2017. Non-ergodic site response in seismic hazard analysis, *Earthq, Spectra*, **33**, 1385-1414.

Theodulidis, N., P.Y. Bard, R. Archuleta, and M. Bouchon, 1996. Horizontal-to-vertical spectral ratio and geological conditions: The case of Garner Valley downhole array in southern California. *Bull. Seismol. Soc. Am*., **86**(2), 306-319.

Tuan, T. T., F. Scherbaum, and P. G. Malischewsky, 2011. On the relationship of peaks and troughs of the ellipticity (H/V) of Rayleigh waves and the transmission response of single layer over half-space models, *Geophys. J. Int*. **184**, 793–800.

Wang, P., 2020. Predictability and Repeatability of Non-Ergodic Site Response for Diverse Geological Conditions. Ph.D. thesis. UC Los Angeles.

Yong, A., A. Martin, K.H. Stokoe, and J. Diehl, 2013, ARRA-funded VS30 measurements using multi-technique approach at strong-motion stations in California and central-eastern United States: U.S. Geological Survey Open-File Report 2013–1102, 59 p. and data files, http://pubs.usgs.gov/of/2013/1102/.

Zhao, J.X., and H. Xu, 2013. A comparison of V_{S30} and site period as site-effect parameters in response spectral ground-motion prediction equations, *Bull. Seismol. Soc. Am.* **103**, 1–18.

ANALYSIS OF GROUND MOTIONS RECORDED DURING THE 2019 RIDGECREST EARTHQUAKE SEQUENCE

Silvia Mazzoni[1], Sean K. Ahdi[1], Tadahiro Kishida[2], Pengfei Wang[1], Chukwuebuka C. Nweke[1], Nicolas Kuehn[1], Victor Contreras[1], Jonathan P. Stewart[1], and Yousef Bozorgnia[1]

1. University of California, Los Angeles, Los Angeles, California
2. Department of Civil Infrastructure and Environmental Engineering, Khalifa University of Science and Technology, Abu Dhabi, United Arab Emirates

Abstract

We summarize an analysis of ground motions recorded during three events that occurred during the July 2019 Ridgecrest earthquake sequence. We collected and uniformly processed 1,483 three-component recordings for the events from an array of 824 sensors spanning ten seismographic networks. Signal processing followed well-established NGA procedures. We developed site condition metadata from available geophysical data and multiple models. We computed intensity measures such as spectral acceleration at a number of oscillator periods and inelastic response spectra. We compared elastic and inelastic response spectra to seismic design spectra in building codes to evaluate ground motion damage potential at spatially-distributed sites.

Introduction

The three events of the 2019 Ridgecrest earthquake sequence started at 10:33 AM local time on July 4, 2019, with a moment magnitude (**M**) 6.5 event located south of China Lake and west of Searles Valley, California. This **M**6.5 event occurred on a left-lateral NE-trending fault (roughly parallel with the Garlock fault to the south) at a hypocentral depth of 10.5 km. This earthquake was followed on July 5 by a **M**5.5 event at 4:07 AM local time at a hypocentral depth of 7.0 km, and a **M**7.1 event at 8:19 PM local time, the latter on a NW-trending right-lateral fault at a depth of 8.0 km (GEER [2019]). These events occurred on faults within the formerly-named greater Little Lake fault zone, but have now been differentiated after the recent earthquakes and are referred to as the Salt Wells Valley fault zone (for the **M**6.5 event; DuRoss et al. [2020]), and the Paxton Ranch fault zone (for the **M**7.1 event; DuRoss et al. [2020]). Since they were proximal in space and time, the **M**6.5 and **M**5.5 events are considered to be foreshocks to the **M**7.1 event (Ahdi, et al., 2020).

In this paper, we present a summary of recorded and processed ground motions, independent (measured) metadata, including information describing the recording stations (sites), and dependent (computed) data and metadata, such as various source-to-site distance metrics and directivity parameters, and computed elastic and inelastic response spectra. The response spectra are compared to the design spectra at each recording station to understand geographic trends. All data are publicly available from the UCLA Natural Hazards Risk and Resiliency Research Center (NHR3), as described in a report by Ahdi et al. (2019). A more complete version of this

paper has been previously published by Ahdi et al. (2020).

Compilation of Site Metadata

Seismological parameters such as magnitude, style of faulting, and fault geometry were reviewed and compiled to facilitate ground motion studies, including calculation of multiple distance metrics such as the epicentral, hypocentral, rupture, and Joyner-Boore distance (closest distance from site to the surface projection of the fault surface). The selection and computation of these parameters is described in Ahdi et al. (2020). The following subsections elaborate on the estimation of site parameters for recording sites.

A site database (SDB) was developed, encompassing information such as (where available for each station) network code, station location information (latitude, longitude, and elevation), information on the time-averaged shear-wave velocity (V_S) in the upper 30 m (V_{S30}) obtained from both measured V_S profiles and from proxy-based V_{S30} estimates, and basin depth parameters (z_x), which are measured as the vertical distance from the ground surface to the first encounter of x = 1.0, 1.5, and 2.5 km/s V_S horizons.

Estimation of V_{S30} at Recording Stations

Figure 1 shows a map of stations in the SDB with site markers color-coded by NEHRP site classes. V_{S30} values were assigned based on the availability of measured V_S profiles from geophysical measurements proximate (< 300 m) to the recording station. Profile data was queried from the Community Shear Wave Velocity Profile Database of Ahdi et al. (2018). When measured V_{S30} values are unavailable, V_{S30} is assigned based on various proxy-based models, including those based on surficial geology, topographic slope, and geomorphic terrain classifications.

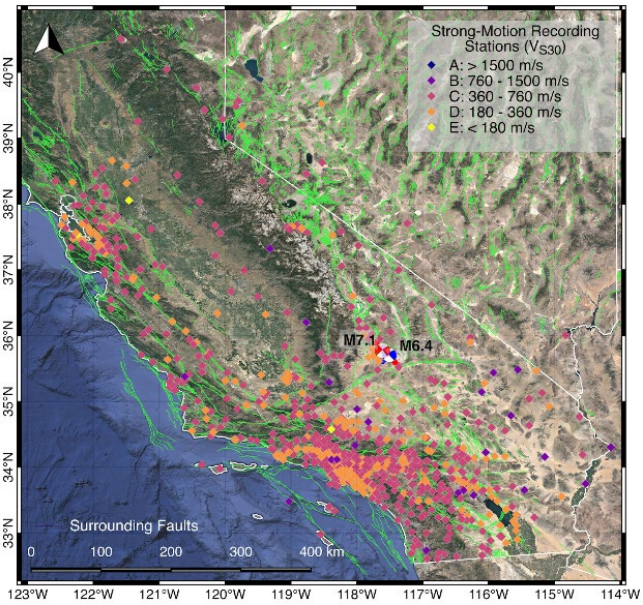

Figure 1. Spatial distribution of recording stations in the ground motion database. Stations are color-shaded according to V_{S30}-based NEHRP site class (Ahdi, et al., 2020).

The following protocol was used in assigning V_{S30} values for a given station:

1. Consider available published databases of measured V_S profiles and V_{S30} values:
   - United States Community V_S Profile Database (PDB, Ahdi et al., 2018), which includes data from the USGS V_{S30} Compilation (Yong et al., 2016)
   - NGA-West2 Site Database (Seyhan et al., 2014)
   - Center for Engineering Strong Motion Data (CESMD, 2019)
2. Match available measured V_{S30} values from all databases to station of interest by computing the distances between the station and the locations of the V_{S30} measurement, and take the closest measurement (using a 300-m cutoff distance) if there are multiple available measurements that do not match the station coordinates exactly (i.e., distance = 0 m).
3. Use proxy-based V_{S30} estimation models if:
   a. There exists no V_{S30} measurement within 300 m of the station; or
   b. The only measured V_{S30} within 300 m of the station was obtained using the Refraction Microtremor (ReMi™) method (Louie, 2001).

Descriptions of various geophysical methods used to obtain V_S profiles are beyond the scope of this paper, but we largely followed the guidelines set forth in V_S data attribution as outlined in Ahdi et al. (2018). The SDB includes 824 recording stations. A total of 203 (25%) stations have measured V_{S30} values, and for the remaining 621 stations, V_{S30} values are inferred using proxy-based methods (described below).

For sites lacking in-situ V_{S30} measurements, one or more of the following four proxy-based models was utilized:

1. krig: a Kriging-based regression map informed by measured V_{S30} data and a hybrid geology-topographic slope model. The Kriging approach is from Thompson et al. (2014) and Thompson (2018), and the hybrid model is from Wills et al. (2015);
2. terr: geomorphic terrain proxy model (Yong, 2016) based on terrain classes from Iwahashi and Pike (2007);
3. slp: topographic slope-based model (Wald and Allen, 2007).

To compute the model output, all sites in the SDB were assigned the relevant values of terrain classes or topographic slope gradients or were plotted on the raster map for the krig model. Figure 2 illustrates the assignment of V_{S30} based on these parameters. The krig model is preferred due to its inclusion of measured V_{S30} values, and thus is utilized wherever data falls within the geographic extent of the model (i.e., the state of California). Weights of 2/3 and 1/3 were applied for sites using both the krig and terr models, respectively. All inferred V_{S30} values from proxy-based models used the krig or krig-terr pair of models, except for 10 sites located in Nevada for which the kriging map is not defined, and one site (CGS station number 13877) which plots in the water due to the relatively coarse resolution of the kriging map and the 1-km spacing of the terrain classifications.

Estimation of Basin Depth Terms at Recording Stations

The z_x parameters were obtained by querying the Unified Community Velocity Models (CVMs) provided by the Southern California Earthquake Center (SCEC; Small et al., 2017). Values were obtained by querying a meta-model, which is a tiled system of multiple velocity models. For this project, the meta-model consisted of five velocity models, which are defined in Table 4 of Ahdi et al. (2020) based on a framework developed in Nweke et al. (2018). The tiled system uses latitude and longitude coordinates to query the CVMs in order of their designated priority. If the coordinates fall within the geographical extents of a model, then the appropriate z_x value will be selected (Small et al., 2017). If the coordinate falls outside the geographical extents of the given model, the next CVM in the tiled order will be checked, and the process is repeated until a CVM is encountered that encompasses the location of interest. To account for locations outside the boundary region of the velocity models in the meta-model, a background 1D velocity model is placed last in the tiled structure as it covers the largest area and serves as a supporting model to the standard CVMs. If a site's coordinates were to fall outside of all tiled CVM extents, the site is not assigned a z_x value. For this dataset, all 824 stations fell within the extent of the tiled CVMs and were thus assigned z_x values. When the model output for a site yields $z_{1.0} = 0$, we check against geological maps. Zero depth is retained for sites located on mapped hard rock geology (crystalline rock, Cretaceous rock, or volcanic rock units), and $z_{1.0}$ is indicated as undefined if the geology is mapped as Tertiary rock or sediments.

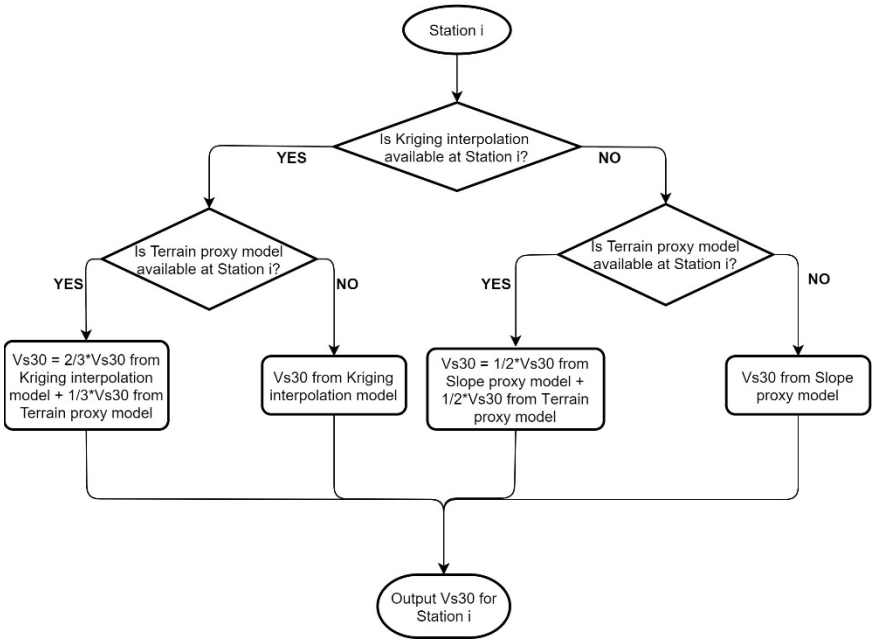

Figure 2. Flowchart depicting logic for assignments for proxy-based V_{S30} values in absence of measurements within proximity to station (see Ahdi, et al., 2020). Note that the geo model (hybrid geology-slope proxy model of Wills et al. 2015) was not considered on its own, as it is a basis for the map used in the kriging-based model of Thompson (2018).

Ground-Motion Intensity Measures

Elastic response spectra were computed for the time series collected for the three main events, including the three individual as-recorded components (H1, H2, and V), the RotD50 and RotD100 components, and the fault-parallel and fault-normal components of the records in the vicinity of the faults. RotD50 and RotD100 are defined by Boore (2010). Figure 3 shows an example of these intensity measures for the site CLC located 2 km from the **M**7.1 rupture, as compared to ground motion models (GMMs) and code-based values. Figure 3a (top left) compares the RotD50 component to predictions from the NGA-West2 GMMs. More comparison cases are provided in Ahdi et al. (2020). Figure 3b compares the RotD100 component to the ASCE 7-10 mapped design values—the Risk-Targeted Maximum Considered Earthquake, MCE_R, and the Design Earthquake, DE (DE = 2/3 * MCE_R), adjusted for its site class (ASCE, 2010, 2016). This comparison shows that the Ridgecrest **M**7.1 mainshock exceeded the Design-Earthquake spectrum at this location for most structural periods. Figure 3c compares the response spectrum of the three as-recorded components to the maximum component (RotD100). The H1 horizontal direction has the highest spectral demand for all periods. Figure 3d compares the response spectra for the FP and FN components to the maximum component shown in Figure 3c. At this location, the FP component carries most of the energy at long periods. These rotated components are valuable to studies of near-fault effects and provide insight on ground motion polarization.

Damage Potential of Recorded Ground Motions

In this section we present a summary of response of a generic single-degree-of-freedom (SDOF) inelastic system to the recorded ground motions. Inelastic analyses of representative structural types using the recorded ground motions provide an opportunity to draw different insights into the geographic distribution of expected generic inelastic-structure response and damage potential in the area affected by the seismic event (Ahdi, et al, 2020). These analyses were performed on a generalized inelastic SDOF model using OpenSees (McKenna et al., 2010). The main feature of an inelastic model is its ability to capture strength reduction and softening due to yielding, as well as hysteretic energy dissipation. The "yield strength" of the SDOF is based on the strength reduction factor (R_d), defined as the ratio between the lateral-force strength for design and the yield strength of the structure, V_y. This value is equivalent to a combination of the strength-reduction factor R and the overstrength factor used in seismic structural design. The typical range for R_d is between 0.5 and 4. When $R_d = 1$, the structure will yield at the DE level. When $R_d > 1$, the structure will yield when subjected to a below-design-level earthquake. When $R_d < 1$, the structure will remain elastic at and below the DE (Ahdi, et al, 2020). The estimated yield strength of the structure is, thus, defined as a function of the design spectrum at the site. The ASCE 7-10 MCE_R spectrum (ASCE, 2010) was obtained for each recording station via the USGS Design-Maps Web-Services tools. Either the ASCE 7-10 standard or ASCE 7-16 specification (ASCE, 2016) could be used; we used the former as it does not require site-specific analyses for softer soil conditions, which would prevent uniform and automated application of the current methodology to all recording stations presented herein. Two values of R_d were chosen for the analyses ($R_d = 2$ and 4). These values are expected to represent structures designed to an R-factor between 4 and 8.

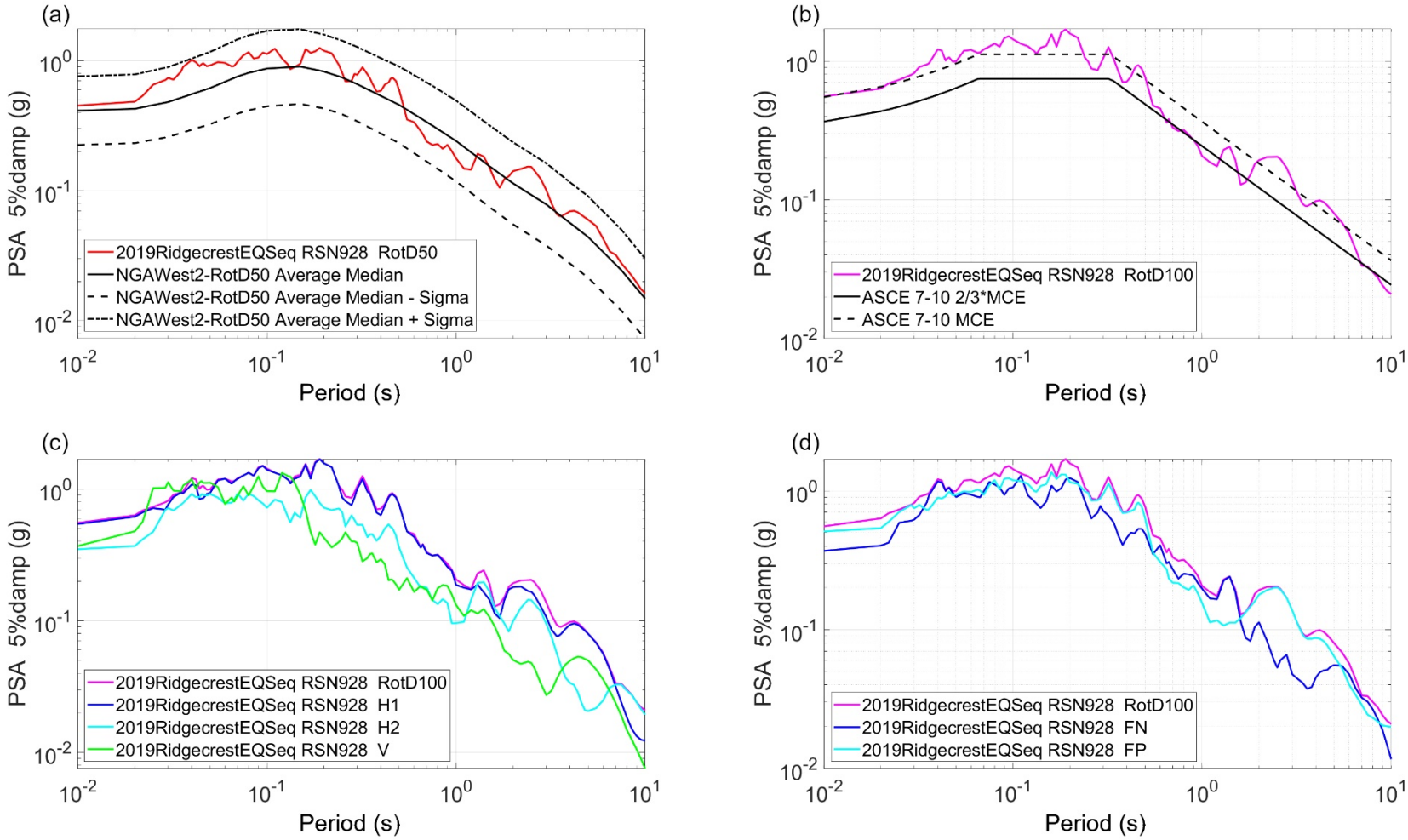

Figure 3. Example plots from the **M**7.1 event for site CLC of (a) observed RotD50 response spectrum compared with the average of the five NGA-West2 predictions; (b) observed RotD100 response spectrum as compared with the ASCE 7-10 MCE_R spectrum and DE (= 2/3 MCE_R) spectrum; (c) observed RotD100, H1, H2, and V response spectra; and (d) observed RotD100, fault-normal (FN) and fault-parallel (FP) response spectra (Ahdi, et al., 2020).

Both inelastic and elastic responses of the SDOF system were computed for all the recordings for the **M**7.1 event for both periods and strength levels. For the elastic case, a damping ratio of 5% was used, which is common in engineering practice. For the inelastic case, a reduced damping ratio of 2% was utilized, as the hysteretic energy dissipation is already captured in these nonlinear analyses as compared to the elastic case, which leverages a higher viscous damping ratio in order to partly capture the hysteretic damping which is not explicitly modeled therein.

An example of the inelastic response parameters is mapped for T = 1.0 s in Figure 4 for $R_d = 2$. The figure consists of 4 maps. The first map, on the top left shows the geographic distribution of the maximum elastic-deformation demand (S_d). The data in this map is the same for both cases of R_d. The second map, on the top right, plots the geographic distribution of D_y, which is defined by expected strength evaluated from the R_d factor and the ASCE 7-10 MCE spectra. The map on the bottom left shows the geographic distribution of the inelastic-deformation demands (D_{max}). The normalized deformation demands show that there are different regions with different levels of expected response, both near and far from the epicenter. The patterns shown in the damage-potential maps show that distance and site conditions are not the only response parameters. Details of such analysis can be found in Ahdi, et al. (2020).

Predicted versus Observed Response Spectra

A comparison of the PSA values computed based on the recorded ground motions and those predicted by the NGA-West2 GMMs was carried out. Figure 3a shows an example of such comparisons for the **M**7.1 event at site CLC. Five NGA-West2 models were considered: Abrahamson et al. (2014), Boore et al. (2014), Campbell and Bozorgnia (2014), Chiou and Youngs (2014), and Idriss (2014); hereafter ASK, BSSA, CB, CY, and ID, respectively.

Ahdi et al. (2020) analyzed residuals (difference between natural log of computed intensity measure and NGA-West2 model medians) to evaluate potential biases in the modeling of source, path, and site effects. Figure 5 shows an example of the average residuals for the **M**7.1 event. Ahdi et al. (2020) present the same plot for the other two events, which are omitted here for brevity. All residuals are slightly positive for the two larger events at short periods. At longer periods, average residuals increase, perhaps due to under-prediction of basin depth scaling by the GMMs.

Summary

A summary of analysis of the ground motions recorded in the 2019 Ridgecrest earthquake sequence is presented. The metadata pertaining to the earthquake source, such as finite-fault solutions, seismic site information including V_{S30} and basin depths, and wave-propagation path distances are compiled. We utilize a relational database to organize and store all data. Comparisons of the response spectra of the recorded ground motions to those of the NGA-West2 GMMs show on average favorable model performance. The large number of recordings and the dense distribution of the recordings in a region that is crossed by significant faults has allowed us to compute intensity measures beyond elastic response spectra so that we can quantify the expected distribution of damage in areas of varying seismic demands (both near

and far from faults).

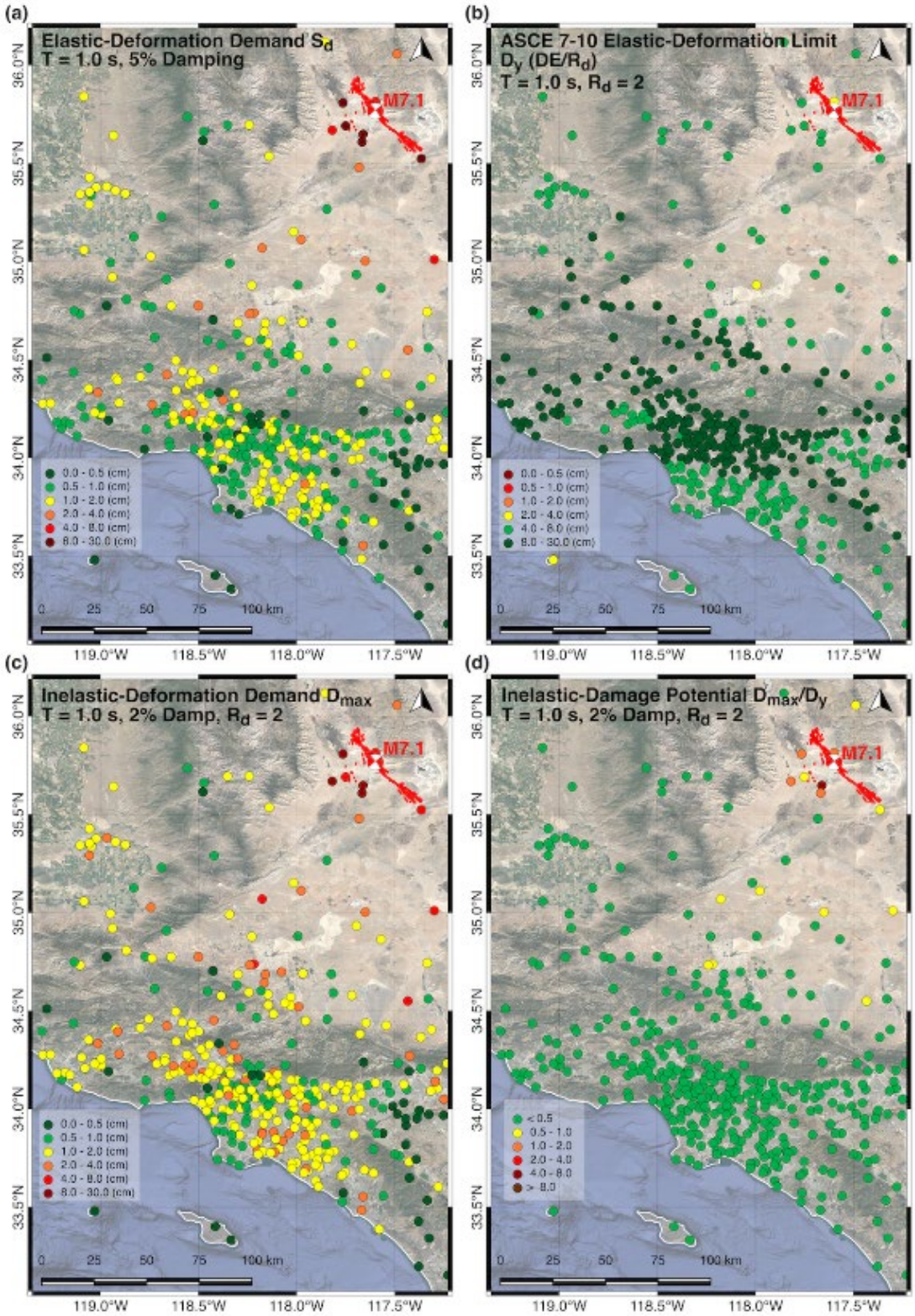

Figure 4. Deformation response of elastic and inelastic models, R_d = 2 (Ahdi et al, 2020).

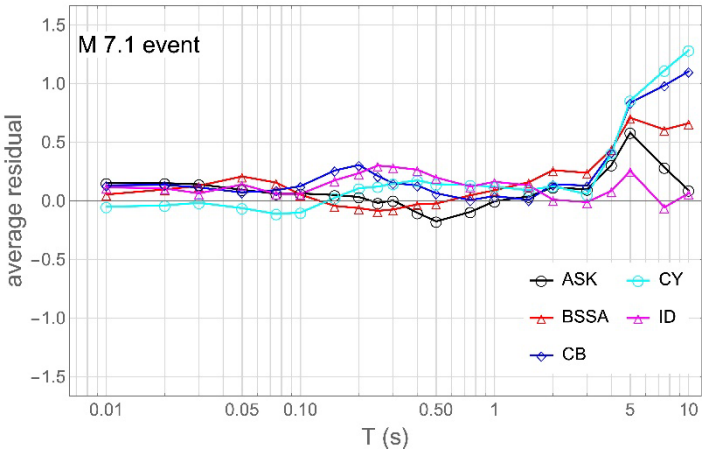

Figure 5. Event terms (average residuals) for the **M**7.1 main shock and the five NGA-West2 models vs. spectral period (Ahdi, et al., 2020).

Acknowledgements

Support from the California Strong Motion Instrumentation Program (CSMIP) and Pacific Gas & Electric Company (PG&E) is gratefully acknowledged. Parts of this effort were initially conducted as part of the GEER deployment (GEER, 2019). The GEER Association is supported by the National Science Foundation (NSF) through the Geotechnical Engineering Program under Grant No. CMMI-1266418. Any opinions, findings, and conclusions or recommendations expressed in this material are those of the authors and do not necessarily reflect those of the supporting agencies.

References

Abrahamson, N. A., W.J. Silva, and R. Kamai (2014). Summary of the ASK14 ground motion relation for active crustal regions, *Earthq. Spectra*, **30**(3), 1025–1055.

Ahdi, S.K., S. Mazzoni, T. Kishida, P. Wang, C.C. Nweke, J.P. Stewart, and Y. Bozorgnia (2019). Processed ground motion recordings of the 2019 Ridgecrest Earthquake Sequence, *Report of the Natural Hazards Risk and Resiliency Research Center (NHR3), B. John Garrick Institute for the Risk Sciences, University of California, Los Angeles*. https://www.risksciences.ucla.edu/nhr3/gmdata/2019-ridgecrest-earthquake-sequence.

Ahdi, S.K., S. Mazzoni, T. Kishida, P. Wang, C.C. Nweke, N.M. Kuehn, V. Contreras, B. Rowshandel, J.P. Stewart, and Y. Bozorgnia (2020). Engineering Characteristics of Ground Motions Recorded in the 2019 Ridgecrest Earthquake Sequence, *Bull. Seismol. Soc. Am*, **110**(4), 1474-1494.

Ahdi, S.K., S. Sadiq, O. Ilhan, Y. Bozorgnia, Y.M.A. Hashash, D.Y. Kwak, D. Park, A. Yong, and J.P. Stewart (2018). Development of a United States Community Shear Wave Velocity Profile Database, *in 5th Conference on Geotechnical Earthquake Engineering and Soil Dynamics (GEESD-V)*, eds. S.J. Brandenberg and M.T. Manzari, Austin, TX, USA, 10–13 June 2018, 330–339.

ASCE (2010). Minimum Design Loads for Buildings and Other Structures, *American Society of Civil Engineers Standard ASCE/SEI 7-10*, Reston VA.

ASCE (2016). Minimum Design Loads and Associated Criteria for Buildings and Other Structures, *American Society of Civil Engineers Standard ASCE/SEI 7-16*, Reston, VA.

Boore, D.M. (2010). Orientation-independent, non-geometric-mean measures of seismic intensity from two horizontal components of motion, *Bull. Seism. Soc. Am.* **100**(4), 1830–1835.

Boore, D.M., Stewart, J.P., Seyhan, E., and Atkinson, G.M. (2014). NGA-West2 equations for predicting PGA, PGV, and 5% damped PSA for shallow crustal earthquakes, *Earthq. Spectra*, ***30***(3), 1057–1085.

Campbell, K.W., and Y. Bozorgnia (2014). NGA-West2 ground motion model for the average horizontal components of PGA, PGV, and 5% damped linear acceleration response spectra, *Earthq. Spectra*, **30**(3), 1087–1115.

Chiou, B.S.-J., and R.R. Youngs (2014). Update of the Chiou and Youngs NGA model for the average horizontal component of peak ground motion and response spectra, *Earthq. Spectra*, ***30***(3), 1117–1153.

DuRoss, C.B., R.D. Gold, Dawson, T.E., K.M. Scharer, K.J. Kendrick, S.O. Akciz, et al. (2020). Surface Displacement Distributions for the July 2019 Ridgecrest, California, Earthquake Ruptures; *Bull Seismol Soc Am.*, **110**(4), 1400–1418.

GEER (2019); Stewart, J.P. (ed.), S.J. Brandenberg, P. Wang, C.C. Nweke, K.S. Hudson, S. Mazzoni, Y. Bozorgnia, C.A. Goulet, K.W. Hudnut, C.A. Davis, S.K. Ahdi, F. Zareian, J. Fayaz, R.D. Koehler, C. Chupik, I. Pierce, A. Williams, S. Akciz, M.B. Hudson, T. Kishida, B. Brooks, R. Gold, D. Ponti, K. Scharer, D. McPhillips, C. DuRoss, T. Ericksen, J. Hernandez, J. Patton, B. Olson, T. Dawson, J. Treiman, K. Blake, J. Bachhuber, C. Madugo, J. Sun, A. Donnellan, G. Lyzenga, and E. Conway. *2019 Ridgecrest Earthquake Sequence. Geotechnical Extreme Event Reconnaissance (GEER) Association Report* GEER-064, https://doi.org/10.18118/G6H66K, 7/19/2019, Revised 8/1/2019.

Idriss, I.M. (2014). An NGA-West2 empirical model for estimating the horizontal spectral values generated by shallow crustal earthquakes, *Earthq. Spectra*, **30**(3), 1155–1177.

Iwahashi, J., and R.J. Pike (2007). Automated classifications of topography from DEMs by an unsupervised nested-means algorithm and a three-part geometric signature, *Geomorphology*, **86**, 409–440.

Louie, J.N. (2001). Faster, better: Shear-wave velocity to 100 meters depth from Refraction Microtremor Arrays, *Bull. Seismol. Soc. Am.*, **91**(2), 347–364.

McKenna, F., M.H. Scott, and G.L. Fenves (2010). "Nonlinear finite-element analysis software architecture using object composition." *J. Comput. Civ. Eng.*, **24**(1), 95–107.

Nweke, C.C., P. Wang, S.J. Brandenberg, and J.P. Stewart (2018). Reconsidering basin effects in

ergodic site response models, *Proceedings of the 2018 California Strong Motion Instrumentation Program (CSMIP) Seminar on Utilization of Strong-Motion Data*, Sacramento, CA, 25 October 2018.

Seyhan, E., J.P. Stewart, T.D. Ancheta, R.B. Darragh, R.W. and Graves (2014). NGA-West2 site database, *Earthq. Spectra*, **30**, 1007–1024.

Small, P., D. Gill, P.J. Maechling, R. Taborda, S. Callaghan, T.H. Jordan, G.P. Ely, K.B. Olsen, and C.A. Goulet (2017). The SCEC Unified Community Velocity Model Software Framework. *Seismol. Res. Lett.*, **88**(5), 1539–1552.

Thompson, E.M. (2018). An Updated Vs30 Map for California with Geologic and Topographic Constraints: U.S. Geological Survey data release, https://doi.org/10.5066/F7JQ108S.

Thompson, E.M., D.J. Wald, and C.B. Worden (2014). A V_{S30} map for California with geologic and topographic constraints, *Bull. Seismol. Soc. Am.,* **104**, 2313–2321.

Wald, D.J. and T.I. Allen (2007). Topographic slope as a proxy for seismic site conditions and amplification, *Bull. Seismol. Soc. Am.*, **97**, 1379–1395.

Wills, C.J., C.I. Gutierrez, F.G. Perez, and D.M. Branum (2015). A next generation VS30 map for California based on geology and topography, *Bull. Seismol. Soc. Am.*, **105**, 3083–3091.

Yong, A. (2016). Comparison of measured and proxy-based V_{S30} values in California, *Earthq. Spectra,* **32**,W 171–192.

Yong, A., E.M. Thompson, D.J. Wald, K.L. Knudsen, J.K. Odum, J.K., W.J. Stephenson, and S. Haefner (2016). Compilation of V_{S30} Data for the United States: U.S. Geological Survey Data Series 978, 8 p., http://dx.doi.org/10.3133/ds978.

CHARACTERIZATION OF NONLINEAR DYNAMIC SOIL PROPERTIES FROM GEOTECHNICAL ARRAY DATA

S. F. Ghahari, and E. Taciroglu

Department of Civil & Environmental Engineering, University of California, Los Angeles

Abstract

Dynamic soil properties are key ingredients of analyses for predicting/assessing soil-structure interaction (SSI) and site response effects under seismic excitations. While there is already a large amount of valuable data recorded by numerous geotechnical arrays worldwide, there is no reliable technique that enables the extraction of dynamic nonlinear/hysteretic properties of soil layers. Herein, a stochastic filtering method devised for estimating the nonlinear soil properties from earthquake data recorded by geotechnical arrays.1D-3C finite element site models are used, and the soil layers' constitutive model parameters and input excitation (bedrock or within motions) time-histories are identified using Unscented Kalman Filtering techniques. The method is first verified using synthetic examples and then validated using real-life data from centrifuge tests as well as the well-known Lotung site. Subsequently, the method is applied to earthquake data recorded by several CSMIP Geotechnical Arrays.

Introduction

Although near-surface nonlinear soil layers have negligible dimensions compared to the path-lengths that seismic waves traverse from the source to the site, they significantly contribute to the observed motion at the ground surface [1]. Realistic physics-based predictions cannot be achieved unless they are the said nonlinearities are into account. While there are several veritable analytical and numerical methods to predict site-response given bedrock or outcrop motions (e.g., [2]–[4]), their accuracies inherently depend on the knowledge of the soil layers' dynamic properties. However, laboratory testing of "undisturbed" soil samples inevitably involves some violation of in-situ conditions. For example, loading paths in the laboratory tests are significantly different from those that the soil experiences in the field. Field measurements had been suggested to resolve this problem. Cross-Hole Tests (CHT), Down-Hole Tests (DHT), Suspension Logging, Seismic Reflection, Seismic Refraction, and Spectral Analysis of Surface Waves (SASW) are among various methods that are used for measuring shear wave velocities of soil layers, which is a key parameter for predicting the linear dynamic responses of a soil deposit. However, even these in-situ tests cannot mimic the site's actual behavior under real-life earthquakes because the sources of real-life seismic waves are inherently different from those used in in-situ tests. Moreover, in-situ tests are typically only able to capture the very-small-strain (and thus linear) soil layers' responses. On the other hand, it is well accepted that soil mostly behaves nonlinearly during even moderate earthquakes and reaches strains well beyond those that can be induced in conventional in-situ tests [5].

Not surprisingly, the estimation of dynamic site properties from recorded ground motions has been an important topic of research (for example, [6], [7]) because earthquakes may be regarded as prototype in-situ dynamic tests carried out by nature and the data recorded during earthquakes offer precious opportunities for the study of in-situ behavior of soil within a strain range that has engineering significance. However, most of the identification studies carried out in the past are limited to linear or equivalent linear soil properties of soil layers [8], [9]. These limited studies, in which soil nonlinearity was considered, have limited applicability because the assumed constitutive nonlinear model was very simple [10]. Moreover, in many of these studies, in-depth motions were used as input excitations through the conventional outcrop method (with absorbing boundary condition), which reduces the method's applicability range. More importantly, it is well accepted that within motions are polluted by down-going waves and should not be used as outcrop input excitations [11].

In this project, within a proposed general framework for nonlinear site characterization, which resolves all of the aforementioned limitations, we developed, tested, and validated input-output and output-only identification algorithms to estimate the nonlinear soil properties form data recorded in a geotechnical array. The proposed framework was verified using synthetic examples and validated using centrifuge data as well as real-life data recorded at the well-known Lotung site.

The Proposed Framework

As schematically shown in Figure 1, the objective is to identify (*i*) the most plausible nonlinear constitutive model, (*ii*) parameters of the selected model, and (*iii*) the incident motion by using data recorded at several depths. A common simplifying assumption is also adopted—namely, the problem is an ideal 1D case with known layering and some relatively good initial but uncertain estimations of the parameters.

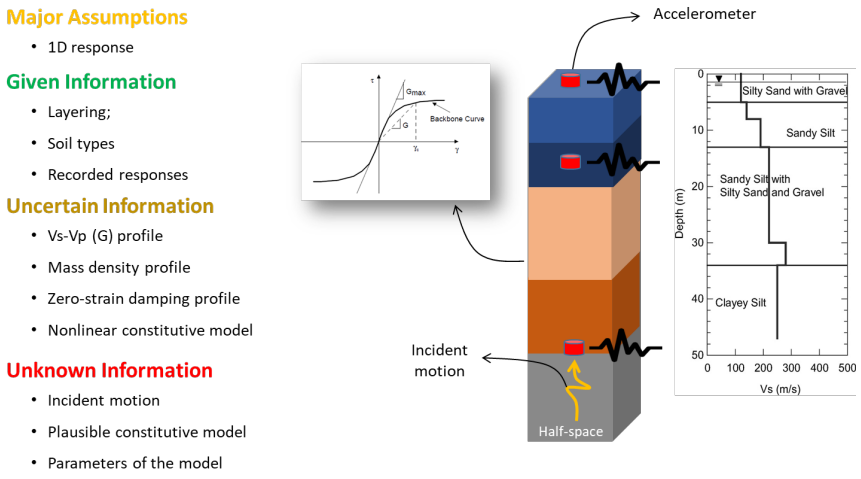

Figure 1. The proposed framework.

There are two approaches to carry out dynamic site response analyses, as shown in **Figure 2**. In the more traditional approach, the site is modeled up to the bedrock (half-space) level; and radiation damping is modeled by using an absorbing boundary to prevent wave

reflection. Through this approach, the incident motion must be used as input excitation, which can theoretically be obtained from the nearby rock outcrop motion (with a ½ factor). As seen, this approach is only valid if there is no impedance contrast below the boundary level, and there is a very close rock outcrop motion. In another approach, the domain can be cut at any depth as long as the so-called within motion is used as input excitation, and a fixed boundary is used.

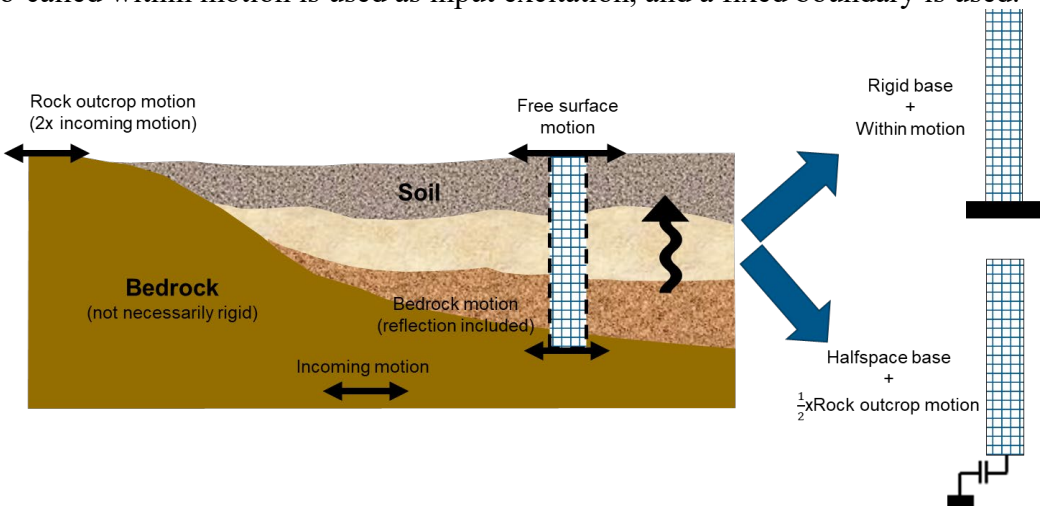

Figure 2. One-dimensional site response analysis approaches.

We propose to solve the inverse problem using output-only sequential Bayesian estimation [12], [13], as shown in **Figure 3**. In this approach, the 1D FE model of the site is modeled up to the bedrock depth with an absorbing boundary condition if the bedrock is not rigid. A soil constitutive model is chosen, and its parameters are identified along with the unknown incident motion through the Bayesian model updating. The entire process is then repeated using different constitutive models, and the most plausible and its optimal parameters are determined through classical model selection criteria [14], [15]. This joint input-parameter estimation solution will be later verified and validated through synthetic and centrifuge test data, respectively. It should be emphasized that input-output estimation can be employed if the bedrock is rigid, and there is a measurement at the bedrock depth to use as input excitation.

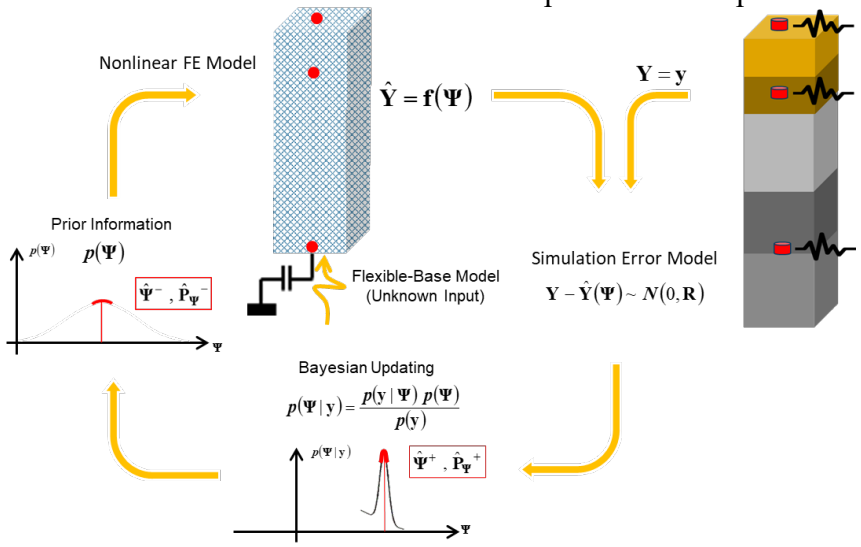

Figure 3. The one-step solution.

The aforementioned joint input-parameter estimation solution is prone to a high level of uncertainty if the number of parameters is large or the number of in-depth recorded data is limited. To resolve this issue, we solve the inverse problem in two sequential steps (see Figure 4). In Step 1, the 1D FE model of the site is fixed at the lowest instrumented level, such that the recorded within motions can be used as input excitation. A soil constitutive model is chosen, and its parameters are identified through the Bayesian model updating. Once completed the first step, the bedrock layer is added to the model in step 2 (through an absorbing boundary condition), and its parameters are estimated along with the incident motion, while the system above this level is known. Note that the first step can be limited to any depth as long as there is measured within motion at that depth. This is a crucial benefit, especially for the cases with deep bedrock level and only a few sensors at shallow depth for which properties of those shallow layers can be estimated with higher reliability. However, the model has to be extended up to the bedrock depth in the second step to be able to estimate incident motions too.

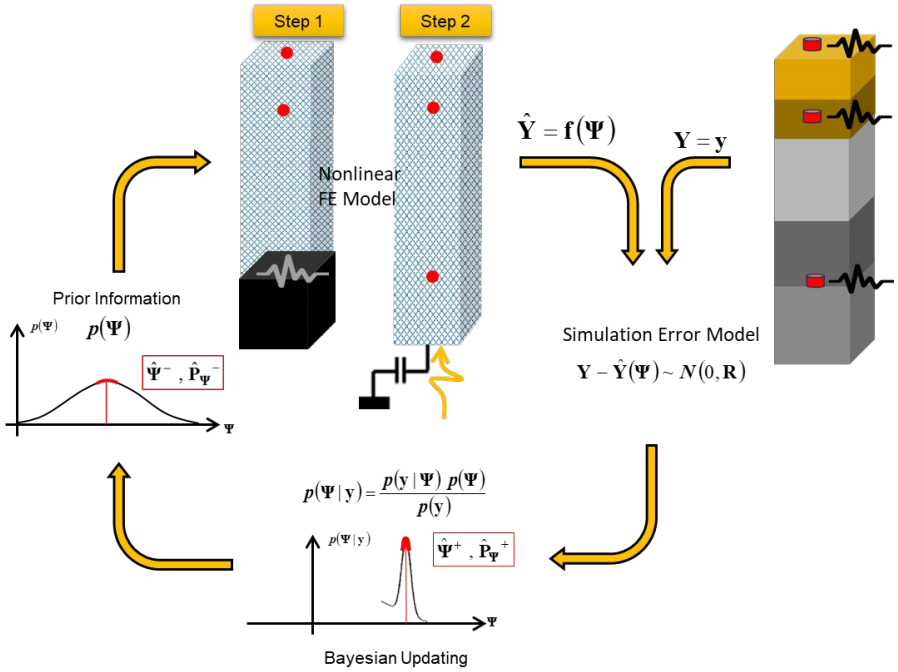

Figure 4. The two-step solution.

The Bayesian Model Updating

Bayesian model updating is briefly reviewed for the readers' convenience. The formulation is presented for the general case of input-parameter estimation, while it is employed partially in Steps 1 and 2 as part of the two-step solution described above.

Let's assume a site with a soil deposit, as shown in Figure 5 (left). There are m soil layers located above an elastic half-space with finite rigidity (bedrock) and excited by vertically propagating earthquake excitations. Absolute accelerations at several points (not necessarily at all layers or even boundaries of layers) are recorded by a geotechnical array. This continuous system can be modeled using a Finite Element (FE) model, as shown in Figure 5 (right) [16]. In this model, the soil is modeled in two-dimensions using plane strain elements. To account for the finite rigidity of the bedrock, a Lysmer-Kuhlemeyer [17] dashpot is incorporated at the base of

the soil column, whose coefficient equals the product of the mass density and shear wave velocity of the bedrock with the area of the base of the soil column (size of the element). The soil column is excited at the base by a horizontal force time-history, which is equal to the ground velocity multiplied by the dashpot's coefficient [18].

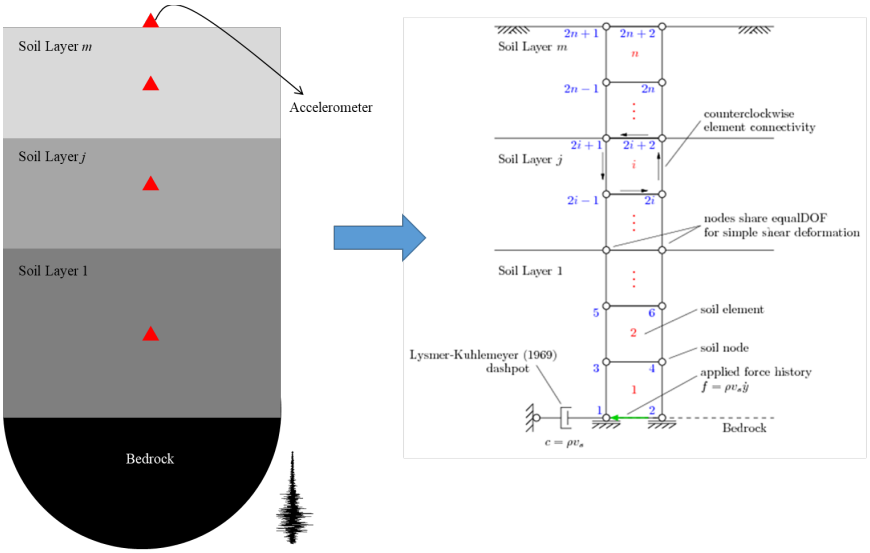

Figure 5. Instrumented soil deposit (left) and its equivalent discrete FE model (right).

The response of the FE model at each time step to the applied force time-history can be expressed as a nonlinear function of the model parameter vector, $\boldsymbol{\theta}$, and the time-history of the force, $\boldsymbol{f}_{1:i}$,

$$\hat{\boldsymbol{y}}_i = h_i(\boldsymbol{\theta}, \boldsymbol{f}_{1:i}), \tag{1}$$

where $\boldsymbol{\theta} = [\theta_1, \dots, \theta_{n_\theta}]$ contains n_θ parameters (e.g., the layers' shear wave velocities, parameters of the constitutive models, etc.) that define the FE model, and $h_i(.)$ is the nonlinear response function of the FE model at time step i, encapsulating all the dynamics of the model from time step 1 to i. The measured response vector of the site, $\boldsymbol{y}_i$, is related to the FE predicted response, $\hat{\boldsymbol{y}}_i$, as

$$\boldsymbol{v}_i(\boldsymbol{\theta}, \boldsymbol{f}_{1:i}) = \boldsymbol{y}_i - \hat{\boldsymbol{y}}_i(\boldsymbol{\theta}, \boldsymbol{f}_{1:i}), \tag{2}$$

where $\boldsymbol{v}_i \in \mathrm{R}^{n_y \times 1}$ is the simulation error vector that accounts for the misfit between the measured responses of the site at n_y locations and the FE-predicted response. The simulation error is ideally modeled as a zero-mean Gaussian white noise vector (i.e., $\boldsymbol{v}_i \sim N(\boldsymbol{0}, \mathbf{R})$) by neglecting the effects of modeling error. The objective of the estimation problem is to find the estimates of the unknown parameter vector, i.e., $\boldsymbol{\psi}_i = \left[\boldsymbol{\theta}^T, \boldsymbol{f}_{1:i}{}^T\right]^T$, for which the discrepancies between the measured and FE predicted responses are minimized in a probabilistic sense. Since the estimation problem is highly nonlinear, a sequential estimation approach is used to improve estimation efficiency. In our approach, the time domain is divided into successive overlapping time windows, referred to as the estimation windows. The problem is then solved at each window to estimate the unknown parameter vector.

Assume that the m-th estimation window spans from time step t_1^m to time step t_2^m. Therefore, the unknown parameter vector at this estimation window is defined as $\boldsymbol{\psi}_m = \left[\boldsymbol{\theta}^T, \boldsymbol{f}_{t_1^m:t_2^m}^{m\,T}\right]^T$, where $\boldsymbol{\psi}_m \in \mathrm{R}^{(n_{\boldsymbol{\theta}}+t_l)\times 1}$, in which $t_l = t_2^m - t_1^m$ is the window length. The unknown parameter vector, $\boldsymbol{\psi}_m$, can be estimated using a parameter-only Kalman filtering method (e.g., [19]). To this end, the unknown parameter vector is modeled as a random vector, the evolution of which is characterized by a Gaussian Markov process—also known as a random walk. Then, a state-space model is set up, in which the state equation governs the evolution of the random parameter vector and the measurement equation corresponds to the discrepancies between the measured and FE predicted responses [20], i.e.,

$$\boldsymbol{\psi}_{m,k+1} = \boldsymbol{\psi}_{m,k} + \boldsymbol{\gamma}_{m,k}, \tag{3}$$

$$\boldsymbol{y}_{t_1^m:t_2^m} = \widehat{\boldsymbol{y}}_{t_1^m:t_2^m,k+1}\left(\boldsymbol{\psi}_{m,k+1}\right) + \boldsymbol{v}_{t_1^m:t_2^m,k+1}, \tag{4}$$

where $\boldsymbol{\gamma}_{m,k} \sim N(\mathbf{0}, \mathbf{Q})$, $\boldsymbol{v}_{t_1^m:t_2^m,k+1} \sim N(\mathbf{0}, \widetilde{\mathbf{R}})$, where $\widetilde{\mathbf{R}} \in \mathrm{R}^{(t_l\times n_{\boldsymbol{y}})\times(t_l\times n_{\boldsymbol{y}})}$ is a block diagonal matrix, whose block diagonals are the simulation error covariance matrix $\mathbf{R}$. In Eqs. (3) and (4), k denotes the iteration number. As can be observed, the estimation process at each estimation window is iterative, i.e., the mean vector and covariance matrix of the unknown parameter vector is iteratively updated based on the discrepancies between the time histories of the measured and estimated responses.

An Unscented Kalman Filtering (UKF) [21] method can then be used to update the unknown parameter vector at each iteration. In our method, the nonlinear FE model is evaluated separately at a set of deterministically selected realizations of the unknown parameter vector, which are referred to as the sigma points (SPs) denoted by $\boldsymbol{\vartheta}^j$. The sigma points are selected around the prior mean estimate $\widehat{\boldsymbol{\psi}}^-$. In this study, a scaled Unscented Transformation (UT) based on $2n_{\boldsymbol{\psi}} + 1$ sigma points (i.e., $j = 1,2,\ldots,2n_{\boldsymbol{\psi}} + 1$) is used, where $n_{\boldsymbol{\psi}}$ denotes the size of the extended parameter vector. The mean and covariance matrix of the FE predicted structural responses, and the cross-covariance matrix of $\boldsymbol{\psi}$ and $\boldsymbol{y}$ are respectively computed using a weighted sampling method as

$$\overline{\boldsymbol{y}} = \sum_{j=1}^{2n_{\boldsymbol{\psi}}+1} W_m^j\, \widehat{\boldsymbol{y}}_i\left(\boldsymbol{\vartheta}^j\right), \tag{5}$$

$$\widehat{\mathbf{P}}_{\boldsymbol{yy}} = \sum_{j=1}^{2n_{\psi}+1} W_e^j \left[\widehat{\boldsymbol{y}}_i\left(\boldsymbol{\vartheta}^j\right) - \overline{\boldsymbol{y}}\right]\left[\widehat{\boldsymbol{y}}_i\left(\boldsymbol{\vartheta}^j\right) - \overline{\boldsymbol{y}}\right]^T + \mathbf{R}, \tag{6}$$

$$\widehat{\mathbf{P}}_{\boldsymbol{\psi y}} = \sum_{j=1}^{2n_{\psi}+1} W_e^j \left[\boldsymbol{\vartheta}^j - \widehat{\boldsymbol{\psi}}^-\right]\left[\widehat{\boldsymbol{y}}_i(\boldsymbol{\vartheta}^j) - \overline{\boldsymbol{y}}\right]^T, \tag{7}$$

where W_m^j and W_e^j denote weighting coefficients [21]. Now, the UKF prediction-correction procedure can be employed to estimate the posterior parameter mean vector $\widehat{\boldsymbol{\psi}}^+{}_{m,k+1}$ and covariance matrix $\widehat{\mathbf{P}}^+_{\boldsymbol{\psi},m,k+1}$ at each iteration. The proposed identification algorithm is summarized in Table 1.

Table 1. Identification algorithm for joint estimation of the model parameters and the FIM time history.

1. Set the estimation window length t_l, and the start and end points of each estimation window.
2. Set the initial mean vector and covariance matrix of the unknown parameter vector as
$$\widehat{\boldsymbol{\psi}}^{+}{}_{0} = \left[\widehat{\boldsymbol{\theta}}_0{}^{T}, \boldsymbol{f}^{0}_{t_1^0:t_2^0}{}^{T}\right]^{T}, \text{ and } \mathbf{P}^{+}_{\boldsymbol{\psi},0} = \begin{bmatrix} \widehat{\mathbf{P}}_{\boldsymbol{\theta\theta},0} & \mathbf{0} \\ \mathbf{0} & \widehat{\mathbf{P}}_{\boldsymbol{f}^0} \end{bmatrix}.$$
3. Define the process noise covariance matrix $\mathbf{Q}$ and the simulation error covariance matrix $\mathbf{R}$. Set up matrix $\widetilde{\mathbf{R}}$.
4. For the m-th estimation window:
   4.1. Retrieve the posterior estimates of the mean vector and covariance matrix of the unknown parameter vector from the last estimation window (i.e., $\widehat{\boldsymbol{\psi}}^{+}{}_{m-1}$, and $\mathbf{P}^{+}_{\boldsymbol{\psi},m-1}$). Set up $\widehat{\boldsymbol{\psi}}^{+}{}_{m,0}$ and $\mathbf{P}^{+}_{\boldsymbol{\psi},m,0}$ based on $\hat{\boldsymbol{\psi}}^{+}_{\boldsymbol{m}-1}$ and $\mathbf{P}^{+}_{\boldsymbol{\psi},m-1}$.
   4.2. Iterate (k = 1, 2, …):
   a. Set $\widehat{\boldsymbol{\psi}}^{-}{}_{m,\mathrm{k}+1} = \widehat{\boldsymbol{\psi}}^{+}{}_{m,\mathrm{k}}$, $\mathbf{P}^{-}_{\boldsymbol{\psi},m,k+1} = \mathbf{P}^{+}_{\boldsymbol{\psi},m,k} + \mathbf{Q}$.
   b. Generate sigma points. Run the FE model for $(2n_{\boldsymbol{\psi}} + 1)$ sigma points. Derive $\bar{\boldsymbol{y}}$, $\widehat{\mathbf{P}}_{\boldsymbol{yy}}$, and $\widehat{\mathbf{P}}_{\boldsymbol{\psi y}}$ using Eqs. (5)-(7).
   c. Compute the Kalman gain matrix: $\mathbf{K} = \widehat{\mathbf{P}}_{\boldsymbol{\psi y}}\left(\widehat{\mathbf{P}}_{\boldsymbol{yy}}\right)^{-1}$.
   d. Find the corrected estimates of the mean vector and covariance matrix of the unknown parameter vector: $\widehat{\boldsymbol{\psi}}^{+}{}_{m,\mathrm{k}+1} = \widehat{\boldsymbol{\psi}}^{-}{}_{m,\mathrm{k}+1} + \mathbf{K}\left(\boldsymbol{y}_{t_1^m:t_2^m} - \bar{\boldsymbol{y}}\right)$, $\mathbf{P}^{+}_{\boldsymbol{\psi},m,k+1} = \mathbf{P}^{-}_{\boldsymbol{\psi},m,k+1} - \mathbf{K}\left(\widehat{\mathbf{P}}_{\boldsymbol{yy}} + \widetilde{\mathbf{R}}\right)\mathbf{K}^{T}$.
   e. Check for convergence: if $\left|\widehat{\boldsymbol{\psi}}^{+}{}_{m,k+1} - \widehat{\boldsymbol{\psi}}^{+}{}_{m,k}\right| < 0.02 \times \widehat{\boldsymbol{\psi}}^{+}{}_{m,k-1}$ or $k + 1 > 10$, then move to the next estimation window ($m = m + 1$, go to step 4); otherwise, iterate again at the current estimation window ($k = k + 1$, go to step 4.2).

The Selected Constitutive Model

During the last few decades, a broad range of nonlinear soil models—uniaxial to multi-axial, phenomenological to physics-based—have been devised (e.g., [22], [23], [24], [25], [26]). For example, one of the most well-known and advanced nonlinear soil models is the one devised by Elgamal and co-workers [26]. In that model, soil plasticity is formulated based on the multi-surface concept, with a non-associative flow rule to reproduce the well-known dilatancy effect. The yield surfaces are of the Drucker-Prager [27] type. This model is frequently used in the direct simulation of SSI problems within the research community and is already available in OpenSees [28]. The multiple hierarchical yield surfaces of this model enable it to approximate the soil behavior within a broad range of strain regimes, but this is also its disadvantage in that a large number of requisite model parameters renders the calibration process formidable. By the same token, the model may exhibit spurious sensitivities. As we are going to solve a massive inverse problem using real-life data, these two major drawbacks are problematic.

A model with a simpler scaffold is that proposed by Borja and Amies [23]. This is also a multi-surface model but it only has a bounding surface and a vanishing elastic region. Incidentally, the Borja-Amies (BA) model only needs a few parameters for calibration. The validity of this model was examined by utilizing the downhole array motions recorded at Lotung, Taiwan, through one-dimensional nonlinear site response analyses [29] with promising success. The model admits an additive decomposition of the stress into inviscid (frictional) and viscous parts, as in:

$$\boldsymbol{\sigma} = \boldsymbol{\sigma}^{inv} + \boldsymbol{\sigma}^{vis}, \quad \boldsymbol{\sigma}^{inv} = \boldsymbol{C}^{e}\colon(\boldsymbol{\epsilon} - \boldsymbol{\epsilon}^{p}), \quad \boldsymbol{\sigma}^{vis} = \boldsymbol{D}\colon\dot{\boldsymbol{\epsilon}} \tag{8}$$

where $\boldsymbol{C}^e$ and $\boldsymbol{D}$ are elastic stiffness and viscous damping tensors, respectively; $\boldsymbol{\epsilon}$ is the total strain tensor; $\boldsymbol{\epsilon}^p$ is the plastic strain tensor; and $\dot{\boldsymbol{\epsilon}}$ is the total strain rate. Given this decomposition, the model can also incorporate material level strain-rate-dependent damping, which enables a modeler to match field-identified damping behavior, even when such behavior is complex. Omitting details here for brevity, the main equation to calibrate this model is,

$$\frac{G}{G_{max}} = 1 - \frac{3}{2\tau_o}\int_0^{2\tau_o}\left[h\left(\frac{R/\sqrt{2}+\tau_o-\tau}{\tau}\right)^m + H_0\right]^{-1} d\tau \tag{9}$$

where $G = \tau_o/\gamma_o$ is the secant shear stiffness, and R is the radius of the bounding surface, and parameters h, m and H_0 control the intensity of the hardening. The model can be directly calibrated using an experimentally obtained (or otherwise estimated from real-life) $G/G_{\max}$ curve [30] and a frequency-dependent damping curve. In the present study, we will explore the capabilities of this soil model in capturing the dynamic response of soils, and we will incorporate it with the UKF-based estimation method we have described above.

The advantages of the BA model are clear:

- It is a thermodynamically consistent model based on the classical viscoplasticity framework with well-defined parameters.
- It is a three-dimensional model, and thus, if it is accurately calibrated, it can accurately predict soil behavior under multi-axial stress states, such as those due to irregular surface topography and soil stratigraphy, or underground scatterers.

As a part of a parallel study, the BA model has been successfully implemented in OpenSees and extensively verified and validated [31]. In this study, we use OpenSees [28] for all needed simulations, and the soil model is this recently implemented BA model.

Verification

Proof-Of-Concept Study

To verify the single-step joint input-parameter estimation solution, we synthetically generated the acceleration response of a 4-layer soil deposit on top of bedrock, as shown in Figure 6. To show that the estimation solution can work regardless of the material model, pressure-dependent elastic-plastic behavior is considered for the soil wherein plasticity is formulated based on the multi-surface concept with a non-associative flow rule to reproduce the dilatancy effect [26]. This model is already implemented in OpenSees [28]. The most important parameters needed to create this model are shown in Figure 6 for reproducibility. A Rayleigh damping matrix is considered, which generates low strain damping ratios of 2% at 0.2 and 20 Hz. The model is excited by the ground motion shown on the bottom-right of Figure 6, which is recorded by the Gilroy #1 array; and the site response (accelerations) is measured at five below-ground locations.

Since the numerical accuracy of the wave transmission is known to be affected by both the frequency content of the input and the propagation wave-speed characteristics of the domain, the spatial element size was considered to be one-tenth of the smallest wavelength [32]. By

limiting the frequency of interest to 20 Hz and by assuming a minimum shear wave velocity of 40 m/s (much lower than available values), the element size of 0.2 m was used in this example. As this is an inverse problem, we used uniform meshing in-depth, while a finer mesh could be used in layers with higher shear wave velocities. Also, while the sampling rate is kept at 200 Hz in the analyses for the accuracy of the direct integration method, the highest reliable frequency would be 20 Hz.

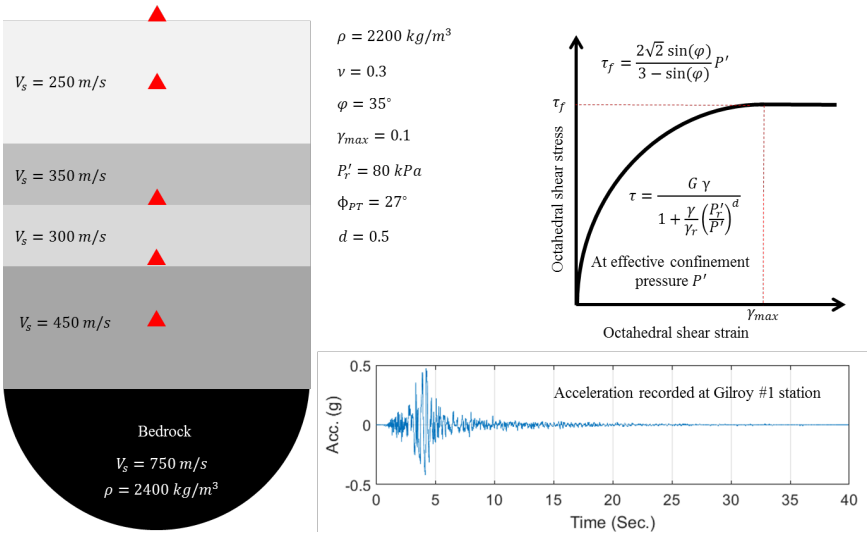

Figure 6. An illustrative example.

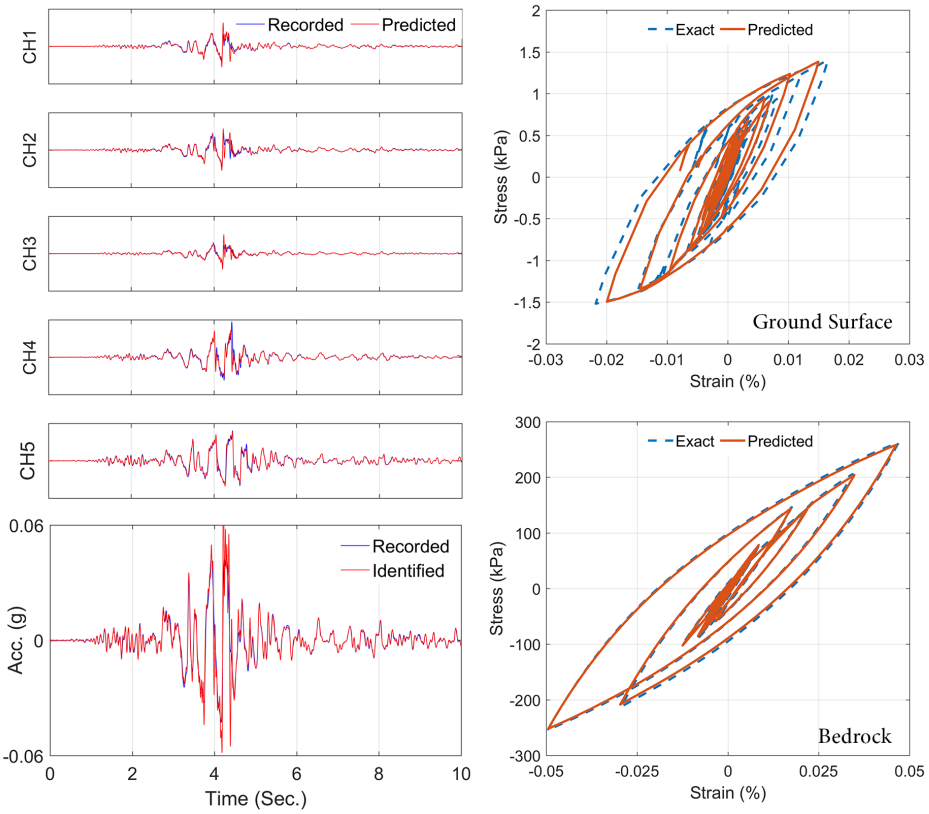

Figure 7. Identification results. Recorded and predicted responses (top-left), exact and identified bedrock acceleration (bottom-left), and Hysteresis loops near the surface and near the bedrock (right).

The input force (i.e., bedrock velocity time history), the shear wave velocities at three top layers, the pressure-dependency coefficient (d), and low-strain damping are assumed as unknown parameters and are estimated through the proposed output-only estimation method. We only used 10 seconds of the signals for the estimation and ran the algorithm in consecutive 2.5-second windows with a 1-second overlap. We assumed a 50% initial error for the unknown parameters. The identification results are shown in Figure 7. As seen, the bedrock acceleration, site response at the instrumented locations, as well as hysteresis loops near the surface and the bedrock are identified with very good accuracy (no stress/strain data was used for the identification). Results show that all of the unknown parameters, except the damping value, are estimated with final errors that are less than 3%. The damping value was not accurately identified because it does not significantly change the site response as seen in Figure 7. The sensitivity of the measured response with respect to the model parameters (parameter identifiability) needs an in-depth identifiability study which will be discussed later.

The Lotung Site

To verify the proposed inverse solution, the Lotung site is simulated which will be later used for the validation studies too. Therefore, this site and its data are briefly reviewed here.

The Lotung Large-Scale Seismic Tests (LSST) site is located in the North-East of Taiwan. This site was established in a seismically active region in 1985 to study seismic soil-structure interactions effects on nuclear power plants. To do so, two scaled structures were constructed by the Electric Power Research Institute (EPRI) and the Taiwan Power Company [33]. In addition to the structures, the responses of the soil were recorded in several locations on the surface, and at different depths, as shown in Figure 8. Due to such dense instrumentation, the data from this site has been the subject of many studies [29], [34]–[38]. Specifically, Zeghal and Elgamal [7], [39] have extensively studied several earthquake data sets recorded at this site between 1985 to 1986 (Table 2)[1].

Out of these 18 events, the first three events and Event No. 13 are not available. Also, the digitized signals' resolution is relatively poor in several cases (Events No. 5, 6, 8, 9, 10, 15, 17, and 18). We also need data with a significant level of motion to observe soil nonlinearity. Moreover, the site's behavior must be close to 1D, so the source of the earthquake should be far from the site. Considering these criteria, events 7 and 16 are the best candidates that have been used by Borja et al. [29], [38], [40] too. The channels mostly used in previous studies and used here are FA1-5, DHB6, DHB11, DHB17, and DHB47 (see Figure 8) which are at depths of 0, 6, 11, 17, and 47 meters, respectively. It is noteworthy that Channel 47 is not available in Event No. 16, so Step 1 (Input-Output identification) can only be carried out for the first 17 meters.

[1] Data is publicly available at http://soilquake.net/Downholearray/Lotung/

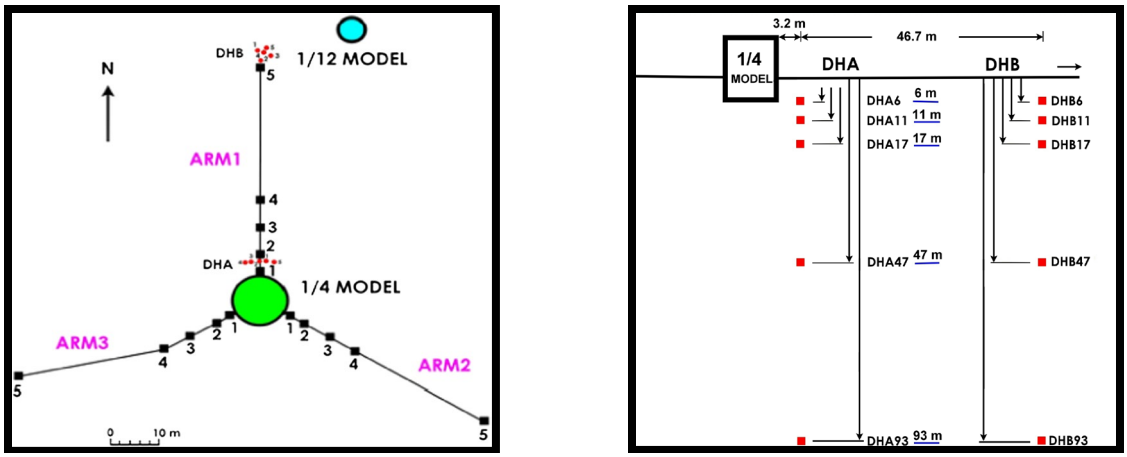

Figure 8. Plan (left) and elevation (right) views of the Lotung site.

Table 2. Recorded earthquake data at the Lotung site [7], [41].

Event (1)	Date (2)	Magnitude (M_l) (3)	Epicentral distance (km) (4)	Focal depth (km) (5)	Distance to zone of energy release (km) (6)	Peak Acceleration[a] EW (g) (7)	NS (g) (8)	V (g) (9)
LSST 1	9/20/85	—	—	—	—	—[b]	—	—
LSST 2	10/26/85	5.3	—	—	—	0.03	0.03	0.01
LSST 3	11/7/85	5.5	—	—	—	0.01	0.01	0.01
LSST 4	1/16/86	6.5	23.7	10.2	25.80	0.15[c]	0.26[c]	0.11[c]
LSST 5	3/29/86	—	—	—	—	0.04	0.03	0.03
LSST 6	4/8/86	5.4	31.4	10.9	33.24	0.04	0.03	0.01
LSST 7	5/20/86	6.5	66.2	15.8	68.06	0.16	0.21	0.04
LSST 8	5/20/86	6.2	69.2	21.8	72.55	0.03	0.03	0.01
LSST 9	7/11/86	4.5	5.0	1.1	5.12	0.07	0.05	0.01
LSST 10	7/16/86	4.5	6.1	0.9	6.17	0.03	0.04	0.02
LSST 11	7/17/86	5.0	6.0	2.0	6.32	0.07	0.10	0.04
LSST 12	7/30/86	6.2	5.2	1.6	5.44	0.16	0.19	0.20
LSST 13	7/30/86	6.2	—	—	—	0.05	0.03	0.02
LSST 14	8/5/86	4.9	4.7	2.3	5.32	0.05	0.03	0.02
LSST 15	11/14/86	—	—	—	—	0.02	0.04	0.05
LSST 16	11/14/86	7.0	77.9	6.9	78.21	0.13	0.17	0.10
LSST 17	11/14/86	—	—	—	—	0.04	0.04	0.02
LSST 18	11/15/86	—	—	—	—	0.03	0.02	0.01

[a]Peak accelerations for the DHB array including the surface FA1-5 station.
[b]LSST 1 records did not include any free field motion.
[c]LSST 4 records were affected by electric glitches.

As the BA model is being used in this study, we model the Lotung site using the information provided by Borja et al. [29], [38]. Figure 9 shows the layered FE model of the first 47 m of the Lotung site with a fixed bottom condition (within boundary condition) and the shear wave velocity and elastic shear modulus profiles. The instrumented depths are specified by red circles (the lowest level is at the fixed boundary). The parameters of the BA model for all layers are the same and taken from [40] as $R = 0.0015G_{max}, H_0 = 0, h = 0.63G_{max}, m = 0.97$ and the Poission ratio is 0.48. The fundamental natural frequency of the elastic model that is fixed at 47m-depth is 1.33 Hz. Note that this frequency could be different from the natural frequency of the Lotung site. The natural frequency of the model is obtained by applying a fictitious fixed boundary condition (imposing an infinite impedance contrast), but the dominant frequency observed in the recorded data could be different depending to the depth at which there is actually such significant impedance contrast [42].

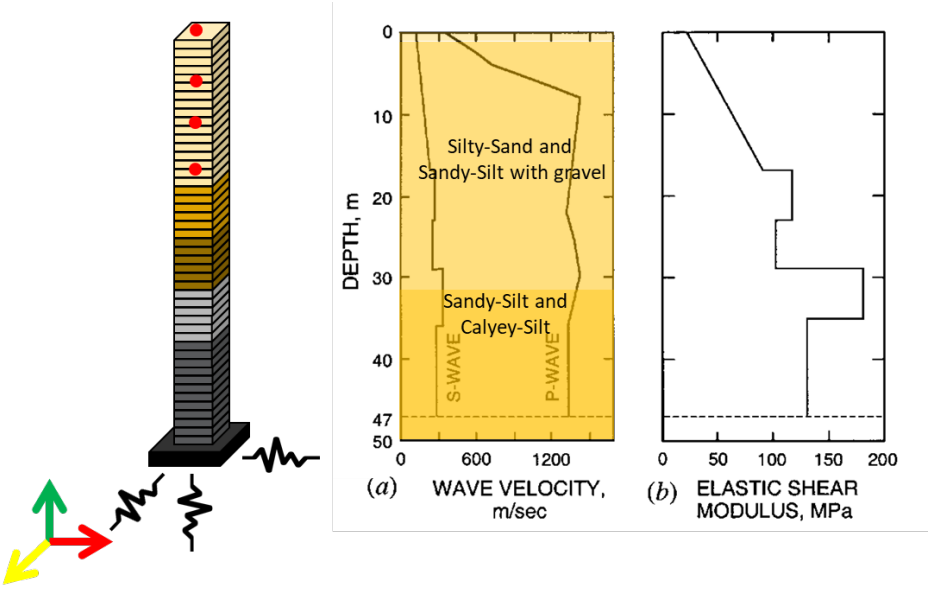

Figure 9. The FE model of the first 47 m of the Lotung site with a fixed bottom condition (left) and shear wave velocity and elastic shear modulus profile (right) [40].

To set the damping parameters, Borja et al. [40] identified a dominant excitation frequency of 0.65 Hz from the recorded signal at a depth of 47 m in the LSST7 event. They assumed a 1% stiffness proportional damping resulting in a factor of 0.005. So, the same level of damping was assumed in this study whenever simulations are carried out. To make the results comparable, the same modeling and analysis assumptions are used. An element size of 1 m is used through which frequencies up to 25 Hz can be resolved. So, all recorded signals are decimated to 50 Hz. Analyses are also carried out at the same rate, but subsampling is used whenever there is a convergence issue. Similar to [40], the Hilber-Hughes-Taylor (HHT) integration method with $\alpha = -0.1, \beta = 0.3025$, and $\gamma = 0.6$ is employed for all analyses. The effect of pore water pressure is neglected and all analyses are carried out in a total stress state.

Verification Studies

As mentioned earlier, the first step of the proposed two-step solution can be carried out for any depth as long as there is a sensor at that depth to record the "within motion." So, we present results for the first 17 m because there is a large gap between this depth and 47 m.

As shown before (see Figure 9), the modulus of elasticity increases linearly in the first 17 m. So, the parameters P_1 to P_9 are considered as candidate updating parameters to represent the soil properties using the following definitions:

$$G_{max} = P_1 + zP_2 \tag{10}$$

$$\nu = P_3 \tag{11}$$

$$S_u = P_4 + zP_5 \tag{12}$$

$$h = P_6 + zP_7 \tag{13}$$

$$m = P_8 \tag{14}$$

$$a_1 = P_9 \tag{15}$$

where z is the depth from the ground surface and S_u is undrained shear strength. An identifiability study [43] is first carried out using LSST7 simulation data to find out which parameters are identifiable. Figure 10(left) shows the entropy gain of these 9 parameters. As seen, the Poisson's ratio is unidentifiable (at least around the assumed value), while the other 8 parameters are identifiable. However, there are two important notes: 1- the identifiability here means the responses are sensitive to the variation of these parameters, but the results of the identification could be sensitive to the start point, as the problem is not convex. 2- There is no absolute threshold above which parameters are guaranteed to be identifiable. Indeed, this index can only detect the identifiability of parameters with respect to each other. Another fact that can reduce the identifiability of the parameters is their mutual correlation. Figure 10(right) shows the severity of this correlation among these nine parameters (scaled to their entropy to be comparable). As seen, the only significant correlation is between parameters defining depth variation of S_u and h. That is, S_u and h might not be properly identified.

Figure 11 shows how the identification algorithm performs having 8 unknown parameters (the Poisson ratio is excluded) and using simulated data from LSST7 event. We started the identification assuming a 50% initial error. As seen, while the predicted responses are perfectly matched to the recorded (here simulated) responses, some parameters are not identified very well due to the observed cross-correlation in the identifiability results.

We repeated the same problem with depth invariant parameters in simulation and identification, i.e., $G_{max} = P_1$, $S_u = P_4$, $h = P_6$, $m = P_8$, and $a_1 = P_9$. As shown in Figure 12, this is a healthy identification problem because there is no information sharing among parameters, so all five parameters are identified with an acceptable level of accuracy.

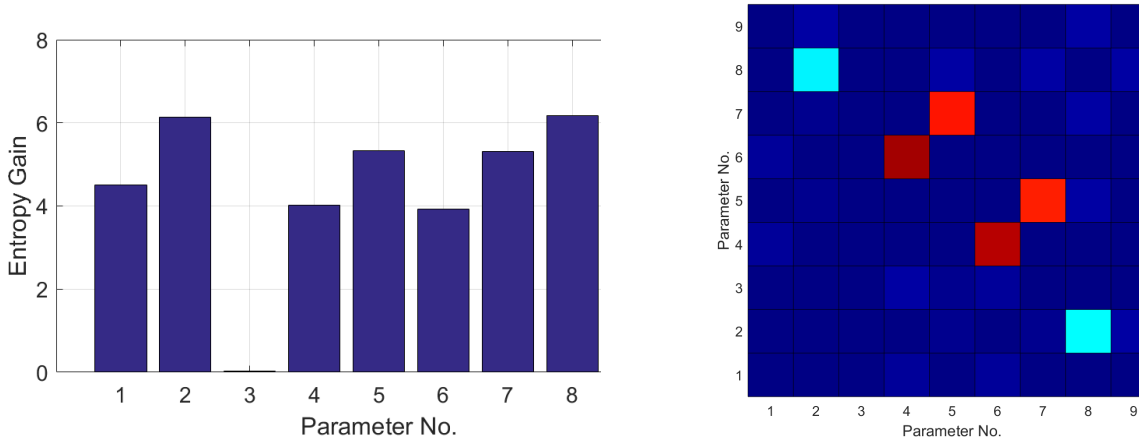

Figure 10. The identifiability study: entropy gain of each parameter (left), and the mutual information (right).

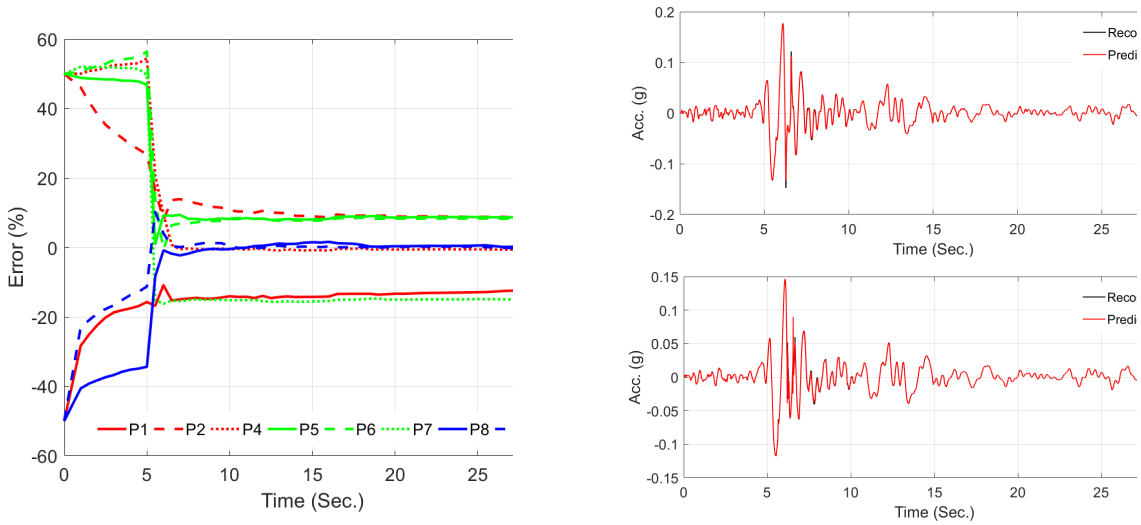

Figure 11. The identification results using 8 parameters. Left: identification progress, right: comparison between recorded (simulated) and predicted responses in the EW direction at the ground surface and depth 6m.

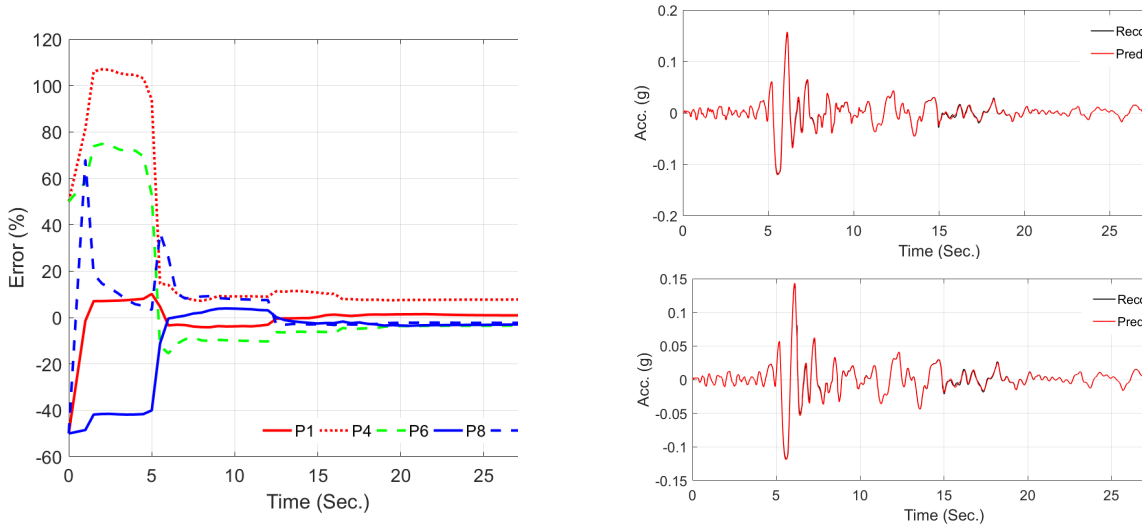

Figure 12. The identification results using 5 parameters. Left: identification progress, right: comparison between recorded (simulated) and predicted responses in the EW direction at the ground surface and depth 6m.

Validation

The Earthquake Data of The Lotung Site

Having a good understanding of the parameters' identifiability and the algorithm's performance, we use the real data from the LSST16 event to validate the estimation method. This event was selected because the behavior of the site is more close to 1D due to the long distance to the earthquake source [38]. We carry out the identification using two sets of updating parameters. In the first case, we use the same set of 8 parameters used in the simulated case

study, and we start the identification using the values suggested in [38]. Figure 13(left) shows how the parameters change in time when different time windows of data are received by the identification algorithm. The comparison between recorded, initial, and updated responses in Figure 14(left) shows that the updated model can predict responses, 22%, 15%, and 13% more accurately than the initial model in the EW-direction, respectively. By fixing the shear strength and consequently reducing the number of parameters, the accuracy of the updated model is even higher as shown in Figure 14(right). The percentage numbers are 27%, 19%, and 16%, respectively, in this case.

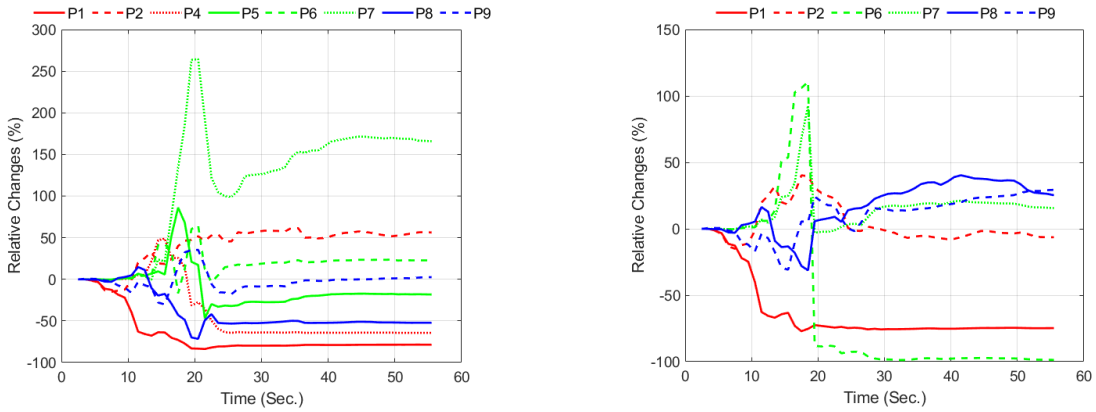

Figure 13. The identification results using two different parameter sets.

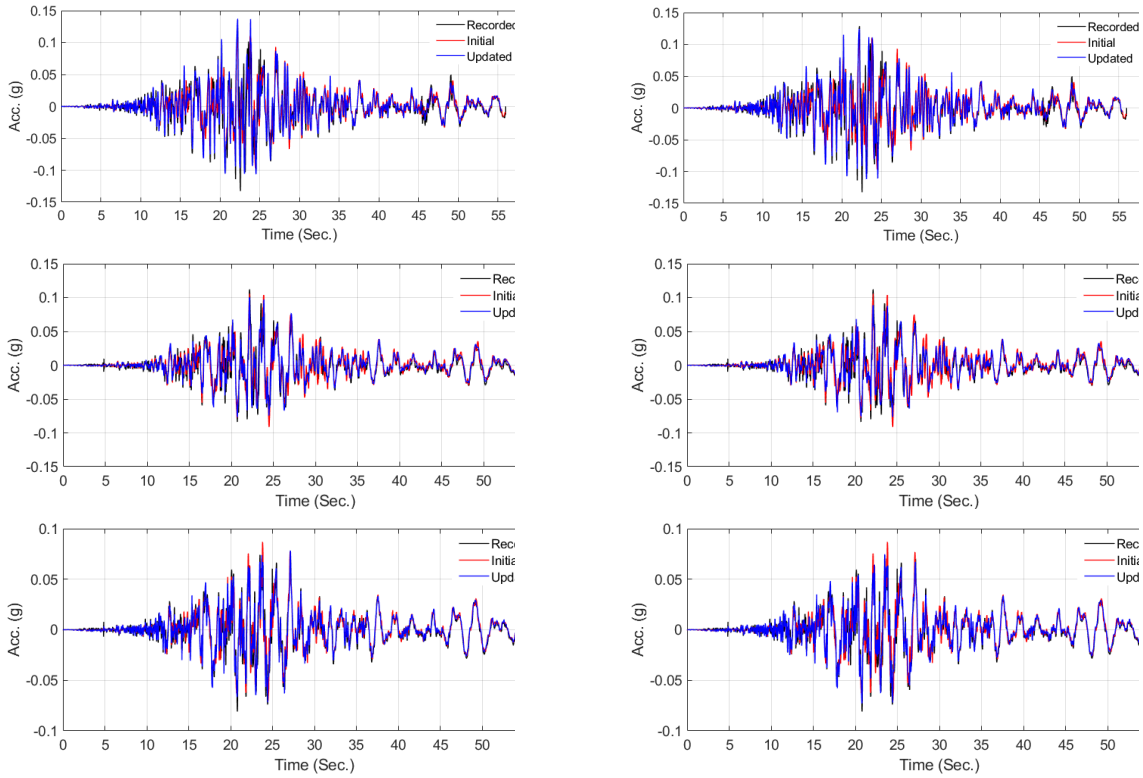

Figure 14. Comparison between recorded, initial, and updated responses using two different sets of parameters. The plots from top to bottom are responses at the ground surface to a depth of 11 m, respectively.

The Centrifuge Test Data

The centrifuge test data is precious data for the validation studies because parameters of the domain and input excitations are largely under control. Herein, we use data from a very recent centrifuge test series on buried culvert structures. The configuration of the test and the types of input excitations used to excite the domain are shown in Figure 15. The details of these tests can be found in [44]. The data from the free-field column (far from structures) under Event #10 is used here. The 1D-3C FE model, the sensor location, and the parameters of the BA model, which are obtained from [45], are shown in Figure 15 too. Assuming these values as exact parameters, the simulated responses at 5 instrumented elevations under Motion #10 are compared with the recorded signals in Figure 16. The simulation was carried out in both OpenSees and Abaqus for further verification of the OpenSees BA implementation. As seen, the model can simulate the response very well.

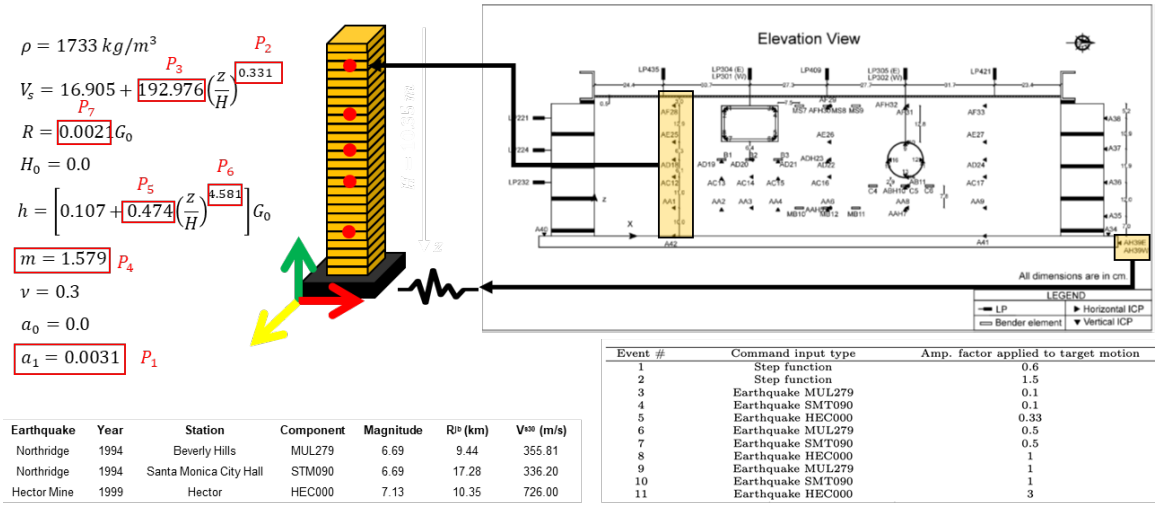

Earthquake	Year	Station	Component	Magnitude	R_{jb} (km)	V_{s30} (m/s)
Northridge	1994	Beverly Hills	MUL279	6.69	9.44	355.81
Northridge	1994	Santa Monica City Hall	STM090	6.69	17.28	336.20
Hector Mine	1999	Hector	HEC000	7.13	10.35	726.00

Event #	Command input type	Amp. factor applied to target motion
1	Step function	0.6
2	Step function	1.5
3	Earthquake MUL279	0.1
4	Earthquake SMT090	0.1
5	Earthquake HEC000	0.33
6	Earthquake MUL279	0.5
7	Earthquake SMT090	0.5
8	Earthquake HEC000	1
9	Earthquake MUL279	1
10	Earthquake SMT090	1
11	Earthquake HEC000	3

Figure 15. Centrifuge experiment.

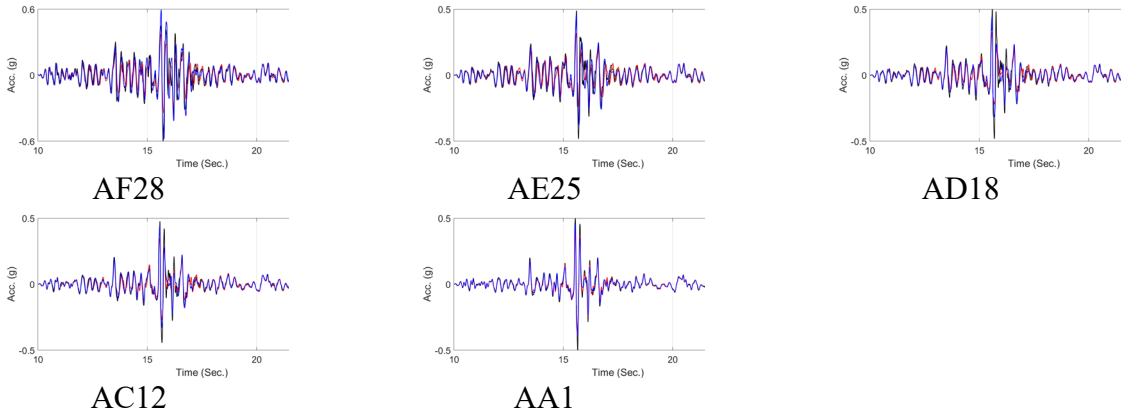

Figure 16. Forward simulation using assumed considered exact values.

We use this model and data to validate the single-step solution, as the model is physically fixed at the base. The base motion along with seven parameters specified in Figure 15 are considered as unknown parameters. We start the updating assuming a 50% initial error for the

parameters and 10% initial Coefficient Of Variation (COV). The results of the identification are shown in Table 3. As seen, out of these 7 parameters, Parameter 3 has a very large estimation COV showing that the problem is almost insensitive to this parameter, and the estimated value is unreliable. All other parameters are estimated with small COV, and the estimated values are reliable, and most of them are close to the considered exact values with various differences. However, Parameter 5 shows a very large difference with respect to the considered exact value. To see how the predicted responses using these values differ from Figure 17 is presented. In this figure, the comparison between recorded and predicted using the estimated parameters are shown on the right side, while the previous simulations are shown on the left side. As seen, the responses obtained from the updated model are closer to the recorded responses. As these responses are used for the model updating, it is not surprising to see such better prediction, but as shown in Figure 18, the estimated input excitation is very close to the recorded motion at the base of the shake table, confirming the results of the output-only model updating is very reliable.

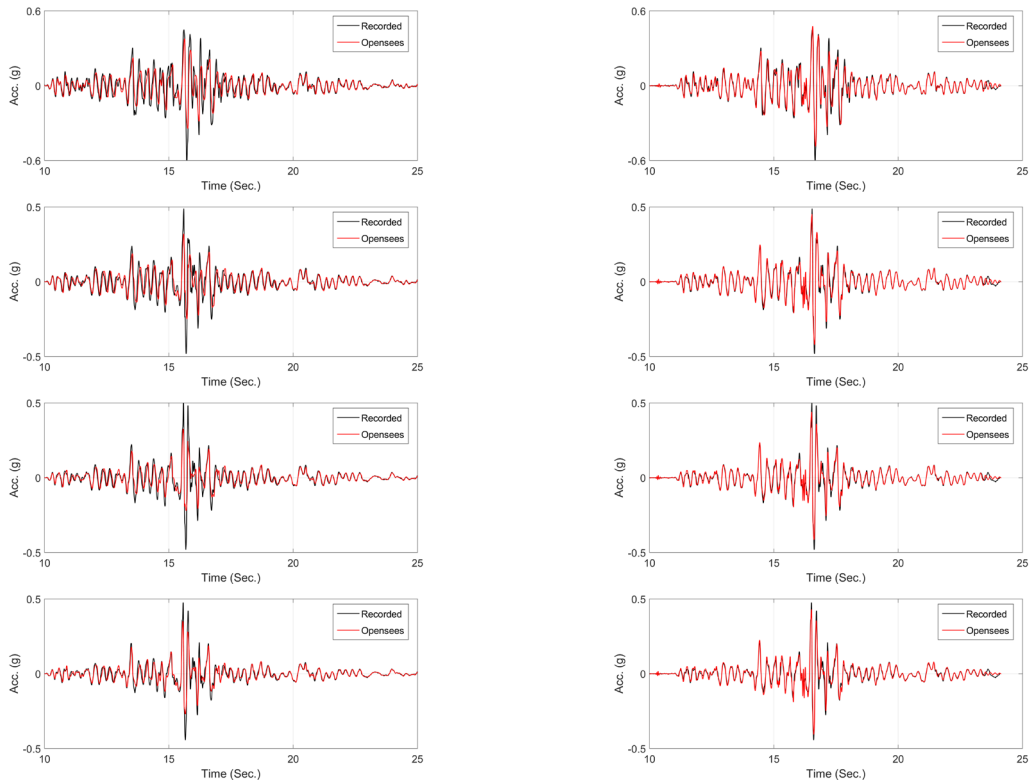

Figure 17. Comparison between recorded and predicted acceleration responses at four top sensors using considered exact (left) and identified (right) parameters.

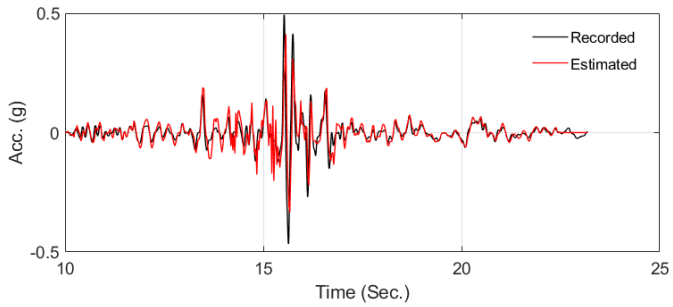

Figure 18. Comparison between exact and estimated input excitations.

Table 3. identification results.

Parameter	Initial Value	Final Value	Initial COV	Final COV
1	+50%	-1.4%	10%	0.0%
2	+50%	+91%	10%	0.2%
3	+50%	+50%	10%	70%
4	+50%	+7%	10%	1.0%
5	+50%	+800%	10%	3.2%
6	+50%	-33%	10%	2%
7	+50%	-13%	10%	0.0%

Application to CSMIP Geotechnical Arrays

As a real-life application, the data from the CSMIP station 68323 is used. Figure 19(left) shows the instrumentation layout and the P- and S-wave velocity profiles. The idealized version of the V_s profile was taken from [46] as shown in Figure 19(right). this idealized profile was later more idealized into 6 layers as colored in Figure 19(right). By the time of this study, 8 earthquake events have been recorded by this station, which are all very weak motions. The largest event is the 2014 South Napa event in which Peak Ground Acceleration (at the surface) was about 0.03g.

The V_s profile below 35 m is unknown, so we only carry out the first step (input-output) identification. Figure 20 shows the comparison between the predicted responses using the updated model and the recorded signals. The comparison between the updated Vs profile and the initial and modified profiles are shown in Figure 21. The modified profile is the idealized version of the initial profile as shown in Figure 19(right).

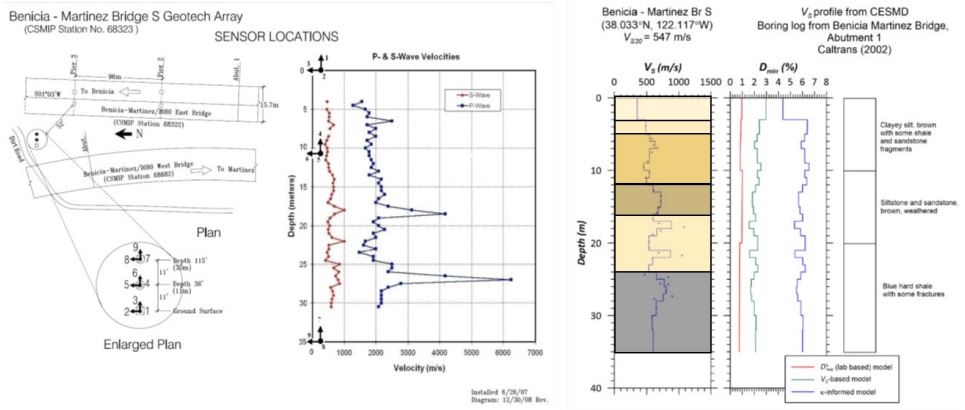

Figure 19. Benicia-Martinez Geotechnical Array. Instrumentation layout from CESMD (left), shear wave velocity, and small-strain damping profile.

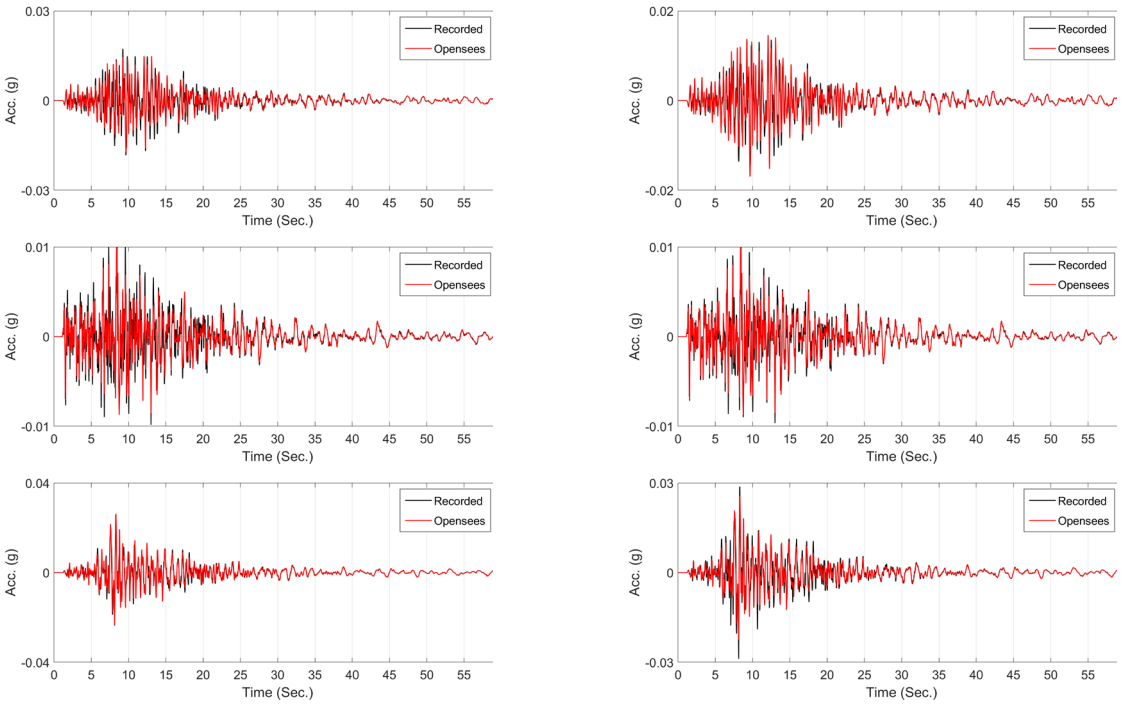

Ground surface Depth 11 m

Figure 20. Comparison between recorded and predicted responses in the South Napa 2014 earthquake. Plots from top to bottom show NS, vertical, and EW directions.

To see how this updated model works under another earthquake event, we carried out a blind prediction under El Cerrito 2010 event. Figure 22 shows a comparison between recorded and predicted ground surface motions using initial(modified) and updated models. As seen, the updated model can predict the ground surface more accurately.

Several other CSMIP stations were also studied using the proposed method. The results of those cases will be presented in the final report of the project.

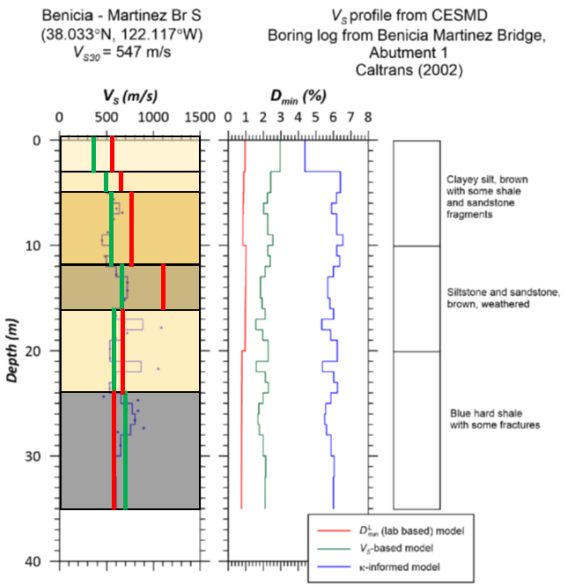

Figure 21. Comparison between initial, modified, and updated V_s profile.

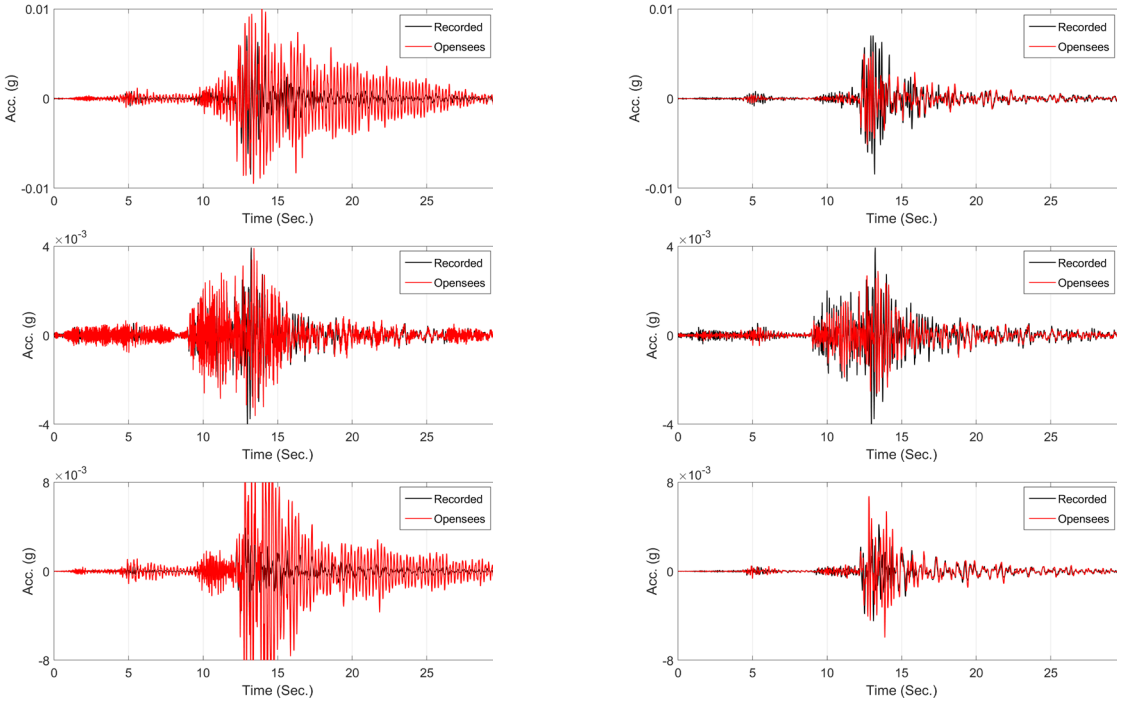

Initial(modified) model Updated model

Figure 22. Comparison between recorded and predicted ground surface responses in the El Cerrito 2010 earthquake. Plots from top to bottom show NS, vertical, and EW directions.

Conclusions

Dynamic soil properties are key ingredients of analysis for predicting/assessing soil-structure interaction (SSI) and site response effects under seismic excitations. Although there are various techniques and tools to carry out forward site response analysis with various complexity

levels, there could be significant uncertainty due to the available uncertainties in nonlinear soil models and their parameters. In this project, we developed, tested, and validated input-output and output-only identification algorithms to estimate nonlinear soil properties from data recorded in the geotechnical array. The method was verified using synthetic examples and validated using centrifuge data and data recorded in the well-known Lotung site. The method was also applied to several CSMIP Geotechnical Arrays.

Acknowledgment

The authors would like to acknowledge Prof. Pedro Arduino from the University of Washington for his fruitful comments, OpenSees implementation of the BA model, and Prof. Hamed Ebrahimain from the University of Nevada at Reno, who kindly shared his Bayesian estimation computer codes. The contributions of Dr. Wenyang Zhang and Dr. Fariba Abazarsa are greatly appreciated. The work presented in this manuscript was funded by the California Geological Survey (Contract No. 1019-015). Any opinions, findings, conclusions, or recommendations expressed in this material are those of the authors and do not necessarily reflect the views of the sponsoring agencies.

References

[1] S. L. Kramer, *Geotechnical Earthquake Engineering*, vol. 6. New York: Prentice-Hall, 1996.

[2] I. M. Idriss and H. B. Seed, "Seismic Response of Horizontal Soil Layers," *J. Soil Mech. Found. Div.*, vol. 94, no. 4, pp. 1003–1034, 1968.

[3] J. M. Roesset, "Soil amplification of earthquakes," *Numer. methods Geotech. Eng.*, pp. 639–682, 1977.

[4] D. Park and Y. M. a. Hashash, "Soil Damping Formulation in Nonlinear Time Domain Site Response Analysis," *J. Earthq. Eng.*, vol. 8, no. 2, pp. 249–274, 2004, doi: 10.1080/13632460409350489.

[5] I. a Beresnev and K. Wen, "Nonlinear Soil Response-A Reality ?," *Bull. Seismol. Soc. Am.*, vol. 86, no. 6, pp. 1964–1978, 1996, doi: 10.1061/(ASCE)0733-9410(1996)122:9(725).

[6] E. H. Field and K. H. Jacob, "A comparison and test of various site-response estimation techniques, including three that are not reference-site dependent," *Bull. Seismol. Soc. Am.*, vol. 85, no. 4, pp. 1127–1143, 1995.

[7] A. W. Elgamal, M. Zeghal, H. T. Tang, and J. C. Stepp, "Lotung Downhole Array. I: Evaluation of Site Dynamic Properties," *J. Geotech. Eng.*, vol. 121, no. 4, pp. 350–362, 1995, doi: 10.1061/(ASCE)0733-9410(1995)121:4(350).

[8] S. F. Ghahari, F. Abazarsa, C. Jeong, A. Kurtulus, and E. Taciroglu, "Blind identification of site effects and bedrock motions from surface response signals," *Soil Dyn. Earthq. Eng.*, vol. 107c, pp. 322–331, 2018.

[9] S. F. Ghahari, F. Abazarsa, and E. Taciroglu, "Probabilistic blind identification of site effects from ground surface signals," *Bull. Earthq. Eng.*, 2017, doi: 10.1007/s10518-017-0253-0.

[10] J.-S. Lin, "Extraction of dynamic soil properties using extended Kalman filter," *J. Geotech. Eng.*, vol. 120, no. 12, 1994, doi: 10.1061/(ASCE)0733-9410(1994)120:12(2100).

[11] E. Şafak, "Models and methods to characterize site amplification from a pair of records," *Earthq. Spectra*, vol. 13, no. 1, pp. 97–129, 1997, doi: 10.1193/1.1585934.

[12] H. Ebrahimian, R. Astroza, J. P. Conte, and C. Papadimitriou, "Bayesian optimal estimation for output-only nonlinear system and damage identification of civil structures," *Struct. Control Heal. Monit.*, vol. 25, no. 4, 2018, doi: 10.1002/stc.2128.

[13] H. Ebrahimian, S. F. Ghahari, D. Asimaki, and E. Taciroglu, "A Nonlinear Model Inversion to Estimate Dynamic Soil Stiffness of Building Structures."

[14] C. Papadimitriou, J. L. Beck, and S. K. Au, "Entropy-based optimal sensor location for structural model updating," *JVC/Journal Vib. Control*, 2000, doi: 10.1177/107754630000600508.

[15] J. L. Beck and L. S. Katafygiotis, "Updating Models and Their Uncertainties. I: Bayesian Statistical Framework," *J. Eng. Mech.*, vol. 124, no. 4, pp. 455–461, 1998, doi: 10.1061/(ASCE)0733-9399(1998)124:4(455).

[16] C. McGann and P. Arduino, "Site response analysis of a layered soil column (total stress analysis)," *Opensees Ex. Wiki. Univ. Washingt.*, 2010.

[17] J. Lysmer and R. L. Kuhlemeyer, "Finite Dynamic Model For Infinite Media," *J. Eng. Mech. Div.*, vol. 95, no. 4, pp. 859–878, 1969, doi: 10.1089/dia.2007.0302.

[18] W. B. Joyner and A. T. F. Chen, "Calculation of nonlinear ground response in earthquakes," *Bull. Seismol. Soc. Am.*, vol. 65, no. 5, pp. 1315–1336, 1975.

[19] H. Ebrahimian, R. Astroza, J. P. Conte, and R. A. de Callafon, "Nonlinear finite element model updating for damage identification of civil structures using batch Bayesian estimation," *Mech. Syst. Signal Process.*, vol. 84, pp. 194–222, 2017, doi: 10.1016/j.ymssp.2016.02.002.

[20] S. Haykin, *Kalman Filtering and Neural Networks*, vol. 5, no. 3. 2001.

[21] S. J. Julier and J. K. Uhlmann, "New extension of the Kalman filter to nonlinear systems," in *Signal Processing, Sensor Fusion, and Target Recognition VI*, 1997, vol. 3068, p. 182, doi: 10.1117/12.280797.

[22] M. Vucetic and R. Dobry, "Effect of soil plasticity on cyclic response," *J. Geotech. Eng.*, 1991, doi: 10.1061/(ASCE)0733-9410(1991)117:1(89).

[23] R. I. Borja and A. P. Amies, "Multiaxial cyclic plasticity model for clays," *J. Geotech. Eng.*, vol. 120, no. 6, pp. 1051–1070, 1994.

[24] M. T. Manzari and Y. F. Dafalias, "A critical state two-surface plasticity model for sands," *Geotechnique*, 1997, doi: 10.1680/geot.1997.47.2.255.

[25] F. Pisanò and B. Jeremić, "Simulating stiffness degradation and damping in soils via a simple visco-elastic-plastic model," *Soil Dyn. Earthq. Eng.*, vol. 63, pp. 98–109, 2014, doi: 10.1016/j.soildyn.2014.02.014.

[26] Z. Yang, A. Elgamal, and E. Parra, "Computational Model for Cyclic Mobility and Associated Shear Deformation," *J. Geotech. Geoenvironmental Eng.*, vol. 129, no. 12, pp. 1119–1127, 2003, doi: 10.1061/(ASCE)1090-0241(2003)129:12(1119).

[27] D. C. Drucker and W. Prager, "Soil mechanics and plastic analysis or limit design," *Q. Appl. Math.*, vol. 10, no. 2, pp. 157–165, 1952, doi: 10.1090/qam/48291.

[28] F. McKenna, "OpenSees: a framework for earthquake engineering simulation," *Comput. Sci. Eng.*, vol. 13, no. 4, pp. 58–66, 2011.

[29] R. I. Borja, H. Y. Chao, F. J. Montans, and C. H. Lin, "Nonlinear ground response at Lotung LSST site," *J. Geotech. Geoenvironmental Eng.*, vol. 125, no. 3, pp. 187–197, 1999, doi: 10.1061/(ASCE)1090-0241(1999)125:3(187).

[30] M. B. Darendeli, "Development of a new family of normalized modulus reduction and material damping curves," 2001.

[31] M. Arduino, P; Taciroglu, E; Bonilla, F.; Taiebat, "Development of a numerical nonlinear soil module to expand the capabilities of the SCEC BroadBand Platform," 2019.

[32] R. L. Kuhlemeyer and J. Lysmer, "Finite element method accuracy for wave propagation problems," *J. Soil Mech. Found. Div.*, vol. 99, no. 5, pp. 421–427, 1973.

[33] H. T. Tang, Y. K. Tang, and J. C. Stepp, "Lotung large-scale seismic experiment and soil-structure interaction method validation," *Nucl. Eng. Des.*, 1990, doi: 10.1016/0029-5493(90)90260-5.

[34] X. S. Li, C. K. Shen, and Z. L. Wang, "Fully coupled inelastic site response analysis for 1986 Lotung earthquake," *J. Geotech. Geoenvironmental Eng.*, 1998, doi: 10.1061/(ASCE)1090-0241(1998)124:7(560).

[35] G. Elia, M. Rouainia, D. Karofyllakis, and Y. Guzel, "Modelling the nonlinear site response at the LSST down-hole accelerometer array in Lotung," *Soil Dyn. Earthq. Eng.*, 2017, doi: 10.1016/j.soildyn.2017.08.007.

[36] S. D. Glaser and L. G. Baise, "System identification estimation of soil properties at the Lotung site," *Soil Dyn. Earthq. Eng.*, 2000, doi: 10.1016/S0267-7261(00)00026-9.

[37] C. Y. Chang, C. M. Mok, and H. T. Tang, "Inference of dynamic shear modulus from Lotung downhole data," *J. Geotech. Eng.*, 1996, doi: 10.1061/(ASCE)0733-9410(1996)122:8(657).

[38] R. I. Borja, B. G. Duvernay, and C.-H. Lin, "Ground response in Lotung: total stress analyses and parametric studies," *J. Geotech. Geoenvironmental Eng.*, vol. 128, no. 1, pp. 54–63, 2002.

[39] M. Zeghal, A.-W. Elgamal, H. T. Tang, and J. C. Stepp, "Lotung Downhole Array. II: Evaluation of Soil Nonlinear Properties," *J. Geotech. Eng.*, vol. 121, no. 4, pp. 363–378, 1995, doi: 10.1061/(ASCE)0733-9410(1995)121:4(363).

[40] R. I. Borja, C. H. Lin, K. M. Sama, and G. M. Masada, "Modelling nonlinear ground response of non-liquefiable soils," *Earthq. Eng. Struct. Dyn.*, 2000, doi: 10.1002/(SICI)1096-9845(200001)29:1<63::AID-EQE901>3.0.CO;2-Y.

[41] M. Zeghal, A. W. Elgamal, H. T. Tang, and J. C. Stepp, "Lotung downhole array. II: Evaluation of nonlinear soil properties," *J. Geotech. Eng.*, 1995, doi: 10.1061/(ASCE)0733-9410(1995)121:4(363).

[42] Y. Tao and E. Rathje, "The Importance of Distinguishing Pseudoresonances and Outcrop Resonances in Downhole Array Data," *Bull. Seismol. Soc. Am.*, 2020, doi: 10.1785/0120190097.

[43] R. R. Ebrahimian, H.; Astroza, R.; Conte, J.P.; Bitmead, "An Information-theoretic Approach for Identifiability Assessment of Nonlinear Structural Finite Element Models," *ASCE J. Eng. Mech.*, vol. in press, 2018.

[44] E. Esmaeilzadeh Seylabi, E. Agapaki, D. Pitilakis, J. Stewart, S. Brandenberg, and E. Taciroglu, "Development of validated methods for soil-structure interaction analysis of buried structures," *Des. Dataset*, 2017.

[45] E. E. Seylabi, H. Ebrahimian, W. Zhang, D. Asimaki, and E. Taciroglu, "Bayesian Estimation of Nonlinear Soil Model Parameters Using Centrifuge Experimental Data," in *Geotechnical Special Publication*, 2018, doi: 10.1061/9780784481486.042.

[46] K. Afshari and J. Stewart, "Implications of California vertical array data for the analysis of site response with 1D geotechnical modeling," 2017.

ESTIMATION OF SITE AMPLIFICATION FROM GEOTECHNICAL ARRAY DATA USING NEURAL NETWORKS

Daniel Roten and Kim B. Olsen

Department of Geological Sciences, San Diego State University

Abstract

We use deep learning to predict surface-to-borehole Fourier amplification functions (AFs) from discretized shear-wave velocity profiles. Specifically, we train a fully connected and a convolutional neural network (NN) using observed mean AFs observed at $\sim$600 KiK-net and California Strong Motion Instrument Program (CSMIP) vertical array sites. Compared to predictions based on theoretical SH 1D amplifications, the NN results in up to 50% reduction of the mean squared log error between predictions and observations at sites not used for training. In the future, NNs may lead to a purely data-driven prediction of site response that is independent of proxies or simplifying assumptions.

Introduction

The densification of seismic networks, such as the CSMIP strong motion network in California and the KiK-net observatory in Japan, have vastly increased the number of earthquake records available for strong motion research. In addition, the deployment of borehole accelerometers at many locations has resulted in a large volume of vertical array data which has contributed to a better understanding of linear and nonlinear site response during strong shaking [e.g. 1–4].

However, despite the increased amount of data, the standard deviations of intensity measures in ground motion prediction equations (GMPEs) have barely decreased over the past four decades [5, 6]. Standard deviations in GMPEs remain high because empirical methods use very simple models to approximate highly complex wave propagation phenomena [7]. Site conditions in most GMPEs are typically reduced to the average velocity in the top 30 meters, V_{S30} and in some cases basement depth (e.g. the depth to a constant shear-wave velocity of 1 km/s, Z_1) [8]. Similarly, ground motions recorded on vertical arrays have demonstrated the shortcomings of current site response prediction techniques, in particular the assumption of a laterally constant medium [2, 9, 10]. Three dimensional simulations with sophisticated structural models and nonlinear wave propagation codes are needed to study the response of such sites [e.g., 11, 12]. Although such case studies may shed light on the wave propagation effects behind the site response observed at a particular location, it is not clear how this approach can be generalized to sites for which no sophisticated 3D velocity models are available. Clearly, new methods are needed which harness the sheer volume of strong motion data (including data acquired on vertical arrays) to improve seismic hazard analysis.

While seismology has always been a data intensive field, enormous amounts of data are

nowadays being collected in a broad spectrum of fields ranging from technology to finance to healthcare. Combined with increasingly powerful computers, the availability of these very large datasets has been driving progress in machine learning (ML) techniques, in particular deep learning applications which thrive under large amounts of data.

An exciting aspect of deep neural networks (NNs) is their ability to detect patterns in the input data which allows them to make sense of labeled output data. In contrast to shallow learning algorithms, deep neural networks are less dependent on feature engineering, i.e., the process of transforming input data into features from which the output can be derived using a simple mathematical expression. In site response prediction, one could think of proxies such as V_{S30} or Z_1 as engineered features needed to carry out regression analysis for calibration of traditional GMPEs (i.e., a shallow learning method). A deep learning algorithm would not depend on such engineered features, and could process the entire velocity information available for a site, without resorting to simplifications which discard valuable data. The idea is that the network will identify new features from the provided velocity profile, which guide a more accurate site response prediction compared to proxies such as V_{S30} or Z_1.

In this study, we propose to train a deep neural network to learn the observed site response at CSMIP and KiK-net sites based on the entire soil stratigraphy and potentially other parameters characterizing the incoming wavefield. The goal is to develop a method which predicts site response based entirely on observed vertical array data, without relying on simplifying assumptions, such as one-dimensionality or a vertically-incident wave field, made in traditional site response assessment.

We have arranged the content of our paper as follows. In section 2, we provide a quick overview of deep learning and elaborate on the design of the NN. We have tested the feasibility of the method by by calculating theoretical, one-dimensional SH transfer functions (SH1D) for 662 real KiK-net soil profiles, and for training a fully connected neural network to predict the amplification functions (AFs) from the soil profiles. In second section 3, we describe the data preparation methods used in the calculation of transfer functions from CSMIP geotechnical arrays and KiK-net strong motion sites. Results of site response prediction using the deep learning are presented in section 4.

Deep Learning and Design of Neural Networks

Artificial neural networks (ANNs) are modeled after biological neural networks found in animal brains, and consist of a collection of artificial neurons interacting with each other. ANNs are typically organized in layers, and every ANN consists of an input layer accepting the input parameters and an output layer which produces the desired prediction.

Overview of Neural Networks

Deep neural networks feature at least one, but typically several hidden layers located between the input and output layers. In a fully connected ANN, also called multi-layer perceptron (MLP), each artificial neuron in each layer is connected to every other neuron of the previous and next layer. (Fig. 1). Therefore, each neuron receives an input signal from every

neuron in the previous layer, and redirects a modified signal to every neuron in the next layer. The input function $z(\mathbf{x})$ into a neuron consists of a weighted sum of the inputs $\mathbf{x} = (x_1, x_2, x_3, ...x_m)$ from the m individual neurons of the previous layer:

$$z(\mathbf{x}) = \mathbf{w}\mathbf{x} + b,$$

where **w** is a vector describing the weights of each neural connection. The offset b is also called bias. If the current layer has n nodes and the previous layer has m nodes, there are n m connections from the current to the previous layer, and the weight matrix connecting the two nodes has shape n m. In addition, there are n offsets that must be trained. The weights **w** and offset **b** are trainable parameters.

Activation functions allow the ANN to learn nonlinear functions. Without activation functions, the total output of the ANN would represent a linear function regardless of the depth of the networks (i.e., regardless of the number of hidden layers). Typical choices of activation functions include sigmoids, rectified linear units (ReLUs) or hyperbolic tangent functions (tanh) [13]. If the ANN is used for regression, the output node uses a linear activation, allowing the ANN to output any real number.

The weights and biases are optimized by training the ANN. The goal of training is to minimize the loss function, which quantifies the difference between the desired output provided in the training data and the network's actual output. Forward propagation in a feedforward ANN refers to the computation of the network's output value based on the chosen input and the ANN's current weights and biases, with information flowing from the input to the output layer. This order is reversed during backpropagation, where the gradient of the loss function with respect to the ANN's weight is computed based on the input and desired output of one or several training examples. Training consists in minimizing the loss by performing gradient descent on the loss function.

Because there are many trainable parameters in an ANN, and the number of training examples is often limited, deep neural networks are prone to overfitting [e.g. 13]. An overfitted model will perform very well on the input set but will generalize poorly to the test set, with low misfit error on the training set but high error on the test set (i.e., the model exhibits high variance). Overfitting also affects inversion problems encountered within different domains of seismology, such as seismic tomography [e.g. 14]. A common technique to reduce variance (overfitting) in such scenarios is to add L1 or L2 regularization, which penalizes large weights and thereby reduces the number of free parameters in the model. Although this type of regularization can also be applied to deep neural networks, it is more common to reduce variance using a technique called dropout [15]. In dropout regularization, a predefined fraction of neurons is randomly eliminated during each training iteration. This prevents the network from relying on a single feature, and allows it to generalize better to data it has not encountered during training.

FCNN Architecture

In the fully connected ANN design used in this study, the input layer expected the shear-wave velocities extracted at 100 predefined depths from the soil profile (Fig. 1a,c); the sampling

interval gradually increased from 1 m near the surface to 30 m at 1,500 m depth. The properties of the last layer were projected onto the remaining depth intervals at shallower sites. The desired frequency of site amplification was also provided to the ANN algorithm and represented the last value in the input layer. The output layer consisted of a single neuron with the site amplification value at the specified frequency (Fig. 1b,c). Our design chosen for the fully connected neural network (FCNN, Fig. 1c) used a many-to-one layout, accepting many inputs but producing just a single output value. That is, the ANN only predicted the amplification at one frequency at a time. One could also design a similar network using a many-to-many configuration, and predict the amplification at several frequencies at the same time. We experimented with both many-to-one and many-to-many designs and found that the many-to-one configuration was superior for the FCNN. However, a many-to-many design was adopted for the convolutional neural network (CNN) described below.

Our FCNN used 7 hidden layers, and the number of neurons decreased gradually from 256 nodes in the first hidden layer towards the single-node output layer. Following DeVries et al. [16], the activation function assigned to the hidden layers alternated between hyperbolic tanh and ReLUs; and a linear activation function was applied at the output layer (Fig. 1).

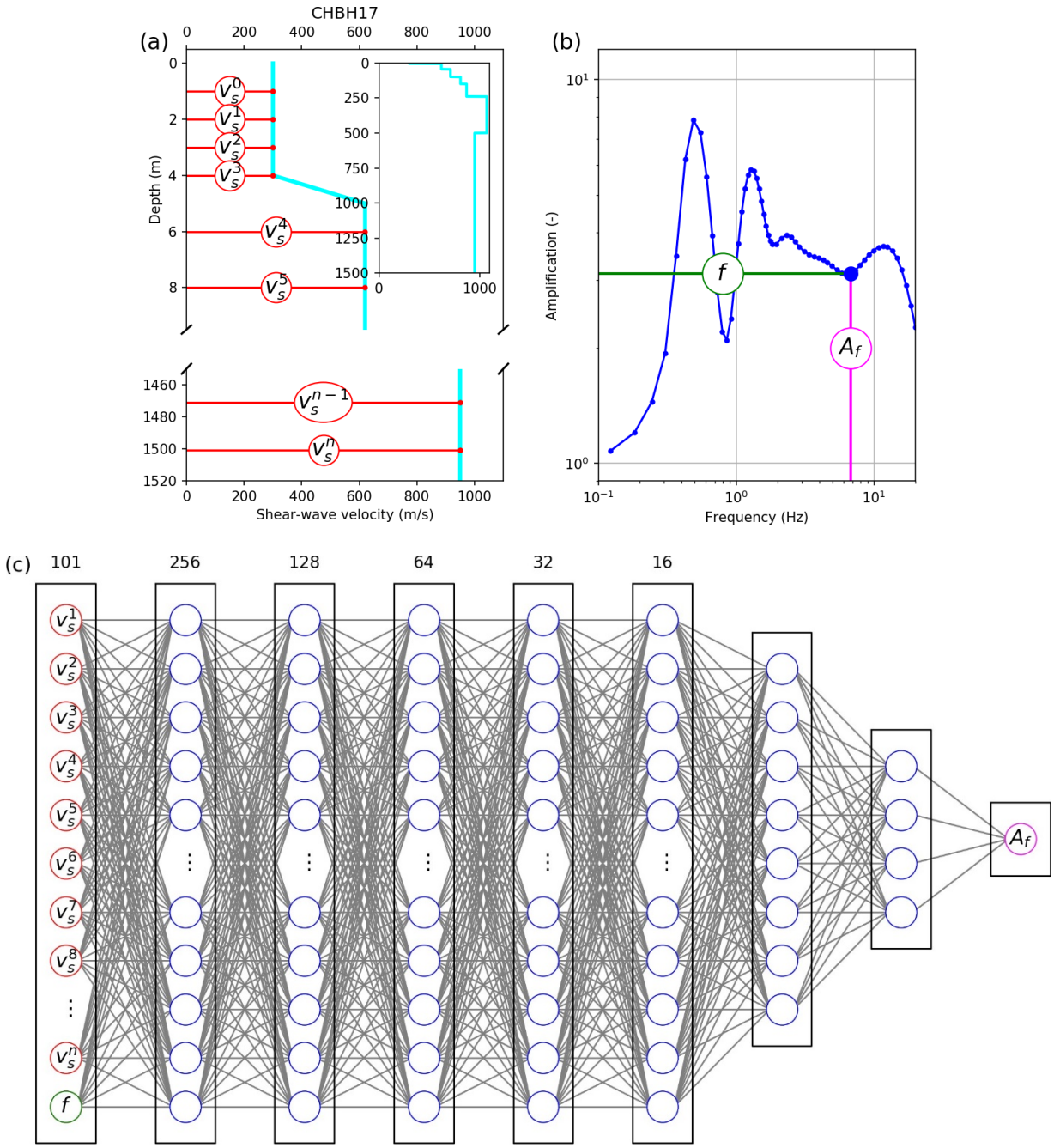

Figure 1: Prototype of ANN for prediction of simulated transfer functions. (a) Shear-wave velocities (v_s, red nodes) were discretized at $n = 100$ discrete depths and (c) fed into the input layer along with the frequency f of amplification (green node). Hidden layers in (c) are shown by blue neurons. Where not all nodes are shown, the true number of nodes are given at the top of the layer. The output node contains the amplification A_f at the specified frequency (b).

CNN Architecture

In a convolutional layer, nodes are not directly connected to nodes in the next layer. Instead, the data in the layer are convolved using a series of filters. The dimensions of the convolutional layer's output depend on the type of convolution (overlap and stepping size) and the number of filters, with each filter creating a new representation of the input data. However, as most convolutional layers use many filters, the output is typically large, and downsampled in a pooling layer following the convolutional layer. A set of convolutional and pooling layers may either be followed by another set of convolutional and pooling layers, or the data is flattened and directed into a fully connected layer.

CNNs are especially effective for image recognition or classification problems, as they are able to extract information from the spatial arrangement of the pixels. Although predefined filters have long been used in image processing, the effectiveness of CNN derives from the network's ability to optimize the filters depending on the training data. In other words, the filter parameters are optimized during back-propagation such that the features extracted by the different filters are effective at carrying out the CNN's task.

In our case, we applied a CNN to take advantage of the spatial information in the velocity profile. We used v_s and the P-wave velocity v_p as different image 'channels', analogous to the red, green and blue channels used in image recognition. In contrast to image recognition, where the input image is three-dimensional (two spatial dimensions plus three channels), our input was only two-dimensional (v_s and v_p at different depths). We did not use densities as they were not provided for KiK-net profiles.

In our CNN design, we used a single convolutional layer with 16 filters of dimensions 5 2 (Fig. 2) right after the input layer (dimension 1002, with v_s and v_p at 100 predefined depths). The output of the convolutional layer consisted of 100 16 values, which we reduced to 25 16 values using a pooling layer. The output of the pooling layer was flattened and fed into a fully connected layer of 512 nodes. Two more hidden layers with 256 and 128 nodes followed. The output layer contained 50 nodes, which represented the desired amplification function at 50 predefined frequencies (Fig. 2). A ReLU function was used for activation right after the pooling layer, and we alternated between ReLU and tanh functions in the three fully connected layers. As in the FCNN, a linear activation was used in the output layer. Dropout regularization was applied after each layer. Batch normalization (Fig. 2) was carried out before each activation to improve

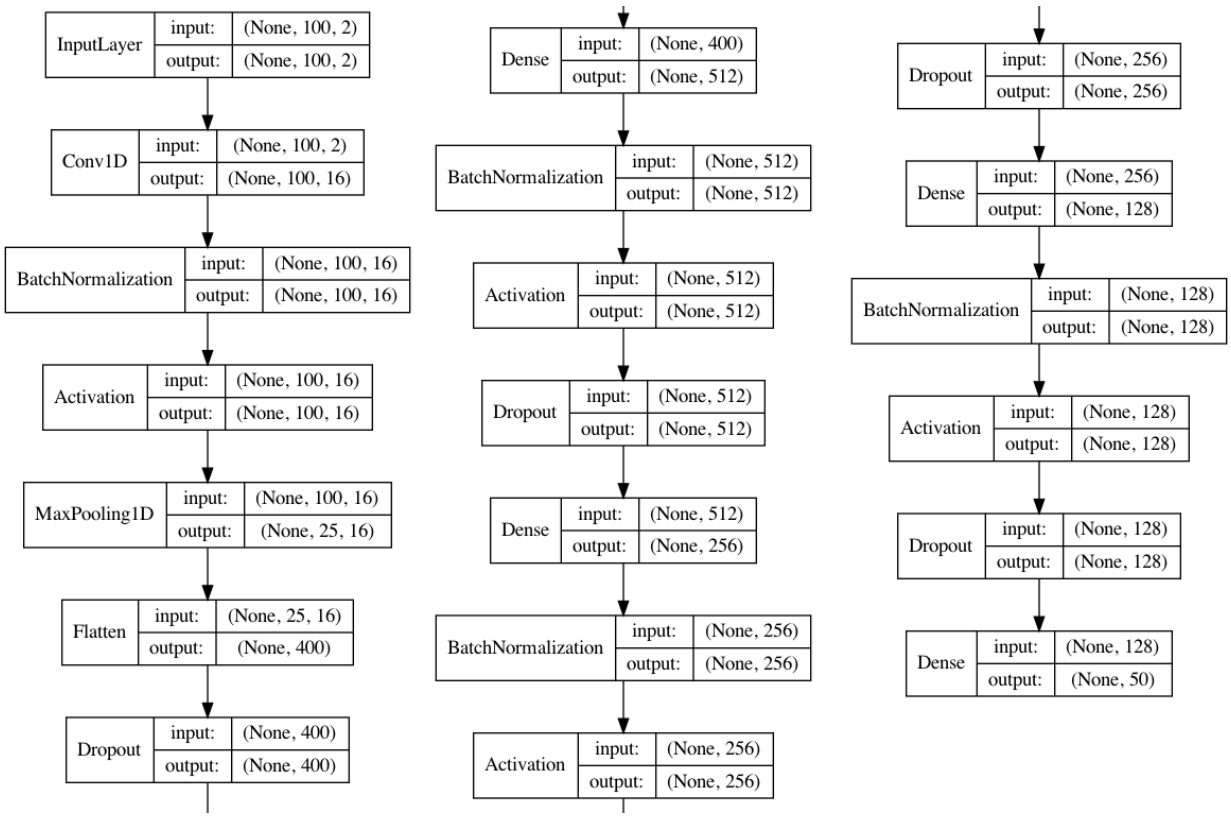

Figure 2: Architecture of convolutional neural network (CNN) for prediction of site response.

convergence (this was also done in the FCNN). Both the FCNN and the CNN were implemented with the Keras library for Python [17] using the TensorFlow[18] backend.

Data Preparation

Because data from CSMIP and KiK-net are stored in different formats, separate workflows were developed to extract transfer functions from CSMIP and KiK-net data, respectively.

CSMIP Data

Records from vertical arrays in the CSMIP network were downloaded from the Center for Engineering Strong Motion Data website [19]. In a first step, all earthquakes which resulted in peak ground accelerations (PGA) > 0.01*g* on geotechnical arrays within the CSMIP network were identified and retrieved from the network's website. We were able to download these records directly from the web interface as the amount of data was relatively small. The search resulted in a total of 209 suitable records pertaining to 99 different local and regional earthquakes with magnitudes between 3.1 and 7.3 (Fig. 3). The retrieved records include 4 records of the M7.1 Ridgecrest earthquake of July 5, 2019 that were acquired on geotechnical arrays in Palmdale, Oxnard and Los Angeles. 41 out of the total 44 CSMIP geotechnical arrays are represented in these records.

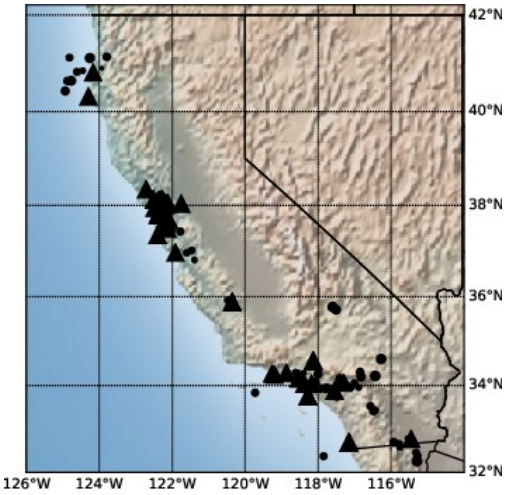

Figure 3: Location of CSMIP geotechnical arrays (triangles) and selected earthquakes (circles).

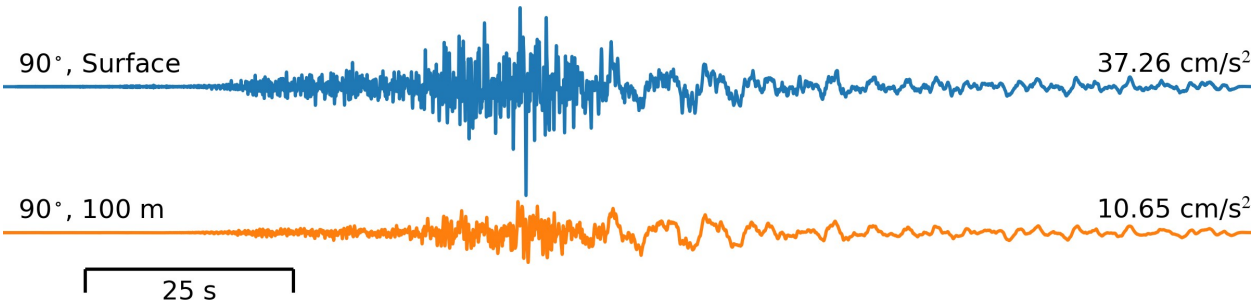

Figure 4: Surface and borehole accelerograms recorded at the La Cienega (Los Angeles) geotechnical array during the 2019 *M* 7.1 Ridgecrest earthquake.

A workflow was developed which parses the CSMIP ASCII files [20] to extract ground motions, performed Fast Fourier Transform, smoothing with a Konno-Ohmachi filter [21] and the computation of the AF. Figure 4 shows an example of surface and downhole accelerograms used to train the NN, namely records from the La Cienega (Los Angeles) geotechnical array during the *M* 7.1 Ridgecrest earthquake (rupture distance 205 km). Although the incoming wavefield is dominated by long-period ground motions (period *T* 10 s) ground motions (Fig. 5a), the amplification by the deep alluvium can clearly be observed at frequencies between 1 and 10 Hz (Fig. 5b). The observed Fourier amplification at different frequencies obtained from the chosen records represents the output that the NN is trained to predict. Shear-wave velocities at different depths, along with selected earthquake parameters (e.g., magnitude, rupture distance) represent the input layer of the NN.

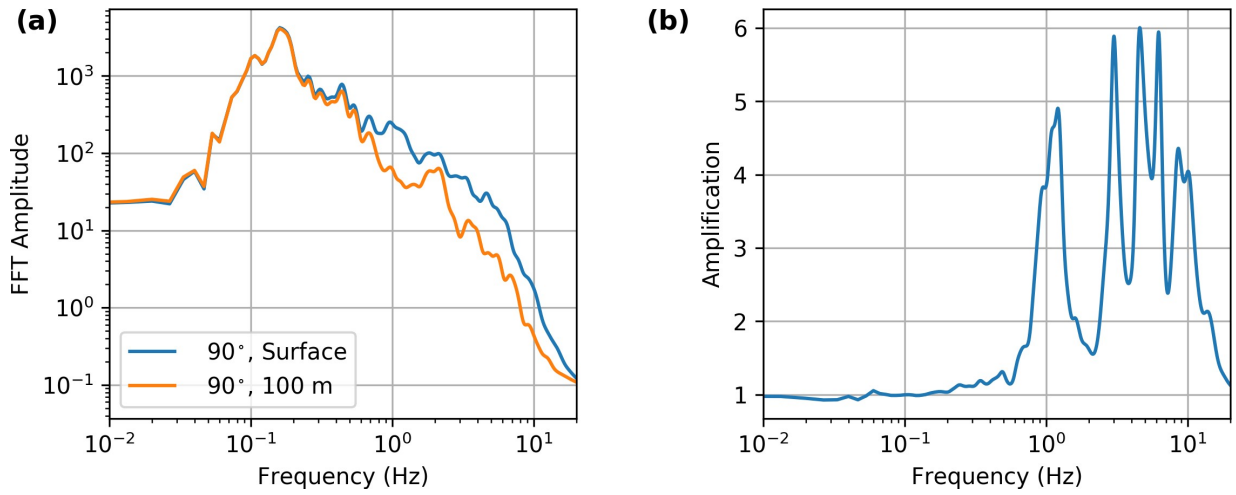

Figure 5: (a) Fourier amplitude and (b) AF (amplification function) from La Cienega records of *M* 7.1 Ridgecrest earthquake.

KiK-net Data

Although the KiK-net data website provides the option to search for earthquake records based on different parameters, we found that the interface was not suitable to select and download the relatively large amount of records that we wanted to use for this project. Instead, we developed a script that downloads all the earthquake records from the KiK-net website and stores them locally. This 'data scraper' was programmed in Python using the requestslibrary [22].

Acceleration time series from all earthquakes recorded by KiK-net stations between January 1997 and August 2020 were downloaded from the Kyoshin web site [23]. Five parallel download sessions were executed to retrieve the records, which amount to about 105 Gb in total. Records of acceleration time series in K-NET ASCII format were kept in event tar archives for all KiK-net sites which recorded the event. Earthquake and station metadata were extracted from event files and stored in a local database. Three separate tables with station information (i.e., station code, location, elevation, sensor depth), event information (event ID, date, magnitude, hypocenter) and record informations (event ID, station code, peak ground acceleration, distance) were generated and stored in Python Pandasdataframes.

Based on the record's PGA (peak ground acceleration), we selected 20 representative events for each station. Two different selection strategies were used to generate training datasets for prediction of mean amplifications or event-specific amplifications, described below.

For the prediction of mean site amplifications, we only used records with surface PGAs below 0.2*g* to exclude nonlinear effects. Where available, we randomly picked 20 events with PGAs within 0.05 and 0.2*g*. If less than 20 events with 0.05*g* < PGA < 0.2*g* were available, we selected the 20 events with the highest PGA. The number of 20 events per site was chosen because all except 4 sites (KNMH18, FKOH02, SOYH3, AICH23) recorded more than 20 events until August 2020, and no site recorded less than 10 events. Using more events per site would be

possible, but would require the introduction of training weights to give all sites equal consideration; otherwise the neural network would tend to automatically give more weight to stations that are represented by more entries in the training dataset.

For the prediction of event-specific site amplification, events were selected such that their PGAs were roughly uniformly distributed between a minimum PGA of 0.05*g* and the maximum PGA recorded at that site. If less than 20 events with PGA > 0.05*g* were available at a site, we picked the 20 events with the highest PGAs. This approach was chosen to ensure sufficient representation of events with high PGAs for the prediction of nonlinear effects. However, results presented in this paper are focused on the prediction of mean AFs, which do not include nonlinearity.

The next step in the KiK-net data processing workflow consisted in the extraction of time series data from the selected observations. We used the ObsPyFramework for Python [24] to read the data. Surface-to-borehole transfer functions were computed for both horizontal components, smoothed using a Konno-Ohmachi filter (bandwith $w = 10$) and the geometric mean of both horizontals was computed. We then interpolated the amplification at 50 frequencies of interest, which are logarithmically spaced between 0.3 and 20 Hz. This procedure was carried out for a total of 13,210 events. Computationally, the data preparation was expensive because two Fast Fourier Transforms and Konno-Ohmachi filtering operations were executed for each record. In order to accelerate the process, the web scraper and data processing workflow were deployed on the commodity cluster Rhea at the Oakride Leadership Computation Facility (OLCF). We used the Apache Spark Engine [25] to distribute the data processing on up to 5 nodes and 80 CPU cores. This approach resulted in a wall-clock time of less than two hours for the computation and smoothing of the amplification functions for all the 13,210 records.

Training and test datasets were created as follows: First we randomly selected 95% of the sites to contribute to the training set, while the remaining sites were assigned to the test set. Figure 6 shows the distribution of training and test sites among the KiK-net stations. We used the same selection of training and test sites for all different neural network layouts and hyperparameter choices shown in this paper, in order to allow for a one-by-one comparison of network performances. We created training and test datasets by iterating over all the records pertaining to each given training and test site. In the many-to-many layout used in the convolutional neural network for the prediction of mean AFs, the training and test sets contained just one data point per site. In the many-to-one design of the fully connected network, one data point for training / testing was created for each site and frequency for the prediction of mean amplification. The number of datapoints per site equals the number of events at the site times the number of frequencies in the prediction of event-specific amplifications using the many-to-one NN layout.

The training and test sets for the prediction of event-specific amplifications using the many-to-one NN layout contain one data point for each frequency and each observation per site. The many-to-many design in the CNN requires just one data point per observation and site in the training and test sets.

NN Training and Prediction Results

We initially trained a network to predict event-specific site amplifications. As this turned out to be quite difficult and computationally expensive, we reverted to working with mean site

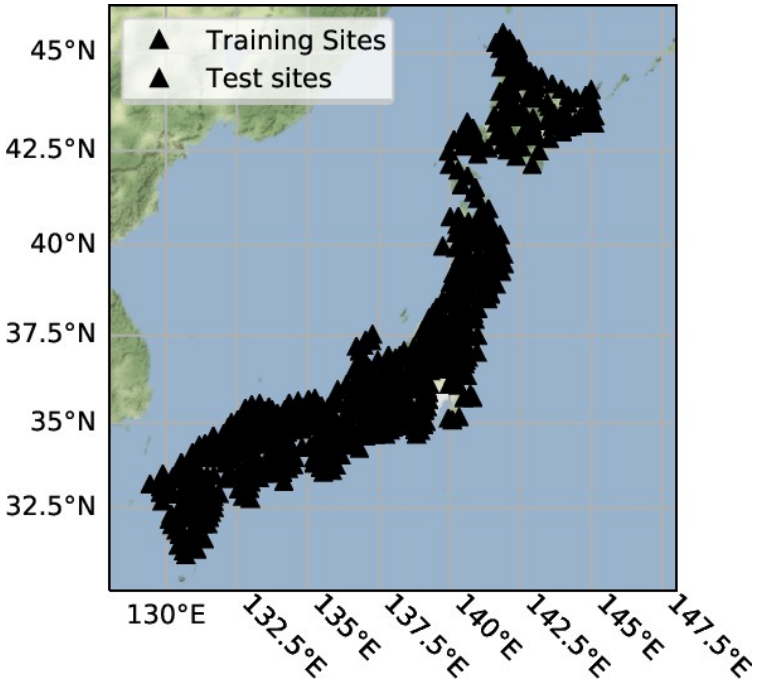

Figure 6: Locations of KiK-net sites assigned to training and test sets in this study.

amplification in a first step.

We trained the fully connected NN and convolutional NN with the mean AFs for 596 KiK-net sites assigned to the test test. Mini-batch gradient descent using the Adam optimizer [26] was carried out to minimize the mean square logarithmic error (MSLE) between observed and predicted theoretical AFs. We chose the MSLE as our loss function to incorporate the large range of amplifications observed between different sites and frequencies. A low MSLE is consistent with good visual agreements if AFs are plotted in logarithmic space as is conventionally done. We also report the mean absolute error (MAE) between predicted and observed amplification functions. The batch size was set to 2048 for the FCNN and to 50 for the CNN. We trained the ANNs for 1,000 epochs using the default learning rate of 10^{-3}.

Prediction of Mean Amplification Functions using the FCNN

Figure 7 shows the learning curve obtained during training of the fully connected neural network (FCNN) with mean amplification functions. The training loss (MSLE) is reduced from an initial value of 1.36 to 0.015 (Table 1). Input features (i.e., v_s and frequency of amplification) were standardized by removing the mean and scaling to unit variance using 'StandardScaler' from the scikit-learn library [27] before training. To control the amount of overfitting to the training

data, we used dropout regularization in the first five hidden layers. The dropout rate was adjusted to a value of 0.15 by trial and error. Lower values resulted in a higher validation error, while higher values increased the training error without further reducing the validation error. Figure 8

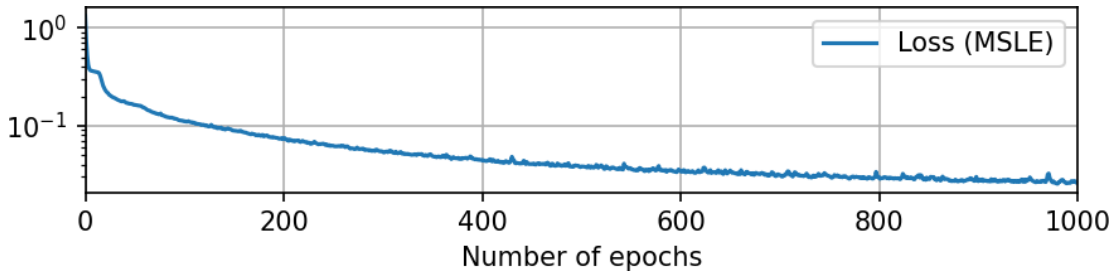

Figure 7: Learning curve with mean absolute training and validation errors during Adam optimization of the fully connected neural network (FCNN) for prediction of mean site response

	MSLE (train)	MAE (train)	MSLE (test)	MAE (test)
Baseline*			0.216	2.005
FC	0.015	0.521	0.140	1.593
CNN	0.021	0.595	0.104	1.307

Table 1: MAE and MSLE (loss) between observed amplifications and amplifications predicted from the preferred fully connected (FC) and convolutional (CNN) neural networks.

Theoretical SH1D amplification compares observed and predicted mean amplification functions for 9 randomly selected training sites. The low training error is reflected in the good match between observed and predicted mean amplification functions.

We used the trained FCNN to predict mean site amplifications at the 66 test sites and obtained a MSLE of 0.014 (Table 1). Figure 9 compares the observed and predicted mean amplifications at 9 randomly selected test sites. The MSLE at the displayed test sites ranges from about 0.040 for sites where the predicted AF is close to the observations (e.g., ISKH04, MIEH06, KOCH13) to values above 0.150 for sites where the predicted AF does not reproduce the observation (e.g., YMNH14, SRCH01, YMTH07) well. However, predicting the site response from a soil profile is generally difficult due to multi-dimensional effects, modeling inaccuracies and uncertainties in soil property estimates [e.g. 9, 10]. In order to put the quality of the AFs predicted by the NN into perspective, we compare them with a more conventional method for site response prediction. We computed theoretical SH1D AFs for a vertically incident plane wave, with densities and quality factors derived from the shear-wave velocity profiles using an empirical relation [28].

Theoretical AFs were smoothed in the same way as observed mean AFs. The MSLE between theoretical and observed AFs is listed for each site in Figure 9 (as well as Fig. 8 for reference, although we note that is makes little sense to compare training losses to theoretical predictions). With the exceptions of sites GIFH25 and SRCH01, the theoretical model results in a larger prediction error than the NN. The MSLE of 0.22 between theoretical and observed AFs

for the 66 test sites (Table 1) is used as a baseline to assess the NN's performance, and shows that the NN is generally predicting mean AFs more accurately than the theoretical model.

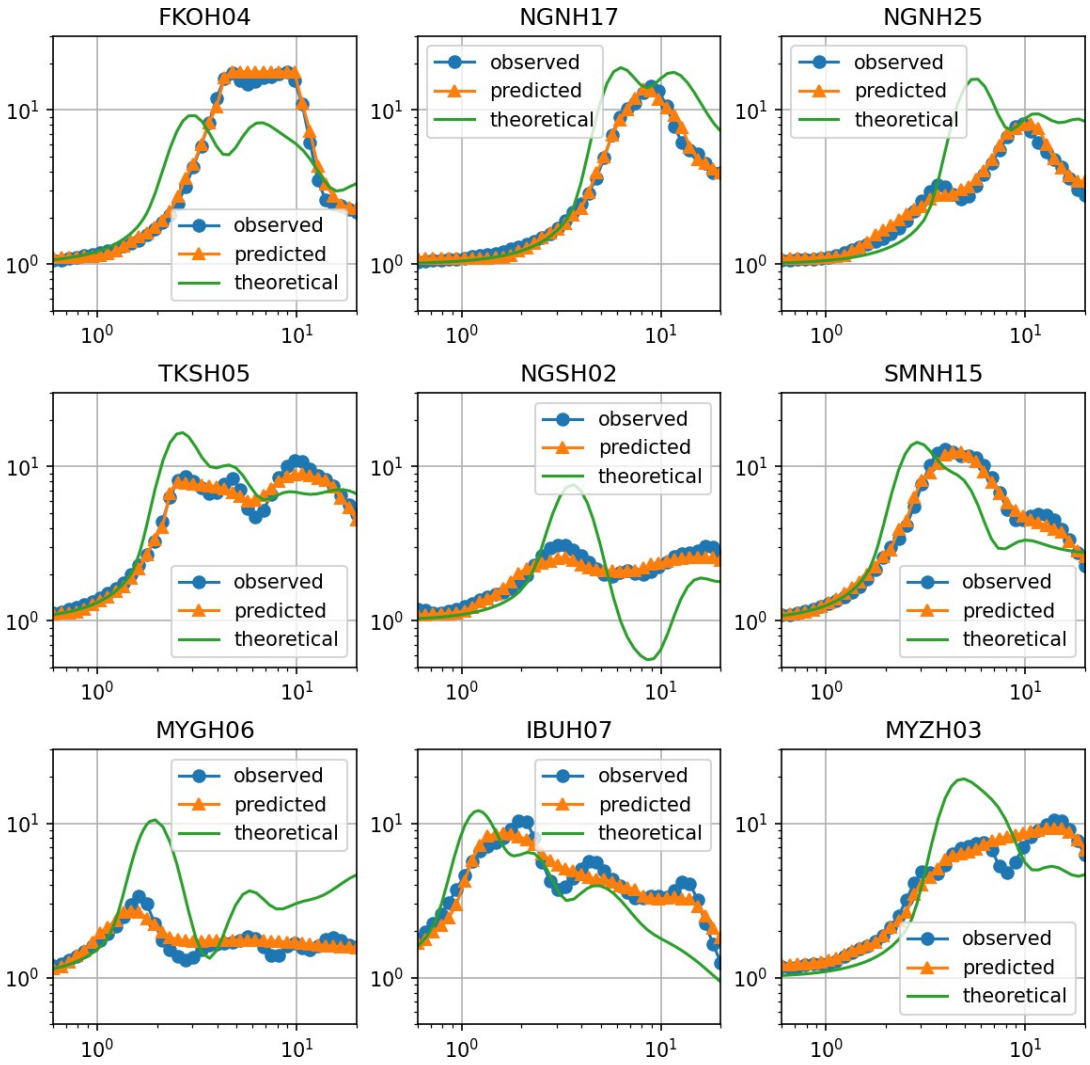

Figure 8: Comparison between observed mean amplification functions (blue) and amplification functions predicted by the FCNN (orange) for 9 randomly selected training sites. Solid green lines show theoretical 1D site amplification functions. Numbers in brackets next to the site name give the training loss (MSLE) for the site. Green numbers in the upper left corner show the baseline loss (based on the theoretical SH1D amplification function) for the site.

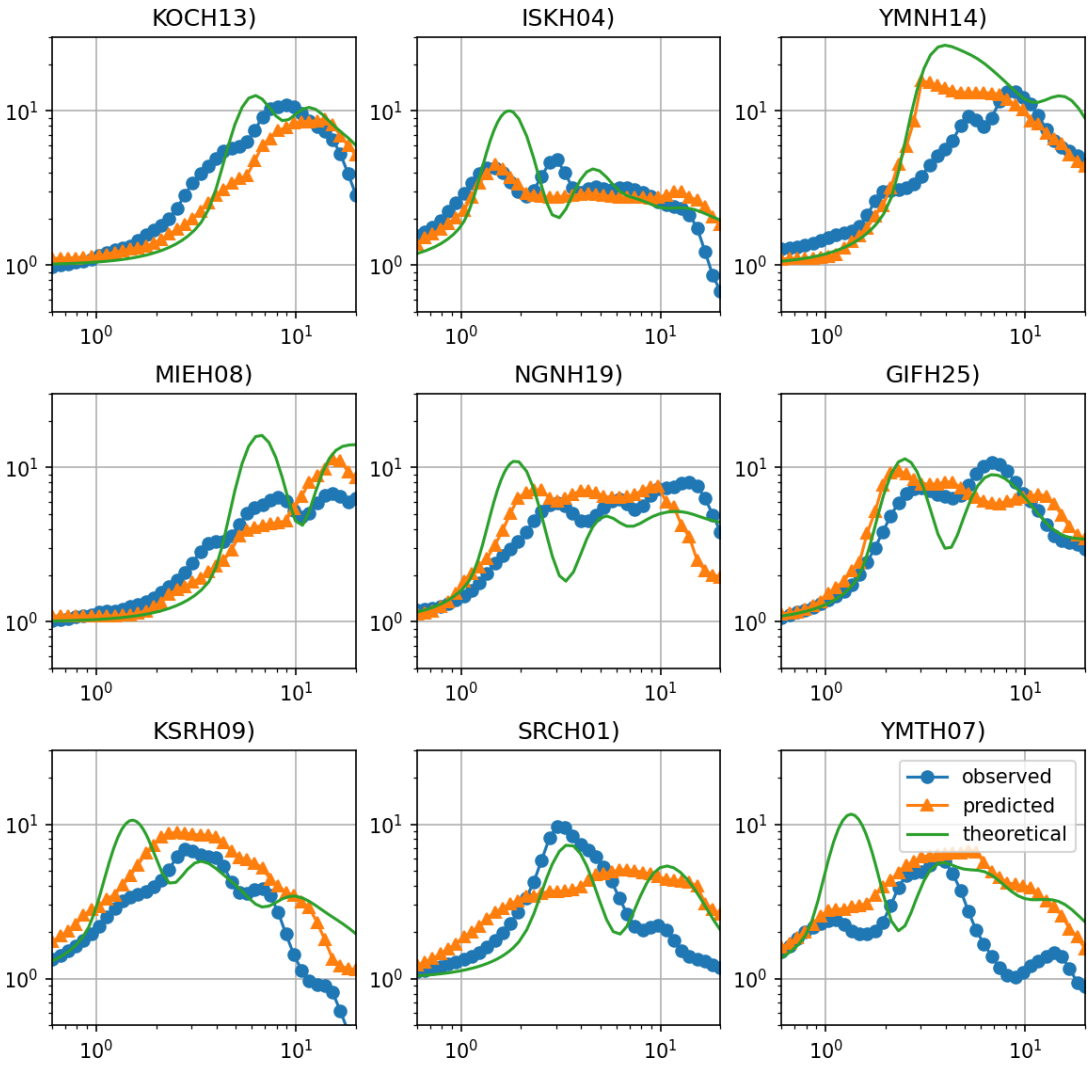

Figure 9: Same as Figure 8, but showing mean and predicted mean amplifications for 9 randomly selected test sites.

Prediction of mean amplification functions using a CNN

The convolutional CNN was trained using observed mean site amplifications for the same 596 training sites as for the FCNN. As with the FCNN, we adjusted drop-out rates for the CNN by trial and error to minimize the trade-off between high model bias (in case of poor performance for training sites) and high variance (in case of overfitting). For the CNN we tuned to drop-out rates to different values for each layer. A drop-out rate of 0.5 was used after the pooling layer (Fig. 2), while drop-out rates of 0.3, 0.15 and 0.10, respectively, were used for the three subsequent, fully connected hidden layers.

The CNN was trained for 2,000 epochs using a batch size of 50 sites. The loss was reduced from an initial value of 1.45 to a minimum of 0.043. We used the trained model to predict AFs for training and test sites and obtained a MSLE values of 0.021 and 0.104, respectively (Table 1). Note that the MSLE for predicted AFs at training sites (0.021, Table 1) is lower than the lowest minimum value obtained during optimization (0.043). This discrepancy is caused by drop-out regularization. Drop-out regularization randomly eliminates neurons during training, resulting in a relatively high training error. However, all neurons are enabled during prediction (drop-out rate is set to zero), which results in a lower prediction error than training error.

Both MSLEs and MAEs at test sites sites are lower for the CNN than for the FCNN. Moreover, the CNN achieves a test MSLE that is 50% lower than baseline (Table 1). Figure 10 compares observed, predicted and theoretical (baseline) AFs for the same 9 test sites as shown for the FCNN (Fig. 9). The CNN results in more accurate predictions especially for sites YMNH14 (MSLE reduction from 0.146 to 0.028), MIEH08 (0.043 to 0.020) and GIFH25 (0.064 to0.030).

Figure 11a shows the distribution of the MSLE obtained by the baseline, FCNN and CNN at the 66 test sites. The CNN clearly represents an improvement with respect to both the FCNN and baseline. For example, the CNN distribution peaks at an MSLE of 0.05, with a median MSLE of 0.073. Baseline (SH1D) errors are more uniformly distributed with a median MSLE of 0.181. Compared to the FCNN, the CNN achieves an MSLE below 0.075 for more sites, and less sites with errors above 0.225. We also computed the change in MSLE between the two NN designs and the baseline for each site and plotted up the distribution of the change of error (Fig. 11b). With respect to baseline, the NNs results in an improvement at most sites; the CNN also outperforms the FCNN in terms of number of sites where an improvement is observed.

Summary and Outlook

We have calculated mean observed AFs for 662 KiK-net sites and 41 CSMIP geotechnical arrays. 95% of the sites were assigned as training sites, with the remaining 5% withheld as test sites. A FCNN and a CNN were trained to predict the observed amplification functions from a discretized representation of the velocity profiles.

Both NN designs converged to a solution with minimal loss, and accurately reproduced the observed AFs at the training sites. While the quality of the prediction at the test sites varied, both the FCNN and the CNN outperformed predictions based on the theoretical SH1D site

response in terms of MSLE (mean squared logarithmic error) between observed and predicted AFs.

Predictions made by the CNN resulted in an MSLE that was 50% lower than the SH1D baseline, and 25% lower than the predictions by the FCNN. Proper regularization and fine fine-tuning of the drop-out rate was found to be essential to obtain good predictions at test sites not used for training.

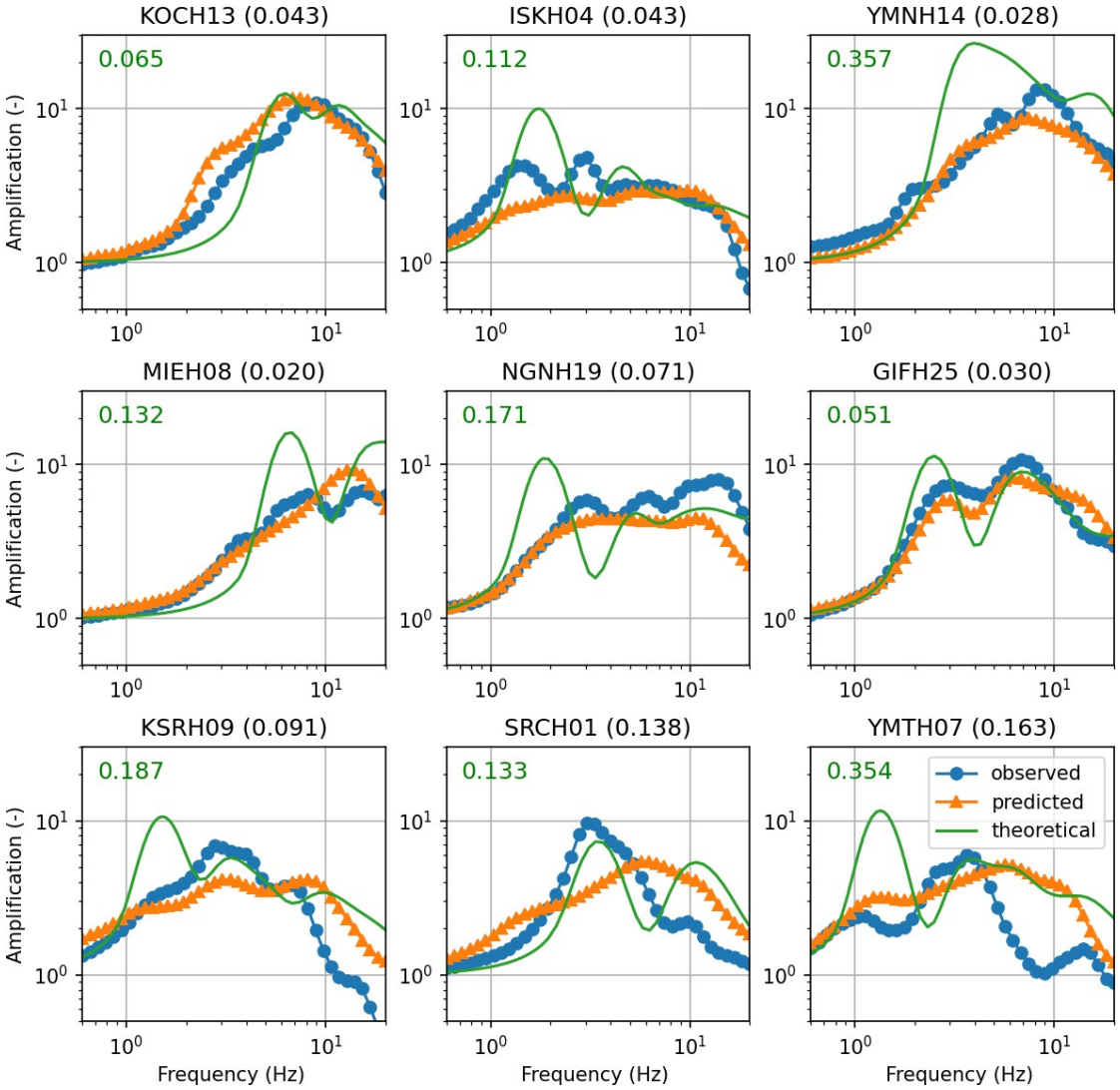

Figure 10: Same as Figure 9, but showing predictions by the convolutional neural network (CNN) at the same test sites.

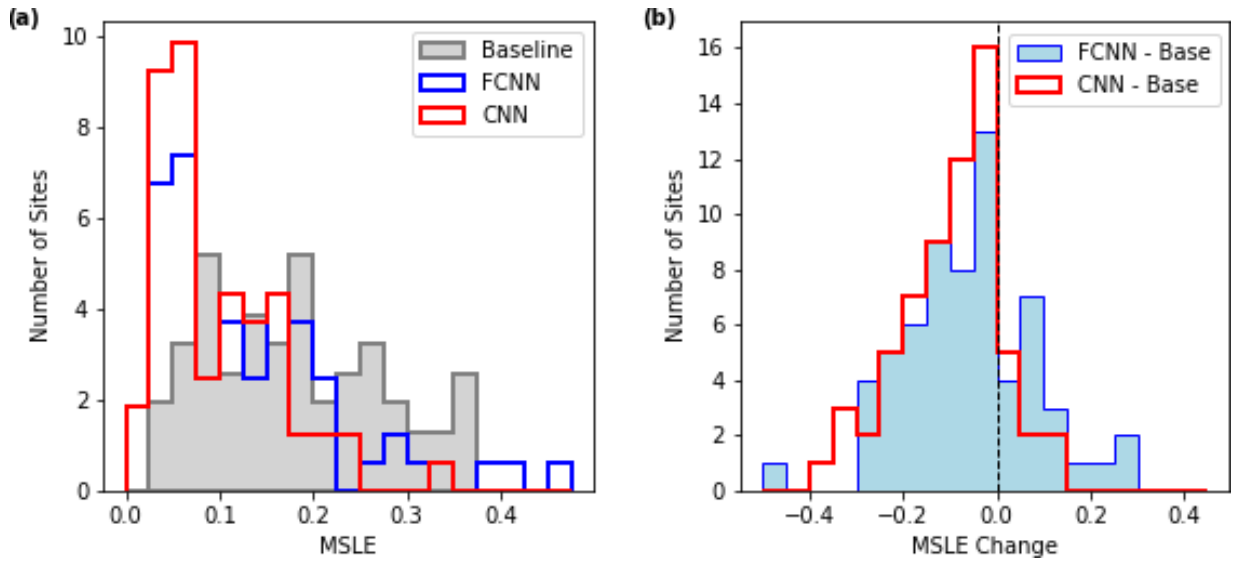

Figure 11: (a) Distribution of site-specific MSLE obtained from baseline, FCNN and CNN results. (b) Distribution of change in MSLE achieved by use of FCNN and CNN with respect to the baseline ('Base').

These results show that artificial NNs have the potential to take advantage of the full velocity profile information for more accurate predictions of observed AFs. Although a simple SH1D amplification function does not represent the state of the art for site-specific seismic hazard analysis in engineering seismology, it serves as a useful benchmark that demonstrates the limits of commonly made assumptions (in particular a horizontal, 1D layered structure and a vertically incident plane wave). A NN which learns to predict AFs purely from data is not bound by such assumptions, and we have demonstrated the level of improved accuracy with respect to the baseline that can be learned from data.

In future work, we will also evaluate the accuracy of the NN-predicted AFs against empirical site amplification functions, which are typically based on the V_{S30}. While our efforts in this paper were focused on the prediction of mean AFs, future work should address the prediction event-specific amplification. Here, effects of incident wavefield characteristics, scattering and nonlinearity would be captured by feeding the network with earthquake magnitude, hypocentral distance, and input signal metrics (e.g. PGA, spectral accelerations at different frequencies, duration). In case of a CNN, this requires a slightly more complicated design with mixed data inputs. We also recommend for future work to explore the use of information on the multi-dimensionality of a site structure.

The best-performing network design will be re-trained using all the extracted AFs and made available to the community for data-informed site response prediction using the full soil profile.

Disclaimer

The contents of this report were developed under Contract No. 1019-014 from the California Department of Conservation, California Geological Survey, Strong Motion Instrumentation Program. However, these contents do not necessarily represent the policy of that agency or endorsement by the State Government.

Acknowledgements

This project is supported by the California Department of Conservation, California Geological Survey, Strong Motion Instrumentation Program, Contract 1019-014. The authors thank Daniel Swensen at the California Department of Conservation for providing soil profiles of CSMIP vertical array sites. We are grateful to the Center for Engineering Strong Motion Data (CESMD) and the National Research Institute for Earth Science and Disaster Resilience (NIED) for providing vertical array strong motion data. Data pre-processing was carried out on the OLCF (Oak Ridge Leadership Computational Facility) cluster Rhea under an INCITE research allocation.

References

[1] L. Bonilla, C. Gelis, and J. Regnier. The challenge of nonlinear site response: field data observations and numerical simulations. In *4th IASPEI/IAEE International Symposium: Effects of Surface Geology on Seismic Motion, August 23-26, 2011, University of Santa Barbara*, 2011.

[2] E. M. Thompson, Y. Tanaka, L. G. Baise, and R. E. Kayen. Three-dimensional site response at KiK-net downhole arrays. In *7th International Conference on Urban Earthquake Engineering & 5th International Conference on Earthquake Engineering*, pages 3–5, 2010.

[3] D. Roten, D. Fäh, and L. Bonilla. High-frequency ground motion amplification during the 2011 Tohoku earthquake explained by soil dilatancy. *Geophys. J. Int.*, in press, 2013.

[4] D. Roten, D. Fäh, and L. Bonilla. Quantification of cyclic mobility parameters in liquefiable soils from inversion of vertical array records. *Bull. seism. Soc. Am.*, 104(6):3115–3138, 2014.

[5] J. Douglas. Earthquake ground motion estimation using strong-motion records: a review of equations for the estimation of peak ground acceleration and response spectral ordinates. *Earth-Science Reviews*, 61(1-2):43–104, 2003.

[6] F. O. Strasser, N. A. Abrahamson, and J. Bommer. Sigma: Issues, insights, and challenges. *Seismological Research Letters*, 80(1):40–56, 2009.

[7] J. Bommer and N. Abrahamson. Why do modern probabilistic seismic-hazard analyses often lead to increased hazard estimates? *Bull. seism. Soc. Am.*, 96(6):1967–1977, 2006.

[8] N. A. Abrahamson, W. J. Silva, and R. Kamai. Summary of the ASK14 ground motion relation for active crustal regions. *Earthquake Spectra*, 30(3):1025–1055, 2014.

[9] E. M. Thompson, L. G. Baise, R. E. Kayen, and B. B. Guzina. Impediments to predicting site response: Seismic property estimation and modeling simplifications. *Bulletin of the Seismological Society of America*, 99(5):2927–2949, 2009.

[10] E. M. Thompson, L. G. Baise, Y. Tanaka, and R. E. Kayen. A taxonomy of site response complexity. *Soil Dynamics and Earthquake Engineering*, 41:32–43, 2012.

[11] F. Gatti, F. Lopez-Caballero, D. Clouteau, and R. Paolucci. On the effect of the 3-D regional geology on the seismic design of critical structures: the case of the Kashiwazaki-Kariwa Nuclear Power Plant. *Geophysical Journal International*, 213(2):1073–1092, 2018.

[12] Z. Hu, D. Roten, O. K.B., and S. Day. Modeling of empirical transfer functions with 3d velocity structure. *submitted to Bull. Seism. Soc. Am.*, 2020.

[13] I. Goodfellow, Y. Bengio, A. Courville, and Y. Bengio. *Deep learning*, volume 1. MIT press Cambridge, 2016.

[14] G. Nolet. *A breviary of seismic tomography*. Cambridge University Press, 2008.

[15] N. Srivastava, G. Hinton, A. Krizhevsky, I. Sutskever, and R. Salakhutdinov. Dropout: a simple way to prevent neural networks from overfitting. *The Journal of Machine Learning Research*, 15(1):1929–1958, 2014.

[16] P. M. DeVries, T. B. Thompson, and B. J. Meade. Enabling large-scale viscoelastic calculations via neural network acceleration. *Geophysical Research Letters*, 44(6): 2662–2669, 2017.

[17] F. Chollet et al. Keras: the Python deep learning API, 2015. https://keras.io/, [Last accessed October 2020].

[18] M. Abadi, A. Agarwal, P. Barham, E. Brevdo, Z. Chen, C. Citro, G. S. Corrado, A. Davis, J. Dean, M. Devin, S. Ghemawat, I. Goodfellow, A. Harp, G. Irving, M. Isard, Y. Jia, R. Jozefowicz, L. Kaiser, M. Kudlur, J. Levenberg, D. Mané, R. Monga, S. Moore, D. Murray, C. Olah, M. Schuster, J. Shlens, B. Steiner, I. Sutskever, K. Talwar, P. Tucker, V. Vanhoucke, V. Vasudevan, F. Viégas, O. Vinyals, P. Warden, M. Wattenberg, M. Wicke, Y. Yu, and X. Zheng. TensorFlow: Large-scale machine learning on heterogeneous systems, 2015. Software available from tensorflow.org/, [Last accessed October 2020].

[19] CESMD. Center for Engineering Strong Motion Data, 2020. https://www.strongmotioncenter.org/,[LastaccessedOctober2020].

[20] A. Shakal and M. Huang. Standard tape format for CSMIP strong-motion data tapes. Report osms 85-03, California Department of Conservation, Division of Mines and

Geology, 1985.

[21] K. Konno and T. Ohmachi. Ground-motion characteristics estimated from spectral ratio between horizontal and vertical components of microtremor. *Bull. seism. Soc. Am.*, 88(1): 228–241, 1998.

[22] K. Reitz. Requests: HTTP for Humans™, 2020. https://requests.readthedocs.io/en/master/, [Last accessed October 2020].

[23] NEID. Strong-motion seismograph networks (k-net, kik-net), 2020. https://www.kyoshin.bosai.go.jp/, [Last accessed October 2020].

[24] O. D. Team. A Python Framework for Seismology, 2020. https://docs.obspy.org/, [Last accessed October 2020].

[25] T. A. S. Foundation. Apache Spark™ - Unified Analytics Engine for Big Data, 2020. https://spark.apache.org/, [Last accessed October 2020].

[26] D. P. Kingma and J. Ba. Adam: A method for stochastic optimization. *arXiv preprint; arXiv:1412.6980*, 2014.

[27] F. Pedregosa, G. Varoquaux, A. Gramfort, V. Michel, B. Thirion, O. Grisel, M. Blondel, P. Prettenhofer, R. Weiss, V. Dubourg, J. Vanderplas, A. Passos, D. Cournapeau, M. Brucher, M. Perrot, and E. Duchesnay. Scikit-learn: Machine learning in Python. *Journal of Machine Learning Research*, 12:2825–2830, 2011. scikit-learn.org/, [Last accessed October 2020].

[28] T. Brocher. Key elements of regional seismic velocity models for ground motion simulations. In *Proc. of Int. Workshop on Long-Period Ground Motion simulations and velocity structures, Tokyo, Nov 14-15, 2006*, 2006.

ASSESSING ASCE-41 ACCEPTANCE CRITERIA FOR LINEAR AND NONLINEAR PROCEDURES USING INSTRUMENTED BUILDING DATA

Laura L. Hernández-Bassal and Sashi K. Kunnath

Department of Civil and Environmental Engineering

Abstract

Current provisions in ASCE-41 for performance-based assessment are applied to an existing three-story steel moment frame building that was designed and constructed prior to the 1961 UBC code revisions. A computer model of a perimeter frame that comprises the primary lateral system of the building was developed and validated against available instrumented data from two earthquakes. Both linear and nonlinear procedures were used in the assessment. Findings from the study indicate that the linear static and dynamic procedures produced consistent demand-to-capacity ratios. The nonlinear static procedure resulted in the most severe demands at the lowest level with two beams failing the Collapse Prevention limit state whereas the nonlinear dynamic procedure produced the lowest demands on the building; however, the fact that some individual motions caused some beams to exceed Life Safety or Collapse Prevention limits indicates that ground motion selection can play a major role in the outcome of the assessment when using the nonlinear dynamic procedure.

Introduction

The development of ASCE-41 (ASCE 2017) and other ongoing efforts directed towards the enhancement of performance-based codes represent a significant advancement in the practice of earthquake engineering. However, calibration and validation of the modeling parameters and acceptance criteria to real building performance is clearly needed for practicing engineers to gain confidence in the proposed methodologies. The use of strong motion data obtained from instrumented buildings experiencing strong ground shaking is an essential part of this process.

ASCE-41 permits as many as four analytical procedures to estimate seismic demands: Linear Static Procedure (LSP), Linear Dynamic Procedure (LDP), Nonlinear Static Procedure (NSP), and Nonlinear Dynamic Procedure (NDP). This implies that the assessment of a regular low to mid-rise building using any of the methods should reach the same conclusion on the performance of the system. Recently, Harris and Speicher (2018) carried out a detailed ASCE 41-based assessment of six modern steel frames varying in height from four to sixteen stories designed to the provisions of ASCE-7 (ASCE 2016). Their study identified numerous inconsistencies in the different evaluation procedures: for example, LDP consistently resulted in lower demand-to-capacity ratios (DCRs) than LSP and likewise NSP consistently resulted in lower DCRs than NDP – though it is recognized that nonlinear responses are sensitive to model and analysis parameters.

The results reported in this paper are part of a larger study investigating three instrumented buildings and examining several ASCE-41 provisions. It can be viewed as an extension of the study by Harris and Speicher to an existing building where the numerical model has been calibrated to observed responses.

Building and Instrumentation Data

The first structure selected for assessment is a 3-story office building designed in 1958 and located in San Bernardino, California. The structure is composed of moment frames along the exterior serving as the lateral load resisting system in both directions. The gravity system is a wood truss-joist system supported on steel columns that spans in the north-south direction. Figure 1 shows the plan view of the building and the elevation of the perimeter frame used in the assessment.

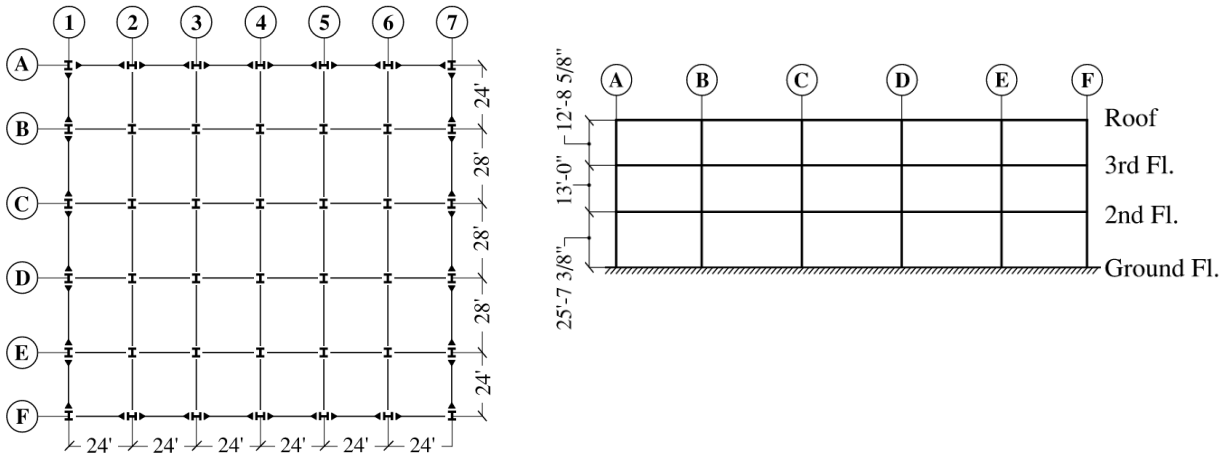

Figure 1. Plan view of building and elevation of perimeter frame on line 1

The building has been instrumented by the California Strong Motion Instrumentation Program (CSMIP Station 23516) with thirteen accelerometers: three at the ground level to record base accelerations in all three orthogonal directions, three each at the 2nd floor and roof, and four at the third level of the building – as shown in Figure 2.

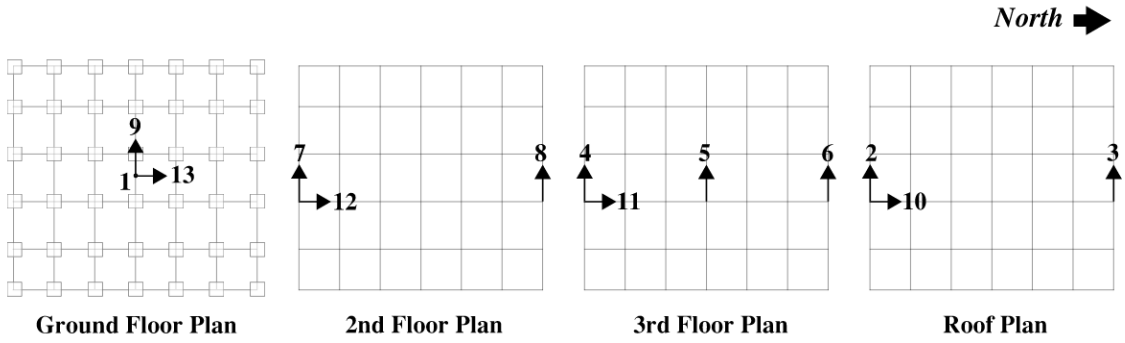

Figure 2. Locations of installed sensors

Instrumented data from several earthquakes are available for this building, as indicated in Table 1. Of the available data, two recorded motions with the highest ground peak accelerations

(PGA) were selected to calibrate the simulation model: Landers (1992) and San Bernardino (2009).

Table 1. Available instrumented data for selected building

Earthquake	Year	Peak Acceleration (g)	
		Ground	Structure
Landers	1992	0.110	0.280
San Bernardino	2009	0.102	0.155
Chino Hills	2008	0.052	0.076
Lake Elsinore	2007	0.036	0.050
Whittier	1987	0.030	0.090
Calexico	2010	0.022	0.108
Borrego Springs	2016	0.019	0.062
Borrego Springs	2010	0.018	0.077
Inglewood	2009	0.010	0.029
Beaumont	2010	0.009	0.016

When examining the time series for the Landers earthquake, unusual long-period content was observed throughout the record, particularly in the floor displacement histories (see roof history shown in Fig. 3). Therefore, a high-pass filter was applied with a corner frequency of 0.5 Hz using an 8th order zero phase delay Butterworth filter. Figure 3 shows the base acceleration as well as the relative roof displacement before and after filtering.

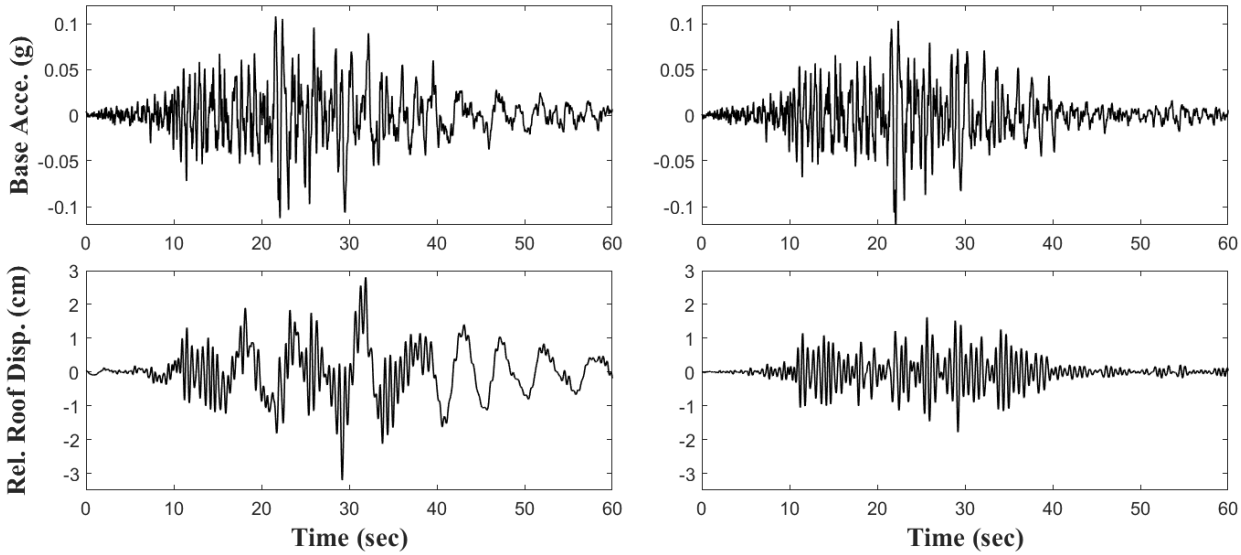

Figure 3. Unfiltered (left) and filtered (right) time histories

Modeling and Validation

Given the general symmetry of the building plan and the fact that torsional motions were not evident in the profile of the recorded floor displacement histories, the analyses were carried out on a two-dimensional model (Fig. 4) of the perimeter moment frame in the east-west direction.

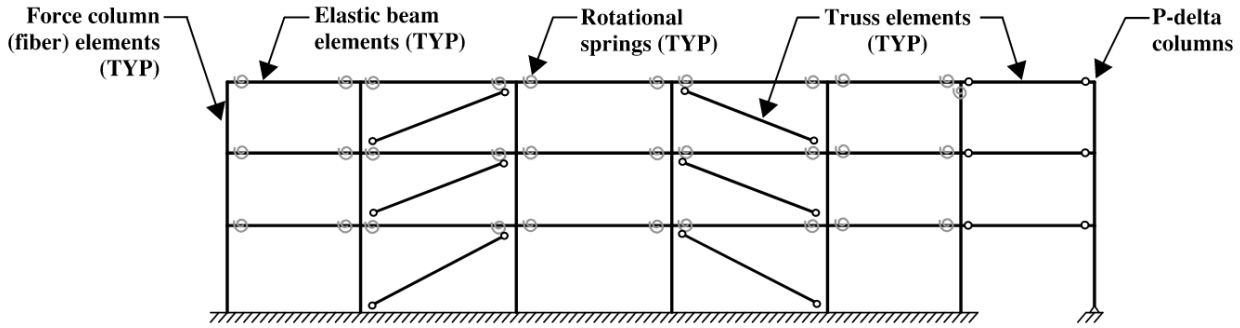

Figure 4. Two-dimensional model of perimeter frame used in assessment

Beams are modeled using elastic beam-column elements with inelastic springs (constructed with zero-length elements) at the ends as shown in Figure 4. All inelastic action (for nonlinear procedures) is lumped into these concentrated springs whose cyclic response is represented using the Modified Ibarra-Medina-Krawinkler deterioration model (Ibarra et al. 2005). In order to capture the axial load-moment interaction, columns were modeled as force-based elements with five Lobatto integration points and the Voce-Chaboche material model was used to represent the inelastic cyclic behavior of steel. Center-line dimensions are used for beams and columns to indirectly account for the flexibility of the panel zones. The building has embedded column bases connected to spread footings and grade beams and therefore the base was assumed to be fully restrained – an assumption that was shown to be reasonable for such a base connection (Falborski et al. 2020). An additional leaning column is attached to the moment frame using rigid links with pinned connections at each end to account for P-Delta effects and contributing gravity loads from the interior frames are applied at each level. A set of diagonal braces were also added at each level to represent the stiffness contribution of non-structural elements – the process by which the brace stiffness was determined is described in the following section.

Calibration of Non-Structural Stiffness

An eigenvalue analysis was carried out on the bare frame structure without the diagonal braces and the fundamental period of the structure was estimated as 0.70 sec. A Fast Fourier Transform (FFT) was carried out using the acceleration time histories at each level and Transfer Functions (relative to the base) were obtained for both the Landers and San Bernardino earthquakes. The resulting plots for the Landers recordings are shown in Fig. 5 where a predominant frequency is evident at approximately 1.8 Hz or a period of 0.56 sec.

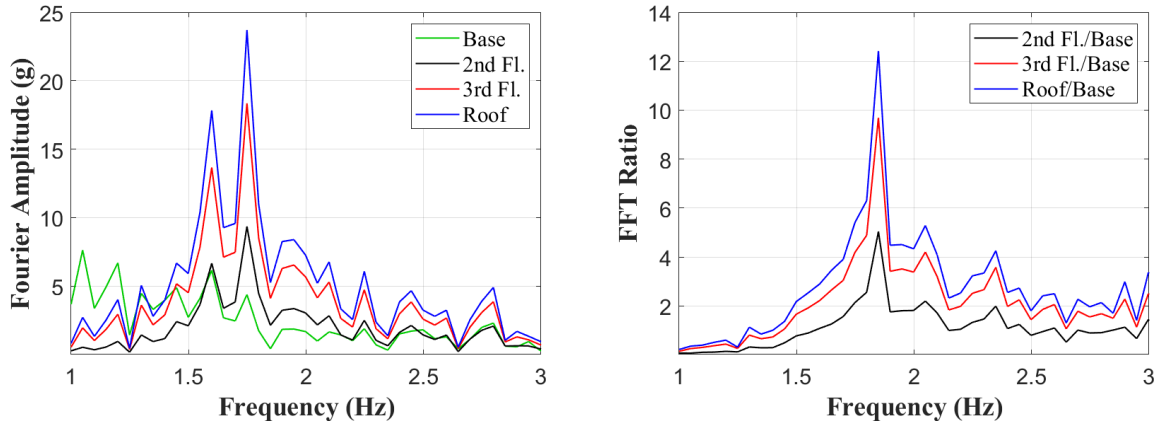

Figure 5. Fourier transform and transfer functions from acceleration histories recorded during Landers earthquake

The procedure outlined in Falborski et al. (2020) was utilized to establish the non-structural stiffness at each story level. At any time instant during the dynamic response of the structure, the shear in any story K can be estimated from:

$$V_k^{story}(t) = V_K^{NS}(t) + V_K^{STR}(t) + C_K \cdot \dot{\Delta}_K(t) = \sum_{i=K}^{N} m_i \ \ddot{u}_i(t) \tag{1}$$

In the above equation, $V_K^{story}(t)$ is the instantaneous shear in story K at time t, $V_K^{NS}(t)$ and $V_K^{STR}(t)$ are the story shears from the non-structural and structural components, respectively, $C_K \cdot \dot{\Delta}_K(t)$ is the story force due to damping, and $\sum_{i=K}^{N} m_i \ \ddot{u}_i(t)$ is the sum of the inertia forces above story K.

Using the recorded time histories, the time instants at which the interstory velocities are zero are determined for each story K. At these instants, the damping force is eliminated in Equation (1). The lateral displacements at each floor corresponding to these time instants are determined and applied statically to the model. The resulting shears will be structural story shears at each level. The total shear is determined by summing the inertia forces above that level, hence the non-structural contribution can be established. At each time instant when the interstory velocity is zero, the nonstructural story shear can be plotted vs. the corresponding interstory drift at story K. Linear regression can be used to fit the data points and the resulting slope represents the nonstructural story stiffness. Likewise, the total and structural stiffness at each floor can be estimated using a similar approach. The estimated story stiffnesses are shown for a typical floor in Fig. 6 for the San Bernardino recordings. Table 2 lists the numerical values of the estimated stiffness quantities.

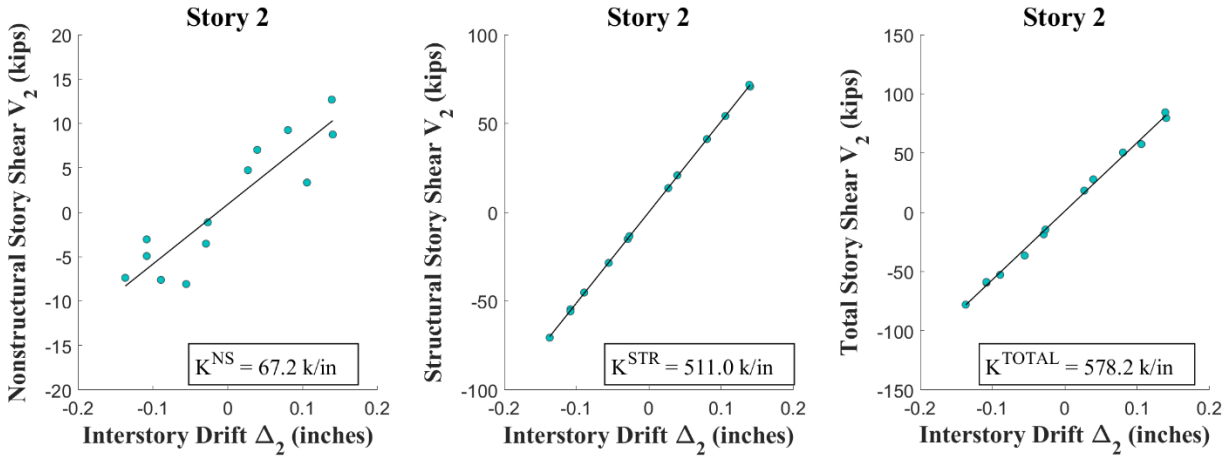

Figure 6. Estimating non-structural stiffness for a typical story (Data from San Bernardino earthquake)

In order to add the nonstructural stiffness, braces were introduced in two bays at each floor through the use of truss elements as shown previously in Fig. 4. The properties of the braces were adjusted until the total story stiffness matched the calculated values shown in Table 2. This was accomplished iteratively by updating the areas of the braces, applying static lateral loading to the model and determining the total story stiffness. The addition of the braces to the model as well as incorporating the additional stiffness of the joist floor system altered the fundamental period of the frame to 0.54 sec, consistent with the estimated building period in the east-west direction from the FFT analysis (Fig. 5).

Table 2. Estimated components of story stiffness

Story	*Stiffness (k/in)*			
	K^{NS}	K^{STR}	K^{TOTAL}	K^{NS}/K^{TOTAL}
1	51.9	551.1	603.0	0.09
2	67.2	511.0	578.2	0.12
3	102.9	340.3	443.2	0.23

Calibration of Damping

The concept behind Equation (1) can also be used to calibrate damping. In this case, the time instants at which the interstory drifts are zero are considered. Therefore, the total damping force in any story at these time instants will be equal to the sum of the inertia forces above that story. However, the damping coefficients will correspond to the lateral degree-of-freedom of the floor and additional calibration will be needed to establish Rayleigh coefficients associated with the mass and stiffness matrices of the system. Hence, in the present study, damping was estimated using the logarithmic decrement method by examining the displacement histories of the floors at the end of the recordings. Shown in Figure 7 are the floor displacement histories at the end of the recording during the San Bernardino earthquake which is assumed to represent the free vibration phase of the response. The decay in the response over the final two cycles is used to estimate damping. The estimated damping ratio varies from 13% in the first floor to 19% in the third floor. The high damping obtained with this approach indicated some anomaly in the

data and/or assumption about the free vibration phase. Hence, an additional method was utilized to estimate damping – the analysis model (with nonstructural stiffness already calibrated) was subjected to both the Landers and San Bernardino base motions and the response spectra, based on the roof accelerations, was compared to that obtained with the actual recorded motions. Results are presented in Fig. 8 which suggest that a damping of 10% (assigned to both the 1st and 2nd mode) produced a reasonable match. Hence the time history simulations presented in this paper are based on Rayleigh damping with coefficients corresponding to 10% of critical damping in the 1st and 2nd mode.

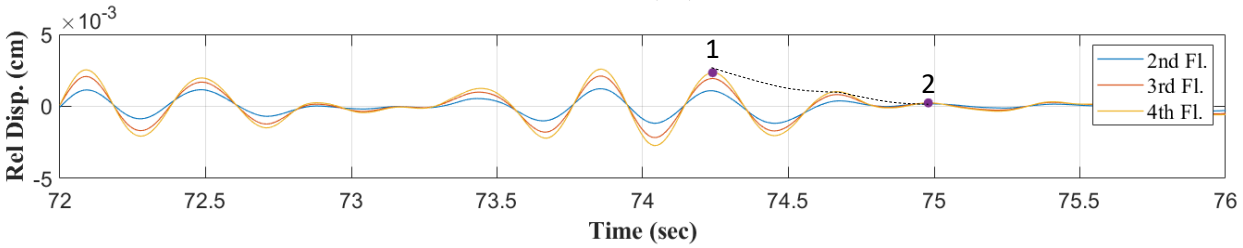

Figure 7. Free vibration response following the San Bernardino earthquake

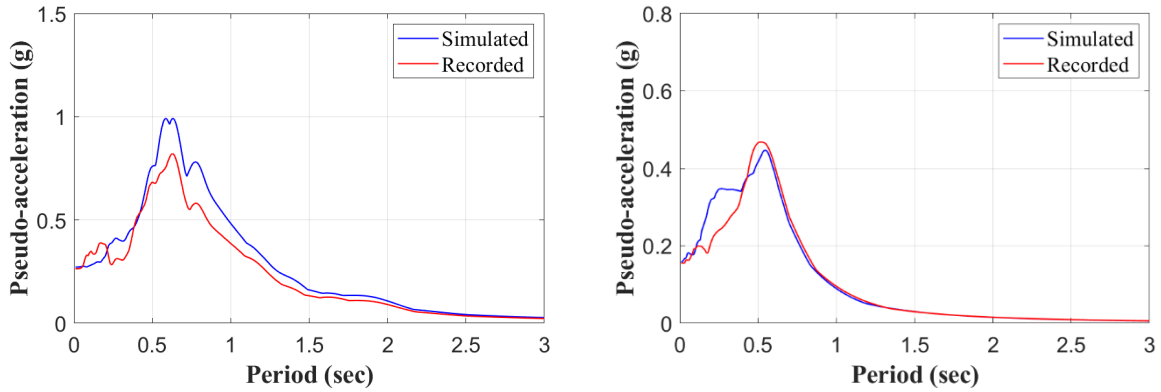

Figure 8. Comparison of acceleration spectra using data from the roof response: (a) Landers; (b) San Bernardino

Model Validation

The model was calibrated assuming elastic behavior during each of the recorded motions based on the following facts: (1) the fundamental period did not shift during these motions, and (2) there was no evident structural damage in the building following the seismic events. The simulated and recorded roof displacement histories during the Landers and San Bernardino shaking are shown in Fig. 9. The peak displacements during the Landers earthquake is slightly over-estimated – this is attributed to the fact that the 10% damping used in the simulation was lower than the observed damping (see Fig. 8). The magnitude of the response during the San Bernardino earthquake was negligible during the first 25 seconds, hence roof displacement history is shown beyond this point.

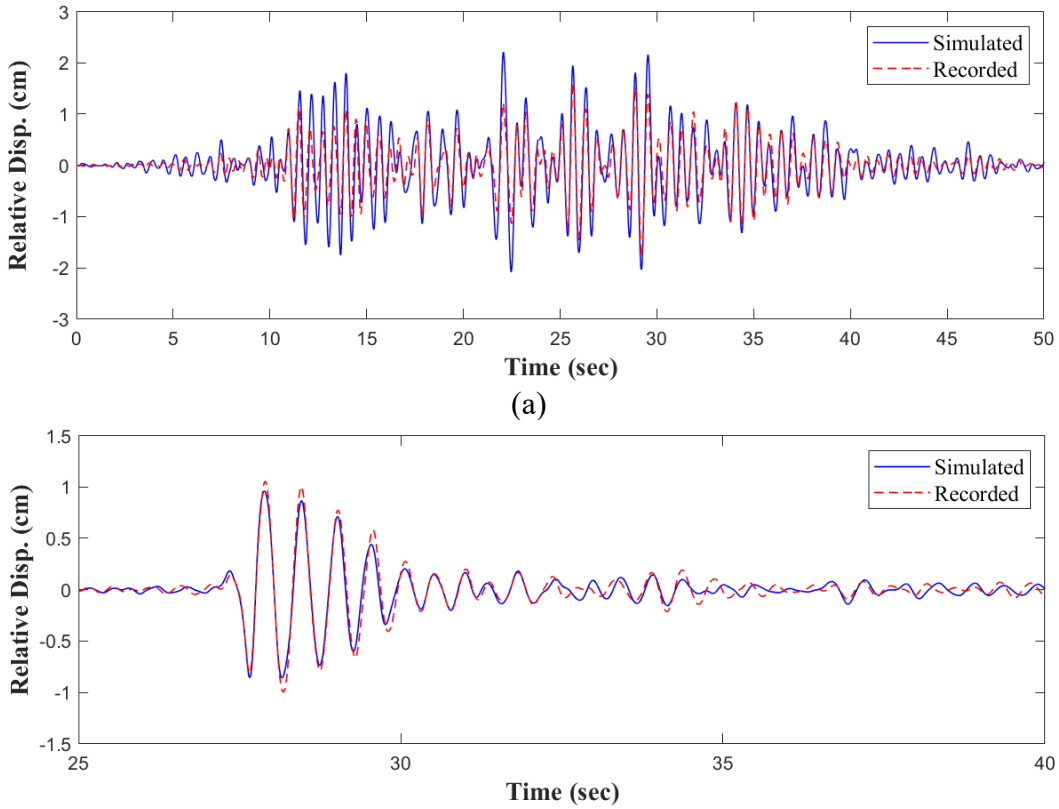

Figure 9. Comparison of recorded vs. simulated roof displacement histories: (a) Landers; (b) San Bernardino

Building Assessment using ASCE 41 Guidelines

A seismic performance assessment of the building was carried out by analyzing the validated computer model of the perimeter frame and using both linear and nonlinear analysis procedures prescribed in ASCE 41. Note that in all procedures described hereafter, the lateral load application is preceded by the application of the sustained gravity loads on the frame. The seismicity considered in the assessment is based on the BSE-2E hazard level, which represents a 50% probability of occurrence in 50 years. The resulting response spectrum for the site is shown in Fig. 10 with the following key parameters: S_{XS} = 1.9 g; S_{X1} = 1.25 g; T_O = 0.13 sec and T_S = 0.66 sec.

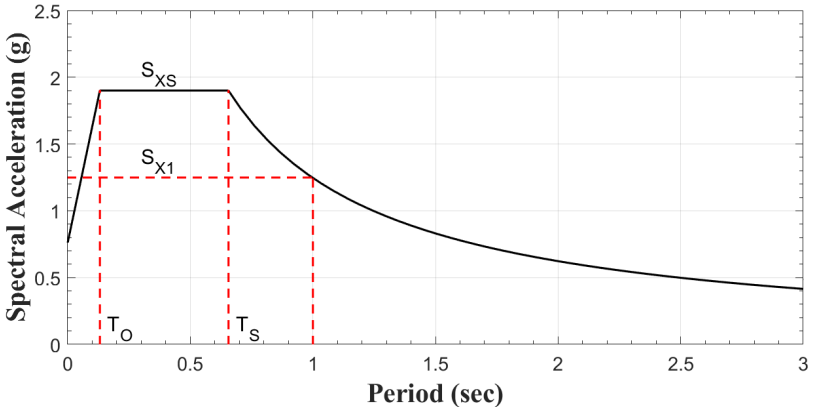

Figure 10. Response spectrum for site

Linear Procedures

For the Linear Static Procedure (LSP), an equivalent static load, representative of the seismic hazard, is applied over the height of the building. First, the pseudo lateral force V is calculated by using the following expression provided in ASCE 41:

$$V = C_1 C_2 C_m S_a W \tag{2}$$

The modification factors that account for inelastic behavior C_1 and hysterisis characteristics C_2 were both determined to be 1.0, whereas the effective mass factor C_m = 0.9. The spectral acceleration S_a was obtained from Fig. 10. The effective seismic weight of the building is 2058 kips and half this value was used to estimate the total lateral load on the perimeter frame. All elements were deformation-controlled, hence the maximum moment demands in each element was obtained due to the applied lateral forces and the corresponding demand-to-capacity ratios (DCRs or m-factors) are plotted in Fig. 11 (a) and 12 (a).

For the Linear Dynamic Procedure (LDP), the assessment was based on the response spectrum method. Considering the first three modes was sufficient to capture at least 90% of the participating mass of the frame. The equivalent static lateral load vector was then determined from:

$$\{p\} = [m]\{\Phi\}\Gamma\, S_a \tag{3}$$

where $[m]$ is the lumped mass matrix, $[\Phi]$ is the modal vector, Γ is the modal participation factor, and S_a is the spectral acceleration at the fundamental period of the frame, obtained from the target response spectrum (Fig. 10). Peak responses are recorded for each set of lateral loads and the modal demands are combined using the square root sum of squares (SRSS). The DCRs are shown in Fig. 11 (b) and 12 (b) alongside the LSP results. It is seen that both linear procedures produce very similar DCR values – several beams exceed Life Safety (LS) performance level at the lower two levels whereas the columns exhibited much better performance just exceeding Immediate Occupany (IO) limits at the first floor level.

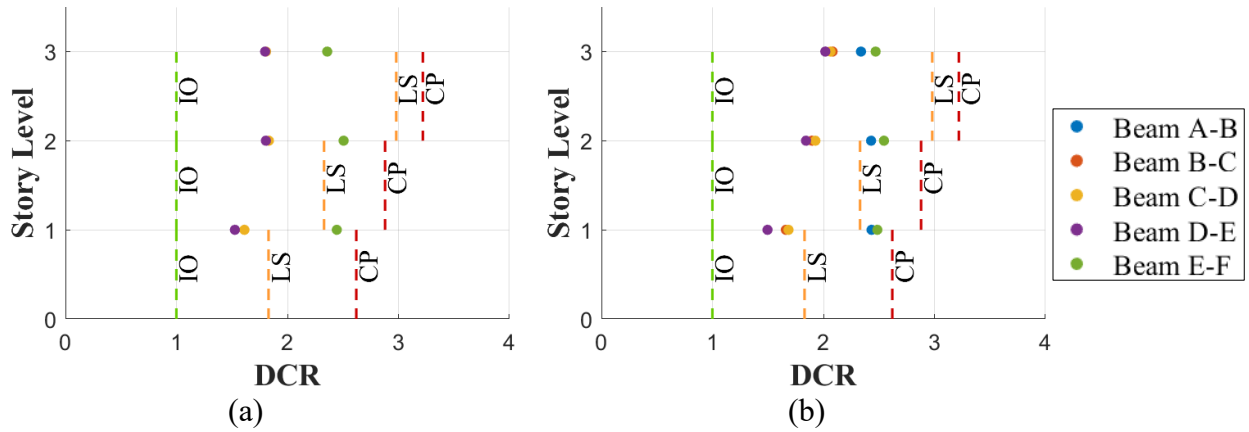

Figure 11. Demand-to-capacity ratios for beams:
(a) Linear Static Procedure; (b) Linear Dynamic Procedure

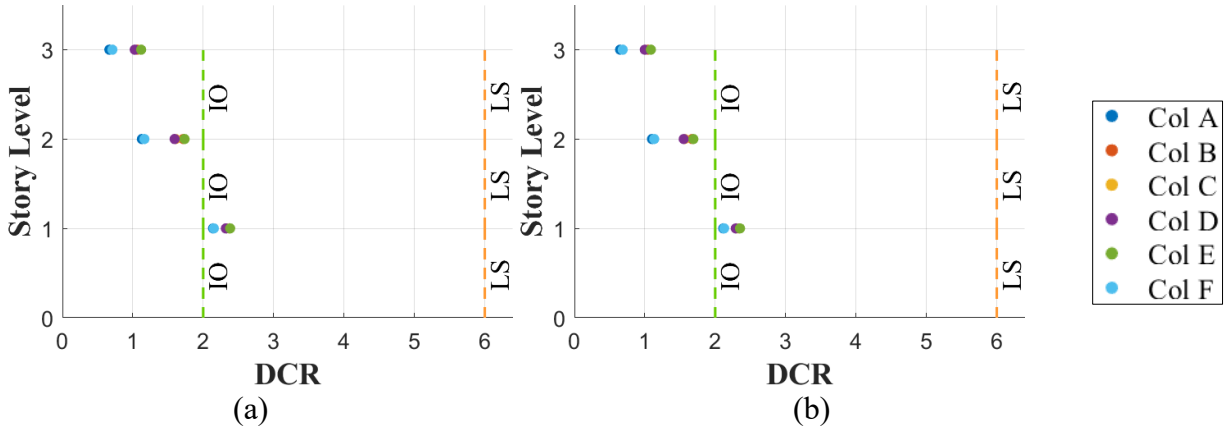

Figure 12. Demand-to-capacity ratios for columns:
(a) Linear Static Procedure; (b) Linear Dynamic Procedure

Nonlinear Procedures

As described previously, nonlinear action in the beams is represented by concentrated springs while columns are modeled using distriuted plasticity elements with fiber sections to capture axial force-moment interaction effects. The response of each nonlinear spring is based on the Modified Ibarra-Medina-Krawinkler (I-K) model – the transformation of the I-K model into the ASCE 41 backbone envelope for use in nonlinear procedures is displayed in Fig. 13.

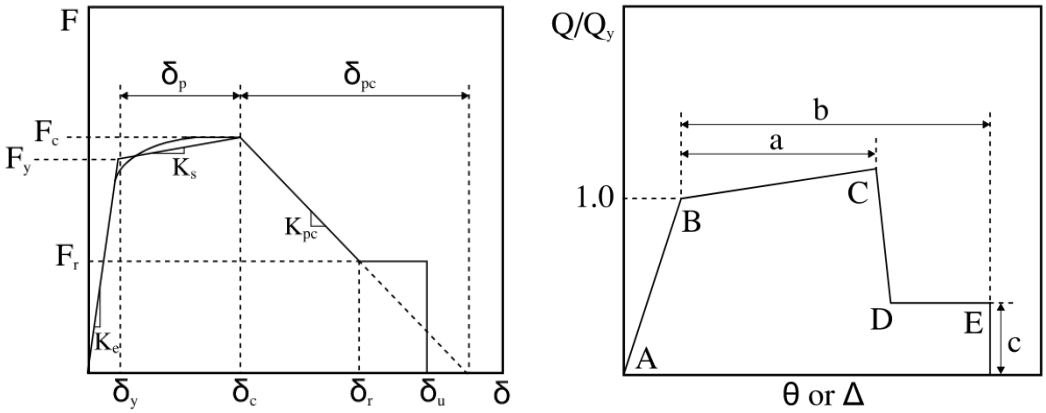

Figure 13. Modified Ibarra-Medina-Krawinkler model (left) and transformed backbone parameters (right) used in nonlinear procedures

For the Nonlinear Static Procedure (NSP), the target displacement δ_t is calculated using:

$$\delta_t = C_0 C_1 C_2 S_a \frac{T_e^2}{4\pi^2} g \quad (4)$$

The modification factors that accounts for the multi to single degree-of-freedom transformation, inelastic behavior, and hysteretic characteristics, respectively, were determined to be: C_0 = 1.3, C_1 = 1.034 and C_2 = 1.0. The effective fundamental period, and consequently the target displacement, was estimated through an iterative process to establish a converged effective period. The final computed target displacement was 11.28" (corresponding to a roof drift of 2.3 %) and an effective to initial stiffness ratio of 1.24. The inelastic demands in the beams and columns at the target displacement are estimated using OpenSees and are compared to the ASCE 41 acceptance criteria in Fig. 15 (a) and Fig. 16 (a).

Ground Motion Selection for NDP

In order to select ground motions that are representative of the seismic hazard at the site, the United States Geological Survey (2017) *Unified Hazard Tool* was used for the site deaggreation. The hazard at the site is controlled primarily by the San Jacinto fault with expected magnitude 8.0 and fault distances less than 1 km and the San Andreas fault with magnitude range 7.0 – 8.0 and fault distances between 7 – 12 km. A total of 51 ground motions were downloaded from the PEER NGA ground motion database (ngawest2.berkeley.edu) with the following filters: fault type: strike slip; magnitude: 6 to 8; distance to rupture: 0 to 12; and shear wave velocity Vs30: 180 to 360 m/s. Ground motions with spectral shapes signficantly different from the target spectrum were discarded. The final 11 sets of ground motion (pairs) were selected such that the average maximum direction spectra (RotD100) was at or above 90% of the target response spectrum in the period range $0.2T_1 – 1.5T_1$. Given that the site is classified as near-fault, the horizontal components of each selected set was rotated to the fault-normal and fault-parallel directions of the causative fault. The fault closest to the site is the San Jacinto fault, hence this fault angle was used as the reference for rotating the ground motions. ASCE 41-17 does not provide specific guidance on ground motion selection for 2D analysis. Therefore, the following procedure was implemented: for each ground motion set already rotated in the fault parallel and normal orientations, the base motions and their spectra in each direction were compared; the

motion with a larger evident pulse in the time history or a larger spectral value within the target period range was selected. A additional scale factor of 1.1 was necessary to ensure that the actually applied ground motions had a mean spectra that was equal to or above the target spetrum in the required period range. Figure 14 shows the final ground motion spectra and Table 3 summarizes essential details of the selected records.

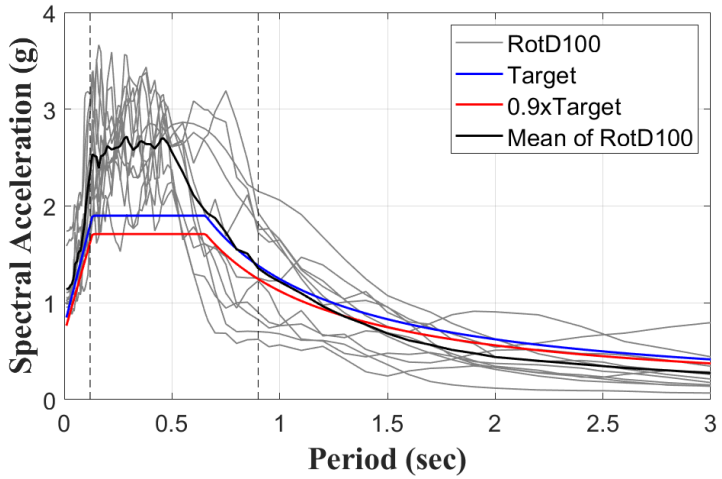

Figure 14. Maximum direction spectra of scaled motions and comparison of mean spectrum with target spectrum at site

Table 3. Selected ground motions

GM #	Record Sequence Number	Earthquake Name	Year	Station Name	Magnitude	R_{rup} (km)
1	6	"Imperial Valley-02"	1940	El Centro Array #9	6.95	6.1
2	30	"Parkfield"	1966	Cholame-Shandon Array #5	6.19	9.6
3	95	"Managua_-Nicaragua-01"	1972	"Managua_ ESSO"	6.24	4.1
4	162	"Imperial Valley-06"	1979	"Calexico Fire Station"	6.53	10.5
5	165	"Imperial Valley-06"	1979	"Chihuahua"	6.53	7.3
6	185	"Imperial Valley-06"	1979	"Holtville Post Office"	6.53	7.5
7	558	"Chalfant Valley-02"	1986	"Zack Brothers Ranch"	6.19	7.6
8	725	"Superstition Hills-02"	1987	"Poe Road (temp)"	6.54	11.2
9	4098	"Parkfield-02_ CA"	2004	"Parkfield - Cholame 1E"	6.00	3.0
10	4102	"Parkfield-02_ CA"	2004	"Parkfield - Cholame 3W"	6.00	3.6
11	4108	"Parkfield-02_ CA"	2004	"Parkfield - Fault Zone 3"	6.00	2.7

Nonlinear simulations of the calibrated numerical model were carried out using OpenSees for each of the eleven ground motions, and mean values of the plastic rotations in the beams and columns at each end of the element were determined. The maximum plastic rotation among all eleven motions was also recorded. Results are presented in Fig. 15 (b) and Fig. 16 (b) alongside the estimates from NSP. Two beams at the first floor level fail the Collapse Prevention (CP) limit when using NSP but pass Immediate Occupancy (IO) under NDP when considering the average rotation for the eleven motions. If the peak rotation among all motions are considered, the LS limit was exceeded in two beams and the CP limit was exceeded in one beam at the first floor level. Column demands in general were small and meet or slightly exceeded the criteria for IO performance level at all levels for both NSP and NDP.

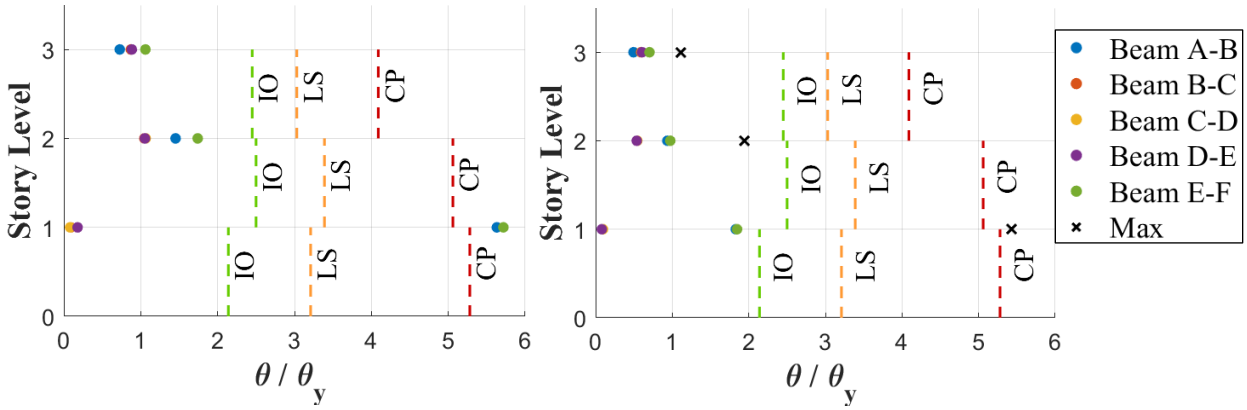

Figure 15. Ductility demands for beams:
(a) Nonlinear Static Procedure; (b) Nonlinear Dynamic Procedure

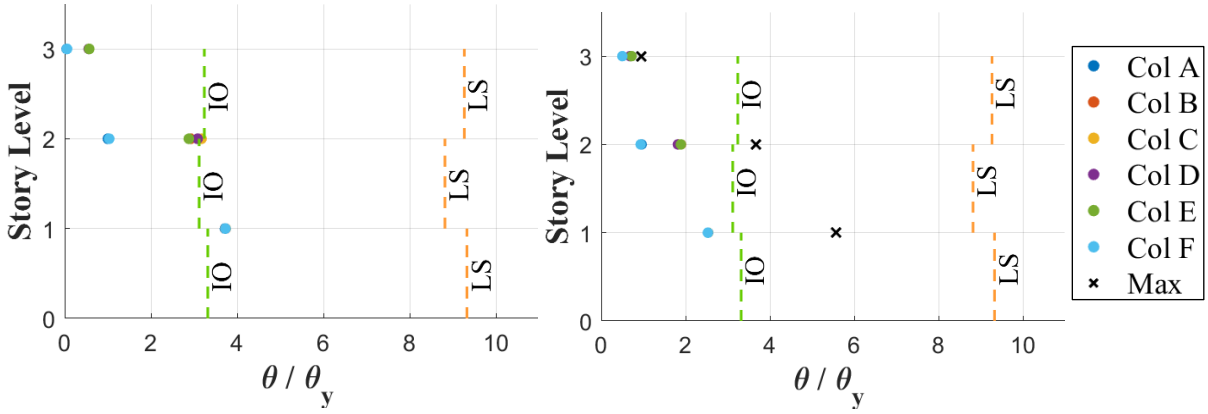

Figure 16. Ductility demands for columns:
(a) Nonlinear Static Procedure; (b) Nonlinear Dynamic Procedure

Conclusions

An existing three-story steel moment frame building that was designed and constructed prior to the 1961 UBC code revisions was analyzed using the modeling and acceptance criteria

outlined in ASCE-41. Significant effort was directed towards identifying the nonstructural stiffness of the system, estimating damping and validating the computer model of the perimeter frame used in the assessment of the building.

Results of the simulations indicate that both linear procedures resulted in consistent DCRs for both beams and columns at all floor levels. The nonlinear static procedure resulted in the most severe demands at the first floor with two beams failing the CP limit state. Simulations using NDP resulted in the lowest demands when considering the mean demands for all eleven ground motions. However, when the response to individual motions are examined, beams on the first floor failed LS performance in two cases and CP performance level in one event. This highlights the importance of ground motion selection and scaling when using NDP.

Acknowledgements

Funding for this study was provided by the California Department of Conservation, California Geological Survey (Strong Motion Instrumentation Program) under Contract 1019-013. However, the contents of the paper do not necessarily represent the policy of that agency nor is an endorsement by the State Government of California.

References

ASCE (2017). Seismic Evaluation and Retrofit of Existing Buildings, ASCE/SEI 41-17, American Society of Civil Engineers, Reston, Virginia.

ASCE (2016). Minimum Design Loads and Associated Criteria for Buildings and Other Structures, ASCE/SEI 7-16, American Society of Civil Engineers, Reston, Virginia.

Falborski, T., Hassan, A.S., Kanvinde, A.M (2020). Column Base Fixity in Steel Moment Frames: Observations From Instrumented Buildings, Journal of Constructional Steel Research. 168. 105993. 10.1016/j.jcsr.2020.105993.

Harris, J. and Speicher, M. (2019). Assessment of Performance-Based Seismic Design Methods in ASCE 41 for New Steel Buildings: Special Moment Frames, Earthquake Spectra. **34** (3).

Ibarra, L. F., and Krawinkler, H. (2005). Global Collapse of Frame Structures under Seismic Excitations. Technical Report 152, The John A. Blume Earthquake Engineering Research Center, Department of Civil Engineering, Stanford University, Stanford, CA.

U.S. Geological Survey (2017). Unified Hazard Tool, accessed September 7, 2020 at URL https://earthquake.usgs.gov/hazards/interactive/

CRITICAL ASSESSMENT OF CODE TORSIONAL PROVISIONS FOR LOW-RISE BUILDINGS WITH SEMI-RIGID DIAPHRAGMS DATA

Yijun Xiang, Farzad Naeim, Farzin Zareian

Department of Civil & Environmental Engineering
University of California, Irvine

Abstract

Our research puts the accidental torsion provisions in ASCE-7 for low-rise buildings in perspective; various combinations of plan aspect ratios, irregularity, and diaphragms rigidity are investigated. The presented work is based on simulations; however, the building models used in the study are proportioned to represent a wide range of code conforming buildings. 4-story building prototypes with a plan aspect ratio of 1:1, 1:2, 1:4, and 1:8 are modeled. The building models possess translational to rotational period ratios (Ω) ranging from 1.1 to 2.0. Type 1a (Torsional Irregularity) and Type 1b (Extreme Torsional Irregularity) – according to ASCE 7 – is considered as the measure of floor plan irregularity. Uncertainty in stiffness is treated as the source of accidental eccentricity. Results are compared with corresponding MDOF models having regular plans (i.e., symmetric) and rigid diaphragms. We conclude that the magnification in deformation demands due to accidental torsion in buildings with a semirigid diaphragm, or inherent plan irregularity, is smaller than building with regular floor plan and rigid diaphragm. Equivalent design eccentricities obtained from this body of work indicate that the 5% equivalent eccentricity rule is conservative to capture the deformation's magnification due to accidental torsion in low-rise buildings possessing floor plan irregularity or semirigid diaphragms if median estimates of all stories are the basis of code calibration.

Introduction

ASCE 7 (ASCE, 2010, 2017) traditionally requires an increase in the inherent torsional moment by applying a 5% offset (perpendicular to ground motion direction) to the location of the center of mass on each floor. Accidental torsion is intended to account for the randomness in the distribution of floor mass and stiffness of Vertical Lateral Load Resisting systems (VLLRs). These design provisions require a magnification of accidental torsional moment for structures with torsional irregularity Type 1a and Type 1b and designed with Seismic Design Category (SDC) C to F assignment. Meanwhile, ASCE 7 does not distinguish any difference between rigid and semirigid floor diaphragms when it comes to the issue of accidental torsion. These requirements seem counterintuitive; one may expect that accidental torsional effects in semirigid diaphragms are less severe than rigid diaphragms due to the floor system's in-plane deformations. Moreover, the inherent torsional moment of torsionally irregular floor plans dwarfs the effect of accidental torsion, rendering their magnification less plausible.

One of the earliest research endeavors for characterizing accidental torsional moment in symmetric-in-plan structures originated by De la Llera and Chopra (1992); they used instrument

data from three low-rise buildings (by California Strong Motion Instrumentation Program, CSMIP) and concluded that the 5% accidental torsional rule is adequate. They employed linear response spectrum analysis (De la Llera & Chopra, 1994;1995) to show 5% eccentricity is adequate for most steel and concrete special moment-resisting frames. Following a similar approach for reduction of MDOF systems to analytical models with three degrees of freedom (two translational and one rotational), other researchers such as Lin et al. (2001), Hernandez & Lopez (2004), De-la-Colina & Almeida (2004), Basu et al. (2014), have made recommendations on enhanced approaches to include accidental torsion in the response assessment of buildings for seismic design purposes.

The sensitivity of buildings' seismic performance to the inclusion (and exclusion) of accidental torsion provisions in their structural design was tackled by a few researchers to shed light on the issue from another angle. DeBock et al. (2014), and ATC (2018), have used a reduced form of MDOF models for ordinary and special reinforced concrete moment frames and investigated the collapse performance of such models with and without the inclusion of accidental torsional moment in their design. They conclude that ASCE 7 accidental torsion design requirements are only significant for buildings with SDC D assignment if their torsional irregularity is beyond Type 1a (i.e., TIR>1.2). They suggest that the inclusion of accidental torsional moment for structural design in the form suggested by ASCE 7 is typically not needed except for extreme plan irregularities. With a similar focus and performance objective (i.e., collapse), Flores et al. (2018) has focused on steel buildings (9-story with Buckling Restrained Brace Frames). They recommend that accidental torsion should be included in the nonlinear analysis of torsionally irregular buildings. Failure to add accidental torsion in the nonlinear analyses can lead to significant underprediction of deformations.

In contrast with Debock et al. (2014) and Flores et al. (2018), who used a rigid diaphragm assumption in their analytical building models, Fang and Leon (2018) investigated the difference between the response of low-rise steel buildings with rigid and semirigid diaphragms. Accidental eccentricity was created by shifting the center of mass as much as 5% of the diaphragm dimension. They observe that the drift demands in the asymmetric structures are higher for those with semirigid diaphragms than those with rigid diaphragms. This observation is argued to be due to the diaphragm's finite in-plane rigidity, leading to significant higher-mode effects and larger lateral deformation.

Compared with other studies summarized above, our study aims to quantify the needed amount of accidental torsional moment that can represent uncertainty in stiffness of VLLRs in response assessment at the design level seismic excitation. The intention is to put the seismic design provisions of ASCE 7 in perspective. To this end, our study is aligned with De la Llera and Chopra (1994) because both studies aim to find an equivalent eccentricity to account for the accidental torsional moment. This study, however, is in contrast with DeBock et al. (2014) in which the impact of including (and excluding) accidental torsional moment suggested by ASCE 7 in the design process is evaluated. The research work presented here is complementary to Xiang et al. (2018), where the accidental torsional moments in symmetric buildings with rigid diaphragms were investigated. We have expanded our previous research to address asymmetric floor plans and peculiarities that arise from including the diaphragm's finite stiffness (i.e., semirigid diaphragm) in the context of accidental torsion. The focus here is on low-rise buildings.

Methodology

In this study, uncertainty in VLLR stiffness is the only source of accidental torsion in buildings. This uncertainty is assumed to arise from the variability of element cross-section dimensions, second moment of inertia, and material strength. Using the information suggested in Xiang et al. (2018), a coefficient of variation (CoV) of 0.14 is set for the stiffness of VLLRs.

Three-dimensional (3-D) models of 4-story buildings with a combination of three different plan aspect ratios (1:2, 1:4 and 1:8), three levels of diaphragm rigidity (rigid, and two levels of semirigid, denoted as RI, S1, and S2, respectively), and three levels horizontal irregularity (i.e., TIR = 1.0, 1.2, 1.4) are created. Given that translational and torsional mode of vibrations simultaneously affect a building's general response, the factor Ω is defined as the ratio of the dominant translational period (T_{tran}) to the dominant rotational period (T_{rot}). Large Ω values associated with perimeter frame buildings and small Ω values represent core-wall systems with low torsional stiffness. Building models with Ω ranging from 1.1 to 2.0 are developed, which covers most of the building cases. These models are denoted as *base* models.

The 3-D analytical models' realizations are created by randomizing beam and column stiffness and strength properties using CoV = 0.14. We assume accidental torsional moments are caused by the asymmetric stiffness introduced through randomness in stiffness of VLLRs. Such phenomena lead to a torsional moment at any horizontal irregularity (i.e., TIR = 1.0, 1.2, 1.4). Nonlinear Time History Analysis (NLTHA) is conducted using the Opensees platform and 60 single component ground motion excitations at 475 year return period for San Francisco (37.7749°, -122.4194°). Disaggregation using OpenSHA is first employed to obtain magnitude, distance, and epsilon for each dominant scenario. Conditional spectrum (Baker, 2011) covering a period range from 0.2 times the smallest first translational period to 1.5 times the largest first translational period is then used to select 30 pairs of ground motion with scaling factor larger than 0.5 and lesser than 2.0. For each *base* model, two random realizations are created, leading to 180 (= 3 × 60) models for each combination of plan aspect ratio, diaphragm rigidity, horizontal irregularity, and Ω. Measurements are taken for the largest displacement amplification among four corners of each floor based on the rigid and semirigid diaphragm assumption. Deformation demands are recorded and transformed into two deformation magnification factors α_1 and α_2 (will be explained in the following) to quantify accidental torsion's impact on building response. Statistical measures (e.g., median and 84%) of α_1 are used to estimate the equivalent design eccentricity (represented by e(%) shown in the following), which is used to account for the effect of accidental torsion during design procedures.

Parameters that characterize building torsional response

Parameters α_1 and α_2 are introduced, Eq. (1) and Eq. (2), to quantify the magnification in displacement response due to uncertainty in VLLR stiffness. α_1 and α_2 are defined for each floor; for a 4-story building, four distinct values of α_1 and α_2 is computed for each random case. Similar factors are computed for drift demands for each story; however, to keep notations simple, we rely on α_1 and α_2 to represent floor displacement and story drift. In these equations, δ_{tot}^{base} denotes the maximum displacement of a floor (or drift of a story) for the *base* model. Conversely, δ_{tot}^{rand} denotes the maximum displacement of a floor (or drift of a story) for a random model. There are

two random models for each *base* model; therefore, one can compute two distinct values for α_1, and α_2 for each floor (or story) given a ground motion record. δ_{Tran}^{base} and δ_{Tran}^{rand} denotes the maximum translation of the middle of the floor (or middle of the story) of a *base* model and a random model, respectively. α_1 is formulated to quantify the magnification in deformation demands due to uncertainty in VLLR stiffness compared to the *base* model. α_2 is suggested to quantify the magnification of deformation compared to the middle of the floor (in the spirit of calculating TIR), or story, compared with the same magnification for the *base* model. The denominator of Eq. (2) for symmetric buildings is unity.

$$\alpha_1 = \left(\frac{\delta_{tot}^{rand}}{\delta_{tot}^{base}}\right) \quad \text{Eq. (1)}$$

$$\alpha_2 = \frac{\left(\frac{\delta_{tot}^{rand}}{\delta_{Tran}^{rand}}\right)}{\left(\frac{\delta_{tot}^{base}}{\delta_{Tran}^{base}}\right)} \quad \text{Eq. (2)}$$

We suggest equivalent eccentricity be calculated in a manner that maximum deformation obtained by application of lateral loads (from ASCE 7) with a distance from the center of mass result in a similar statistical measure of α_1. One can use median, or 84%, of α_1 for the calculation of equivalent eccentricity.

Building Models and Ground Motions

4-story building models are generated in the OpenSees platform. The 3-D building models comprise four 2D frames. Each frame is designed as a single bay generic frame with 20' bay width and 12' story height. (see Figure 1). The ratio of the moment of inertia of beams and columns in this idealized model is set to be 1.0, which leads to a reasonable beam to column stiffness ratio and strong column weak beam ratio (assuming proportional strength and stiffness).

Distribution of moment of inertia along the building height follows story shear distribution according to the ASCE 7 Equivalent Lateral Force (ELF) method. Moment of inertia of beams and columns of *base* models with symmetric floors are computed through an optimization method targeting a period of 1.6s for the *base* model with symmetric floor plans and rigid diaphragms. Asymmetric *base* models are created by moving the center of mass laterally and perpendicular to the direction of ground motion application to achieve TIR = 1.2 and 1.4. Rotation of beams and columns are computed at story yield point (i.e., 0.01 drift ratio) from which moment capacity of beams and columns is obtained. Springs with bilinear hysteretic (Ibarra et al., 2005) characteristics are placed at the beam, as illustrated in Figure 1. Parameters for the bilinear hysteretic springs are shown in Figure 1b.

Symmetric *base* models with a plan aspect ratio of 1:1, 1:2, 1:4, and 1:8 are generated with rigid diaphragms. These *base* models are later modified to develop *base* models with a semirigid diaphragm. Figure 2 shows the plan view of the 3-D models used in this study. A 3-D model with a plan aspect ratio of 1:*n* is modeled as *n* number of 1:1 square buildings being placed in a row.

This model is further simplified using four VLLRs, with each VLLR being n times stiffer and stronger, and with rotational stiffness K_θ, period ratio Ω. The dimension of the slab is unchanged. Each building model represents a certain case with fixed Ω and plan aspect ratio, and only those cases with two translational periods (in two orthogonal directions) ratio larger than 0.5 and less than 2 are retained for NLTHA.

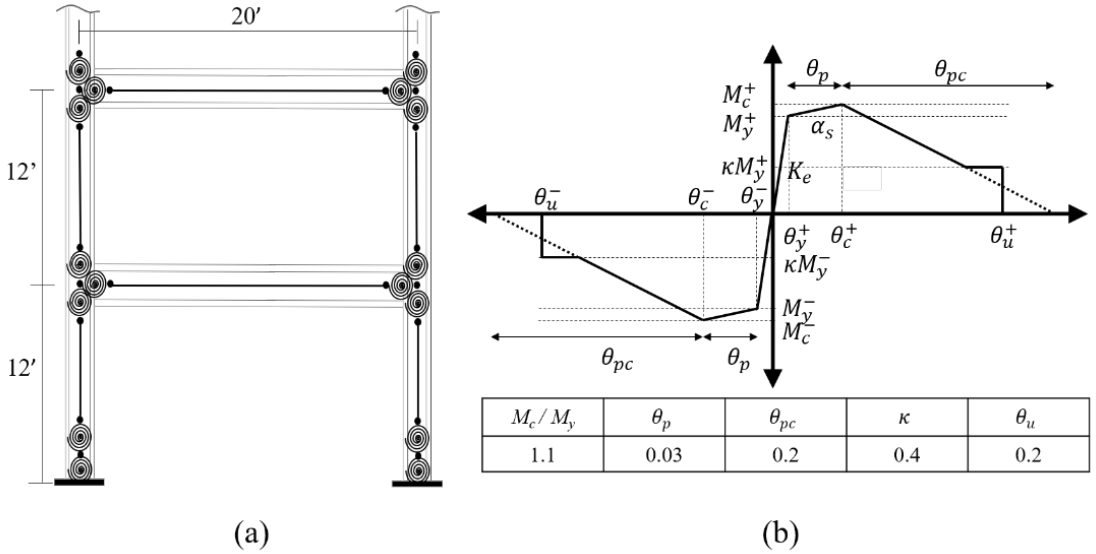

M_c / M_y	θ_p	θ_{pc}	κ	θ_u
1.1	0.03	0.2	0.4	0.2

(a) (b)

Figure 1. Generic frame used in this study: (a) geometry, (b) spring backbone curve

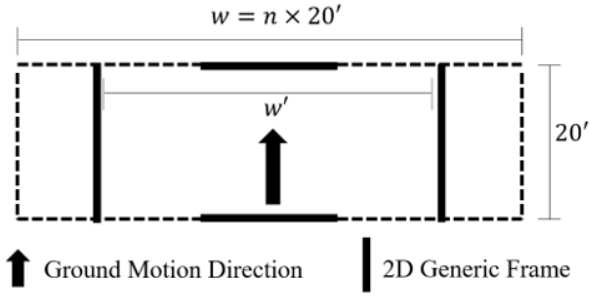

Figure 2. Floor plan to achieve various plan aspect ratios

The semirigid diaphragm is modeled as a beam in the middle of the floor, from one end to another. This beam's in-plane stiffness is uniform for all floors and is calibrated for the most critical level (i.e., roof). Two levels of finite diaphragm stiffness are defined, inspired by ASCE 7, Section 12.3.1.3, denoted with the variable β. $\beta = 1$ represents the case in which the floor's in-plane stiffness leads to an extra amount of lateral drift (in the middle) equal to the story drift if lateral loads are applied as an equivalent tributary lateral load. For $\beta = 2$, the floor's in-plane stiffness is calibrated to two times the lateral drift obtained for $\beta = 1$.

General Observations and Trends

Statistics of torsional characteristics α_2 and equivalent eccentricity (i.e., e%) are computed at all floor and story levels. One may focus on statistics of the most critical floor (or

story) with the largest value of α_2 and *e*%, representing the worst-case scenario. On the other hand, utilizing all floors' statistics results in a more refined understanding of accidental torsion's effect on low-rise buildings' deformation response. Both forms are presented in this section, alongside the effect of floor asymmetry and finite in-plane rigidity. We start by investigating the effect of floor asymmetry on α_2 and *e*% separately from the effect of finite in-plane rigidity on the same parameters. The intention is to grasp the needed understanding of each of these two building characteristics' impact before studying their combined effect. The combined effect of floor asymmetry and finite in-plane rigidity on α_2 will follow this early discussion.

A short explanation about the format of the presented figures (Figures 3-7) can assist in a better understanding of their intent. Figures are presented in a 3 by 2 mosaic format; the left and right columns show the parameter under study's statistical measures for the critical floor/story and the entire building, respectively. Black and red colors, respectively, indicate 50% and 84% statistics of the parameter studied (i.e. α_2 or *e*%). Markers are presented for different floor plan aspect ratios of 1:1, 1:2, 1:4, and 1:8. Given its lack of viability, there is no structure with a semirigid diaphragm and a 1:1 floor plan aspect ratio. The horizontal of all plots is set to show Ω with values ranging from 1.1 to 2. Xiang et al. (2018) studied the Ω values of CSMIP instrumented buildings using collected instrument data; the range Ω used here covers a wide range of Ω values observed by Xiang et al. (2018).

Figures 3 and 4 show the impact of plan irregularity and finite in-plane rigidity on α_2, respectively. Both figures show a reduction in median amplification of deformations due to accidental torsion compared to the case with a symmetric floor plan and rigid diaphragm. This observation is stable for both the most critical floor and all floors alike, although the median α_2 once all floors are considered is less. The reduction in the median of α_2, however, because of the inclusion of finite in-plane stiffness of diaphragms is much larger than what is observed for considering asymmetric floor plans. It appears that diaphragm rigidity provides the opportunity of transferring floor rotations (due to accidental torsion) to the frames rather than absorbing it in the form of in-plane curvature. The impact of diaphragm finite in-plane rigidity on the reduction of α_2 is stable and has caused a major reduction in the 84% statistics of α_2 indicating there are not a significant number of cases that do not follow the suggested trend.

The cases with asymmetric floor plan and rigid diaphragm (i.e., Figure 3) show a reduction in the median value of α_2 especially for low values of Ω that represent torsionally flexible structures. We postulate that randomness in VLLR stiffness ameliorates the impact of asymmetric plan in increasing α_2. Given the dynamics of such a system, it is likely that the value of α_2 is less than unity; for this reason, the 50% values of α_2 are low once all the floors are included in the statistics. The slope of α_2 to Ω is reduced for larger values of TIR, which mainly shows that the torsional flexibility of the building is less important once the system is inherently asymmetric. 84% of α_2 for asymmetric floor plan and rigid diaphragm does not show the same level of drop that 84% of α_2 for cases with finite in-plane rigidity of diaphragms show. This shows that the reduction of α_2 for asymmetric floor plans with a rigid diaphragm is not as determined as to when the diaphragm is semirigid. The variability of α_2 has increased for torsionally stiff structures (large Ω) with asymmetric floor plans.

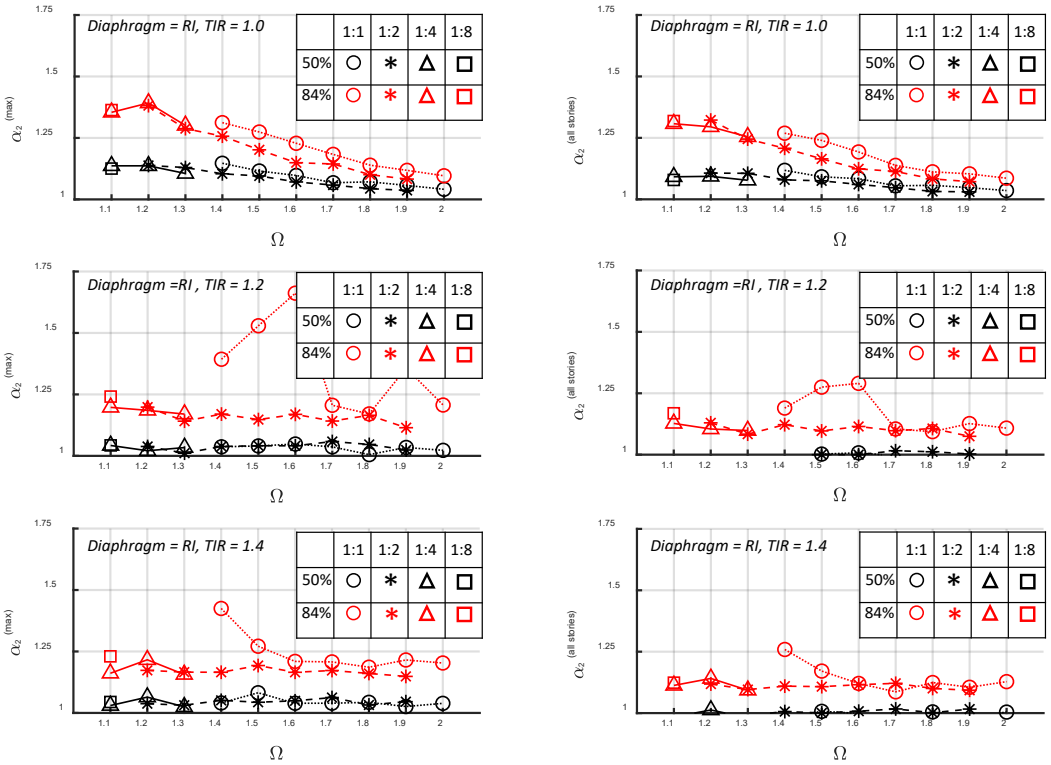

Figure 3. Variation of statistical measures of α_2 concerning Ω, plan aspect ratio, and floor plan irregularity for rigid diaphragm structures: critical story, all stories

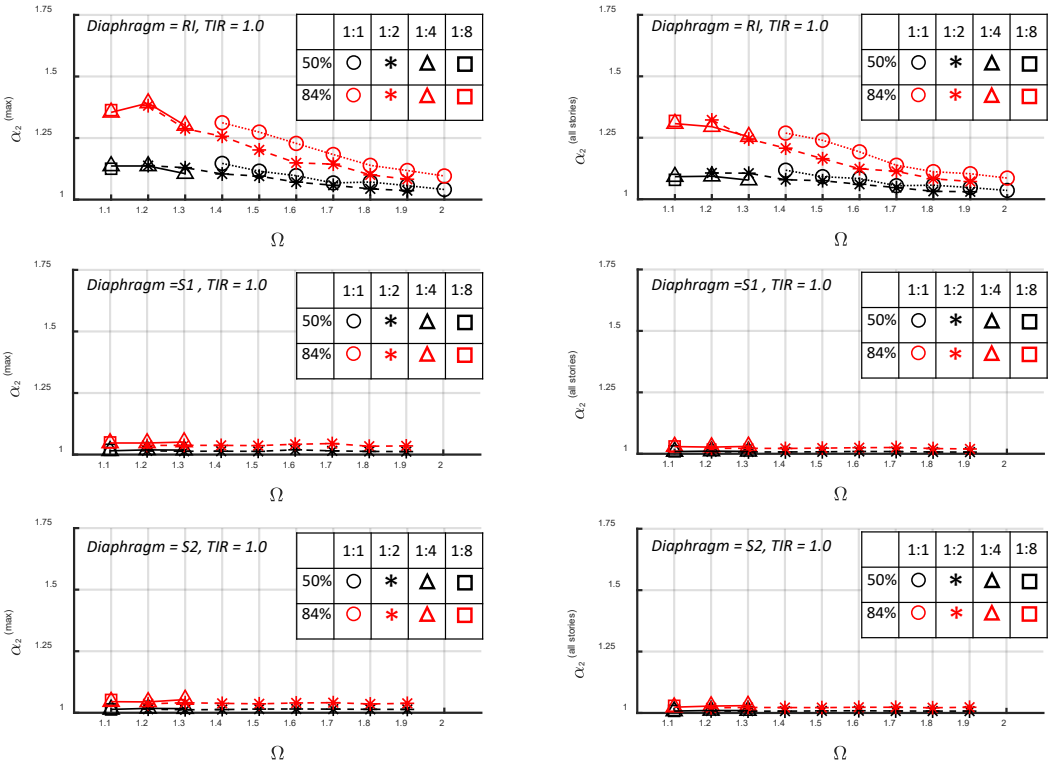

Figure 4. Variation of statistical measures of α_2 concerning Ω, plan aspect ratio, and diaphragm in-plane rigidity for symmetric structures: critical story, all stories

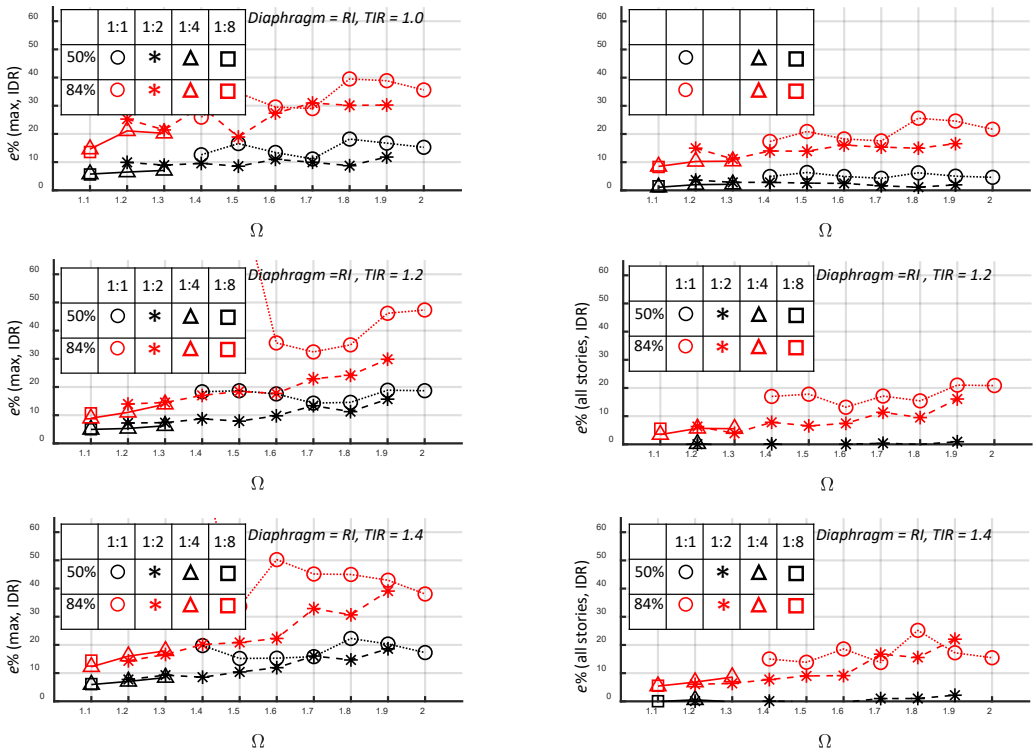

Figure 5. Variation of statistical measures of *e*% concerning Ω, plan aspect ratio, and floor plan irregularity for rigid diaphragm structures: critical story, all stories

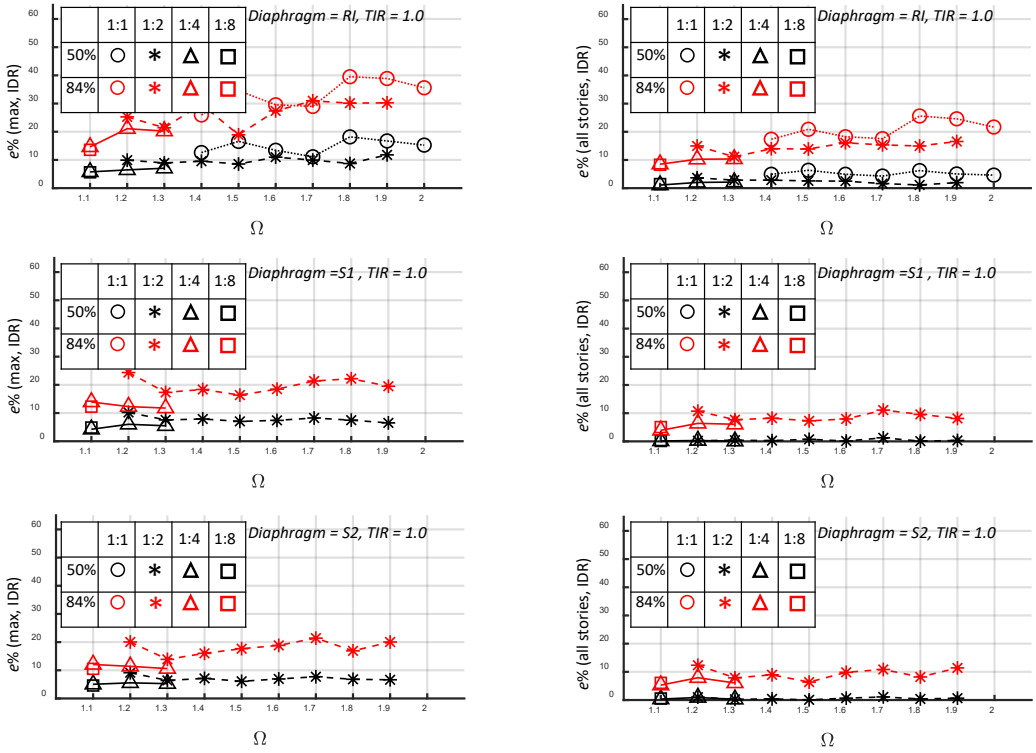

Figure 6. Variation of statistical measures of *e*% concerning Ω, plan aspect ratio, and diaphragm in-plane rigidity for symmetric structures: critical story, all stories

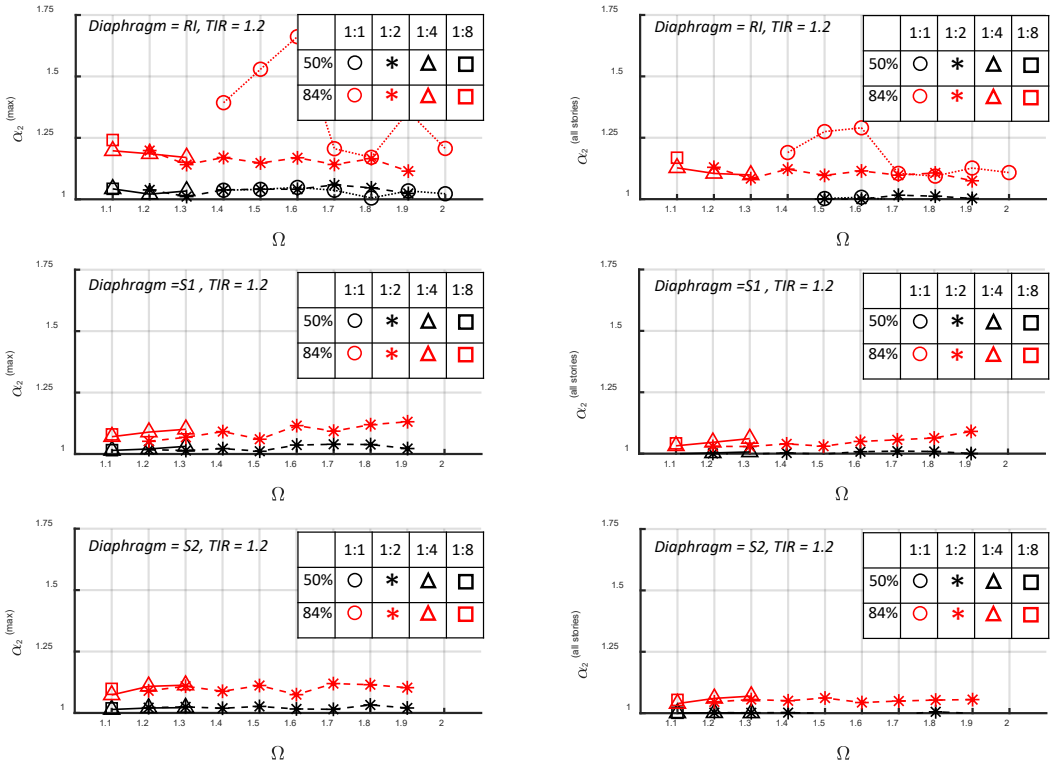

Figure 7. Variation of statistical measures of α_2 concerning Ω, plan aspect ratio, and diaphragm in-plane rigidity for TIR = 1.2 structures: critical story, all stories

The sensitivity of statistical measures of equivalent eccentricity due to plan irregularity and finite in-plane rigidity, respectively, is illustrated in Figures 5 and 6. The estimated equivalent eccentricity is based on the similarity of story drifts for pushover and NLTHA results. The observations and discussion presented for the median of α_2 is applicable for e%; the median of e% is reduced compared to the case with a symmetric floor plan and rigid diaphragm. The reduction is mostly observed for the median of e% of all stories. The statistics for the most critical story was relatively unchanged when floor asymmetry was introduced. For cases with a semirigid diaphragm, the reduction in e% is not as severe as it is for α_2; this is mainly because both pushover and NLTHA estimates of drift are reduced and their ratio (which is how e% is calculated) remains unchanged. Based on the presented results, it is plausible to declare that the 5% accidental torsion provisions of ASCE 7 is relatively conservative for low-rise buildings with semirigid diaphragms or with plan asymmetry if median estimates of e% for all stories are the basis of such code calibration.

The combined effects of plan irregularity and finite in-plane rigidity on α_2 is illustrated in Figures 7. A comparison between Figure 7 and Figure 4 shows that the combination of plan asymmetry and finite in-plane rigidity does not affect the trends observed earlier. Still, the median of α_2 is reduced as finite in-plane rigidity is considered. The increase in observed variations (i.e., 84% estimate of α_2) compared to the case of a symmetric floor plan is an expected phenomenon, as observed in Figure 3.

Concluding Remarks and Future Work

We quantified the equivalent eccentricity and displacement amplifications that capture the accidental torsional moment's effects in low-rise building structures. It is assumed that randomness in VLLRs stiffness is the source of accidental torsion. 4-story buildings with plan aspect ratios of 1:1, 1:3, 1:4, and 1:8, and period ratio Ω ranging from 1.1 to 2.0 are considered. For each combination, 3-D models are generated, and each model consists of a single-bay generic frame whose stiffness and strength are calibrated to meet target dominant periods. Models with various plan asymmetry and diaphragms in-plane rigidity were developed. The coefficient of variation of the stiffness of all structural elements is set to 0.14. By selecting 30 pairs of ground motions representing seismic hazard with average 475 years return period at San Francisco, Monte-Carlo simulation was employed to obtain statistical measures of α_2 and e% due to randomness in VLLRs stiffness.

The results demonstrate that the 5% equivalent eccentricity rule is conservative to capture the effect of accidental torsion in low-rise buildings; in all cases, this value is conservative unless statistics other than the median of all stories are planned to be used as the basis of code calibration. We plan to use instrumented buildings data with recorded translational and rotational responses to validate the presented simulation results.

Acknowledgments

This report's contents were developed under Agreement No. 1019-017 from the California Department of Conservation, California Geological Survey, Strong Motion Instrumentation Program. However, these contents do not necessarily represent that agency's policy or endorsement by the State Government.

References

ATC. (2018) Assessing Seismic Performance of Buildings with Configuration Irregularities: Calibrating Current Standards and Practices. *FEMA P-2012*. Federal Emergency Management Agency

ASCE-American Society of Civil Engineers (2017). *Minimum Design Loads for Buildings and Other Structures* (ASCE/SEI 7–16). American Society of Civil Engineers: Reston, VA.

ASCE-American Society of Civil Engineers (2010). *Minimum Design Loads for Buildings and Other Structures* (ASCE/SEI 7–10). American Society of Civil Engineers: Reston, VA.

Baker, JW. (2011). Conditional Mean Spectrum: Tool for Ground-Motion Selection. ASCE Journal of Structural Engineering, 137 (3), 322-331.

Basu, D., Constantinou, M., Whittaker, A. (2014). An Equivalent Accidental Eccentricity to Account for The Effects of Torsional Ground Motion on Structures. *Engineering Structures,* 69: 1-11.

DeBock, DJ., Liel, AB., Haselton, CB., Hooper, JD., Henige, RA. (2014). Importance of Seismic Design Accidental Torsion Requirements for Building Collapse Capacity. **43**(6) 831-850.

De-la-Colina, J., Almeida, C. (2004). Probabilistic Study on Accidental Torsion of Low-Rise Buildings. *Earthquake Spectra*, 20(1):25-41.

De la Llera, JC., Chopra, A. (1992). Evaluation of Code-Accidental Torsion Provisions using Earthquake Records from Three Nominally Symmetric-Plan Buildings. *SMIP92 Seminar Proceedings*.

De la Llera, JC., Chopra, A. (1994). Accidental Torsion in Buildings Due to Stiffness Uncertainty. *Earthquake Engineering and Structural Dynamics*, 23:117-136.

De la Llera, JC., Chopra, A. (1995). Estimation of Accidental Torsion Effects for Seismic Design of Buildings. *Journal of Structural Engineering*, 121(1):102-114.

Fang, CH., Leon, RT. (2018). Seismic Behavior of Symmetric and Asymmetric Steel Structures with Rigid and Semirigid Diaphragms. Journal of Structural Engineering. **144**(10).

Flores, F., Charney, FA., Lopez-Garci, D. (2018). The Influence of Accidental Torsion on the Inelastic Dynamic Response of Buildings during Earthquakes. **34**(1), 21-53.

Hernandez, JJ., Lopez, O. (2004). Dependence of Accidental Torsion on Structural System Properties. *Proceedings of the 13th World Conference on Earthquake Engineering,* Vancouver, Canada.

Ibarra L.F., Medina R. A., and Krawinkler H. (2005). "Hysteretic models that incorporate strength and stiffness deterioration", Earthquake Engineering and Structural Dynamics, 34(12), 1489-1511.

Lin, WH., Chopra, A., De la Llera, JC. (2001). Accidental Torsion in Buildings: Analysis versus Earthquake Motions. *Journal of Structural Engineering*, 127(5):475-481.

Xiang, Y., Naeim, F., Zareian, F. (2018). Critical Assessment of Accidental Torsion In Buildings with Symmetric Plans using CSMIP Data. *SMIP18*, Sacramento, California.

HUMAN-MACHINE COLLABORATION FRAMEWORK FOR BRIDGE HEALTH MONITORING

Sifat Muin[*], Chrystal Chern[†], and Khalid M. Mosalam[‡]

University of California, Berkeley

Abstract

The importance and relevance of structural health monitoring (SHM) for highway bridges in the United States is highlighted by the bridges' poor condition and the growing amount of resources for data-driven condition assessment in the field of artificial intelligence (AI), particularly, machine learning (ML). To tackle this issue, a human-machine collaboration (H-MC) framework for highway bridge SHM is developed in this study to take advantage of the strengths of both AI and engineering domain expertise. The H-MC framework uses a *physics-based* model (human) to conduct probability of exceedance (POE) analysis coupled with *novelty detection* ML model (machine) to establish a damage detection and assessment algorithm. To produce the training data for the model, nonlinear time history analyses (NTHA) are performed on analytical bridge model for vibration responses to many selected ground motions. Feature extraction and selection are performed using an *Ordinal Fisher Score* analysis with *k-fold cross-validation* parameter tuning to produce the input for training the ML model. A component capacity-based damage state model is used to produce the output for training the ML model. During model validation, the benefit of the H-MC is demonstrated through significant increase in the classification accuracy when the POE analysis is coupled with the ML model. Once the ML model is trained, it is tested on the seismic responses of two instrumented bridges, El Centro - Hwy8/Meloland Overpass and Parkfield - Hwy46/Cholame Creek Bridge. The model accurately classified all 14 undamaged events and one damaged event, including damage assessment consistent with reported visual inspection of the bridge after the damaging event.

Introduction

Structural health monitoring (SHM) of highway bridges is becoming essential as the civil infrastructures in the United States are aging. According to ASCE's 2019 report card for California's infrastructures, 7% of California's bridges are structurally deficient and the largest percentage of bridges in "Poor" condition in the nation belongs to California. Moreover, approximately 50% of bridges in the state have exceeded their design life. The backlog of recommended maintenance, repair, and replacement continues to grow. Therefore, continued health monitoring of these bridges is essential for safe operation and for prioritizing replacement. The monitoring of these vulnerable structures becomes more critical after natural disasters such as earthquakes. The loss of accessibility due to damages and closures of the transportation network can greatly affect the rescue and recovery of a city after major seismic

[*]Post-Doctoral Researcher, sifat.muin@berkeley.edu.

[†]PhD Student, cchern@berkeley.edu.

[‡]Corresponding author, Taisei Professor of Civil Engineering & PEER Director, mosalam@berkeley.edu.

events, turning them into disasters. Utilizing the advances in remote sensing, computing technologies, and data science is an effective and feasible way of structural monitoring of bridges.

Data-driven SHM brings in the capability of machine learning (ML) and deep learning (DL) techniques in developing automated and online damage detection and/or assessment tools for civil infrastructures. With the recent advances in sensor technologies, wireless sensor networks, remote sensing, and computer vision, data science can now be used to develop SHM techniques to assess and quantify the conditions of structures in near-real-time utilizing ML and DL algorithms. ML gives computers the ability to learn about the trends and features of a process without being explicitly programmed (Samuel, 1959) for this process. Currently, ML is the core of artificial intelligence (AI) which has excelled in classification and prediction capabilities. However, ML still lacks contextual intelligence and minimal reasoning capability. The main problem with this approach to AI is that it requires thousands, if not millions, of data examples for training the ML algorithm to be able to function properly. Therefore, ML cannot be adopted in the current form for applications where data is limited. One such application is SHM of bridges to detect damage conditions and categories after seismic events.

In order to enable widespread adoption, AI systems need to shift away from this data-heavy approach and focus on methods that use a combination of different approaches, including systems modelling based on domain expertise. Through such collaborative approaches, humans and AI will actively enhance each other's complementary strengths. However, to fully extract the benefit of this collaboration, humans need to understand and trust the AI systems as they become more involved in making critical decisions alongside the humans. Transparency of the explainable AI (XAI) systems can foster this trust. One way to gain explainability in AI systems is to use ML algorithms that are inherently explainable. In this paper, such a ML tool and structural engineering expertise are utilized to develop the human-machine collaboration (H-MC) framework for highway bridge health monitoring.

Proposed Framework

Human-machine collaboration (H-MC) is a model in which humans co-work with artificial intelligence to complete specific tasks (National Research Council, 2012). The goal of an H-MC model is to utilize the forte of both types of intelligence and minimize the impact of their weaknesses. In this study, an algorithm is developed by following the basic principal of the H-MC model which is employed towards developing an SHM framework. The proposed algorithm leverages the advancements in the field of ML and utilizes response data from undamaged bridge structures (more abundantly available than from damaged bridges) to develop a ML model for a specific structure. Concurrently, an analytical model is developed by a domain expert, i.e., the structural engineer in this case, in order to simulate data of the damaged structure. This approach reduces the uncertainty associated with the computational model by using real data recorded from the structure and at the same time it provides a possible range of data (possibly unseen) from the damaged condition which is not usually available from in-situ measurements of structures. This is because engineered structures are typically damaged due to rare (low occurrence probability) events of natural hazards with high consequences, e.g., earthquakes or hurricanes.

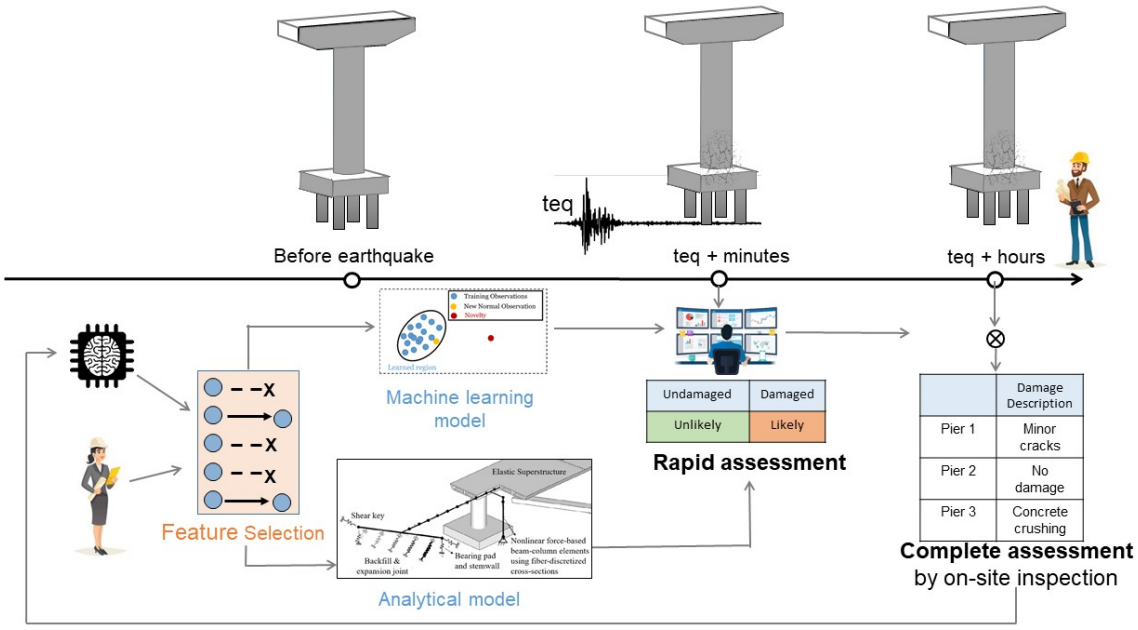

Figure 1: H-MC framework for SHM making use of ML and knowledge of human experts.

Figure 1 illustrates the H-MC framework for bridge SHM. There are two distinct phases. The first phase of the framework is completed before an earthquake occurs. In this phase, the task of feature selection is conducted, and both the analytical model and the ML model are developed[1]. The second phase of the framework takes place during and shortly following an earthquake, where the response of an instrumented bridge is measured and relayed to a remote location where damage sensitive features can be rapidly generated. Consequently, using the previously developed H-MC model, damage detection can be performed in *real time* within minutes after an earthquake. Detailed analytical models along with ML tools can provide further information on damage levels and locations within minutes. However, if a detailed model is missing, the measured response data can be reviewed by a skilled human counterpart to provide a *near real-time* assessment within hours after an event. This can be followed up by a complete on-site investigation by a professional structural engineer as part of a field inspection team if it is deemed necessary following the assessment phase. This complete assessment including field inspection may take days after the event. Following the complete assessment process, the ML model can be updated using the annotated response data including the damage information. In the subsequent sections, this proposed H-MC framework is described in detail including several applications.

ML Model

The proposed framework uses the *novelty detection* method as the ML model. Novelty detection has gained much research attention in application domains of critical systems particularly with those involving large datasets. Conventional ML typically focuses on the classifica-

[1]This dual H-MC model is sometimes referred to in modern literature as a *digital twin*.

tion of two or more classes. The problem of novelty detection, however, is approached within the framework of one-class classification. It can be defined as the task of recognizing unseen data that differs in some respect from the training data.

In the novelty detection approach to classification, "normal" patterns are available for training, while "abnormal" ones are missing. A model of normality M(θ), where θ represents the free parameters of the model, is inferred and used to assign novelty scores $z(x)$ to previously unseen test data x. Larger $z(x)$ corresponds to increased "abnormality" with respect to the model of normality. A threshold $z(x) = k$ is defined to identify novelty as follows,

$$\text{If } z(x) \geq k \rightarrow x \text{ is novelty.} \tag{1}$$

Due to the practical importance and challenging nature of novelty detection, many approaches have been proposed to determine the model of normality M(θ) and the threshold k. In this study, a distance-based approach has been conceived. The responses from undamaged structures are used to develop the M(θ). Multiple features, selected following a feature engineering process (described in a later section of this paper), are utilized. The distance of a point to the centroid of M(θ) is computed using the Mahalanobis distance (Mahalanobis, 1936). Since M(θ) is a multivariate model, not only distance but also the shape and size of the data need to be considered, quantified by the covariance matrix. The Mahalanobis distance[2] takes this covariance matrix into account. For a p-dimensional multivariate sample $\mathbf{x_i} = \{x_{i1}, \ldots, x_{ip}\}$, the Mahalanobis distance is defined as follows,

$$MD_i = \sqrt{(\mathbf{x_i} - \boldsymbol{\mu})^T \mathbf{C}^{-1} (\mathbf{x_i} - \boldsymbol{\mu})} \tag{2}$$

where $\boldsymbol{\mu}$ is the p-dimensional arithmetic mean vector consisting of the mean values of all the variables, and $\mathbf{C}$ is the covariance matrix. For multivariate normally distributed data, the values of the square of MD_i are approximately chi-square distributed with p degrees of freedom, χ^2_p. Conventionally, a certain quantile q (e.g., 0.95) of the χ^2_p distribution is set as the threshold k. In this study, q is considered as a parameter of the novelty model and estimated using the k-fold cross-validation technique.

POE Envelope

The human aspect of the framework is manifested in the probability of exceedance (POE) envelope where structural engineering domain expertise is applied. For this part of the analysis, a structure-specific analytical model based on a single degree of freedom (SDOF) idealization, is developed. This idealization is selected herein for simplicity but more sophisticated models can be equally utilized. The SDOF model properties are based on the structure under consideration and discussed in the "Numerical Example" Section. For this numerical example, the SDOF properties are listed in Table 1. The SDOF model has a nonlinear (inelastic) material that follows Özdemir's rate-independent force-displacement model (Özdemir, 1976).

[2]It is a measure of the distance between a point $\mathbf{x}$ and a distribution $\mathscr{D}$ as a multi-dimensional generalization of measuring how many standard deviations away $\mathbf{x}$ is from the mean of $\mathscr{D}$.

Table 1: Material and dynamic properties of the SDOF model representing Bridge-A.

Yield stress	68 ksi
Yield displacement	0.67 in
Hardening ratio	0.01
Period	0.6 sec
Damping	5%

Nonlinear time history analysis (NTHA) is performed on the model using a set of ground motions from the PEER[3] NGA[4]-West2 database (PEER, 2020; Ancheta et al., 2014). At the time of writing this paper, this database has 21,539 records of shallow crustal earthquakes in active tectonic regions. Due to the possibility of anomalies from older data collection systems, only records from the past 30 years have been selected. Moreover, records with peak ground acceleration (PGA) less than 1% of the acceleration of gravity (g) may not produce enough excitation useful for this study. Therefore, only records with PGA more than 0.01g are considered. To avoid homogeneity in response, not more than 20 records from a single earthquake event are selected. Thus, $n = 1,710$ records matched these criteria. From the SDOF analysis, a damage feature vector $\mathbf{X} = \{X_1, X_2, \ldots, X_m\}$ is computed from the responses. Subsequently, a probability of exceedance (POE) envelope is developed as follows,

$$\begin{aligned}\hat{G}_i = P(DS \geq 1|\mathbf{X_i}) &= \frac{P(DS \geq 1, \mathbf{X} = \mathbf{X_i})}{P(\mathbf{X} = \mathbf{X_i})} \\ &= \frac{\frac{1}{n}\sum_{j=1}^{n}[I(DS)K_H(\mathbf{X_j} - \mathbf{X_i})]}{\frac{1}{n}\sum_{j=1}^{n}[K_H(\mathbf{X_j} - \mathbf{X_i})]} = \frac{\sum_{j=1}^{n}[I(DS)K_H(\mathbf{X_j} - \mathbf{X_i})]}{\sum_{j=1}^{n}[K_H(\mathbf{X_j} - \mathbf{X_i})]}\end{aligned} \tag{3}$$

where $\hat{G}_i$ is the POE of damage at the i^{th} sample (i.e., earthquake event) $(i = 1, 2, \ldots, n)$, DS is the damage state or the damage class with discrete values. Here, $DS = 0$ corresponds to undamaged state and $DS = 1, 2, \ldots$ correspond to different levels of damage. Moreover, $\mathbf{X_i}$ corresponds to the m-dimensional feature vector, $I(DS)$ is the indicator function ($I = 0$ for undamaged state, i.e., $DS = 0$, and $I = 1$ for the damaged state, i.e., $DS \geq 1$), $j = 1, 2, \ldots, n$ refers to the observed data represented by the considered events, and K_H is a multivariate Gaussian kernel.[5] For any vector $\mathbf{V}$, $K_H(\mathbf{V})$ is defined as follows,

$$K_H(\mathbf{V}) = \frac{1}{\sqrt{(2\pi)^m |\mathbf{H}|}} \frac{1}{\sqrt{e^{\mathbf{V}^T \mathbf{H}^{-1} \mathbf{V}}}} \tag{4}$$

where the $m \times m$ bandwidth matrix $\mathbf{H}$ is analogous to the covariance matrix controlling the amount and orientation of the induced smoothing, $|\mathbf{H}|$ is the 2-norm of the matrix $\mathbf{H}$, and superscript T indicates transpose. The kernel assigns a different weight to each data point of $\mathbf{X_i}$

[3]Pacific Earthquake Engineering Research Center.

[4]Next Generation Attenuation Ground Motion Database.

[5]Kernel density estimation is a nonparametric technique for the estimation of the probability density function. In this case the estimate of the density function with bandwidth (smoothing) characterized by H is expressed as $\hat{f}_H(\mathbf{X_i}) = \frac{1}{n}\sum_{j=1}^{n} K_H(\mathbf{X_j} - \mathbf{X_i})$.

that is inversely related to the distance between the data point j and the point of interest i. The Gaussian kernel is centered at the event of interest, i.e., at $\mathbf{X_i}$ and the developed envelope is analogous to the fragility curves. Several studies have applied Gaussian kernel densities to develop univariate fragility curves (Noh et al., 2012, 2015; Lallemant et al., 2015). However, in this study, multiple variables are used.

Figure 2 shows an example POE envelope on a parallel coordinates plot. In this plot, each feature is represented by a vertical axis and individual samples (i.e., earthquake events) are displayed as a line connected across each axis. The colored areas show the POE envelope. The color represents the probability values of the distribution. Green and red represent undamaged and damaged zones, respectively. Moreover, probability of damage increases with shade of the zone, with red zone having the high probability of damage. In this figure two example samples are shown. One falls in the undamaged zone and is hence labelled as undamaged. The other one falls in the red zone and is labelled as damaged.

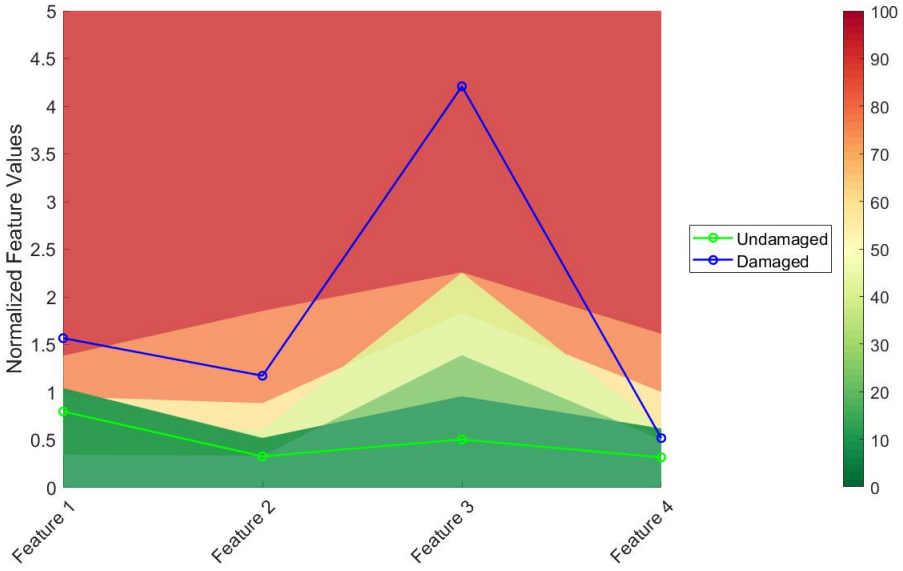

Figure 2: Parallel coordinate plot showing POE envelope with undamaged and damaged zones.

Damage Detection

In this section, the damage detection routine of the H-MC framework is described. For an instrumented bridge, data from previous earthquakes is used to develop the novelty model $\mathrm{M}(\theta)$. The POE envelope for the bridge is developed simultaneously using a SDOF model prior to the earthquakes. In this POE model, the threshold POE value (POE_{th}) for undamaged events and the entries of the bandwidth matrix $\mathbf{H}$ are used as model parameters. The optimal values of these parameters are determined using a 5-fold cross-validation technique.

When data becomes available from a new earthquake, the H-MC framework is activated. It first calculates the features and runs the novelty model. If novelty is not detected, the bridge is identified as undamaged. On the other hand, if novelty is detected, the second phase

of the framework is initiated where the POE value is computed as follows,

$$\hat{G}_i = P(DS \geq 1|\mathbf{X_i^{rec}}) = \frac{\sum_{j=1}^{n}[I(DS)K_H(\mathbf{X_j^{com}} - \mathbf{X_i^{rec}})]}{\sum_{j=1}^{n}[K_H(\mathbf{X_j^{com}} - \mathbf{X_i^{rec}})]} \tag{5}$$

where $\mathbf{X_i^{rec}}$ and $\mathbf{X_j^{com}}$ are respectively the m-dimensional feature vectors of the recorded data and the computed data using the SDOF analysis where $j = 1, 2, \ldots, n$. Subsequently, $\hat{G}_i$ is compared against POE_{th}. When $\hat{G}_i \leq \text{POE}_{th}$, the bridge response to the i^{th} event is identified as undamaged. On the other hand, when $\hat{G}_i > \text{POE}_{th}$, i.e., the data falls in the high probability region, the bridge response to the i^{th} event is identified as damaged.

Damage Assessment

The probability of different damage states for the i^{th} sample is calculated as follows,

$$\hat{G}_{id} = P(DS = d|\mathbf{X_i^{rec}}) = \frac{\sum_{j=1}^{n}[I(DS_d)K_H(\mathbf{X_j^{com}} - \mathbf{X_i^{rec}})]}{\sum_{j=1}^{n}[K_H(\mathbf{X_j^{com}} - \mathbf{X_i^{rec}})]} \tag{6}$$

where $\hat{G}_{id}$ is the probability that the i^{th} sample (i.e., earthquake event) belongs to the damage state d for different levels of damage, i.e., $d = 1, 2, \ldots, D$ where D is the number of considered damage (limit) states, and $I(DS_d)$ is the indicator function ($I = 1$ when $DS = d$, and $I = 0$ otherwise).

When data becomes available from a new earthquake, novelty analysis is conducted. When the data is detected as a novelty, first the damage detection with the POE envelope is checked. The damage assessment follows the damage detection phase. This assessment step is conducted only on the samples for which damage has been detected in the previous step. Once the values of $\hat{G}_{id} \; \forall \; d = 1, 2, \ldots, D$ are computed for the i^{th} sample, the damage state with the highest probability value is assigned as the damage state of this sample.

Numerical Example

A finite element (FE) model of a selected bridge is developed for the study to determine important damage features. A damage feature is some quantity extracted from the measured system response data that is used to indicate the presence of damage in a structure. The simulated vibration response histories of the FE bridge model to a set of 400 selected ground motions is used to extract initial damage features, such as peak accelerations, and corresponding damage states, which range from no damage to extreme damage. The dataset of corresponding damage features and damage states is later used in a feature engineering process called *feature selection* to identify the best damage features for classification of the damage states.

Analytical Bridge Model

The selected bridge for the analytical model is the Jack Tone Road Overcrossing Bridge (referred to for simplicity as Bridge-A), which is a two-span reinforced concrete (RC) highway bridge located in San Joaquin County, California, spanning approximately 220 feet with a

total height of approximately 25 feet. As shown in the photograph of the structure and its original design elevation drawings in Figure 3, the bridge is supported on a single column bent and on seat-type abutments. The FE model of the bridge includes 20 nodes along the deck length and a fiber-section model of the column bent. NTHA of this bridge has been studied extensively to determine the effect of abutment skew-angle on the probability of collapse (Kaviani et al., 2012), improve direct integration algorithms for nonlinear seismic response (Liang et al., 2016), and select and modify bidirectional ground motions for bridge seismic behavior evaluation (Liang and Mosalam, 2020).

Figure 3: Photograph and design elevation of Jack Tone Road Overcrossing Bridge (Bridge-A).

The superstructure and column bent of the Jack Tone Road Overcrossing Bridge both have concrete strength of 5 ksi. The column bent is reinforced with ASTM A706 steel, with 44 #11 bundles of 2 longitudinal bars at a volumetric ratio of 2.00%, and #6 spiral transverse reinforcement at a spacing of 3.34 inches. The structural properties are summarized in Table 2.

Table 2: Jack Tone Road Overcrossing Bridge (Bridge-A) properties (Liang et al., 2016).

# of spans	2
Column bent	Single-column
Column radius	33.1 in.
Column height	22.0 ft.
Abutment	Seat type
Seat length	33.85 in.
Superstructure concrete	$f'_c = 5$ ksi, $E_c = 4030.5$ ksi
Column bent concrete & reinforcing materials	Concrete: 5 ksi, Steel: ASTM A706
Reinf. details of column bent cross-section	Long.: 44 #11 (bundles of 2), $\rho_l = 2.00\%$ Trans.: Spiral, #6 @ 3.34 in.

The bridge FE model simplifies the deck into two symmetric spans of $110'$-$3''$ each, with 20 nodes along the length of the deck. The column bent is modeled with three nodes at

the base of the column, the interface of the column-to-deck joint, and the center of the column-to-deck joint. For the abutments, nonlinear springs connected in series to gap elements are used to model the passive backfill response and the expansion joint, and the shear key response is modeled using an elastic-perfectly-plastic backbone curve (Liang et al., 2016). The super-structure FE modeling details are shown in Figure 4. In order to capture progressive column yielding and damage, the column bent is modeled as a nonlinear beam-column with nonlinear fiber-based beam FE's at 10 quadrature points (Kaviani et al., 2012); refer to Figure 5.

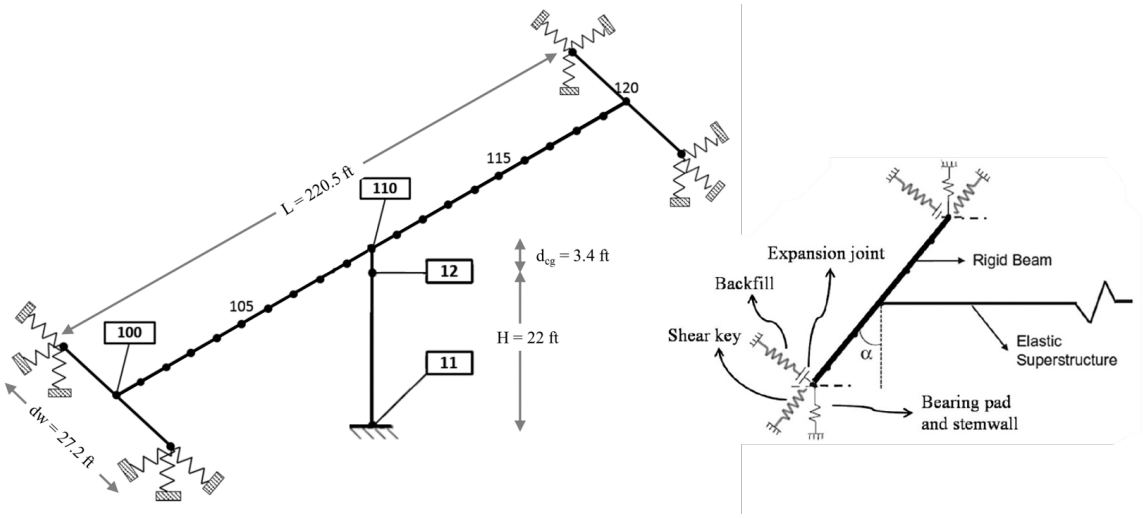

Figure 4: Bridge-A superstructure FE modeling details (Liang et al., 2016).

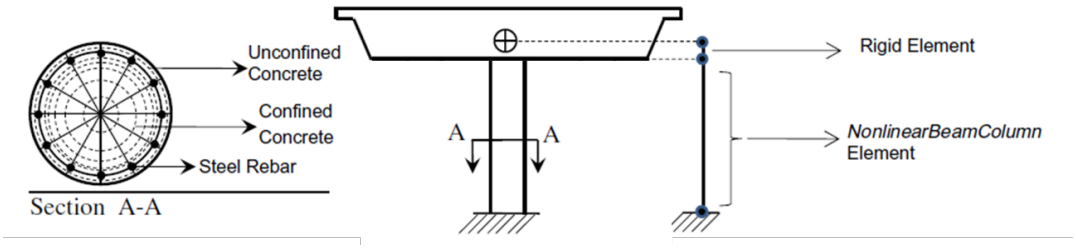

Figure 5: Bridge-A column FE modeling details (Kaviani et al., 2012).

Ground Motion Selection

To produce the vibration response histories from which damage features are extracted, NTHA is performed on the bridge model using 400 ground motions, selected and scaled from the PEER NGA-West2 (Bozorgnia et al., 2014) database, which has 21,539 records of shallow crustal earthquakes in active tectonic regions. Before selecting and modifying the records, they are restricted to the 1,710 ground motions mentioned in "POE Envelope" Section.

Unconditional Selection (US), a spectrum shape matching ground motion selection and modification method, is used to select and scale the ground motions. In the US method, the

median+1.5 standard deviation, σ, spectrum is used as the target spectrum. First, a Monte Carlo simulation is used to probabilistically generate multiple response spectra from a multivariate normal distribution with the logarithmic spectral acceleration means and variances. Then, ground motion records, whose response spectra match the simulated spectra, are selected. Finally, a *greedy optimization* algorithm is applied to improve the match between the target and the sample means and variances. In each iteration of the optimization, one previously selected record is replaced with a record from the database that generates the best improvement in the match (Jayaram et al., 2011).

Out of four common ground motion selection and modification methods, the US method was shown in (Liang and Mosalam, 2020) to produce the best prediction for the covariances of the probability distributions of the seismic demands (PDSD), and the most conservative estimates for the probability of collapse for RC highway bridges with nonlinear responses due to large bidirectional ground motions. Thus, the US method was used to select ground motions for three ground motion scenarios, each with site soil shear wave velocity V_{s30} of 222.95 m/s, strike-slip fault type, and target spectrum of 1.5σ above the median spectrum (for all periods) using the attenuation model in (Campbell and Bozorgnia, 2008). Each ground motion scenario is summarized in Table 3 with 100, 50, and 50 ground motions for the M7d23, M5d50, and M8d23 ground motion scenarios, respectively. These ground motions were each rotated by 90° for a total of 400 ground motions. The results of the US method are summarized in Table 4, which lists the PEER NGA-West2 earthquake ID numbers, earthquake names, and the number of ground motions per earthquake event for the selected set of ground motions with the corresponding response spectra shown in Figure 6.

Damage State Definition

During the NTHA of the bridge model response to the selected ground motions, the stress and strain response histories are recorded at the base and top of the bridge column in order to determine the resulting damage state of the bridge. This study employs a component capacity-based damage state model. In this model, the damage states are defined in seven levels. The damage state criteria are based on Caltrans and PEER visual inspection criteria for levels of column flexural capacity for RC highway bridges. The capacity levels are translated into strain-based limit states at different locations of the cover concrete, core concrete, and longitudinal reinforcing bars, as listed in Table 5. The pushover curve for the bridge model is labeled with each component capacity-based damage state in Figure 7. For the analytical bridge model used in this study, limit states 2, 3, and 4 lie in close proximity to each other on the pushover curve because of the large size of the column, which results in the cover thickness

Table 3: Ground motion scenario summary.

Ground Motion Scenario	Magnitude (M)	Distance (R) [km]	# Records Selected	# Rotated (90°) Records	Total # Records
M7d23	7.0	23	100	100	200
M5d50	5.0	50	50	50	100
M8d23	8.0	23	50	50	100
		Total			**400**

Table 4: Description of selected ground motions.

PEER NGA-West2 earthquake ID number	Earthquake name	Number of ground motions per earthquake event
163	Anza-02	2
170	Big Bear City	1
123	Cape Mendocino	1
173	Chi-Chi (aftershock 3), Taiwan	1
174	Chi-Chi (aftershock 4), Taiwan	1
137	Chi-Chi, Taiwan	34
171	Chi-Chi, Taiwan-02	4
172	Chi-Chi, Taiwan-03	5
173	Chi-Chi, Taiwan-04	6
174	Chi-Chi, Taiwan-05	5
175	Chi-Chi, Taiwan-06	2
346	Christchurch, New Zealand	5
278	Chuetsu-oki	7
281	Darfield, New Zealand	11
169	Denali, Alaska	5
138	Duzce, Turkey	1
280	El Mayor-Cucapah	15
166	Gilroy	1
164	Gulf of California	1
158	Hector Mine	8
279	Iwate	12
129	Kobe, Japan	2
136	Kocaeli, Turkey	3
125	Landers	14
275	L'Aquila (aftershock 1), Italy	2
274	L'Aquila, Italy	1
152	Little Skull Mtn,NV	1
162	Mohawk Val, Portola	1
180	Niigata, Japan	3
127	Northridge-01	5
150	Northridge-05	1
151	Northridge-06	1
179	Parkfield-02, CA	2
176	Tottori, Japan	2
250	Umbria Marche (aftershock 16), Italy	1
277	Wenchuan, China	8
283	Wenchuan, China-02	1
284	Wenchuan, China-03	1
285	Wenchuan, China-04	1
292	Wenchuan, China-11	1
295	Wenchuan, China-14	1
297	Wenchuan, China-16	1
320	Wenchuan, China-39	1
167	Yorba Linda	1
1015	9753485	2
1018	10370141	1
1011	10410337	5
1014	14138080	1
1003	14151344	1
1002	14383980	3
1049	21266207	2
1001	40204628	2
Total (before rotation)		**200**

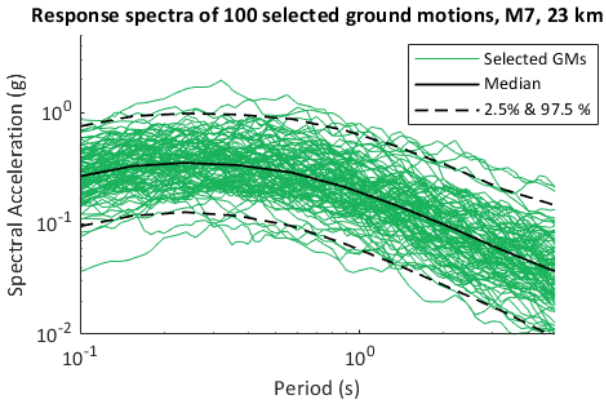

(a) Response Spectra of M7d23 ground motions

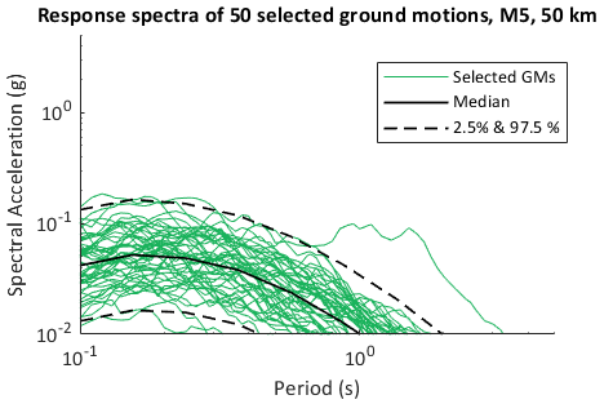

(b) Response Spectra of M5d50 ground motions

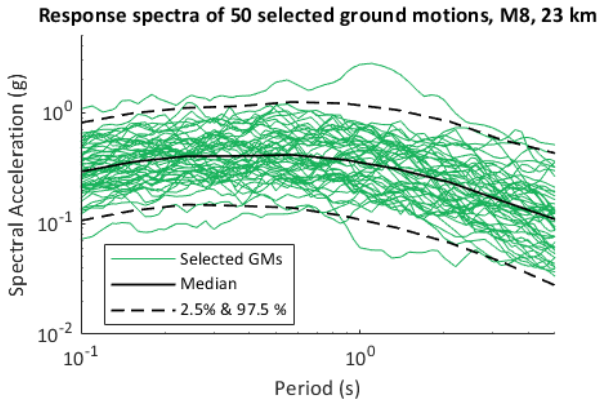

(c) Response Spectra of M8d23 ground motions

Figure 6: Response spectra plots for each of the three ground motion scenarios: (a) M7d23, (b) M5d50, and (c) M8d23, including median and 2.5 & 97.5 percentiles.

constituting a small percentage (i.e., ∼6%) of the column depth. Using the assumption of a linear strain profile throughout the column section (i.e., the assumption made by the Bernoulli-Euler beam theory that "plane sections remain plane"), small changes in the curvature result in the inner cover fibers reach the spalling strain quickly after the outer cover fibers reach the spalling strain. The definitions of limit states 2, 3, and 4 are highly dependent on the model discretization of the cover due to fiber mesh sensitivity. Such sensitivity to model discretization in the nonlinear response of RC beam-columns is discussed in (Kenawy et al., 2020).

Feature Engineering

Feature Extraction

Feature extraction refers to the process of transforming the measured data into some alternative form where the correlation with the damage is more readily observed. After NTHA is performed on the bridge model with the details shown in Figure 4 and using the selected ground motions from the "Ground Motion Selection" Section, damage features are extracted from the resulting vibration response histories. The vibration response at the top of the col-

Table 5: Damage state criteria for component capacity-based model.

Limit State	Caltrans-PEER Description	Criteria Used to Define Strain-Based Limit State	Strain-Based Limit State		
			Fiber Location	Compression or Tension	Strain
0	No damage	–	–	–	–
1	EQ-related tight cracking of cover	Cover cracking: the cover surface reaches tensile strength	Any outermost cover fiber	Tension	$\varepsilon_t = 1.32 \times 10^{-4}$
2	Moderate cracking (mixed orientations) & minor spalling/flaking	Minor spalling: the cover surface reaches compressive strength	Any outermost cover fiber	Compression	$\varepsilon_{sp} = 0.005$
3	Open cracking or major spalling (exterior to confinement)	Major spalling: a significant depth of the cover reaches compressive strength	Any cover fiber at 1/2-3/4 of the cover depth	Compression	$\varepsilon_{sp} = 0.005$
4	Exposed core (interior of confinement)	Exposed core: the entire depth of the cover reaches compressive strength	Any innermost cover fiber	Compression	$\varepsilon_{sp} = 0.005$
5	Visible bar buckling; confinement loss or core shedding	Core shedding: the outer surface of the core begins to fail	Any outermost core fiber	Compression	$\varepsilon_{cu} = 0.025$
	Multi-bar rupture or buckling; large drift; or core crushing	Bar rupture: longitudinal bars reach ultimate tensile strength	Any longitudinal bar	Tension	$\varepsilon_{su} = 0.10$
6	Column collapse (Near-total loss of axial capacity)	Loss of axial capacity: approximately 1/2 of the core fails	All core fibers at 1/4 of the core depth	Compression	$\varepsilon_{cu} = 0.025$

umn bent (Node 110 in Figure 4) is used because the top of the bridge piers are commonly instrumented locations, allowing direct future comparisons to instrumented bridges. The damage features extracted from the vibration response histories include one-dimensional vibration characteristics that have been studied as structural damage indicators by researchers in the past (Farrar and Worden, 2012). In addition to indicating damage on a global level, these features can also be measured at specific locations on the structure, as in the case of this study, to identify the local damage. Other examples of features which have been studied as structural damage indicators include cumulative absolute velocity (*CAV*) (Muin and Mosalam, 2018), higher exponentiations of the acceleration intensity (Sajedi and Liang, 2019), standardized *CAV* (CAV_{STD}) (Campbell and Bozorgnia, 2012), and instantaneous power (*IP*) (Zengin and Abrahamson, 2020). Sixteen damage features, Table 6, are extracted herein in two directions, longitudinal and transverse, for a total of 32 damage features. After the features are extracted, feature selection is performed to identify the best features for the intended damage classification.

Fisher Score Analysis

Feature selection is the process of identifying a subset of the original feature set which increases the learning efficiency while minimizing the reduction in the classification performance. It is performed to determine the best feature vector for this study. Moreover, a filter-based feature selection method, or one in which a *score* is assigned to each feature in order to compute its expected contribution to solving the classification task, is chosen as a computationally inexpensive approach that allows feature selection before the learning phase (Baccianella et al., 2014). One such method is the *Fisher score*, which determines the relative ability of fea-

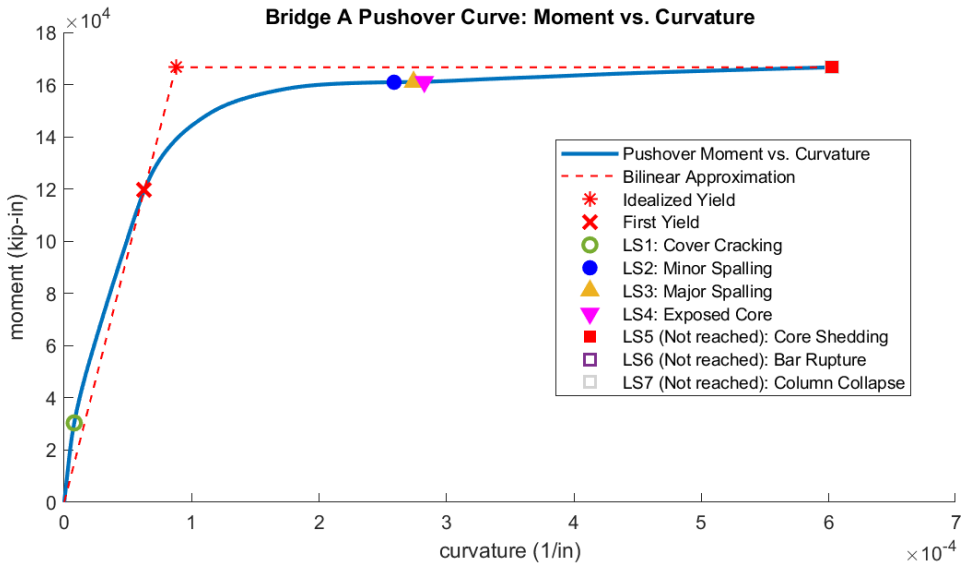

Figure 7: Bridge-A model pushover curve labeled with component capacity-based damage states.

tures to discriminate between categorical classes in a classification model. The Fisher Score is also known in statistical modeling as Fisher ratio, Fisher method, Fisher combined probability score, or information score. The Fisher score for a given feature is defined as the average distance between classes, normalized by the average spread of each class, and a larger Fisher score indicates that the feature is more discriminative. A visualization of the discriminatory power concept used to develop the Fisher score is shown in Figure 8, where 8a shows two features showing a clear distinction among classes, and thus a high Fisher score, and 8b shows two features not ideal for detecting damage, and thus a low Fisher score. Although the Fisher score is known to have limitations in that it considers each feature separately and therefore cannot reveal *mutual information* between features, it is widely used as a heuristic algorithm for feature selection (Gu et al., 2012).

In this study, the goal of the classification model is to determine which class of damage state is indicated by the feature vector. Due to the ordering of the classes in this model (e.g., the 5^{th} damage (limit) state is more severe, and thus ordered higher than the 3^{rd} damage (limit) state, refer to Table 5), feature selection which considers ordinality is required. Thus, an ordinal variant of the Fisher score, termed here as the *Ordinal Fisher Score*, is used for feature selection in this study. The Ordinal Fisher Score is shown to perform better for feature selection in an ordinal classification model than the original Fisher score (Pérez-Ortiz et al., 2016).

The Ordinal Fisher Score for the i^{th} feature, $F_{OR}(x^i)$, is computed following a procedure discussed below. First, the class discrimination term, $F_O(x^i)$ is defined as follows,

$$F_O(x^i) = \frac{\sum_{k=1}^{K}\sum_{j=1}^{K}|k-j|\cdot d^i(\mathscr{C}_k,\mathscr{C}_j)}{(K-1)\sum_{k=1}^{K}(\sigma_k^i)^2} \tag{7}$$

where the class $\mathscr{C}_k$ indicates data from one of the K classes, $k \in 1,\ 2,\ldots,K$, σ_k^i indicates the variance of the i^{th} feature in class k, and $d^i(\mathscr{C}_k,\mathscr{C}_j)$ indicates the distance between classes

Table 6: Description of initial damage features extracted from NTHA for later feature selection.

Feature	Definition or Equation
Peak acceleration	$\max_t(\lvert\ddot{u}(t)\rvert)$
Peak displacement	$\max_t(\lvert u(t)\rvert)$
Peak velocity	$\max_t(\lvert\dot{u}(t)\rvert)$
Arias Intensity	$I_a = \int_0^T [\ddot{u}(t)]^2 dt$
Significant Duration	time between 5% & 95% of the total Arias energy $= t_{0.95} - t_{0.05}$
Cubed Absolute Acceleration Intensity (Sajedi and Liang, 2019)	$\int_0^T [\ddot{u}(t)]^3 dt$
Spectral Acceleration at 0.6 s	$S_a(0.6)$
Spectral Acceleration at 1.0 s	$S_a(1.0)$
Spectral Acceleration at 2.0 s	$S_a(2.0)$
Spectral Acceleration at 5.0 s	$S_a(5.0)$
CAV	$CAV = \int_0^T \lvert\ddot{u}(t)\rvert dt$
R_{CAV}	$R_{CAV} = \frac{CAV_s}{CAV_l}$
Sum of absolute displacements	$\int_0^T \lvert u(t)\rvert dt$
Sum of absolute velocities	$\int_0^T \lvert\dot{u}(t)\rvert dt$
CAV_{STD} (Campbell and Bozorgnia, 2012)	$CAV_{STD} = \sum_{i=1}^{N} \left(H(PGA_i - 0.025) \int_{i-1}^{i} \lvert\ddot{u}(t)\rvert dt \right)$ $H(x)$: Heaviside function ($= 0$ if $x < 0$ & $= 1$ otherwise) N: # non-overlapping 1 sec. time intervals
Instantaneous Power (Zengin and Abrahamson, 2020)	$IP(T_1) = \max_t(\frac{1}{\Delta t} \int_t^{t+\Delta t} V_{filtered}^2(t) dt)$ $V_{filtered} = bandpass\,(\ddot{u}(t), [0.2T_1, 3T_1])$

$\mathscr{C}_k$ and $\mathscr{C}_j$. Next, an ordinality term, $O_R(x^i)$, which incorporates the relative distance between classes, is defined as follows,

$$O_R(x^i) = \frac{\sum_{k=1}^{K-2} \sum_{j=k+1}^{K-1} \sum_{h=j+1}^{K} [\![(d^i(\mathscr{C}_k, \mathscr{C}_h) - d^i(\mathscr{C}_k, \mathscr{C}_j)) > 0]\!]}{\sum_{j=2}^{K-1} (K-j)} \tag{8}$$

where $[\![\cdot]\!]$ is a Boolean test which is 1 if the inner condition is true, and 0 otherwise. This $O_R(x^i)$ score measures the number of ordinal requirements fulfilled for a specific feature i. Finally, the two terms $F_O(x^i)$ and $O_R(x^i)$ are combined in a weighted sum to determine the Ordinal Fisher Score for the i^{th} feature, $F_{OR}(x^i)$ as follows,

$$F_{OR}(x^i) = \alpha \cdot F_O(x^i) + (1-\alpha) \cdot O_R(x^i), \quad \alpha \in (0,1). \tag{9}$$

The distance between classes, $d^i(\mathscr{C}_z, \mathscr{C}_j)$, can be computed in several ways, and this study uses the *Hausdorff distance*, $d_h^i(\mathscr{C}_z, \mathscr{C}_j)$, formulated to allow for use of nonlinear, multi-modal, or non-normal data, and shown in (Pérez-Ortiz et al., 2016) to perform best for ordinal classification. The Hausdorff distance is defined as follows,

$$d_h^i(\mathscr{C}_z, \mathscr{C}_j) = \max \left\{ \max_{x_h^i \in \mathscr{C}_z} \Delta_m(x_h^i, \mathscr{C}_j), \max_{x_v^i \in \mathscr{C}_j} \Delta_m(x_v^i, \mathscr{C}_z) \right\} \tag{10}$$

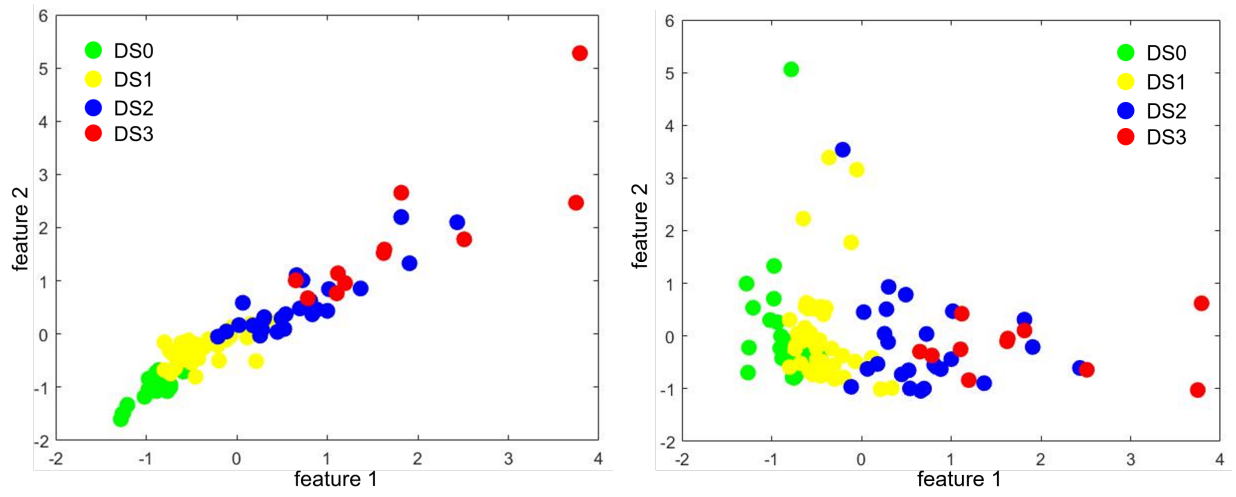

(a) Features with higher discriminatory power

(b) Features with lower discriminatory power

Figure 8: Visualization of discriminatory power using a 2D feature class comparison. (a) Features with a clear distinction among different classes have higher discriminatory power and are more useful for classification. (b) Features without clear distinction are not useful in classification.

where $\Delta_m(x_h^i, \mathscr{C}_j)$ is the minimum Euclidean distance between a point x_h^i and the points in class $\mathscr{C}_j$, expressed as follows,

$$\Delta_m(x_h^i, \mathscr{C}_j) = \min_{x_v^i \in C_j} d(x_h^i, x_v^i) = \min_{x_v^i \in C_j} \sqrt{(x_h^i - x_v^i)^2}. \tag{11}$$

Starting with the 32 initial damage features extracted from the NTHA (Table 6), the Ordinal Fisher Score with weighting factor set to $\alpha = 0.5$ is used to identify which features best discriminate between the different classes of the damage states. The scores of each feature are compared in Figure 9. The results of the Ordinal Fisher Score analysis show that the best features for classification are: 1) peak acceleration in X (longitudinal) direction, 2) spectral acceleration at 0.6 seconds, $S_a(0.6)$, in X direction, 3) sum of absolute velocities in X direction, 4) CAV_{STD} in X direction, 5) CAV_{STD} in Y (transverse) direction, 6) CAV in X direction, and 7) and CAV in Y direction. The results indicate that these features discriminate well between classes of the damage states. The best features for classification based on the Ordinal Fisher Score analysis, Table 7, form a reduced feature vector which allows for greater computational efficiency and are next evaluated in the H-MC analysis for classification accuracy.

k-fold Cross-Validation Analysis

k-fold cross-validation is a resampling procedure used to evaluate ML models where k is the number of groups a given data sample is split into. The general procedure is as follows:

1. Shuffle the dataset randomly.
2. Split the dataset into k groups.

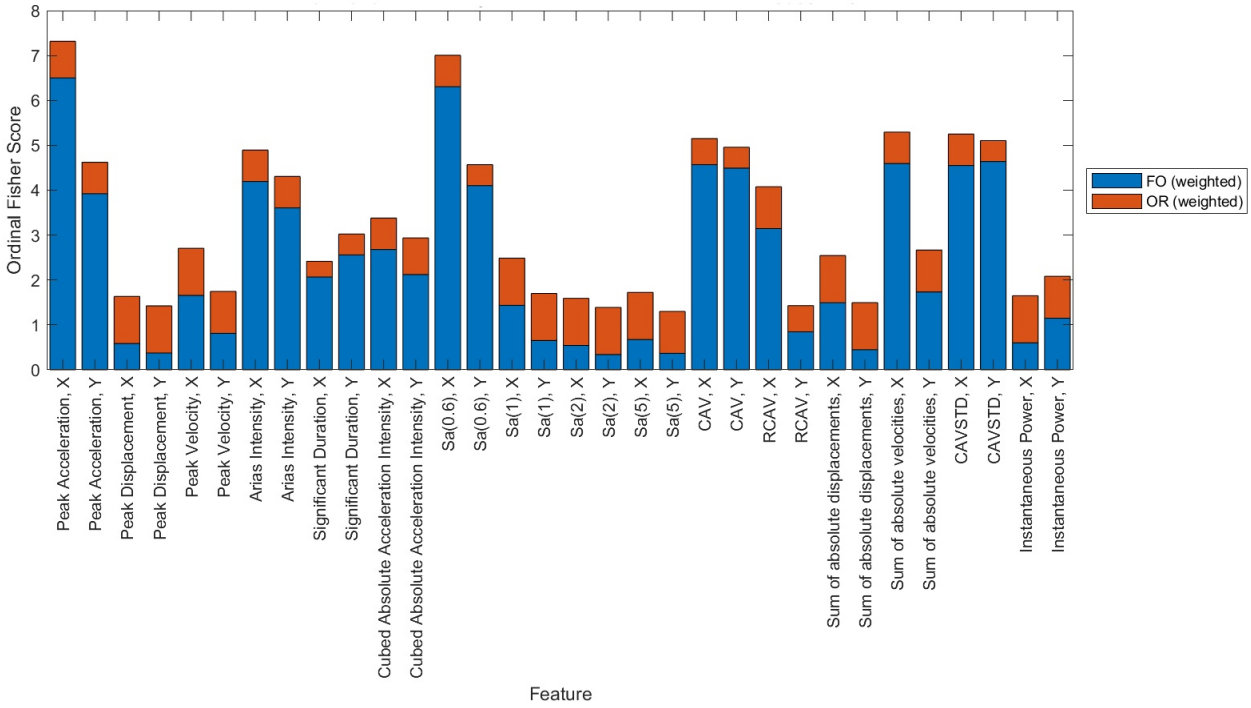

Figure 9: Comparison of Ordinal Fisher Scores for the extracted 32 damage features for the component capacity-based damage state model of Bridge A. *X* & *Y* denote the bridge longitudinal and transverse directions, respectively.

3. For each unique group:
    - Take the group as the validation data set;
    - Take the remaining groups as a training data set; and
    - Fit a model on the training set and evaluate the accuracy on the validation set.
4. Summarize the skill[6] of the model using the average accuracy.

This validation phase gives an opportunity to tune the complexity of the ML model to perform better. In this study, this technique is utilized to finalize the number of features. The first seven selected features from the Ordinal Fisher Score analysis are used to develop a POE model with the SDOF response data. At first, the 5-fold cross-validation technique is applied to the model with one feature (feature with the highest F_{OR}). For each training-validation group, the accuracy is computed as follows,

$$\text{Accuracy} = \frac{\text{\# of correct prediction in the validation set}}{\text{Total \# of samples in the validation set}} \times 100\%. \tag{12}$$

[6]Prediction *skill* is a measure of the accuracy and/or degree of association of prediction to an observation or estimate of the actual value of what is being predicted. An example of a skill calculation is based on the error metric "Mean Squared Error (MSE)".

Table 7: Ordinal Fisher Score analysis results for component capacity-based damage state model. X & Y denote the bridge longitudinal and transverse directions, respectively.

Features with highest Ordinal Fisher Scores
Peak acceleration in X (Feature 1)
$S_a(0.6)$ in X (Feature 2)
Sum of absolute velocities in X (Feature 3)
CAV_{STD} in X (Campbell and Bozorgnia, 2012) (Feature 4)
CAV_{STD} in Y (Campbell and Bozorgnia, 2012) (Feature 5)
CAV in X (Feature 6)
CAV in Y (Feature 7)

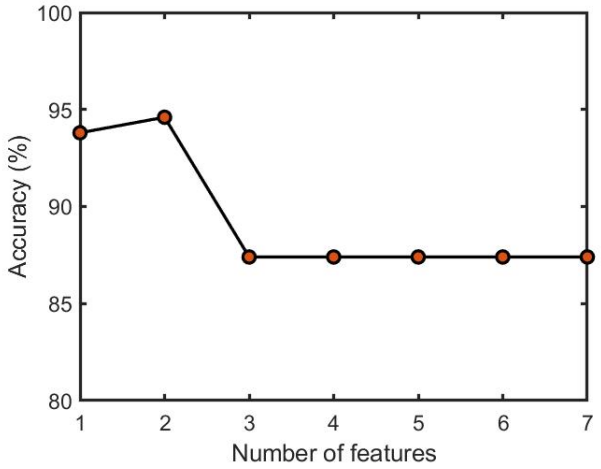

Figure 10: Model complexity (number of features) vs. validation accuracy (skill).

At the end of the 5^{th} groups' analysis, the average accuracy is calculated for the model with one feature. Subsequently, average accuracy is calculated for increasing model complexity (i.e., number of features). Figure 10 shows that the accuracy improves when feature number 2 is introduced in the model but it drops once feature number 3 is added. For the rest of the features, the accuracy remains stable. Therefore, feature number 3 (the sum of absolute velocities in the X direction) is removed as a feature. The final features utilized in the model development are listed in Table 8.

H-MC Analysis

H-MC analysis is performed on the analytical bridge model of Bridge-A using the six selected features (Table 8) and the 400 (Table 4) event responses mentioned earlier. The novelty model is trained on the undamaged responses only. For this purpose, the undamaged responses are separated out of the 400 responses. Three different training and test sets (Set-1, Set-2, and Set-3) are used in the study to evaluate the performance of the model. For each set, 80% of the undamaged sample is randomly selected to train the novelty model. The rest of the undamaged sample is combined with randomly selected damaged events to make up the test set (150 samples).

Table 8: Final feature set after k-fold cross-validation tuning for optimal model complexity; X & Y denote the bridge longitudinal and transverse directions, respectively.

Final Feature Set
Peak acceleration, X (Feature 1)
$S_a(0.6)$, X (Feature 2)
CAV_{STD} (Campbell and Bozorgnia, 2012), X & Y (Features 3 & 4)
CAV, X & Y (Features 5 & 6)

Table 9 presents the accuracy values of the analysis for the three test sets indicating that an average accuracy of 90.2% is achieved when novelty detection alone is used. In contrast, when coupled with the POE analysis for the complete H-MC framework, the average accuracy improves significantly to 98.7%. Therefore, it is evident that the H-MC model is very successful in detecting damage. However, when it comes to assessing damage, the model does a good job with an average accuracy of 82.0%. Figure 11 shows visually the performance of the novelty detection alone and the H-MC method on a tSNE[7] plot. It shows that the novelty detection successfully detects the majority of the damaged events but also misclassifies some of the undamaged events as damaged ones, hence, the accuracy decreases. However, when combined with POE analysis in the H-MC framework, these misclassifed events are correctly classified as undamaged ones.

Although accuracy is an important evaluation measure, it does not present the whole picture. Figure 12 presents the confusion matrices for damage detection using novelty only and H-MC. It shows that novelty detection alone misclassifies a significant portion of the undamaged cases as damaged (58% for Set-1 and Set-2 and 38% for Set-3). In contrast, the H-MC analysis has misclassification rate in all three sets of less than 4% for both the undamaged and damaged states, which further shows the effectiveness of the H-MC framework in damage detection. H-MC classifies a very small fraction of the damaged samples as undamaged which could be a problem for SHM. However, this can be improved by a better model for POE beyond the SDOF.Figure 13 shows the confusion matrices for damage assessment which shows DS1 (Damage (Limit) States (DS) are shown in Table 5) as the dominant class, i.e., most of the test samples are classified as DS1. This can be attributed to the fact that both datasets (60% of the Bridge-A data and 57% of the SDOF data) are governed by the DS1 limit state. Furthermore, none of the 400 samples (corresponding to the simulations using the 400 ground motions of the selected 200 records augmented by their 90° rotations, Table 4) belonged to DS2 and only one sample belonged to DS3. In contrast, DS1 and DS4 had 240 and 57 samples, respectively. This disproportionate distribution of samples occurred due to the close proximity of DS2, DS3, & DS4, which was also reflected on the SDOF training dataset. Therefore, it is expected that the damage assessment performance will be improved when limit states are well-separated and data from all the damage states are equally represented in the SDOF dataset.

[7] t-Distributed Stochastic Neighbor Embedding (tSNE) is a nonlinear technique for dimensionality reduction that is particularly well suited for the visualization of high-dimensional datasets. It is extensively utilized in ML applications. The axes of the tSNE plots, herein labeled $tSNE_1$ and $tSNE_2$, have non-physical meaning due to mappings through iterative nonlinear transformations.

Table 9: Accuracy of the novelty and H-MC model for the three test sets.

Test	Accuracy		
	Novelty Detection	H-MC: Damage Detection	H-MC: Damage Assessment-POE
Set-1	90.7%	100%	82.7%
Set-2	90.7%	97.3%	81.3%
Set-3	89.3%	98.7%	82.0%
Average	**90.23%**	**98.7%**	**82.0%**

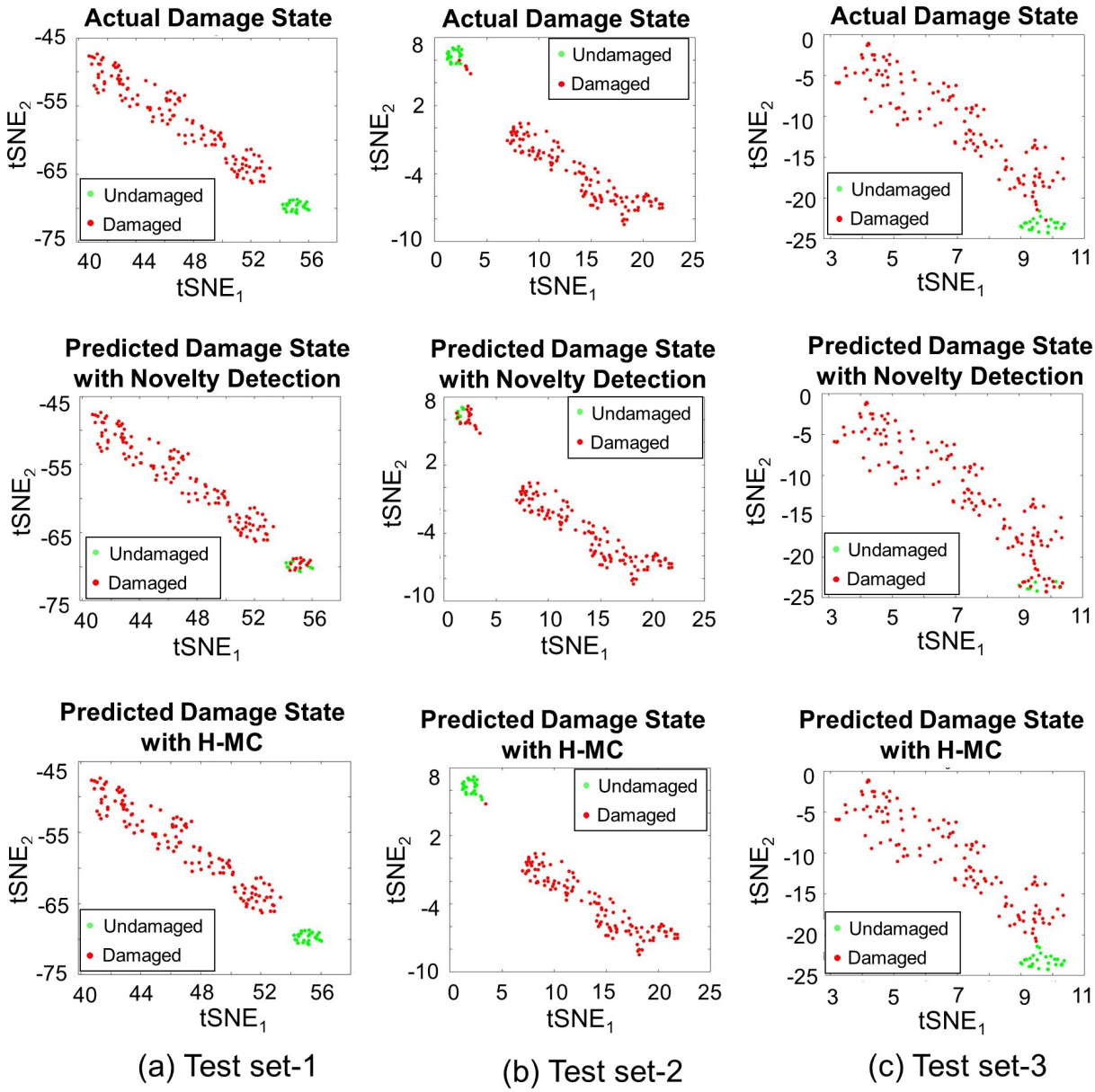

Figure 11: tSNE visualization of the actual and predicted damage states for test sets: (a) Set-1, (b) Set-2, and (c) Set-3.

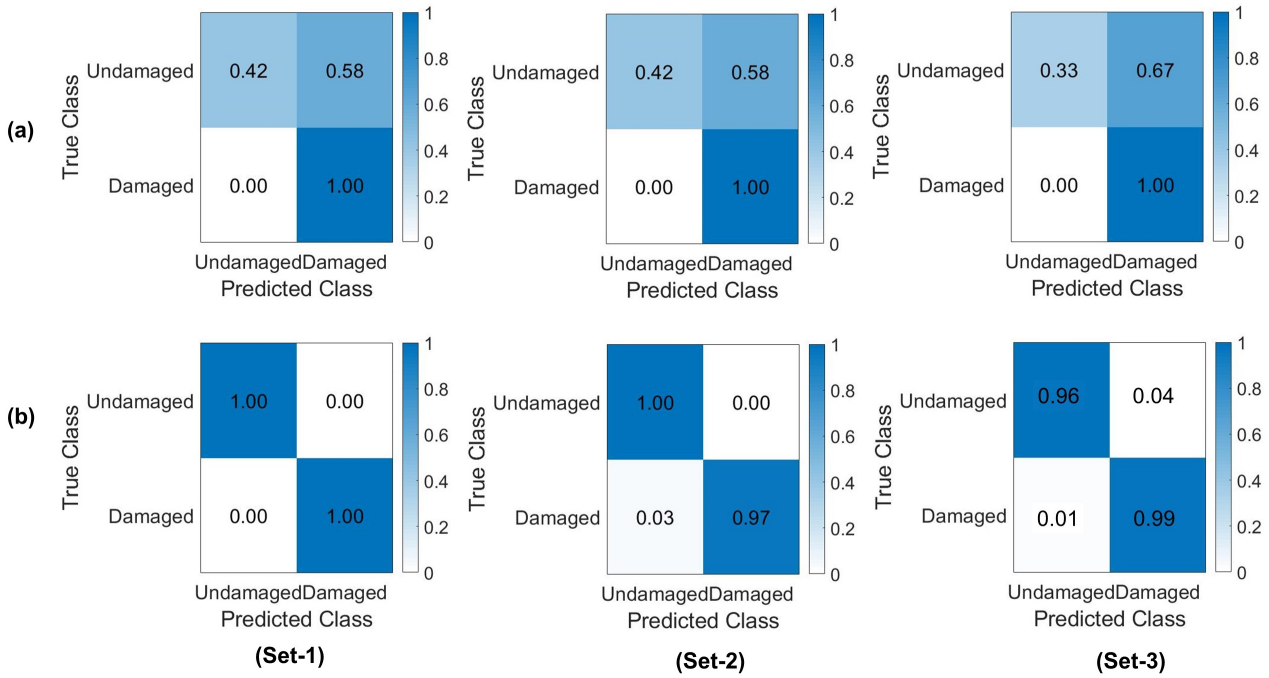

Figure 12: Confusion matrices for damage detection of the three test sets for: (a) Novelty detection model, and (b) H-MC framework (novelty + POE).

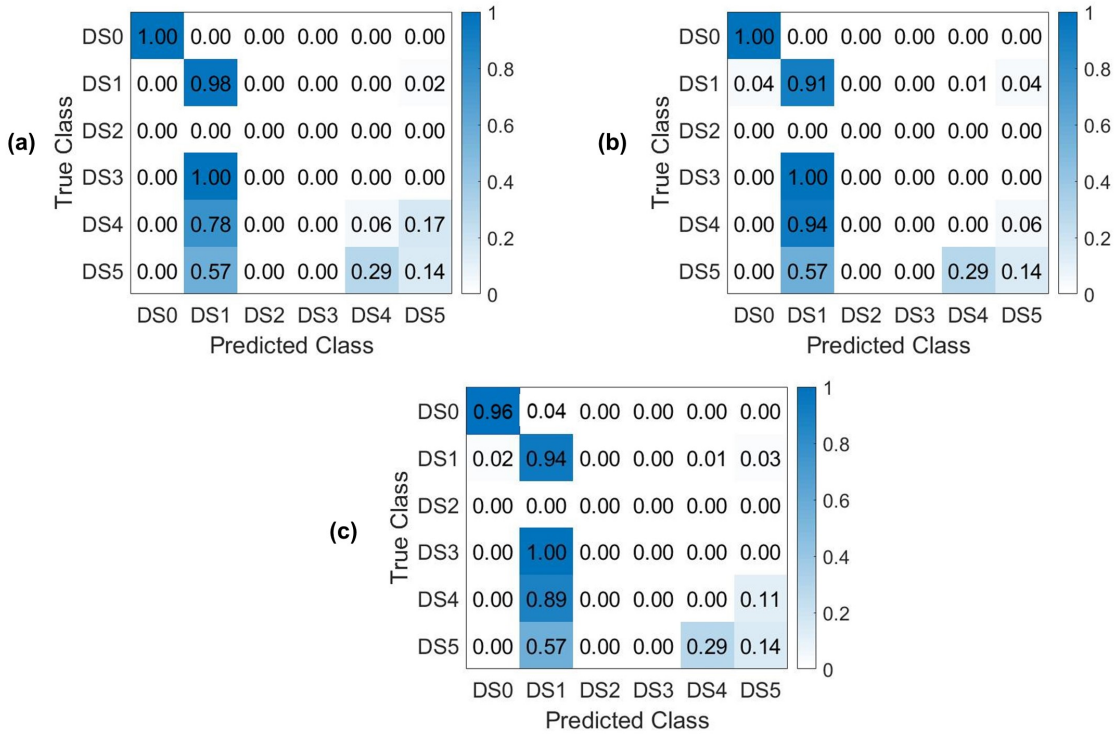

Figure 13: Confusion matrices for damage assessment using H-MC for test sets: (a) Set-1; (b) Set-2; (c) Set-3.

Applications

El Centro - Hwy8/Meloland Overpass

The Meloland Road Overpass which is located near El Centro, California is a non-skewed bridge. It is approximately 208 ft long and 34 ft wide with each span measuring 104 ft. The depth of the deck is 5.5 ft. The height of its 5 ft-diameter column is approximately 21 ft, which is supported on 25 timber piles with a square concrete cap. The monolithic abutment backwalls have a height of approximately 13 ft. The bridge is instrumented with 29 sensors. Figure 14 shows the sensor locations of the bridge. The average feature values of the sensors from 13 recorded earthquake events are utilized in this study.

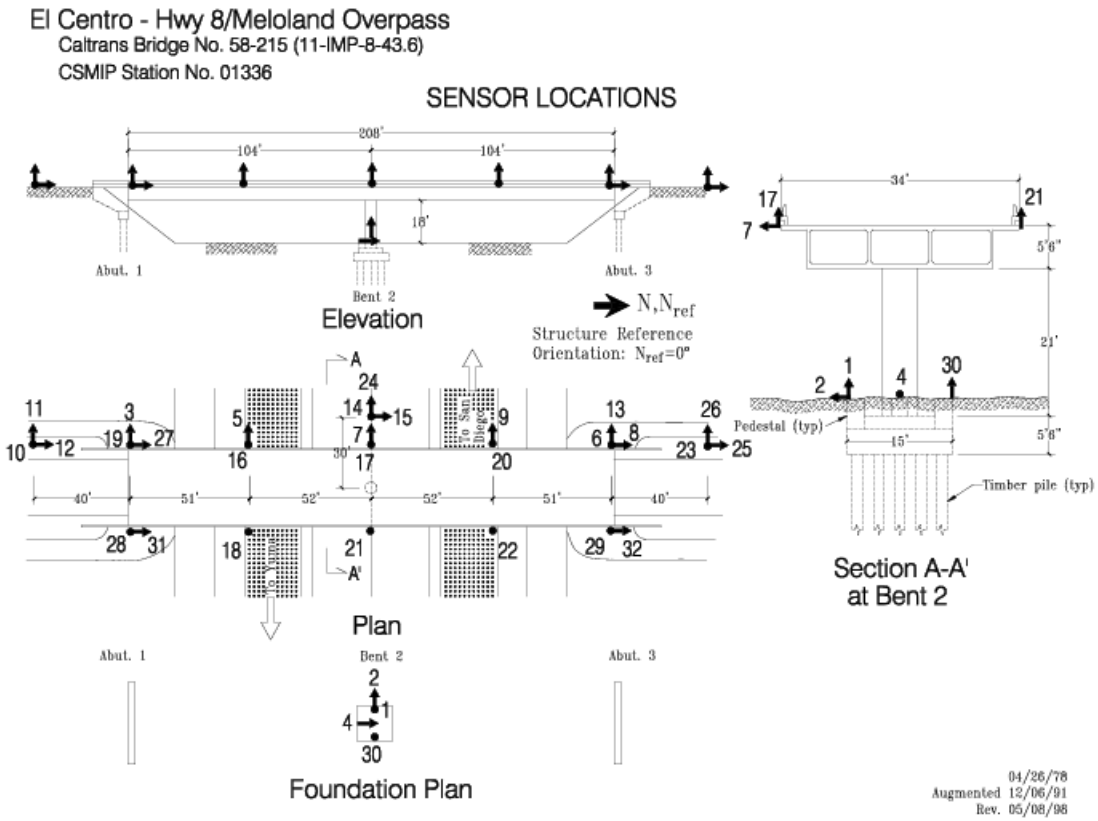

Figure 14: Sensor locations of the Meloland Road Overpass.

For the novelty model, 7 randomly selected events were used to train the model. All 13 events are utilized as the test set. In order to develop the POE envelope, the period reported in (Shamsabadi et al., 2011) is used to develop the SDOF model. Figure 15 shows the actual and predicted tSNE plots for the 13 events. It shows that all the undamaged events have been correctly detected as undamaged. Figure 16 compares the events with the POE envelope. Here, the POE envelope for Feature 1 (peak acceleration, X) spans a smaller distribution than the

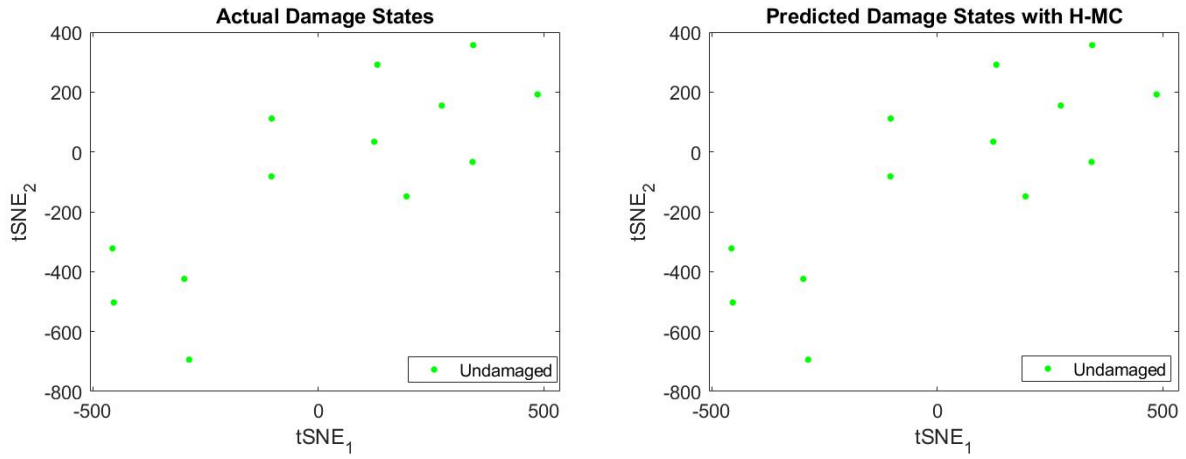

(a) Actual damage states (b) Predicted damage states

Figure 15: tSNE plots for the 13 events of Meloland Overpass Bridge.

other features, which results in white space at the top left corner of the plot. In addition, overlapping regions between POE values result in variations in darkness of the shaded regions. The order of features from left to right corresponds to Ordinal Fisher Scores of these features from highest to lowest. Figure 16 shows that the bridge experienced a higher level of shaking for one event (Calexico Earthquake on April 4, 2010). However, this event in 2010 was not strong enough to cause any damage.

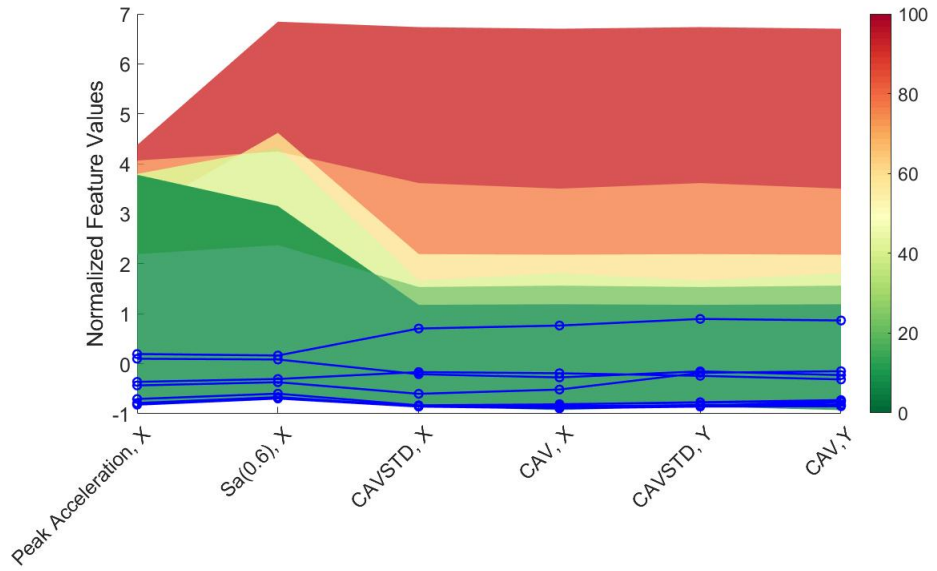

Figure 16: Normalized features and POE envelope of the Meloland Overpass Bridge.

Parkfield - Hwy46/Cholame Creek Bridge

The Cholame Creek Bridge located near Parkfield, California is a slightly-skewed RC slab bridge with five spans and supported by piles. The bridge spans Cholame Creek and is

130 ft long and 44 ft wide, widened in 1979 from its original width of 33 ft. The west end of the bridge is supported by a monolithic diaphragm abutment and the east end is supported on a seat abutment at the original portion and a diaphragm abutment at the widened portion. The bridge is instrumented with six sensors, and Figure 17 shows the sensor locations. The average feature values of the sensors from 2 recorded earthquakes are utilized in this study. In particular, one of these recorded earthquakes, the 2004 M_w[8] 6.0 Parkfield Earthquake, induced a peak structural horizontal acceleration of 1.047g measured by the bridge sensors, and signs of minor damage were observed during inspection after the event. With only 2 recorded events, it was not possible to develop the novelty model using recorded data. In this case, the novelty model for Bridge-A was utilized. The two recorded events are used as the test set. In order to develop the POE envelope, the period reported in (Boardman et al., 2006) is used to develop the SDOF model.

Figure 18 shows the actual and predicted tSNE plots for the 2 events. It is noted that the novelty model labelled both events as novelty. However, the H-MC method correctly detected the undamaged and damaged cases. Figure 19 compares the events with the POE envelope. It shows that San-Simeon earthquake (December 22, 2003) produced low levels of shaking for which the bridge falls in the green (undamaged) zone. For the Parkfield earthquake (September 28, 2004), however, the first two features fall in the red (damaged) zone. The damage assessment algorithm indicated the damage level to be DS1 in this case, consistent with the observed minor damage upon inspection following the 2004 earthquake.

Discussion and Conclusion

This study establishes an H-MC framework for bridge structural health monitoring. The framework uses a *novelty detection* ML model and a feature engineering procedure including feature selection using the *Ordinal Fisher Score* and model parameter tuning using *k-fold cross-validation*. First, the response of an analytical bridge model from nonlinear time history analysis with 400 ground motions is used to extract 32 one-dimensional damage features and damage states. The damage features are based on vibration characteristics with potential to indicate structural damage, and the damage states are based on levels of strain response according to a component capacity-based model. Next, an Ordinal Fisher Score feature selection analysis is used to determine the features with highest discriminatory power between classes of damage state. Using the seven highest-scoring features, k-fold cross-validation with $k = 5$ is performed with a POE analysis to determine the set of features which achieves optimal model complexity.

Following the feature engineering process, a ML model is trained using the selected feature set and the 400 ground motion responses to form the H-MC analysis, which is used to perform binary damage detection and multiclass damage assessment. Coupling the novelty detection model with a POE analysis is shown to increase average damage detection accuracy to 98.7%, an 8% increase from the novelty detection model alone. Furthermore, misclassification within the undamaged test set decreased by 34-58% when the POE analysis is applied together with the novelty detection. For multiclass damage assessment, the H-MC analysis achieved an

[8]The moment magnitude scale is a measure of an earthquake's magnitude ("size" or strength) based on its seismic moment (a measure of the work done by the earthquake).

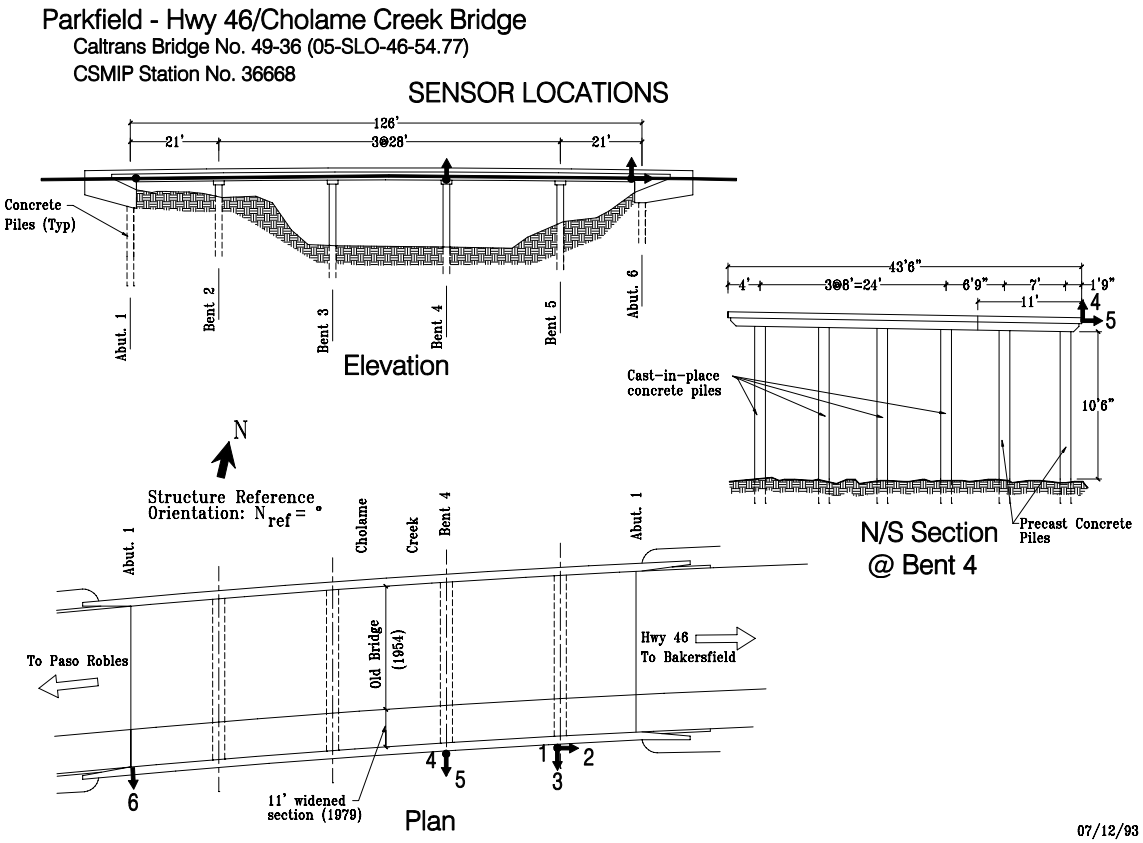

Figure 17: Sensor locations of the Cholame Creek Bridge.

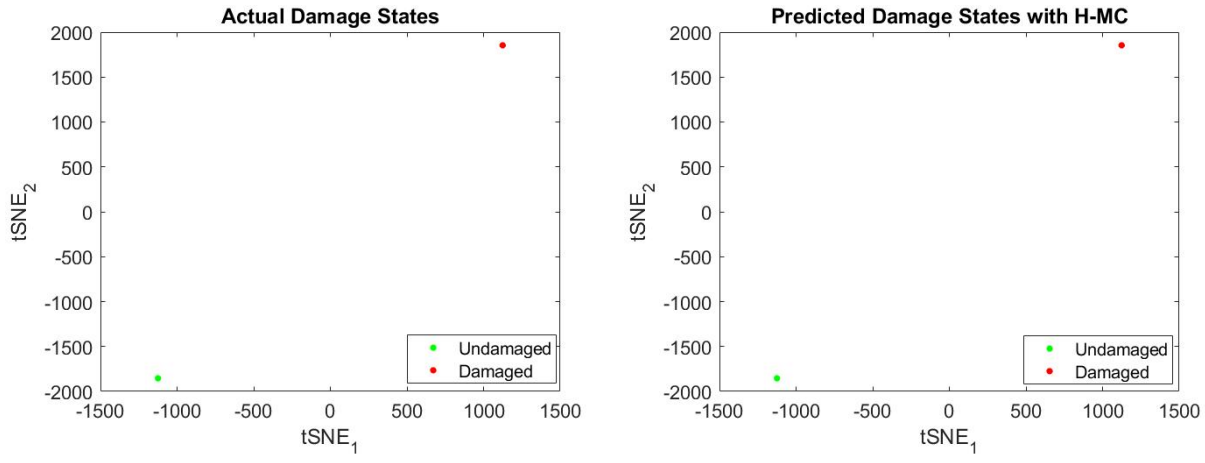

(a) Actual damage states

(b) Predicted damage states

Figure 18: tSNE plots for the 2 events of the Parkfield Cholame Creek Bridge.

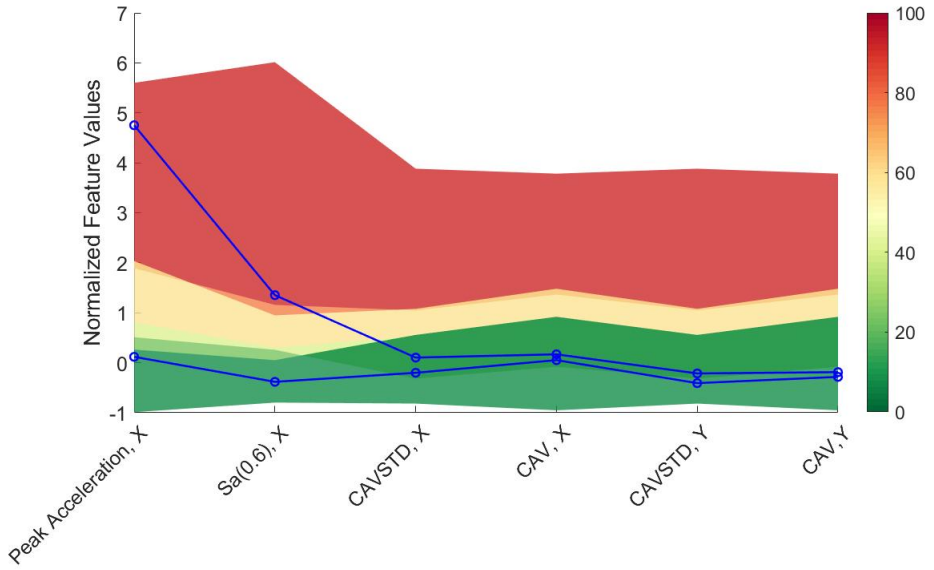

Figure 19: Normalized features and POE envelope of the Parkfield Cholame Creek Bridge.

average accuracy of 82%, which is judged to be reasonable and can be improved further in the future by using a more sophisticated analytical model than the SDOF for the POE analysis.

The application of the H-MC framework on two CSMIP[9]-instrumented bridges, namely El Centro-Hwy8/Meloland Overpass and Parkfield-Hwy46/Cholame Creek bridge, resulted in accurate classification of all fourteen undamaged events as undamaged and the one damaged event as damaged. In addition, the one damaged event was classified as DS1, which is consistent with the reported minor cracking observed during visual inspection after the event. Overall, the proposed framework will facilitate a rapid and efficient decision-making process regarding emergency response and immediate use/closure of bridges. These lifelines are essential transportation infrastructure that should remain functioning for community resiliency, before, during and after major earthquake events.

Acknowledgements

This research is supported by the California Department of Conservation, California Geological Survey, Strong Motion Instrumentation Program agreement 1019-016. The second author thanks the US NSF for the financial support provided by the NSF's Graduate Research Fellowship Program. The authors appreciate Dr. S. Günay's valuable input during this study.

References

ANCHETA, T. D., R. B. DARRAGH, J. P. STEWART, E. SEYHAN, W. J. SILVA, B. S.-J. CHIOU, K. E. WOODDELL, R. W. GRAVES, A. R. KOTTKE, D. M. BOORE ET AL., "NGA-West2 database," *Earthquake Spectra* 30 (2014), 989–1005.

[9]California Strong Motion Instrumentation Program.

BACCIANELLA, S., A. ESULI AND F. SEBASTIANI, "Feature selection for ordinal text classification," *Neural computation* 26 (2014), 557–591.

BOARDMAN, B. T., A. V. SANCHEZ, G. MARTIN, Z. ZAFIR, E. RINNE AND J. TOGNOLI, "Seismic Response of the Hwy 46/Cholame Creek Bridge During the 2004 Parkfield Earthquake," in *Fifth National Seismic Conference on Bridges & HighwaysMultidisciplinary Center for Earthquake Engineering ResearchCalifornia Department of TransportationFederal Highway AdministrationTransportation Research Board*A23 (2006).

BOZORGNIA, Y., N. A. ABRAHAMSON, L. A. ATIK, T. D. ANCHETA, G. M. ATKINSON, J. W. BAKER, A. BALTAY, D. M. BOORE, K. W. CAMPBELL, B. S.-J. CHIOU ET AL., "NGA-West2 research project," *Earthquake Spectra* 30 (2014), 973–987.

CAMPBELL, K. AND Y. BOZORGNIA, "Use of cumulative absolute velocity (CAV) in damage assessment," in *Proc. of 15th World Conf. in Earthquake Eng* (2012), 1–10.

CAMPBELL, K. W. AND Y. BOZORGNIA, "NGA ground motion model for the geometric mean horizontal component of PGA, PGV, PGD and 5% damped linear elastic response spectra for periods ranging from 0.01 to 10 s," *Earthquake Spectra* 24 (2008), 139–171.

FARRAR, C. R. AND K. WORDEN, *Structural health monitoring: a machine learning perspective* (John Wiley & Sons, 2012).

GU, Q., Z. LI AND J. HAN, "Generalized fisher score for feature selection," *arXiv preprint arXiv:1202.3725* (2012).

JAYARAM, N., T. LIN AND J. W. BAKER, "A computationally efficient ground-motion selection algorithm for matching a target response spectrum mean and variance," *Earthquake Spectra* 27 (2011), 797–815.

KAVIANI, P., F. ZAREIAN AND E. TACIROGLU, "Seismic behavior of reinforced concrete bridges with skew-angled seat-type abutments," *Engineering Structures* 45 (2012), 137–150.

KENAWY, M., S. KUNNATH, S. KOLWANKAR AND A. KANVINDE, "Concrete Uniaxial Nonlocal Damage-Plasticity Model for Simulating Post-Peak Response of Reinforced Concrete Beam-Columns under Cyclic Loading," *Journal of Structural Engineering* 146 (2020), 04020052.

LALLEMANT, D., A. KIREMIDJIAN AND H. BURTON, "Statistical procedures for developing earthquake damage fragility curves," *Earthquake Engineering & Structural Dynamics* 44 (2015), 1373–1389.

LIANG, X. AND K. M. MOSALAM, "Ground motion selection and modification evaluation for highway bridges subjected to Bi-directional horizontal excitation," *Soil Dynamics and Earthquake Engineering* 130 (2020), 105994.

LIANG, X., K. M. MOSALAM AND S. GÜNAY, "Direct integration algorithms for efficient nonlinear seismic response of reinforced concrete highway bridges," *Journal of Bridge Engineering* 21 (2016), 04016041.

MAHALANOBIS, P. C., "On the generalized distance in statistics," (National Institute of Science of India, 1936).

MUIN, S. AND K. M. MOSALAM, "Localized Damage Detection of CSMIP Instrumented Buildings using Cumulative Absolute Velocity: A Machine Learning Approach," in *SMIP18 Seminar on Utilization of Strong-Motion Data, Sacramento, California* (2018).

NATIONAL RESEARCH COUNCIL, *Intelligent Human-machine Collaboration: Summary of a Workshop* (National Academies Press, 2012).

NOH, H. Y., D. LALLEMANT AND A. S. KIREMIDJIAN, "Development of empirical and analytical fragility functions using kernel smoothing methods," *Earthquake Engineering & Structural Dynamics* 44 (2015), 1163–1180.

NOH, H. Y., D. G. LIGNOS, K. K. NAIR AND A. S. KIREMIDJIAN, "Development of fragility functions as a damage classification/prediction method for steel moment-resisting frames using a wavelet-based damage sensitive feature," *Earthquake Engineering & Structural Dynamics* 41 (2012), 681–696.

ÖZDEMIR, H., "Nonlinear transient dynamic analysis of yielding structures [Ph.D. Thesis]," (1976).

PEER, *PEER NGA West2 Database* (2020), available at `https://ngawest2.berkeley.edu/`, accessed February 3, 2020.

PÉREZ-ORTIZ, M., M. TORRES-JIMÉNEZ, P. A. GUTIÉRREZ, J. SÁNCHEZ-MONEDERO AND C. HERVÁS-MARTÍNEZ, "Fisher Score-Based Feature Selection for Ordinal Classification: A Social Survey on Subjective Well-Being," in *International Conference on Hybrid Artificial Intelligence Systems* (Springer, 2016), 597–608.

SAJEDI, S. O. AND X. LIANG, "Vibration-based semantic damage segmentation for large-scale structural health monitoring," *Computer-Aided Civil and Infrastructure Engineering* (2019).

SAMUEL, A. L., "Some Studies in Machine Learning Using the Game of Checkers," *IBM Journal of Research and Development* 3 (1959), 211–229.

SHAMSABADI, A., T. OSTROM AND E. TACIROGLU, "Three dimensional global nonlinear time history analyses of instrumented bridges to validate current bridge seismic design procedures," in *Seminar on Utilization of Strong-Motion Data, Los Angeles, CA* (2011).

ZENGIN, E. AND N. A. ABRAHAMSON, "A vector-valued intensity measure for near-fault ground motions," *Earthquake Engineering & Structural Dynamics* 49 (2020), 716–734.

RECENT DEVELOPMENTS IN STRUCTURAL HEALTH MONITORING

Charles R. Farrar

The Engineering Institute
Los Alamos National Laboratory

Abstract

The process of implementing a damage detection strategy for aerospace, civil and mechanical engineering infrastructure is referred to as structural health monitoring (SHM). The SHM process compliments traditional nondestructive evaluation by extending these concepts to online, in situ system monitoring on a more global scale. For long term SHM, the output of this process is periodically updated information regarding the ability of the structure to perform its intended function in light of the inevitable aging and degradation resulting from operational environments. After extreme events, such as earthquakes or blast loading, SHM is used for rapid condition screening and aims to provide, in near real time, reliable information regarding the integrity of the structure.

This presentation will briefly summarize the historical developments of SHM technology, which have been primarily driven by four applications: rotating machinery, offshore oil platforms, civil infrastructure, and aerospace structures. Next, the current state of the art is summarized where the SHM problem is described in terms of a statistical pattern recognition paradigm. In this paradigm, the SHM process can be broken down into four parts: (1) Operational Evaluation, (2) Data Acquisition and Cleansing, (3) Feature Extraction and Data Compression, and (4) Statistical Model Development for Feature Discrimination. This talk will then focus on recent developments related to both the sensing hardware and data analysis aspects of SHM. Some final comments will be made on outstanding technology development and validation needs that are necessary for more widespread adoption of SHM.

AN OPTICAL SENSOR AND WIRELESS MESH NETWORK FOR DIRECT MEASUREMENT OF BUILDING INTERSTORY DRIFT

David McCallen

University of Nevada, Reno
and Lawrence Berkeley National Laboratory

Abstract

Advancements in sensor technologies and communication networks are creating new opportunities for advanced methods of measuring earthquake response and damage in critical infrastructure systems. Based on applied R&D sponsored by the U.S. Department of Energy (DOE), new optically-based sensor systems have been developed that provide for continuous measurement and rapid transmission of key infrastructure response observables immediately after an earthquake. The short latency of the underlying physics of optical sensors, and the ability to perform high resolution measurements across a broad frequency bandwidth are attributes that make optical-based measurement systems particularly attractive for applications in earthquake response measurement. Concurrently, transformational progress underway in wireless communications and the Internet of Things (IOT) are enabling new paradigms for expedient deployment of sensor systems and rapid extraction and analysis of time-critical data.

Building interstory drift is a key earthquake response observable that is broadly utilized as a design parameter in many engineering standards to define performance-based limit states, maximum allowable story deformations, and quantification of damage in post-earthquake assessments. Historically, drift measurement has been obtained through signal processing and double integration of accelerometer data, which is challenging particularly if inelastic, permanent drifts occur. To date, there has been no widely accepted methodology or technology for reliable and accurate direct measurement of building drift.

This presentation will describe recent advancements in a new optically-based sensor system for direct measurement of interstory drift. The third generation of a *Discrete Diode Position Sensor* (DDPS), which utilizes laser light to directly measure drift, is described and data from experimental laboratory tests illustrating high-resolution sensor performance are presented. The ability to measure both Transient Interstory Drift (TID(t)) and Residual Interstory Drift (RID) is demonstrated. To facilitate efficient deployment of the optical sensor systems, a practical, wireless mesh network for reliable, rapid extraction of building data has been developed. The mesh network is based on a system of dedicated low-power radio-frequency (RF) nodes that can self-configure and form a dynamic network throughout a building structure. Experience from the first field deployment of the optical sensor and mesh communication network are described for a DOE mission-critical facility in the San Francisco Bay Area.